LYSOSTAPHIN-DELIVERING HYDROGELS TO TREAT ORTHOPAEDIC DEVICE INFECTIONS

A Dissertation
Presented to
The Academic Faculty

by

Christopher Thomas Johnson

In Partial Fulfillment
of the Requirements for the Degree
Doctor of Philosophy in the
Wallace H. Coulter Department of Biomedical Engineering
Georgia Institute of Technology & Emory University

Georgia Institute of Technology
May 2018

LYSOSTAPHIN-DELIVERING HYDROGELS TO TREAT ORTHOPAEDIC DEVICE INFECTIONS

Approved by:

Dr. Andrés J. García, Advisor
George W. Woodruff School of Mechanical Engineering
Georgia Institute of Technology

Dr. Rodney M. Donlan
Clinical and Environmental Microbiology Branch, Division of Healthcare Quality Promotion
Centers of Disease Control and Prevention

Dr. Robert E. Guldberg
George W. Woodruff School of Mechanical Engineering
Georgia Institute of Technology

Dr. Lars F. Westblade
Pathology and Laboratory Medicine, Weill Cornell Medicine
Cornell University

Dr. Edward A. Botchwey
Wallace G. Coulter Department of Biomedical Engineering
Georgia Institute of Technology

Date Approved: December 14, 2017

To my family and friends

ACKNOWLEDGEMENTS

I would like to first start off with thanking my wife for her continuous love, support, and encouragement throughout my graduate training thus far. I never would have been able to complete this work and maintain my sanity without her. Over the past 4.5 years of this PhD and 6.5 years of graduate school you have provided continuous support, both emotionally and financially, allowing me to do my best possible work. You listened to me whine, tolerated me feeling defeated at times, and then gave me the tough love I needed to continue on. Most importantly, you always made sure I kept everything in perspective and knew when it was time for a cocktail and some oysters. I need to thank Noci too. Our beautiful furry apricot miniature goldendoodle named Nocelle. You were a great thesis doggy and made writing so much better. Thank you for always wagging your tail and being happy to see me.

Thank you Mom and Dad. You provided me with continuous love and support my entire life, even if you weren't so sure about my decision to do this whole MD/PhD thing. You have been amazing role models and guides throughout my entire life, and I know for a fact that I would not be where I am today if it weren't for the values you instilled in me growing up. Mom, I never would have gotten through this if some of your lab skills, attention to detail, and precise ways in the kitchen weren't passed down to me. Dad, thank you for teaching me to be productively lazy, which definitely saved me countless hours in lab by making me find ways to work more efficiently. Scott, you have been around almost my entire life and have always pushed me to do good work, whether it be to keep up with

your successes, or for us to achieve things together. Thank you for being a great brother and keeping me in line.

Thank you to the Artymovich family, especially Bob and Elaine, for welcoming me into your family and letting me steal your daughter away to Atlanta. You have always been interested in what I'm doing and supported me throughout my studies.

To my advisor, Andres Garcia. I am incredibly fortunate to have had you as an advisor. Even though I had never pipetted before joining lab, was your first MD/PhD student, and an electrical engineer by training, you decided to take me on as a student. I still remember sitting in your office listening to you tell me that we had the opportunity to shape the field of implant infections. I naively believed you, but truly think we have made significant contributions to the field of orthopaedic implant infections. You have been a fantastic mentor, both personally and professionally, and what I have learned from you will continue to influence my own mentorship style throughout my career. You always provided me with anything I needed to complete my work, and most importantly, listened to me and took my opinions seriously. You always kept everything in perspective and never let me get too lost in the details. In addition to an advisor, you have been a friend. I'll never forget our trip to NYC for the Lysin Meeting. We shared a lot of laughs, food, and drinks throughout my time at GT.

Thank you to my thesis committee. You have been great advisors throughout my graduate training and have provided critical feedback to make this project better. Lars Westblade, you introduced me to so many people and provided countless ideas to make my research better, beginning with our meetings over coffee at CHOA. Thank you Bob

Guldberg for your input on mechanical testing and μCT analysis. Also for giving me the opportunity to travel to Washington DC for the BEMA meeting, and introducing me to everyone there (Go Green!). Rod Donlan, your expert microbiological opinion was invaluable throughout my research process, and your input always pushed me to improve my methodologies. To Ed Botchwey, thank you for your input towards improving the inflammatory profiling studies. The flow cytometry studies added a very interesting perspective to my work.

A big thank you to everyone, past and present, in the Garcia Lab. You made my training a great experience, and I actually looked forward to coming into lab and working with you every day. I need to especially thank Amy Clark, Jose Garcia, Karen Martin, Jessica Weaver, and Rachit Agarwal for all the surgery help. Karen especially, since it seemed like you spent more time in the OR with me than working on your own experiments at times. Amy, thanks for being a great friend and climbing partner, even if I did think you hated me for the first year I was in lab. Jose, you have been a great friend throughout my training, especially since we shared so many GFOGER frustrations. Rachit, I learned so much from you. Thank you for being a great person to work (especially our time at Emory) with and always having time to explain and teach. James, my μCT data would still not be analyzed if it weren't for you. You have been a great undergraduate to work with and I wish you the best of luck in your graduate training. Devon, Efrain, and the rest of the happy our / lunch crew, thanks for instigating and helping to take the edge off. Thank you Eric for always keeping the lab in order, making sure we all have everything we need, and providing important technical suggestions. I also need to thank Susan Lehman, even though

we only worked together a few months, you taught me everything I know about microbiology, and dealt with my non-existent lab skills while training me.

I especially need to thank Caitlin Sok. Your help with all of the flow cytometry studies definitely added a great dimension to my thesis, and the experiments wouldn't have been possible without you. Also, thank you for being a great friend and someone to commiserate with about being an MD/PhD at GT.

Thank you everyone in the Guldberg Lab. You guys were great people to share the Liar and lab space with. Albert, Brennan, and Brett, thank you for being great happy hour and lunch friends.

I need to thank my Atlanta family and friends. I have met so many great people here, both in and out of school, who have made my time in medical and graduate school so much fun. You were all a great outlet for stress relief and fun.

To the PRL veterinarians and support staff: Dr. Richard and Dr. Laura, you provided critical input and training on animal techniques throughout my PhD and completing it would not have been possible without you. Thank you for tolerating my infected mice and keeping their best interest in mind. Thank you Kim Benjamin and all of the support staff, Andrea Gibson, Altair Rivas, Ogeda Blue, Brittany Hunt, Cindy Wheeler, Kim Woodard, Kristen Schuppe, Josh Scarbrough, Rebecca Graham, Nick Parnell, and Malaka Thomas. You all kept both me and my mice smiling.

Thank you IBB staff, for providing me with the core facilities required for completing this research. I would like to especially thank Andrew Shaw, Steve Woodard,

Aqua Asbury, and Angela Lin for all the technical training and advice necessary to complete this research. Thank you Michelle Wong and Allan Echols for always smiling and being supportive.

Thank you to the Emory MD/PhD program, especially the directors, Chuck, Kerry, and Bob, for providing grant letters of recommendation and always advocating for us. Mary, you have done so much for so many students. Thank you for supporting me throughout your time with the program. Anita, thanks for all your help throughout the grant application process. Your expertise was one of the main reasons I was able to obtain a fellowship. Joanna, thank you for putting my anxiety over transitioning to the clinical years at ease. Thank you Paul and Ann for being great role models for aspiring physician scientists. Thank you Cathy and Erica, for your continued administrative support and making sure my grant is handled properly and that I am registered for classes each term.

Research reported in this dissertation was supported by the National Institute of Arthritis and Musculoskeletal and Skin Diseases of the National Institutes of Health under Award Numbers R01AR062920, R01AR062368, a Ruth L. Kirschstein National Research Service Award F30AR069472, and the Emory University Medical Scientist Training Program T32GM008169. The content is solely the responsibility of the authors and does not necessarily represent the official views of the National Institutes of Health or the Centers for Disease Control and Prevention. Use of trade names and commercial sources is for identification only and does not imply endorsement by the Public Health Service or the US Department of Health and Human Services.

TABLE OF CONTENTS

LIST OF TABLES

LIST OF FIGURES

LIST OF SYMBOLS AND ABBREVIATIONS

PEG	poly (ethylene glycol)
MRSA	methacillin resistant staphylococcus aureus
μCT	microcomputed tomography
BMP-2	bone morphogenetic protein 2
VRSA	vancomycin resistant staphylococcus aureus
VPM	bi-cysteine peptide cross-linker containing MMP-sensitive cleavage site
RGD	GRGDSPC adhesive peptide
GFOGER	synthetic triple helical ligand containing 'GFOGER' hexapeptide sequence
PEG-4MAL	4-arm poly(ethylene glycol) with terminal maleimide groups
DNA	Deoxyribonucleic acid
PEEK	Poly (ether ether ketone)
ROS	reactive oxygen species
SPECT	single photon emission computed tomography
IR	infra-red
AMP	antimicrobial peptide
PLLA	poly (L-lactic acid)
PLGA	poly (lactic-co-glycolid acid)
PCL	poly (caprolactone)
MSC	mesenchymal stem cell
rhBMP-2	recombinant human bone morphogenetic protein 2
CFU	colony forming unit
PMMA	poly (methyl methacrylate)

TCP	tricalcium phosphate
FDA	Food and Drug Administration
HMPC	hydroxypropylmethlycellulose
US	United States
H&E	hematoxylin and eosin stain
saf-O/FG	safranin-O and fast green stain
Lst	lysostaphin
ANOVA	analysis of variance
ALP	alkaline phosphatase
MES	2-(N-morpholino)ethanesulfonic acid
TSA	trypitic soy agar
BHI	brain heart infusion
NHS	N-Hydroxysuccinimide
PBS	phosphate buffered saline
MUP	methylumbelliferyl phosphate
TSB	tryptic soy broth
TBS	tris buffered saline
TBS-T	tris buffered saline with 0.05% Tween-20
BSA	bovine serum albumin
RIPA	radioimmunoprecipitation assay
BCA	bicinchoninic acid
BMP-7	bone morphogenetic protein 7
BMP-14	bone morphogenetic protein 14
AST	aspartate aminotransferase
ALT	alanine aminostransferase

AM	anti-inflammatory monocyte
IM	inflammatory monocyte
MDSC	myeloid derived suppressor cells

SUMMARY

Biomaterial implants are a critical component to successful treatment of many types of orthopaedic injuries. In 2004, over 2.6 million orthopaedic devices were placed with 4% developing infections, resulting in an economic burden of nearly $2 billion. In the United States, nearly 112,000 orthopaedic device infections occur annually with *Staphylococcus aureus* being the most common pathogen accounting for roughly 33% of all infections. Bacterial infection of orthopaedic implants frequently results in complete removal of the implant despite aggressive antibiotic therapy. Lysostaphin is an antimicrobial enzyme specific to staphylococcal species. It is composed of a cell wall targeting domain, responsible for its specificity, and a lytic domain that catalytically degrades the peptidoglycan cell wall of bacteria, causing cell lysis. We have previously engineered a poly (ethylene glycol) (PEG)-based hydrogel system for controlled delivery of therapeutic proteins. We have shown that BMP-2 delivery facilitates bone repair in a murine radial segmental defect model. Contamination of these BMP-2 loaded hydrogels with bacteria leads to complete inhibition of bone healing, persistence of bacteria, and bone resorption. The objective of this project was to engineer PEG-based hydrogels that prevent and treat orthopaedic infections while simultaneously repairing orthopaedic injuries. The central hypothesis was that delivery of lysostaphin using a PEG-hydrogel will reduce infection and promote bone repair using mouse models of orthopaedic device infections.

We engineered injectable hydrogels for the delivery of lysostaphin to infected mouse femoral fractures. Encapsulation of lysostaphin within a PEG hydrogel carrier provided an *in situ* polymerizable delivery platform that maintained enzyme activity and

stability while conforming and adhering to the injured tissue. Lysostaphin-delivering hydrogels were effective at eliminating infection, and provided enhanced anti-biofilm activity compared to soluble lysostaphin *in vitro.* Lysostaphin-delivering hydrogels eradicated mouse femoral fracture infections and out-performed soluble lysostaphin delivery as well as prophylactic antibiotic administration. Infected fractures treated with lysostaphin-delivering hydrogels healed equally well as uninfected fractures, as measured by μCT analysis and mechanical testing. The local cytokine milieu of infections treated with lysostaphin-delivering hydrogels was no different than uninfected fractures, demonstrating restoration of a normal healing microenvironment. Additionally, lysostaphin-delivering hydrogels were effective at eliminating methicillin resistant *S. aureus* (MRSA) infections. Taken together these results show that lysostaphin delivery via a hydrogel carrier is effective at treating biomaterial-stabilized femoral fracture infections.

Segmental bone defect injuries have infection rates reported as high as 30% and successful treatment often requires bone grafting, multiple surgeries, and unacceptably high therapeutic failure rates. To address this unmet clinical need, we extended our lysostaphin-delivering hydrogel to co-deliver both lysostaphin and BMP-2 in order to investigate simultaneous elimination of infection, and induction of growth factor-mediated bone repair of non-healing segmental defects. Lysostaphin and BMP-2 co-delivery effectively eliminated bacterial infection and promoted bone regeneration in our mouse radial segmental defect infection model. We characterized the local inflammatory response to infections treated with lysostaphin-delivering hydrogels and showed that the local cytokine profile is no different than uninfected defects at both 1 and 4 weeks post-operation. In addition, no differences between the inflammatory cell profiles were observed

for infections treated with lysostaphin-delivering hydrogels one week after implantation. These results demonstrate that lysostaphin and BMP-2 co-delivery can eliminate infection and facilitate segmental bone defect regeneration.

We also investigated the activity of lysostaphin-delivering hydrogels to reduce established *S. aureus* infections *in vivo*. We developed a novel model of established *S. aureus* infection by modification to the mouse radial segmental bone defect model. Infections were first initiated by placing infected hydrogel implants and bacteria were allowed to colonize the injury for one week. Once the infection was established, the infected implants were removed, the wound was debrided and washed, and a lysostaphin-delivering hydrogel was injected at the injury site. Our results indicated that lysostaphin delivery alone reduced biofilm infection but significant bacteria numbers remained. However, a combined effect was seen when both lysostaphin hydrogels and systemic antibiotic therapy were delivered together. These results show that lysostaphin-delivering hydrogels effectively reduce established *S. aureus* orthopaedic infections.

This research is innovative because it develops bi-functional materials that prevent and treat *S. aureus* infections while simultaneously repairing orthopaedic injuries. Additionally, lysostaphin provides specifically targeted bacteriolytic activity, acting as an alternative to traditional antibiotic therapy, which may help to reduce the spread of antibiotic-resistant bacteria. As outcomes of this research, we have engineered a lysostaphin delivery vehicle to eradicate long bone fracture infections, prevent infection of non-healing segmental defect injuries while simultaneously regenerating bone, and reduced bacteria using a segmental defect model of established biofilm infection. This

research has established a strategy for preventing and treating orthopaedic biomaterials implants that could be extended to other biomedical device infection scenarios.

INTRODUCTION AND SPECIFIC AIMS

1.1 Introduction

Biomaterial-associated infections account for over one million nosocomial infections per year (*1*). Infection prevention and treatment is a critical component to successful regenerative medicine strategies, as infection leads to significant patient morbidity and even mortality, frequently resulting in complete removal of the implant despite aggressive antibiotic therapy (*1*). *Staphylococcus aureus* is the most clinically significant gram-positive pathogen associated with implanted orthopaedic device failure (*2*). Lysostaphin is a bacteriolytic enzyme with specific activity against staphylococcal species. The lysostaphin enzyme is composed of two domains, a cell wall targeting domain, that provides specificity to staphylococcal species, and a lytic domain, which provides antimicrobial activity by catalytically degrading the bacterial cell wall, leading to lysis (*3, 4*). Additionally, lysostaphin is effective at reducing bacteria growing in biofilm, and provides an enhanced effect when administered with antibiotics (*5, 6*). Lysostaphin is effective against methicillin resistant *S. aureus* (MRSA) and vancomycin resistant *S. aureus* (VRSA) (*7-9*), and has been shown to be effective at treating staphylococcal infections in several animal models (*7, 9-13*). Taken together, these characteristics make lysostaphin an ideal candidate for treating infections primarily limited to staphylococcal species. However, lysostaphin therapy has been significantly limited by a lack of effective delivery vehicles.

The **objective** of this project is to engineer novel lysostaphin-delivering hydrogels to reduce infection and enhance bone repair in murine models of implant-associated

orthopaedic infection. The **central hypothesis** is that controlled delivery of lysostaphin from our osseo-repartive hydrogels will reduce infection, allowing for bone repair to occur. The proposed work is **innovative and significant** because it establishes a local strategy to effectively reduce bacterial infections during bone healing using an antimicrobial bacteriospecific enzyme. This proposed work could have implications for other biomedical implants that are associated with morbidity and mortality due to bacterial infection. **By engineering PEG-based hydrogels to release lysostaphin, we will reduce infection and improve bone repair without the need for antibiotics.** This will be achieved through the following specific aims.

1.2 Specific Aim 1

Engineer injectable hydrogels for the delivery lysostaphin to infected bone fractures

We hypothesize that controlled local delivery of lysostaphin to infected bone fractures will eliminate *S. aureus* infection in a murine femur fracture model. We engineered poly(ethylene glycol) PEG hydrogels that release active lysostaphin in response to local environmental cues. We evaluated the ability of lysostaphin-delivering hydrogels to eliminate *S. aureus* infections and support fracture healing using a pin-stabilized femur fracture model. We measured bacterial counts and bone repair by μCT imaging, performed histology and mechanical testing, and characterized the host inflammatory response to lysostaphin therapy using cytokine array profiling. Lysostaphin-delivering hydrogels were benchmarked against systemic antibiotic therapy and soluble lysostaphin delivery. We also tested the ability of lysostaphin-delivering hydrogels against MRSA infections.

1.3 Specific Aim 2

Engineer PEG hydrogels co-delivering lysostaphin and BMP-2 to eliminate *S. aureus* infection and repair non-healing segmental bone defects.

We hypothesize that *in vivo* co-delivery of lysostaphin and BMP-2 will eliminate bacterial infection and promote bone repair in an infected mouse radial segmental defect model. Lysostaphin-delivering hydrogels were investigated *in vivo* using a mouse radial segmental defect model. Hydrogels containing lysostaphin and BMP-2 were infected with *S. aureus*, implanted into the mouse model, and radial defect healing was monitored over time with μCT imaging. Infection clearance was analyzed by histology and bacterial counts, and functional healing was assessed with torsion to failure testing. Lastly, we characterized the inflammatory response to lysostaphin delivering hydrogels by performing cytokine profiling and flow cytometry of the local wound environment.

1.4 Specific Aim 3

Engineer injectable lysostaphin-delivering hydrogels to treat established *S. aureus* infections in non-healing segmental bone defects

We hypothesize that lysostaphin-delivering hydrogels will reduce established *S. aureus* infections *in vivo*. We developed a murine model of an established *S. aureus* infection by implanting infected hydrogels and allowing for the infection to establish itself over the course of one week. One week after the infection was initiated, the implant was removed, the wound was washed and debrided, and a lysostaphin-delivering hydrogel was placed.

One week later, bacterial counts were assessed. Systemic antibiotic therapy with and without lysostaphin delivering hydrogels was also assessed.

1.5 Significance and Innovation

This research is **innovative** because it develops a biomaterial platform that reduces infection without the use of antibiotics, thereby mitigating the development of antibiotic resistant bacteria while minimizing orthopaedic device failure. As outcomes of this research, we established the feasibility of controlled lysostaphin release from hydrogels to reduce infection and promote bone repair. This research established a strategy for infection-resistant biomaterials that is applicable to other biomedical devices.

LITERATURE REVIEW

SCAFFOLD-BASED ANTI-INFECTION STRATEGIES IN BONE REPAIR[1]

Implant-associated infection is a significant clinical problem (*1*). Bacterial colonization of implants is associated with surgical sites, central line access points, ventilators, surgical drains and shunts, urinary and central venous catheters, and others. Current strategies used to prevent such infections include, but are not limited to, antibiotic therapy, healthcare-provider hygiene, environmental controls such as isolation or negative pressure rooms, surface coatings and modifications, sterilization, and the use of sterile technique during procedures. Nearly all types of bacteria and fungi are capable of infecting implanted devices (*1*). Some of the most common pathogens include *Staphylococcus aureus, Staphylococcus epidermidis, Pseudomonas aeruginosa, Cutibacterium acnes,* beta hemolytic *Streptococcus*, *Proteus mirabilis*, and *Escherichia coli* (*14*, *15*). The development of biomaterials with antimicrobial properties to prevent device-associated infection is a rapidly expanding field.

2.1 Device-associated Infections in Bone Reconstruction

In the field of orthopedics alone, 2-5% of all procedures involving implants are complicated by infection (*1*). This number can be as high as 30% when open fractures are present (*16*). Significant morbidity and even death are associated with implant-related infections, with outcomes often leading to complete implant removal, surgical debridement

[1] Adapted from: Johnson CT and García AJ. Scaffold-based Anti-infection Strategies in Bone Repair. Annals of Biomedical Engineering. 2015 Mar;43(3):515-28. DOI: 10.1007/s10439-014-1205-3

of the affected tissue, and long-term antibiotic therapy (*17, 18*). Device-associated infections not only occur from direct implantation of bacteria, but also develop post-operatively following hematogenous bacteremia, or direct spreading from a nearby infection site (*17, 18*). Further complicating treatment is the emergence of antibiotic-resistant bacteria (*19*). Choosing the correct antibiotic for initial treatment is directly correlated with successful infection management and becomes more difficult in the case of nosocomial infections, due to the inherent resistance that these organisms possess (*20*). The above circumstances motivate the development of implantable materials with antibacterial properties to significantly improve surgical outcomes and reduced patient morbidity and mortality. Engineered scaffolds for regenerative medicine applications provide a framework for tissue repair as well as a substrate for the inclusion of antimicrobial properties.

2.2 Biofilm and Nonunion Defects

Device-associated infection is characterized by bacterial adhesion, colonization, and biofilm development, which is outlined in Figure 1 (*21, 22*). The most common organisms associated with orthopedic implant infections include the gram positive strains *Staphylococcus epidermidis*, *Staphylococcus aureus*, and *Propionibacterium acnes*, as well as the gram negative *Pseudomonas aeruginosa* (*22*). Osteomyelitis is inflammation of the bone, which can be due to biofilm formation, causing increased bone resorption and reactive bone formation (*17, 18*). These biofilms are composed of secreted bacterial components, such as protein, lipid, lipopolysaccharide, and DNA (*21*), forming a matrix around the bacteria that provides protection from antibiotic therapy and immune defenses (*23, 24*). Bacteria in a biofilm have higher mutation rates (*25*), and can display increased

virulence (*26*) than if growing planktonically, and when exposed to antibiotics, mutation rates increase further, allowing for accelerated development of a drug-resistant phenotype (*27*). Moreover, incomplete resolution following therapy leads to highly resistant cells, or persistors, that then replenish the biofilm (*28*). These characteristics paired with availability of only semi-effective treatment options leave a significant, unmet need for the development of therapies to combat device-associated biofilm and infection (*21, 29*).

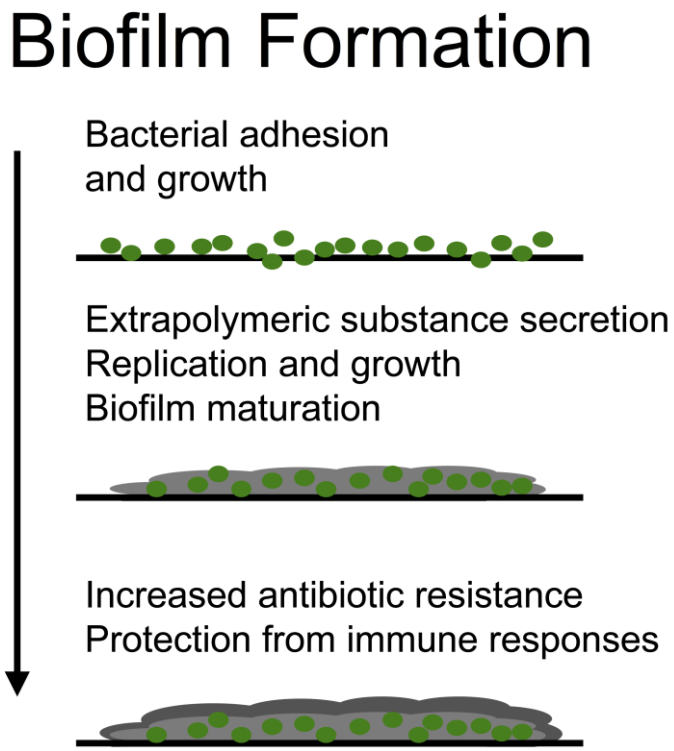

Figure 1: Bacterial adhesion and biofilm development. Biofilm formation begins by bacteria adhering and growing on a surface. As the pathogen continues to replicate a extracellular polymeric substances, including polysaccharide, DNA, and protein is produced, leading to biofilm formation. This matrix protects the pathogen from the host immune system and increases the development of antibiotic resistance.

Non-union bone defects are fracture injuries that cannot heal without intervention. Currently, standard medical therapies include the use of bone auto- and allo-grafts, or

delivering high doses of therapeutic protein, such as bone morphogenetic protein 2 (BMP-2), to facilitate healing. However, there are unacceptably high failure and complication rates associated with these interventions (*30*), which are significantly increased when an infection develops (*31-33*). Advances in biomaterials and regenerative therapies have led to the development of engineered scaffolds capable of correcting non-union defects without the need for bone grafting procedures (*34*). These strategies for bone repair often rely on biomaterial-based scaffolds to bridge the defect. This provides a convenient framework to introduce antibacterial agents to prevent and treat infection after surgical intervention.

Engineering regenerative medicine implants to overcome bacterial contamination is a critical and emerging area of biomaterials research. These technologies require rigorous *in vitro* and *in vivo* evaluation, bringing together the fields of microbiology and biomaterials engineering. Significant progress has been made in the design of infection-resistant surfaces, as recently reviewed by Campoccia *et al.* (*35, 36*). Therefore this review will focus on relevant animal models and techniques to assess antimicrobial tissue scaffolds in the context of bone repair, potential therapeutic additives to fight infection, and the current and future of scaffolds with infection resistant properties to promote bone repair.

2.3 Animal Models to Assess Infection and Bone Repair

Successful evaluation of antimicrobial scaffolds for bone regeneration requires the development of reliable and robust infection models. This proves to be a very challenging task, as pathogenic bacteria are required to induce the infection without causing overly adverse harm to the host. Furthermore, the model should provide a sustained infection over a prolonged period of time to have increased relevance to human health. Several animal

models to assess fracture therapy exist, and appropriate model selection was discussed in depth by Mills and Simpson (*37*). Bone regeneration is most frequently evaluated using critical-sized, segmental defect models. Critical-sized segmental defects are bone injuries that do not spontaneously heal, allowing for assessment of bone regeneration due to the therapy, such as implantation of a scaffold.

Few validated models exist to evaluate bone regeneration in infected defects. These models introduce infection to bone repair models. Table 1 summarizes validated models developed to characterize the efficacy of antimicrobial bone repair scaffolds. The most common repair model extends the rat femoral segmental defect (*38*) to include pathogenic bacteria (*39-43*). Femoral segmental defects have been widely used in regenerative medicine studies, and allow for the evaluation of a long, weight-bearing bone that will not spontaneously heal. This procedure requires bone fixation hardware and effectively tests the reparative capacity of regenerative scaffolds. To introduce infection, two distinct inoculation techniques exist. In one, a segment of the femur is excised, the bone is stabilized, bacteria is introduced, and the surgical site is closed. Once enough time has elapsed for the infection to become established, reoperation occurs and the infected tissue is debrided and a sterile regenerative scaffold is placed (*39-42*). This method has been used to evaluate osteogenic protein-1 (*39*) as well as systemic antibiotic therapy paired with recombinant human BMP-2 (*40*) and recombinant human osteogenic protein-1 (*41*) in the presence of infection. This technique provides clinical relevance, as it mimics how implant infections are treated, but two surgical procedures may increase variability and add more stress to the animal. The second approach requires a single procedure, where the defect is created and stabilized and the implant is placed. Following implant placement, the

pathogen is injected into the implant (or the implant is inoculated prior to implantation), simulating intraoperative contamination (*43*). This technique is advantageous because it only requires a single procedure, which may reduce variability associated with surgery. This model was later adapted to realize a 50% overall infection rate in order to reduce the chances of observing false-negative (type II error) *in vivo* results (*44*). An infected femoral segmental defect model in the rabbit has also been reported where infection was induced 48 hours after bone excision and defect stabilization by a percutaneous injection of a bacterial suspension (*45*). These models provide an economical way to assess bone-healing strategies, but are complicated by requiring defect fixation with plates and wires. Stabilization can pose a problem when assessing the antimicrobial abilities of regenerative scaffolds if the stabilization pins become infected and cause failure (*39*).

Ref.	**Animal**	**Procedure**	**Advantages**	**Disadvantages**
(*39-43*)	Rat	Femoral segmental defect, debridement following 2 weeks later	Evaluates long weight bearing bone, widely validated, not self-healing	Failure if infection extends to fixation pins, two surgical procedures required
(*44*) (*43*)	Rat	Femoral segmental defect, contaminated scaffold	Evaluates long weight bearing bone, widely validated, not self-healing, single operation	Failure if infection extends to fixation pins, complicated procedure
(*45*)	Rabbit	Femoral segmental defect	Evaluates long weight bearing bone, not self-healing	Failure if infection extends to fixation pins
(*46*)	Rabbit	Radial segmental defect	No fixation device required, evaluates long bone, not self-healing, single procedure, simulates intraoperative contamination	Non-weight bearing bone

Table 1: Infection-based segmental defect models.

Self-stabilizing segmental defects could be a means to avoid complications associated with infected stabilization hardware. Self-stabilization is achieved by removing a segment of a non-weight bearing bone, such as the radius. This allows for the study of regenerative implants in critically sized defects of long bones that will not self-heal, but may not be as clinically relevant since many orthopedic procedures require fixation of long bones. Bi *et al.* developed a lapine radial segmental defect infection model to assess localized antibiotic release compared to systemic therapy (*46*). In this model, a defect was created and a bacterial suspension was placed in the wound. After 30 minutes, the area was washed, the implant was placed and the wound was closed. This model only requires a single procedure and also simulates intraoperative contamination.

Although several different animal models have been developed to assess bone repair, to our knowledge a validated critical-sized segmental defect murine model has not yet been published, even though murine models have been used extensively throughout the osteomyelitis literature (*47*). A need exists for smaller animal models that may allow for more rapid screening of therapeutics to both treat infection and repair bone. Three important models have been described, covering a variety of orthopaedic infection scenarios. A common infection model is to simultaneously introduce an implant to an injury and the bacteria together. Prosthetic joint infection models do this by inserting a pin into the femoral canal, leaving 1 mm protruding into the joint space. An infection is then initiated by injecting bacteria over the protrusion (*48-51*). Bioluminescent bacteria have been used in conjunction with this model, allowing for *in vivo* monitoring of bacterial numbers. However, prevention models are limited by not allowing for the establishment of

the bacteria infection before treatment, making this the easiest case to successfully eradicate bacteria.

To address the clinical case of hematogenous seeding of a prosthetic joint, which can occur any time after implantation, Wang *et al.* implanted a titanium K-wire into a mouse femur, and then 21 days later, injected bioluminescent bacteria intravenously to initiate infection (*52*). This effectively models bacteremic seeding of a prosthetic joint. The authors report significantly higher rates of infection in the leg containing the implant. However, roughly 30% of animals infected did not develop an infection. This model serves as an important step towards being able to effectively evaluate a materials ability to resist infection long after implantation. The most rigorous models for evaluating a materials antimicrobial activity is to utilize a two-stage approach to first initiate an infection and then provide treatment at a later time point. Inzana *et al.* developed a novel murine mouse established femoral fracture infection model to screen therapies for fracture fixation hardware associated infections (*53*). In the first surgical procedure, the femur is mechanically fixated using a PEEK fixation plate and then a 0.7 mm osteotomy is performed to mimic a femoral fracture injury. The infection is initiated at the osteotomy site and allowed to develop for 7 days. The second stage involves expanding the osteotomy to 3 mm, debriding the surrounding tissue, and placing an antibiotic impregnated spacer, mimicking what would be done clinically to treat infected defects before bone grafting. This rigorous model allows for the rapid and economical screening of interventions to treat established orthopaedic hardware associated infections.

The advent of *in vivo* imaging systems has significantly improved the analysis of biomaterial-associated infections (*54*). Genetic engineering of bioluminescence genes into

clinically relevant bacterial strains allows for *in vivo* monitoring of infection. Commercially available gram positive (Xen29 *S. aureus*) and gram negative (Xen5 *P. aeruginosa*) strains contain a stable luminescence reporter, and can be tracked over time *in vivo*, providing the assessment of infection progression (*55*), and treatment efficacy (*56*). However, limitations do exist. For example, the luminescence signal detected is not a direct marker of the number of bacteria, but of the metabolic activity of the colony (*55-57*). The population of bacteria making up a biofilm is composed of both rapidly dividing and quiescent cells. This heterogeneity may be a possible explanation for the large variability between bacterial counts and bioluminescent signal. The use of bioluminescent bacteria has been successfully established *in vivo* in the context of osteomyelitis (*58, 59*), suggesting that this technology could be adaptable to monitoring scaffold-associated infections in bone repair. Nevertheless, genetic modification of bacteria through bioluminescent gene insertion could reduce the virulence of the clinically isolated strains, which could complicate the evaluation of infection resistant materials.

In addition to bioluminescent bacteria, several *in vivo* probes utilizing fluorescent, magnetic, and radioactive tracers have been developed. Near infrared (near-IR) imaging probes that specifically identify bacteria have received heightened interest as a viable alternative to luminescent bacteria. Discrimination between infection and inflammation is the key challenge associated with their development (*60*). Eggleston and Panizzi provide an extensive review on this topic (*60*). Our lab has recently developed near-IR probes that specifically discriminate between infection and inflammation through targeting the products produced by the inflammatory response (*61*). Reactive oxygen species (ROS) are characteristic of the body's response to biomaterials implants, whereas large quantities of

nitric oxide (NO) are produced by macrophages and neutrophils in a direct response to bacteria. Dual administration of ROS- and NO-selective probes allows for the simultaneous *in vivo* observation of infection and inflammation with high specificity (*61*). Furthermore, we have shown these fluorescent probes exhibit increased sensitivity compared to bioluminescent strains. Fluorescent probes also have a dose dependent response to the number of bacteria regardless of metabolic activity, in a strain independent manner (*62*). Other strategies to achieve specificity include utilizing antimicrobial peptides that have been labeled with radioactive isotopes and paired with clinically available imaging systems, such as SPECT (single photon emission computed tomography) (*63*), and labeling the antibiotic vancomycin with a near-IR fluorophore to identify gram positive infections (*64*). The technologies described above provide real-time, *in vivo* means to monitor infection initiation, progression, and resolution, and could provide an indispensable tool in the development of infection-resistant scaffolds.

Although significant effort has been made to develop finely tuned animal models for the assessment of a materials antibacterial properties as described above, ethical concerns do exist surrounding these methods. This is especially relevant when evaluating infection resistant properties of scaffolds after a sterile implantation, which is the most clinically realistic scenario. These types of studies require large animal numbers to adequately power the analysis due to the relatively low rates of spontaneous infection developing (less than 7%) and that both the control and treatment groups will require large animal numbers to resolve a difference (*65*). Concerns also exist surrounding animal welfare. Many infection models are highly variable and it can be challenging defining a sub-lethal bacterial dose that does not cause animal suffering. This is particularly difficult,

as simply increasing the bacterial dose could result in sepsis and termination before the desired experimental end point.

2.4 Antimicrobial Agents to Fight Infection

Several different strategies exist to combat bacterial infection. Table 2 provides a list of major antimicrobial strategies (*66-70*). Brief overviews of the major antibacterial classes, including the advantages and limitations of each follow.

Ref.	Antimicrobial	Topics Covered
(*67*)	Antibiotics	Mechanisms of action, and how resistance has emerged
(*70*)	Silver	Antimicrobial properties of silver nanomaterials and effects on human health and the environment
(*66*)	Host Defense Peptides	Host defense peptides as therapeutics for antibiotic resistant infections
(*69*)	Host Defense Peptides	Immunomodulatory aspects of host defense peptides
(*68*)	Bacteriophage	Bacteriophages and how they can be used to treat infection
(*71*)	Bacteriophage Endolysins	Bacteriophage endolysin structure, function, efficacy, antibiotic synergy, and resistance
(*72*)	Lysostaphin	Lysostaphin activity, therapeutic applications, immunogenicity, and limitations

Table 2: Review articles detailing various antimicrobial strategies

Clinically, antibiotics are the most common agent used to clear bacterial infections. They are widely used throughout clinical medicine as treatment and prophylaxis. However, over the past decades, the emergence of antibiotic-resistant bacteria, such as methicillin resistant *Staphylococcus aureus* (MRSA), have become more common (*67*). Sub-inhibitory aminoglycoside antibiotic treatment can induce biofilm formation (*73*). The development of biofilm can potentiate the emergence of resistant cells, further

complicating the infection (*74*). Biofilm requires higher doses and longer trials of therapy to eradicate infection, thereby prolonging the patient's exposure to drug side effects. Moreover, it has been shown that bactericidal antibiotics are toxic to mammalian cells, causing mitochondrial dysfunction (*75*). However, the benefits of treatment far outweigh the risks, and until viable alternatives are available, antibiotics will remain the standard of care. For a comprehensive review of antibiotic therapy including drug mechanisms, specificities, and the development of resistance, refer to Davies and Davies (*67*).

Silver is a broad-spectrum antimicrobial agent used in research and clinically. Silver exerts bactericidal activity on both gram positives and gram negatives through several mechanisms. Silver ions enter the bacterium and generate ROS capable of damaging DNA, they interact with membrane proteins affecting their function, and alter membrane permeability leading to cell death (*70*). It is believed that silver resistance is widespread, but not realized since it is not widely tested for. A Chicago hospital revealed that over 10% of enteric bacteria exhibit silver resistance (*76*), and overuse could potentiate the problem. Furthermore, the bactericidal mechanisms of silver ions are not specific to bacterial cells, and also disrupt mammalian cell function placing significant concern on toxicity (*77, 78*). However, it has been reported that silver can be effective against antibiotic-resistant bacterial strains, and even induce susceptibility towards antibiotics that were ineffective in the absence of silver (*79*). Silver can also be adapted to reduce bacterial adherence to orthopedic implants by killing adherent pathogens (*80*). For a more detailed discussion, the reader is referred to Marambio-Jones and Hoek (*70*). Clinically, silver has translated to several applications, including wound dressings, creams, urinary catheters and endotracheal tubes. However, little if any data has demonstrated efficacy. An analysis of

2066 patients enrolled in several clinical trials failed to show any benefits to silver-doped wound dressings (*81*). Silver-coated endotracheal tubes (*82*) have exhibited modest efficacy in preventing bacterial colonization, whereas silver-coated urinary catheters have shown mixed results (*83*).

Host defense peptides or antimicrobial peptides (AMPs) have activity against bacteria, viruses, and fungi (*84*). Defensins, cathelicidins and histatins are AMPs produced by many mammalian cells (*85*). AMPs are amphiphilic peptides characterized by a several cationic and hydrophobic residues and exhibit broad-spectrum activity against both gram positive and gram negative bacteria (*69, 84, 85*). The cationic residues associate with the negatively charged bacterial membrane. The hydrophobic and hydrophilic residues cause membrane penetration, leading to instability, pore formation, osmotic changes, and bacterial lysis (*84*). As with all antimicrobial strategies, the development of resistance is a concern. This could be especially problematic since AMPs are part of the natural host response to pathogens and resistance could make simple infections dangerous (*66, 86*). Another drawback is the observation that AMPs are not stable over long periods of time in an *in vivo* environment. However, AMPs are easily engineered, and several synthetic peptides have been developed in an attempt to overcome these shortcomings (*87*). It has been well documented that AMPs possess immunomodulatory activity in addition to being antipathogenic (*69, 84, 85*). AMPs modulate both the innate and adaptive immune responses to control infection and stimulate regenerative processes (*69*). These attributes make AMPs an enticing candidate for antimicrobial regenerative scaffolds. However, there are no reports of human safety or efficacy trials for AMPs.

Bacteriophage therapy has gained renewed interest with the increased prevalence of antibiotic resistance (*88*). Bacteriophages are viruses that specifically infect bacteria. The phage binds to a membrane receptor, introducing phage DNA into the cell. This DNA is replicated and translated by the host bacterium, leading to phage replication, progeny assembly, bacterial lysis, release of progeny, and phage propagation to surviving bacteria. Following eradication of the infecting organism, phage replication ceases, allowing for resolution of the affected tissue. Bacteriophage DNA can also code for lysins, lytic enzymes that destroy the bacterial cell wall (*89*), as well as polysaccharide depolymerases, enzymes that break down the biofilm matrix created by bacteria (*90, 91*). This allows bacteriophages to disperse biofilm as well as eradicate infection. In addition, synergism between phage therapy and antibiotics has been demonstrated (*92*). Host bacterial strains can develop resistance to phage infection, which can be reduced using several different phages at once (*93*). There are also concerns surrounding the immunogenicity of *in vivo* phage administration, even though adverse events have not been reported in the literature (*94, 95*). Currently, the safety of bacteriophage therapy administered orally (*96*) and cutaneously (*97*) has been evaluated in humans in phase I clinical trials. Preliminary results of the first controlled trial to evaluate bacteriophage efficacy in chronic otitis to treat antibiotic-resistant *P. aeruginosa* have been positive, demonstrating therapeutic value in humans (*98*).

Bacteriolytic enzymes, such as bacteriophage lysins and lysostaphin, are enzymes that catalytically degrade the bacterial cell wall, leading to cell lysis (*99*). In general, these enzymes are specific to a particular bacterial species or genus; however, there have been reports of some with expanded target ranges (*100*). Structurally, the enzymes are usually

composed of a cell wall binding domain, responsible for the specificity, and a catalytic domain, that degrades pathogens cell wall (*99*). Bacteriophage lysins are enzymes coded by bacteriophage DNA that are directly responsible for lysing the host cell allowing for phage propagation during the bacteriophage life cycle. Notably, resistance to lysins has never been reported, making them an ideal candidate for clinical translation to treat antibiotic resistant bacteria (*101*). Lysostaphin is a bacterial exolysin produced by the bacteria *Staphylococcus simulans* as a defense mechanism to kill *S. aureus (4).* Lysostaphin has similar structure and function to a bacteriophage lysin with a cell wall binding domain and an enzymatic domain (*3*). Bacteriolytic enzymes have several advantages over small molecule antibiotics. First, they carry high activity against bacteria growing in biofilm since they do not require target pathogens to be metabolically active (*102, 103*). Second, they are specific to only the target pathogen of interest. This can help to prevent many of the side effects associated with broad spectrum antimicrobial therapy such as perturbation of native flora and driving the development of antibiotic resistance (*101*). Third, they are often synergistic with small molecule antibiotics and have been shown to resensitize antibiotic resistant strains to the antibiotic they were resistant too (*89, 103, 104*). These characteristics have continued to push bacteriolytic enzyme translation to the clinic.

2.5 Antimicrobial Scaffolds for Bone Repair

Recently, tissue engineered scaffolds for bone repair have started to include antimicrobial agents to prevent or fight infection. These scaffolds provide a substrate for sustained, localized drug release, tunable degradation properties to promote tissue integration, and support for cell delivery. Rigorous evaluation of the antimicrobial efficacy exhibited by these scaffolds has proven difficult, and requires expertise in both

microbiology techniques as well as biomaterials engineering. Antimicrobial scaffolds are required to be toxic to bacterial cells, while promoting local tissue regeneration and minimizing the adverse inflammatory events. Figure 2 is a schematic diagram illustrating how engineering antimicrobial properties into scaffolds for bone repair can improve outcomes associated with bacterial infection. Bacterial contamination is introduced into a model used to evaluate regenerative implants. If the contaminate is not cleared by the immune system or an infection-resistant scaffold, the infection becomes established, which may lead to the development of osteomyelitis. Infection fighting scaffolds can be implanted into defects with ongoing infection or osteomyelitis to remove the existing pathogen and facilitate repair. Further development of these technologies will allow for bone repair to occur in both sterile and contaminated conditions.

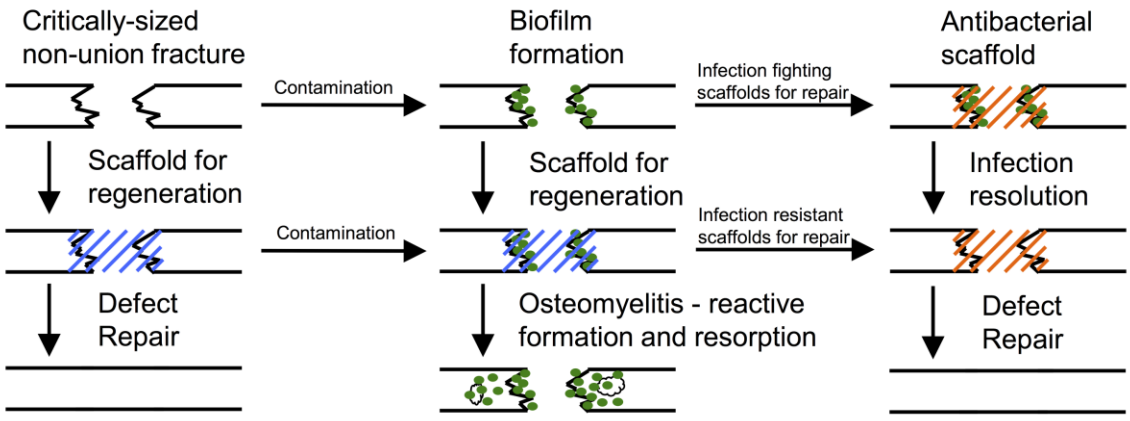

Figure 2: Critically-sized non-union bone defects are used to assess the therapeutic efficacy of regenerative scaffolds. Contamination of these defects can be introduced before or after the scaffold is placed to establish the infection. Absence of antimicrobial agents will lead to the development of osteomyelitis, which is characterized by bone resorption and reactive bone formation. Infection resistant scaffolds are designed to prevent initial bacterial colonization whereas infection fighting scaffolds can be used to resolve an established biofilm and promote defect repair.

2.5.1 Antibiotic-releasing scaffolds

Antibiotic delivery scaffolds are the most well developed area in the literature. In orthopedics, antibiotic-loaded fillers and bone cements have been used clinically for a number of years. Zilberman and Elsner published an extensive review on antibiotic-releasing materials (*105*). We will focus on advances in tissue engineering scaffolds that incorporate antibiotics.

Scaffolds provide an ideal substrate to deliver long-term bactericidal doses of antibiotics to the injury site. This is accomplished by modifying drug release characteristics through encapsulation within degradable matrices. Antibiotic releasing matrices have been used as coatings for orthopedic implants prone to infection. Sol-gel thin films have been engineered to provide sustained release of vancomycin and protect against implant associated infection of titanium rods. The addition of the thin film minimized bacterial adherence to the implant, and protected against the development of osteomyelitis *in vivo* (*106*). A similar has also been applied to stainless steel K-wires (*107*).

Antimicrobial activity can also be engineered into scaffolds for tissue regeneration. Poly (L-lactic acid) (PLLA) nanofiber scaffolds were synthesized with poly (lactic-co-glycolic acid) (PLGA) nanospheres to provide extended release of the antibiotic doxycycline (*108*). These scaffolds provided sustained antimicrobial activity against *S. aureus* and *E. coli* over 42 days in bacterial culture, demonstrating an approach to provide extended, localized antibiotic release, which would reduce the systemic side effects associated with antibiotic therapy. This is especially important when treating osteomyelitis, which typically involves extended courses of high dose antibiotics. Poly(caprolactone)

(PCL) scaffolds were synthesized by electrospinning PCL using 10% and 20% (w/w) rifampin (*109*). These scaffolds exhibited extended rifampin release over eight hours and were bactericidal towards *S. epidermidis* and *P. aeruginosa in vitro*. Shi *et al.* demonstrated the addition of lecithin can increase the encapsulation efficiency of gentamicin and protein into PLGA microsphere-based scaffolds (*110*). After an initial burst release, gentamicin release occurred for 60 days, and protein was released for 18 days. The material was active against *E. coli* while still supporting mesenchymal stem cell (MSC) viability, proliferation, and mineralization. These observations suggest that this scaffold is a viable candidate for delivering protein therapeutics as well as antibiotics, and supporting bone formation for the treatment of infected bone defects. The encapsulation of growth factors has also been paired with antibiotic encapsulation. Calcium sulfate scaffolds with chitosan microspheres containing vancomycin, recombinant human BMP-2 (rhBMP-2), or both were developed and assessed *in vitro* for bactericidal activity and regenerative properties (*111*). It was shown that these scaffolds are bactericidal against *S. aureus* for 18 days and release rhBMP-2 over 6 weeks, causing increased alkaline phosphatase (a marker of osteoblast differentiation) expression. These investigators found that an optimal balance between antibiotic and growth factor release is required for optimal osteoblastic differentiation, as high antibiotic concentrations can lead to inhibition of osteoblastic differentiation. However, these techniques have not yet been extended to *in vivo* models.

As mentioned above, the current standard of care for critically sized bone defects is bone grafting. Infection is one of the most significant side effects associated with grafting procedures. Bi *et al.* engineered bone xenografts (grafts from a different animal species) composed of antigen-free calf cancellous bone combined with calf cortical bone extract

and bovine BMP impregnated with clindamycin to treat critically sized defects contaminated with *S. aureus* (*46*). This scaffold was evaluated *in vivo* within a rabbit radial segmental defect. After the graft was implanted, $1x10^6$ colony forming units (CFU) of *S. aureus* were administered to the injury. All animals in the clindamycin-impregnated graft group healed completely. Defect repair was observed in the clindamycin-graft group including recanalization of the medullary cavity. Systemic clindamycin therapy resulted in either non-union, or delayed union after the 16 week period, whereas the non-treatment control developed osteomyelitis characterized by reactive bone formation and resorption. This study shows that local, sustained delivery of antibiotics can overcome an infection, while still providing regenerative properties.

The bone graft substitute calcium sulfate has also been combined with antibiotics and assessed *in vivo*. The antibiotic moxifloxacin has been evaluated with commercially available Stimulan®, a synthetic semihydrate form of calcium sulfate (*112*). In this study, osteomyelitis was induced in a rabbit tibia by injection of $2x10^7$ CFU of a clinical osteomyelitis isolate of MRSA into the intramedullary cavity. After the infection was allowed to develop for three weeks, the rabbits underwent surgical debridement of all necrotic bone tissue and implant placement. The results showed a significant reduction in viable bacteria throughout the six week observation period. *In vitro* assessment of the delivery system showed sustained moxifloxacin release over 35 days. However, this study did not evaluate whether the regenerative properties of the moxifoxacin doped Stimulan® are still intact in the presence of sustained antibiotic release. Xie *et al.* compared bioactive borate glass to the clinically used calcium sulfate as a carrier for vacomycin to treat MRSA-induced osteomyelitis in rabbits (*113*). Bioactive borate glass provided sustained

vancomycin release over 28 days *in vitro* and improved mechanical properties compared to calcium sulfate. The scaffold was assessed *in vivo* using a rabbit model for osteomyelitis. After three weeks of infection, surgical debridement was performed and scaffolds were placed within the defect. Both the vancomycin-loaded calcium sulfate and vancomycin-loaded borate glass significantly reduced the number of bacteria, improved the radiographic score and improved the histopathologic score at the end of the eight-week observation period. This study further illustrates that scaffolds serve as an effective mechanism to provide sustained antibiotic therapy to eradicate osteomyelitis.

Polyurethane scaffolds have also received interest as a substrate to deliver antibiotics and growth factors for bone repair. Polyurethane scaffolds designed for prolonged release of vancomycin were compared to the clinically used vancomycin-loaded PMMA- beads (*114*). Extended vancomycin release from polyurethane scaffolds could be controlled by changing the solubility of vancomycin. *In vivo* evaluation of the vancomycin-loaded polyurethane scaffolds in a contaminated rat femoral segmental defect reduced viable bacterial counts as well as the clinical standard of vancomycin-loaded PMMA beads. Importantly, nearly 10 times less antibiotic was loaded to the polyurethane scaffolds. Dual delivery of vancomycin and the growth factor BMP-2 to a *S. aureus* infected rat femoral segmental defect using a biodegradable polyurethane scaffold demonstrated increased bone formation as determined by microCT and histological analysis (*115*). The addition of vancomycin to the scaffold reduced the clinical signs of infection while not affecting bone regeneration. Together, these studies illustrate that extended release of vancomycin can eradicate infection and the addition of BMP-2 can enhance regeneration in contaminated defects.

Clearly there has been significant progress in towards the development of antibiotic releasing materials for bone repair. However, as mentioned before, biofilm can offer protection to the microorganisms against antibiotic therapy, leading to the development of resistance. In a study evaluating the efficacy of gentamicin-loaded bone cement against the well-known biofilm former *S. epidermidis* in rats, it was shown that even though the number of bacteria was reduced, there was a significant increase in the number of gentamicin-resistant bacteria (*116*). In another study evaluating vancomycin-releasing polyurethane scaffolds in an infected rat segmental defect, significantly fewer bacteria were recovered at two weeks (*98*). Nonetheless, this was only a roughly three-fold reduction, leaving over $1x10^5$ CFU/gram of bone tissue, demonstrating a significant limitation in effectively treating infections.

Administration of multiple antibiotics simultaneously reduces the chances for antibiotic resistance to develop compared to monotherapy (*117*). Ashbaugh *et al.* engineered an antibiotic releasing electrospun coating to prevent prosthetic joint infections capable or releasing multiple antibiotics from different drug classes simultaneously (*51*). This is in contrast to current local delivery strategies that are limited to heat stable antibiotics, such as those used in antibiotic eluting bone cement (*118*). The electrospun costing was capable of releasing multiple antibiotics, both individually and in combination, above the minimum inhibitory concentration over the course of days to weeks. Release profiles could be controlled through modulation of the material properties. Importantly, combination therapy prevented infection and subsequent bone remodeling using a mouse model of prosthetic joint infection.

2.5.2 Silver-presenting scaffolds

Silver can be easily incorporated into materials through various manufacturing techniques such as reduction or the addition of silver nanoparticles. This ease of incorporation combined with silver's broad spectrum antimicrobial activity has led to the development of several silver-containing antimicrobial scaffolds. Several designs have demonstrated *in vitro* efficacy, but success *in vivo* has been limited.

Naturally derived tissue engineered scaffolds have been used for a multitude of applications, include bone repair. These materials can be modified to present silver and exhibit infection resistance. Collagen scaffolds were fabricated to include silver nanoparticles coated with poly(ethylene glycol) (PEG) and Triton X-100 (*119*). The scaffolds had increased elasticity and antimicrobial effects against both gram positives (*B. cereus* and *S. aureus*) and gram negatives (*E. coli* and *P. mirabilis*). Silver nanoparticles have also been incorporated into type I collagen scaffolds synthesized using UV initiation of a non-toxic, water-soluble benzoin to facilitate polymerization (*120*). The collagen scaffolds served to stabilize the nanoparticles and supported fibroblast and keratinocyte viability at silver concentrations less than or equal to 100 μM. Bactericidal activity (*E. coli*, *B. megaterium* and *S. epidermidis*) was determined using a modified minimum inhibitory concentration assay. These studies show that collagen-based scaffolds that include silver nanoparticles can prevent bacterial growth *in vitro*, while also supporting mammalian cell viability. Further development of these technologies and evaluation in *in vivo* models is necessary to establish the feasibility of silver nanoparticle-containing collagen scaffolds for infection prevention and bone repair. Bioactive glass containing silver has been incorporated into extracellular matrix-derived hydrogels to exhibit sustained antimicrobial

effects and bone regenerative properties (*121*). These materials show sustained silver ion release over 25 days and is bactericidal against *E. coli* and *E. faecalis*. The composite hydrogels support dental pulp cell viability, making them a plausible candidate for tooth or bone regeneration. Silver ions have been added to composite chitosan/nano-hydroxyapatite scaffolds to add antimicrobial properties (*122*). The chitosan/nano-hydroxyapatite scaffolds were immersed in silver nitrate, allowing for an ion-exchange and reduction to occur between the scaffold and silver. The scaffolds support osteoprogenitor and osteosarcoma cell viability and demonstrate antimicrobial effects against both gram positive and gram negative bacteria (*S. aureus* and *E. coli*).

PLGA has been of particular interest for bone repair due to its biocompatibility, degradable properties, and being used in FDA-approved devices. Silver was incorporated into tricalcium phosphate (TCP) nanocomposite, mixed with PLGA and then electrospun to form a fibrous scaffold. These scaffolds provided sustained silver release at bactericidal levels *in vitro* against *E. coli*, a frequent contaminator of dental implants. The scaffolds were equally as effective as the clinical standard of tetracycline-soaked cotton swabs. However, upon media exchange in the assay, the silver scaffolds maintained antimicrobial ability due to sustained release characteristics. This study demonstrates the importance of sustained antimicrobial release, and that scaffolds for tissue engineering provide a convenient avenue to accomplish this. Zheng *et al.* reported a promising antimicrobial regenerative scaffold (*43*). In this study, microporous PLGA scaffolds were fabricated to contain silver nanoparticles. Interestingly, 1.0% silver containing grafts supported increased osteoblastic differentiation and increased alkaline phosphatase activity compared to the 2.0% silver grafts *in vitro*. These scaffolds were evaluated using a rat femoral

segmental defect. After implantation, $1x10^8$ CFUs of vancomycin-resistant MRSA was injected into the implant. Radiographic and histological analysis showed that the 2.0% silver implants completely eliminated infection and supported defect bridging, whereas the 1.0% silver implants only reduced the number of bacteria present, but supported some bone regeneration. Control scaffolds that did not contain silver were grossly infected, demonstrating bone resorption and reactive bone formation, indicative of osteomyelitis. The *in vitro* analysis paired with the *in vivo* data show that although high concentrations of silver can inhibit osteoblast differentiation, it is more important to eliminate the contaminating bacteria to facilitate bone formation. This is a clear demonstration that developing implants capable of resisting infection while providing functional cues to facilitate bone repair is possible.

As an alternative to silver, copper ions loaded into microporous bioactive glass scaffolds reduce bacterial growth and support MSC viability and differentiation (*123*). These scaffolds significantly reduced *E. coli* growth, and promoted human MSC differentiation towards osteoblasts in a dose dependent manner. Vascular endothelial growth factor levels were also elevated, suggesting the scaffold could promote vascularization.

2.5.3 *Antimicrobial Peptides, Bacteriophage, and Other Antimicrobial Strategies*

Interest has been building surrounding technologies that take advantage of alternative antimicrobial therapies. These alternatives to silver and antibiotics could expand the arsenal against infection, while also reducing the chances of bacteria developing resistance to our most efficacious treatments. Scaffolds provide a means to extend the

activity of these agents by providing sustained release characteristics. Antimicrobial peptides have been introduced into scaffolds designed for orthopedic regeneration. Poly(caprolactone) (PCL)-chitosan nanofiber scaffolds were synthesized and PEG-microgels containing the cationic antimicrobial peptide L5 were electrostatically associated with the nanofibers(*124*). These novel scaffolds demonstrated antimicrobial activity against *S. epidermidis*, and maintained L5 stability and activity. The scaffolds supported osteoblast adhesion, spreading, and proliferation.

Stainless steel K wires used in orthopedic procedures coated with a hydroxypropylmethlycellulose (HPMC) hydrogel containing bacteriophage, the antibiotic linezolid, or both were developed to prevent MRSA infection (*125*). The coated wires showed sustained phage and linezolid release over several days, as well as inhibiting MRSA adherence in a dose dependent manner. The bacteriophage and linezolid group exhibited the greatest efficacy toward inhibiting MRSA attachment and growth, suggesting synergism exists between the co-delivery of antibiotics and bacteriophage. This claim was further supported by analysis of recovered MRSA after treatment showing reduced mutation rates in the dual treatment group suggesting lower drug resistance. This *in vitro* evaluation of scaffolds presenting bacteriophage and antibiotics suggests the treatment could be extended to an *in vivo* environment to prevent infection associated with stainless steel implants. Bacteriophage has also been evaluated in a regenerative context. In one study, the *E. coli* bacteriophage λ was loaded into microporous hydroxyapatite or beta-tricalcium phosphate scaffolds with various porosities by passive adsorption (*126*). Bactericidal activity against *E. coli* K12 was observed *in vitro*, demonstrating the prophylactic potential bacteriophage loaded materials could provide.

Polyelectrolyte scaffolds assembled by electrostatic interactions of chitosan gamma-polyglutamic acid and carboxy-methylcellulose were developed for treating dental bone defects. These scaffolds supported pre-osteoblast cell adhesion and viability *in vitro*, and antimicrobial activity against *S. aureus* and *E. coli*. Scaffold biocompatibility was assessed by extracting the second pre-molars of beagle dogs and replacing them with the material. The scaffolds were explanted after 10 weeks and histology revealed no adverse foreign body reaction.

Neutrophils and macrophages produce peroxide and other free radicals to kill invading pathogens. This mechanism was extended to electrospun polycaprolactone (PCL) scaffolds with different concentrations of calcium peroxide to exhibit antimicrobial activity by releasing a significant initial burst of peroxide (*127*). This short-term antimicrobial response was effective in controlling *E. coli* and *S. epidermidis in vitro*, illustrating broad applicability. The nanowires supported osteoblast viability for four days of culture despite the cells being exposed to toxic peroxide levels for the first 24 hours. This novel method of direct peroxide generation from a PLC scaffold shows that burst release from materials can be toxic to bacteria but still provide a means to promote bone growth.

Berberine is a natural antimicrobial agent that exhibits activity against several different organisms and is non-toxic to mammalian cells. For these reasons, Huang *et al.* incorporated it into a chitosan coating on a nano-hydroxyapatite/polyamide66 scaffold developed for bone regeneration (*128*). These scaffolds provided a continuous release of berberine over 150 hours and were bactericidal to *S. aureus*. Furthermore, the scaffolds supported MG63 cell adhesion, proliferation, and spreading, supporting that berberine is nontoxic. However, this material has not been evaluated *in vivo*. These data provided

preliminary evidence that berberine may be suitable for *in vivo* evaluation to provide antimicrobial and regenerative properties in a bone repair setting.

Preventing biofilm formation may be another way to protect against chronic osteomyelitis. Sanchez *et al.* demonstrated biofilm dispersal agents reduce infection *in vivo* (*129*). A polyurethane scaffold containing D-amino acids was contaminated with *S. aureus* and implanted into a rat femoral segmental defect. The treated scaffolds significantly reduced the number of contaminating bacteria, showing that preventing biofilm formation can improve post-operative outcomes, by preventing the biofilm from shielding the bacteria from endogenous antimicrobial defenses.

2.6 Conclusions and Outlook

Preventing infection in the presence of biomaterials implants is a major unmet need and will significantly improve patient outcomes. Currently, implant infection leads to removal, and significant medical costs from reoperations and extended antibiotic therapy. Moreover, after an initial infection, patients are at a much higher risk for relapse, further complicating management and causing increased patient morbidity. As medicine advances, we have become more and more reliant on implantable devices to more effectively correct patient problems, which increase the risk of implant-associated infections (*1*). Demand exists for the prevention of orthopedic implant infections due to the frequency of their occurrence, as well the challenges associated with combating osteomyelitis. Despite improvements in intraoperative techniques and the invention of antibiotic-doped cements and fillers, infection continues to be a significant issue associated with non-union defects. Furthermore, the increased prevalence of antibiotic resistant bacteria raises concern over

widespread use of antibiotic presenting materials. This suggests alternative antimicrobials such as silver, antimicrobial peptides or bacteriophage could help to preserve the efficacy of our most potent weapons against infection. These alternative strategies to fight infection offer exciting opportunities to introduce new properties into scaffolds. For example, the rapid expansion, but self-limiting characteristics of a bacteriophage infection provide a way to engineer materials that respond only when a pathogen is present. Scaffolds can shield the phage from the host response, while providing activity only in the presence of offending bacteria. Antimicrobial peptides can enhance the body's defenses against pathogens, and even promote wound healing. Scaffolds can serve a means to extend the stability of these peptides and enhance their utility.

In addition to extending the stability of antimicrobial agents, scaffolds provide a highly controlled means to release therapeutics. Modulation of scaffold degradation typically correlates with therapeutic drug release. Traditionally, bone repair is driven by a scaffold degradation leading to therapeutic release. The drug release recruits cells and further promotes scaffold degradation, leading to tissue healing. This process is outlined in Figure 3. Degradable scaffolds are also advantageous from an *in vivo* infection resolution point of view. Implanted biomaterials are prone to infection after implantation by transient bacteremia causing colonization and direct bacterial spreading from infection sites (*17, 18*). Degradable scaffolds provide the benefit of controlled therapeutic release while facilitating integration into the native tissue.

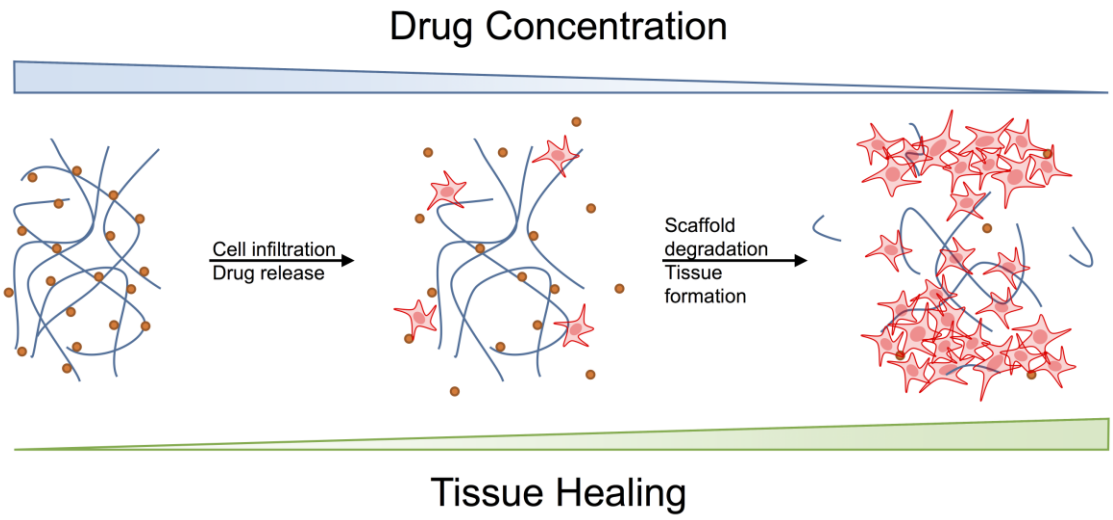

Figure 3: Scaffold based drug delivery for tissue repair. Current regenerative medicine strategies focus on delivering therapeutics to drive cell recruitment and tissue repair. As cells are recruited the scaffold degrades, releasing therapeutics, and promoting integration. Next generation biomaterials will include abilities to prevent or eliminate pathogens and provide regenerative cues.

Degradable scaffolds to treat infection and regenerate bone have been primarily investigated in the bioactive glass literature (*130*). These studies are mostly centered on extending the release of antibiotics to provide continuous antimicrobial activity (*113*, *131*, *132*). However, a significant gap exists in understanding how the degradation properties of scaffolds influence antimicrobial efficacy *in vivo*. Future studies could focus on optimizing scaffold degradation properties to efficiently eliminate pathogens and guide the bone repair process. These studies can then be extended to characterize and understand how engineering extended release of antimicrobial therapies affects drug activity though drug scaffold interactions. Modifications of scaffolds to provide continuous release may negatively impact the efficacy of the loaded therapeutic.

The next generation of antimicrobial scaffolds for bone repair will optimally balance antimicrobial delivery with regenerative therapeutics. This could be achieved by

tuning material properties such as porosity, charge, degradation speed, density, antimicrobial agent, growth factors, and the bulk material. Understanding how material design choices prevent bacterial contamination, biofilm development, eradication of existing osteomyelitis, while simultaneously regenerating bone, will lead to optimized scaffold designs.

In order for these new technologies to translate into the clinic, several challenges need to be overcome. The development of robust, controlled, and reproducible animal models of infected scaffolds is a critical need for the success of this fast emerging field. Animal models that utilize bioluminescent bacteria allow for real time monitoring of infection progression without animal sacrifice, which addresses some of the ethical concerns of biomaterial infection research. Reproducible, controlled infections that accurately simulate clinical scenarios are required to effectively evaluate experimental materials to prevent infection and facilitate bone regeneration.

Scaffolds provide an ideal substrate for designing regenerative therapies due to the exquisite engineering control we have over them. They provide a platform for controlled drug release, a substrate for therapeutic cell delivery, tunable degradation characteristics that facilitate replacement by regenerating tissue, reduced immunogenicity, and response to the surrounding environment. It is clear that progress is being made towards the development of infection-resistant bone repair implants. However, the *in vivo* validation of these technologies is still in its infancy. The advancement of *in vivo* imaging techniques, paired with robust bone repair models will facilitate the translation from the bench to the bedside.

HYDROGEL DELIVERY OF LYSOSTAPHIN ELIMINATES ORTHOPAEDIC HARDWARE INFECTION BY *STAPHYLOCOCCUS AUREUS* AND SUPPORTS FRACTURE HEALING[2]

3.1 Abstract

Orthopaedic hardware infections are a significant clinical problem with current therapies limited to surgical debridement and systemic antibiotic regimens. Lysostaphin is a bacteriolytic enzyme with high anti-staphylococcal activity. We engineered a lysostaphin-delivering injectable poly(ethylene glycol) hydrogel to treat *Staphylococcus aureus* infections in bone fractures. The injectable hydrogel formulation conforms and adheres to the fracture and surrounding tissue, ensuring efficient, local delivery of lysostaphin. Lysostaphin encapsulation within this synthetic hydrogel maintained enzyme stability and activity. Lysostaphin-delivering hydrogels exhibited enhanced anti-biofilm activity compared to soluble lysostaphin. Lysostaphin-delivering hydrogels eradicated *S. aureus* infection and out-performed prophylactic antibiotic and soluble lysostaphin therapy after 7 days in a murine model of femur fracture. Analysis of the local inflammatory response to infections treated with lysostaphin-delivering hydrogels revealed indistinguishable differences in cytokine secretion profiles compared to uninfected fractures, demonstrating clearance of bacteria and associated inflammation. Importantly, infected fractures treated with lysostaphin-delivering hydrogels fully healed by 5 weeks

[2] Submitted: Johnson CT, Wroe JA, Agarwal A, Martin KE, Guldberg RE, Donlan RM, Westblade LF, and García AJ. Hydrogel Delivery of Lysostaphin Eliminates Orthopaedic Hardware Infection by *Staphylococcus aureus* and Supports Fracture Healing.

with equivalent bone formation and mechanical properties to uninfected fractures, whereas fractures treated without the hydrogel carrier were equivalent to untreated infections. Finally, lysostaphin-delivering hydrogels eliminate methicillin-resistant *S. aureus* infections, supporting this therapy as an alternative to antibiotics. These results indicate that lysostaphin-delivering hydrogels effectively eliminate orthopaedic *S. aureus* infections while simultaneously supporting fracture repair.

3.2 Introduction

Orthopaedic disease and injuries often require biomaterial hardware and devices for successful clinical treatment. In 2011, 1.2 million prosthetic joint arthroplasty procedures were performed in the United States (US), and this number is projected to increase to 3.8 million procedures by 2030 (*133*). However, infection of these devices is a major limitation with ineffective treatment options (*134*). For example, over 1,000,000 joint prostheses (*135*) and 6,000,000 fracture-fixation devices (*136*) are deployed each year, with 2% and 5% of these procedures, respectively, developing infection at an economic cost of over $2 billion (*1*). In the US, 112,000 orthopaedic device-related infections occur annually with approximately 66% of these bacterial infections involving *Staphylococcus* species (*2*). Fracture fixation devices have infection rates ranging from 1-2% for closed fractures and rates as high as 30% for open fractures (*137-139*). Current treatment of these infections is limited to a combination of aggressive surgical debridement, device removal, and long-term systemic antibiotic regimens. Antibiotic treatment can lead to the development of opportunistic infections through perturbations to the gut microbiota (*140*) and the development of antibiotic resistance (*141*). Further complicating the scenario is the formation of bacterial biofilms, populations of sessile and slowly dividing bacteria encapsulated within extracellular polymeric substances (*142, 143*). The biofilm matrix provides significant protection from the host immune system and acts as a diffusion barrier for antibiotics. The biofilm induces antibiotic tolerance through sequestration of antimicrobial agents, modulating nutrient gradients, and driving the development of persistor cells, together, allowing for bacteria to be resistant to antibiotic concentrations 1,000 times higher than that required to kill the same planktonic strain (*144*). Bacteria in

biofilms can be exposed to sub-inhibitory antibiotic concentrations, further driving the development of antibiotic resistance (*141*). As such, current treatment strategies for device-related infections are significantly limited, often requiring 1-2 revision surgeries, and causing significant patient morbidity, at a high economic cost of over $50,000 per case (*2*).

The widespread emergence of antibiotic-resistant bacteria is a growing public health threat, leading to a post-antibiotic era, where current therapies are no long effective (*145*). This threat has prompted the investigation of alternative strategies to traditional systemic antibiotic therapy. Lysostaphin is a 27 kDa antimicrobial enzyme with activity specific to *Staphylococcus* species (*4*). The enzyme has two domains, a cell wall targeting domain, responsible for its specificity, and a lytic domain, that cleaves the pentaglycine cross-bridges present in the bacterial cell wall (*i.e.*, peptidoglycan) (*3*). Lysostaphin exhibits activity against antibiotic-resistant *Staphylococcus aureus* strains, including methicillin-resistant *S. aureus* (MRSA), vancomycin-intermediate *S. aureus*, and vancomycin-resistant *S. aureus* (*7-9*), and *Staphylococcus epidermidis* (*103*). Importantly, lysostaphin kills planktonic and quiescent bacteria as well as cells growing in a biofilm (*6*), in contrast to most antibiotics that require active cellular metabolism to be effective (*72*). Widespread resistance to lysostaphin has not been reported from clinical samples (*146*), although several isolates have been generated in laboratory settings (*5, 147*). Additionally, the specificity of lysostaphin allows for only offending staphylococcal species being eliminated, thus preventing adverse effects of gut microbiota perturbation, which is associated with systemic antibiotic therapy. These characteristics make lysostaphin an ideal candidate to treat infections primarily limited to *Staphylococcus* species and where biofilm formation is often implicated in the disease process (*148*). Lysostaphin has been

delivered topically, systemically, or as material coatings in several small animal models to target *S. aureus* infections (*9, 11, 149, 150*). In humans, topical application of lysostaphin reduces *S. aureus* nasal carriage five days after treatment with no reported toxicity (*151*). Additionally, parental administration in a human patient has been reported without major side effects (*152*).

Despite these attributes, lysostaphin therapy has been severely limited by the lack of effective delivery vehicles. Conjugation of poly(ethylene glycol) (PEG) to lysostaphin increases the *in vivo* half-life of systemically administered enzyme from less than one hour to up to 24 hours, but at the expense of reduced enzymatic activity (*153*). Biomaterial carriers have focused on surface conjugation of lysostaphin to a material to prevent bacterial colonization (*150, 154-156*), as opposed to developing enzyme delivery vehicles. Localized delivery of antimicrobial therapeutics allows for higher drug concentrations to be achieved at the infection site over a longer period of time, with a lower risk of toxicity compared to systemic delivery (*157, 158*). Hydrogels are water-swollen polymer networks that exhibit significant therapeutic versatility for localized protein delivery (*159*). We previously engineered injectable PEG-based hydrogels for controlled delivery of protein- and cell-based therapeutics (*160-165*). In this platform, four-arm PEG macromers functionalized with terminal maleimide groups (PEG-4MAL) that react specifically with thiols are functionalized with cell adhesive peptides and cross-linked into a network using thiolated molecules such as protease-degradable peptides with terminal cysteines. These synthetic hydrogels exhibit significant advantages to other delivery vehicles including well-defined composition and structure, minimal toxicity, stoichiometric incorporation of

biomolecules, controlled polymerization kinetics, and non-toxic degradation products that are excreted in the urine (*162, 163*).

Here, we engineered lysostaphin-delivering injectable hydrogels to treat *S. aureus* orthopaedic hardware infections and support fracture repair. We characterized the activity, stability, and release of hydrogel encapsulated lysostaphin, as well as antimicrobial and anti-biofilm performance. The efficacy of lysostaphin-delivering hydrogels was tested *in vivo* using a murine femur fracture infection model. Bacterial reduction, cytokine profiling, and functional healing was measured to assess the therapeutic potential of lysostaphin-delivering hydrogel therapy. Finally, the antimicrobial efficacy of lysostaphin-delivering hydrogels against antibiotic-resistant bacteria was tested.

3.3 Results

3.3.1 Encapsulation of lysostaphin within injectable PEG hydrogels maintains activity

Orthopaedic fractures range from simple closed fracture patterns with minimal soft tissue injury to complex open compound fractures with significant muscle injury, making delivery by injection and *in situ* polymerization desirable features in an antimicrobial delivery system. This property allows for the material to conform to the injury by integrating into the tissue. We synthesized PEG hydrogels in a one-step reaction by mixing PEG-4MAL macromers with the protease-degradable peptide cross-linker GCRDVPMSMRGGDRCG (VPM) (*166*) and cell adhesive peptides (e.g., RGD, GFOGER), which were covalently incorporated into the network by terminal cysteine groups that react specifically with maleimides on the PEG-4MAL macromer (Fig. 1A). Lysostaphin enzyme was physically entrapped within the hydrogel without covalent

incorporation onto the polymer network due to the lack of free thiol groups in the protein (*167*). This injectable format allows for lysostaphin to maintain its activity throughout the hydrogel synthesis process. Sustained release of lysostaphin, both via passive diffusion through the hydrogel network and protease-dependent degradation of the hydrogel, results in lysis of target bacteria and supports bone formation and subsequent fracture repair (Figure 4A). To assess the effect of hydrogel mesh size on diffusion-dependent of release of lysostaphin, we labeled lysostaphin with a fluorescent dye (Figure 5) and measured its diffusion out of the hydrogel. We synthesized hydrogels using different sized PEG-4MAL macromers (10 kDa, 20 kDa) at 8.0% and 4.0% w/vol to generate hydrogels with different mesh sizes. Exponential one-phase association curves were then fit to these data. The 20 kDa hydrogels with a relatively larger mesh size exhibit more rapid lysostaphin release compared to the 10 kDa hydrogels with a tighter mesh structure (Figure 4B). This shows that as the mesh size is reduced the rate of diffusion-mediated release of lysostaphin is decreased. To evaluate lysostaphin activity following encapsulation and release, hydrogels were synthesized and placed in a bacterial suspension of *S. aureus* UAMS-1, a clinical isolate from a pediatric case of osteomyelitis (*168*), and reduction of bacteria was monitored overtime by optical density measurements. In this experiment, no protease was included so lysostaphin is released from the hydrogel only by diffusion. Lysostaphin-containing hydrogels rapidly and completely reduced bacteria levels in suspension (Figure 4C). Importantly, the rate of bacterial clearance was dependent on the dose of encapsulated lysostaphin. Retention of enzyme activity after hydrogel polymerization is a critical design criterion. We assessed the long-term activity of lysostaphin encapsulated within the hydrogel carrier and compared it to enzyme maintained in solution and fresh, reference

lysostaphin. Hydrogels were synthesized with lysostaphin and not swollen to prevent loss of enzyme to directly assess the hydrogel's capacity to maintain enzyme stability. Enzyme activity was determined by calculating the rate of bacterial killing, as defined by the time required to kill 50% of a UAMS-1 bacterial suspension. The rate of bacterial killing was determined by fully degrading the hydrogels in protease and incubating this product with bacteria, then monitoring the reduction in optical density over the course of 1 hour (Figure 6A-D). A one-phase decay curve was then fit to these data to obtain the half-life metric. Remarkably, hydrogel encapsulation preserved lysostaphin activity over 14 days when kept at 25ºC compared to soluble unencapsulated lysostaphin, which rapidly degraded (Figure 4D). There was no difference in lysostaphin activity between hydrogel-encapsulated enzyme throughout 14 days and fresh enzyme.

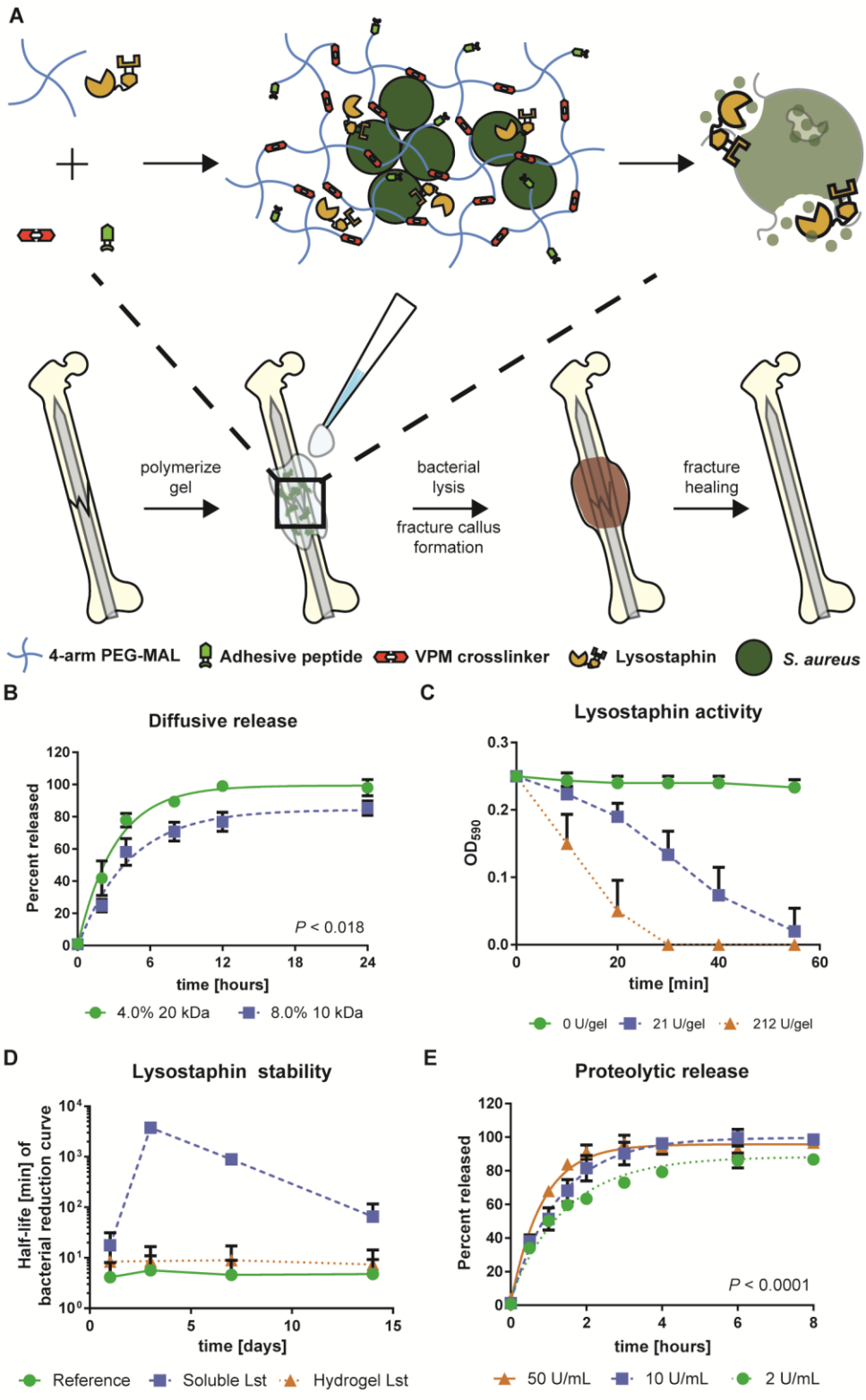

Figure 4: Lysostaphin-delivering hydrogel synthesis and characterization. (A) Schematic diagram of lysostaphin encapsulation within protease degradable PEG-MAL

hydrogel and subsequent application to infected femurs, which leads to fracture callus formation and healing. (B) Passive lysostaphin release with one-phase association fit with extra sum of squares *F* test to compare *K* values are different. (C) Optical density curves of lysostaphin-laden hydrogels placed in *S. aureus* UAMS-1 suspensions as a function of incubation time. (D) Lysostaphin activity as measured by the average half-life of the kinetic bacteria reduction assay (Figure 6A-D) at 1, 3, 7, and 14 days after hydrogel polymerization. (E) Protease-triggered release of lysostaphin with one-phase association fit using extra sum of squares *F* test to compare all *K* values are different. Means ± SD. *N*=3-5.

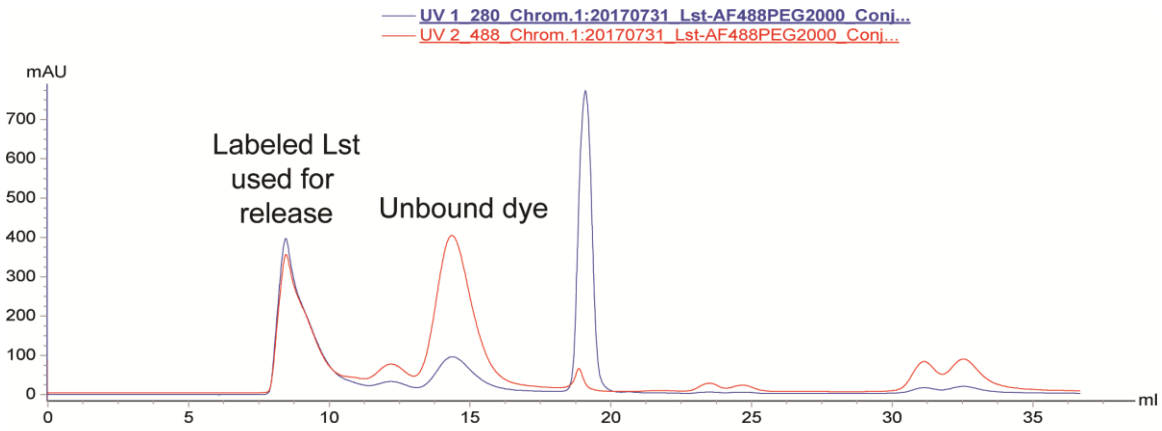

Figure 5: Fluorescent lysostaphin labeling and purification. Lysostaphin was labeled with an AlexaFluor 488 fluorescent dye conjugated to a 2000 Da PEG chain functionalized with an NHS-ester to label free-amines and purified with size exclusion chromatography. During the elution phase, 280 nm light was used to monitor protein content (blue) and 488 nm light monitored dye fluorescence (red). The peak with both 280 nm and 488 nm components was collected and used for the release studies.

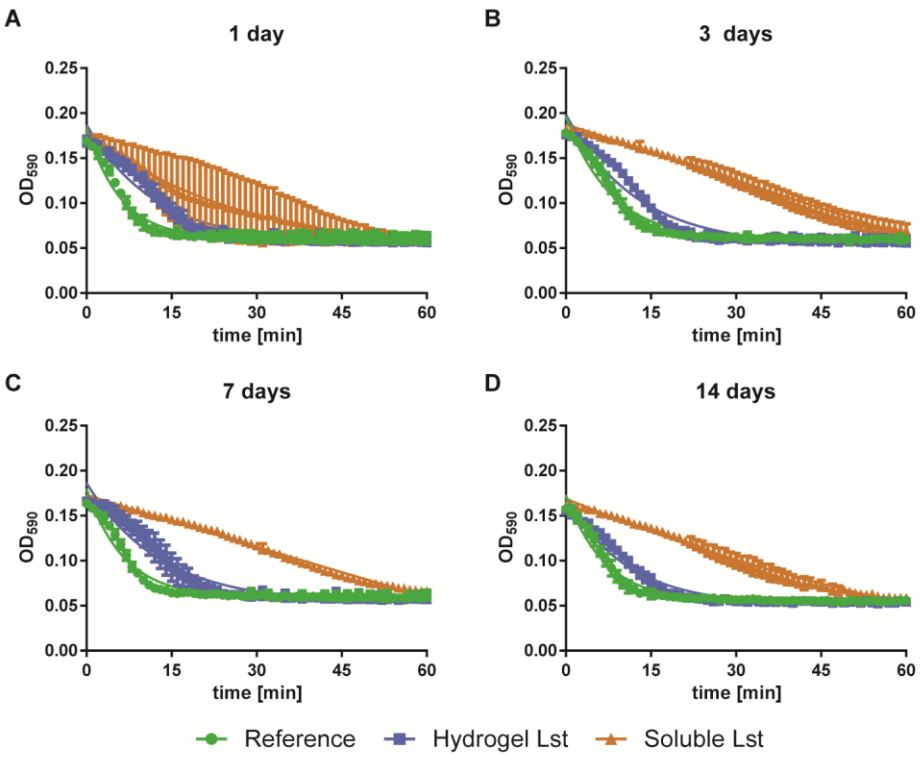

Figure 6: Kinetic optical density plots of UAMS-1 reduction from degraded hydrogels. Hydrogels and soluble lysostaphin were degraded in protease and the sample was added to a bacterial suspension of UAMS-1. The optical density of the suspension was monitored for one hour after (A) one day, (B), three days, (C) seven days, and (D) fourteen days at 25ºC. Solid line represents one-phase decay line of best fit. Means ± SD. *N*=3-5.

Bacterial infection often triggers an inflammatory response, including locally elevated protease levels (*169*). The inclusion of protease-degradable peptide cross-links in lysostaphin-delivering hydrogels allows for lysostaphin to be released on-demand in response to infection and local protease activity. Protease-dependent release of lysostaphin was characterized by monitoring the release of fluorescently labeled lysostaphin from lysostaphin-laden hydrogels (20 kDa, 4.0% w/vol) exposed to different levels of protease (Figure 4E). The results show that higher levels of protease cause faster lysostaphin release, indicating protease-responsive release. Importantly, nearly all of the loaded enzyme was

released in these assays. Measurement of the mechanical properties of lysostaphin-delivering hydrogels reveals that the addition of lysostaphin does not affect the elastic or viscous properties of the hydrogel, as determined by measuring the storage and loss moduli of the gels respectively (Figure 7A-D).

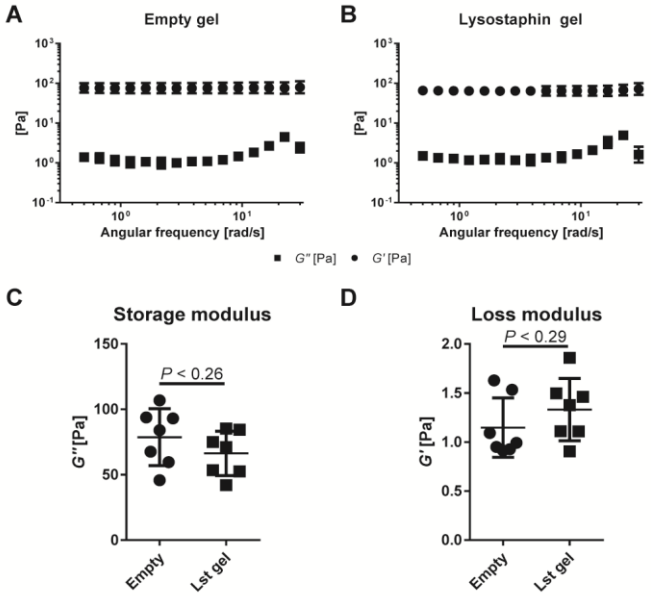

Figure 7: Mechanical properties of lysostaphin-delivering hydrogels. Angular frequency sweep of (A) empty and (B) lysostaphin-delivering hydrogels at a constant strain of 2%. Average (C) storage and (D) loss modulus of empty and lysostaphin-delivering hydrogels of eight data points within the linear region of the angular frequency sweep of each sample. Student *t* test. Means ± SD. *N*=7.

3.3.2 Encapsulated lysostaphin kills bacteria, including in biofilms

Lysostaphin is highly active against both *S. aureus* and *S. epidermidis* (*6*). We examined the bactericidal activity of the enzyme encapsulated in the hydrogel delivery system. Hydrogels were synthesized with different strains of *S. aureus* (Xen29, UAMS-1, 46106) or *S. epidermidis* (IDRL-8883, a clinical strain isolated from a prosthetic joint infection), trapped within the hydrogel matrix with or without lysostaphin (Table 3). The

gels were then cultured overnight in bacterial growth media and after 24 hours were assayed for viable bacteria. Encapsulated lysostaphin reduced viable bacteria to undetectable levels for all bacterial strains tested (Figure 8A-D). After confirming that lysostaphin-laden hydrogels are effective against various strains of bacteria, we tested the *in vitro* cytocompatibility of lysostaphin using human mesenchymal stem cells. We induced human mesenchymal stem cells to differentiate towards an osteogenic lineage and added lysostaphin to the culture media. Lysostaphin had no effects on the osteogenic differentiation of human mesenchymal stem cells as assessed by alkaline phosphatase activity (Figure 9A) and calcium deposition (Figure 9B-C), demonstrating that lysostaphin effectively kills staphylococcal species but does not interfere with osteogenic differentiation by mammalian cells.

Strain	**Source**	**Characteristics**	**Ref.**
S. aureus Xen29	Perkin Elmer - derived from ATCC 12600	Methicillin sensitive, pleural fluid isolate	(*50*)
S. aureus UAMS-1	ATCC 49230	Methicillin sensitive, pediatric osteomyelitis isolate, strong biofilm former	(*168*)
S. aureus 46106	Centers for Disease Control and Prevention Clinical and Environmental Microbiology Branch Culture Collection	Methicillin sensitive, abdominal wound isolate	
S. aureus USA300	ATCC BAA-1556	Methicillin resistant, wrist abscess of HIV positive IV drug user	(*170*)
S. epidermidis IDRL-8883	Mayo Clinic	Methicillin resistant, prosthetic joint infection	(*171*)

Table 3: Source, characteristics, references of bacterial strains used throughout the study.

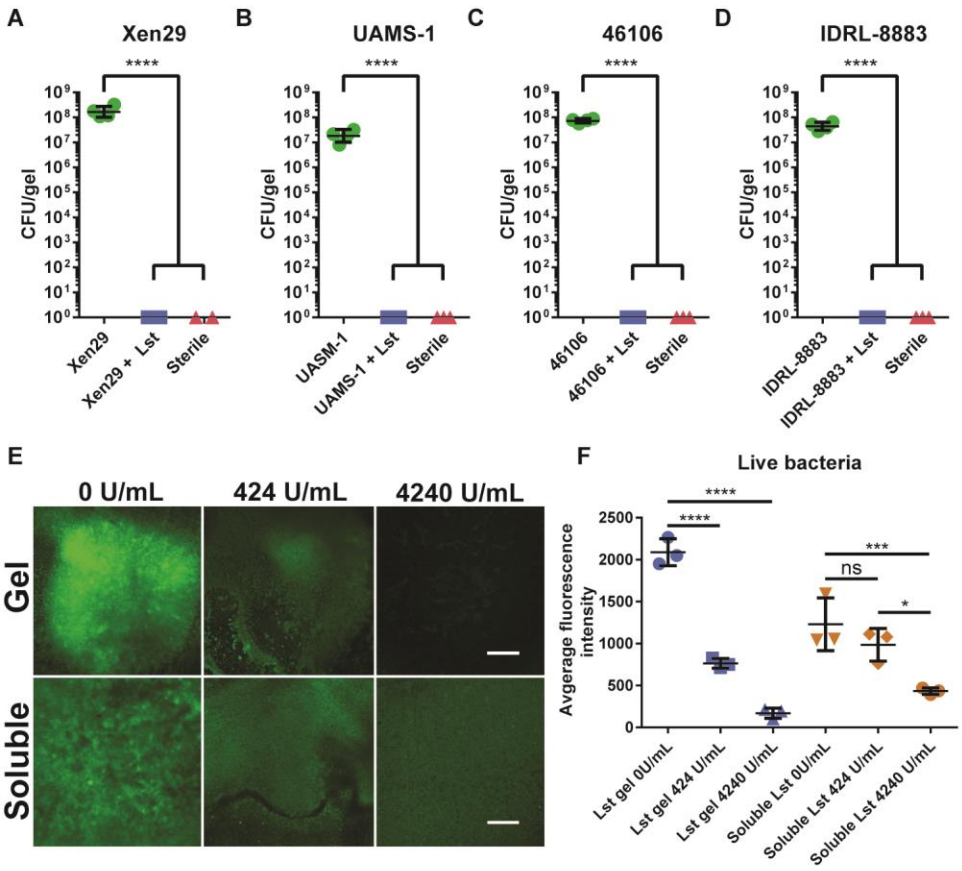

Figure 8: Lysostaphin-laden hydrogels effectively kill bacteria in vitro. Bacterial counts reported as CFU/gel after 24 hours of culture for (A) *S. aureus* Xen29, (B) *S. aureus* UAMS-1, (C) *S. aureus* 46106, and (D) *S. epidermidis* IDRL-8883. (E, F) Biofilms were generated by culturing UAMS-1 for 24 hours statically and were then treated overnight with a hydrogel or soluble enzyme. (E) Images and (F) quantification of average image intensity of live bacteria after treatment. Scale bar is 500µm. Means ± SD. N=3-4 per group. *P < 0.05, ***P < 0.001, ****P < 0.0001, one-way ANOVA with Tukey's post-hoc test.

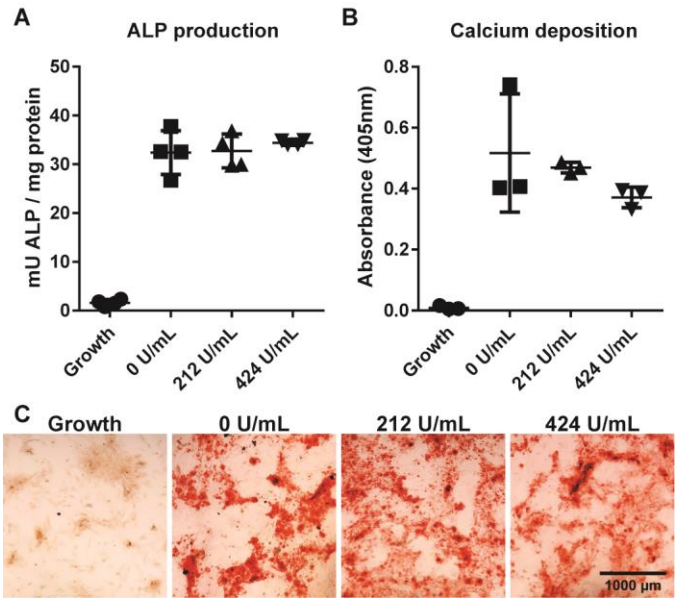

Figure 9: Lysostaphin supports hMSC differentiation. (A) Alkaline phosphatase production of hMSC exposed to lysostaphin after 9 days in culture. (B) Quantification of calcium deposition by Alizarin Red extraction from hMSC after 21 days in culture. (C) Representative images of Alizarin Red staining of hMSC cultures. One-way ANOVA with Tukey's post-hoc test. Means ± SD. *N*=3-4. All comparisons not significant.

Orthopaedic hardware infections typically involve formation of a bacterial biofilm. The biofilm protects the bacteria from the host immune response and acts as a diffusion barrier for antibiotics, making them particularly difficult to eliminate. We evaluated the anti-biofilm activity of lysostaphin-delivering hydrogels. We hypothesized that delivery via the hydrogel carrier would improve the anti-biofilm activity of the enzyme compared to soluble enzyme alone based on our observation that encapsulation within the hydrogel prolonged enzyme stability (Figure 4C). *S. aureus* strain UAMS-1 is a known prolific biofilm former (*172*). We grew UAMS-1 biofilms for 24 hours and then treated them with lysostaphin-laden hydrogels or soluble enzyme. After 18 hours of treatment, bacterial reduction was assessed by staining for live bacteria and subsequently imaging the biofilm. Figure 8E shows representative images of biofilms after treatment. There is a clear

lysostaphin dose-dependent reduction in live bacteria for the hydrogel-treated group, which is confirmed by image quantification (Figure 8F). Soluble delivery of the enzyme had little effect at the lower concentration tested with a reduction in live bacteria only at the higher concentration (Figure 8F).

3.3.3 Lysostaphin-laden hydrogels effectively reduce S. aureus infection of bone fractures

Treatment of long bone fractures, such as the femur, often requires fixation devices to stabilize the injury, enable healing, and promote return to mobility. However, bacterial infection of devices used to stabilize orthopaedic injuries leads to the inability of fractures to heal, characterized by bone resorption, reactive bone formation, implant loosening, and ultimately device failure (*134*). To model this situation *in vivo*, we developed a mouse model of orthopaedic hardware infection. In this model, the femur is fractured using a custom three-point bending device, the fracture is then stabilized with a 25G needle placed in the femoral shaft (*173*), and then a hydrogel is polymerized *in situ* over the fracture (Figure 10A). Importantly, the injectable hydrogel formulation conforms and adheres to the fracture and surrounding tissue, ensuring efficient, local delivery. For mice receiving an infection, bacteria is mixed with the hydrogel components and polymerized *in situ* over the fracture. We then measure bacterial counts one week after fracture or assess fracture healing five weeks post-implantation.

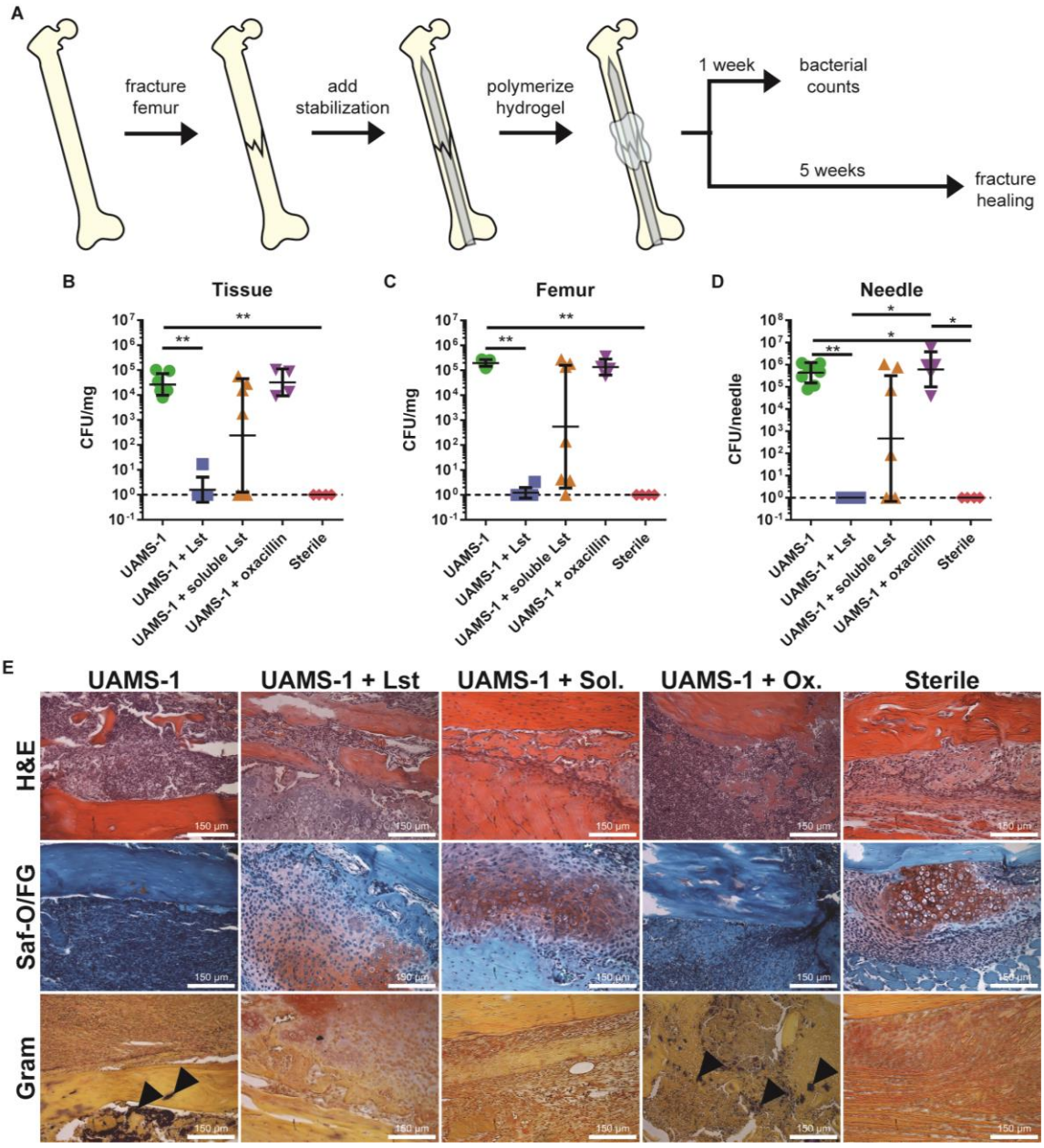

Figure 10: Lysostaphin-delivering hydrogels eliminate bacteria in infected fractures. (A) Schematic diagram of mouse femur infection model. Quantification of *S. aureus* UAMS-1 recovered from the (B) tissue surrounding the femur, (C) femur bone, and (D) stabilization needle 7 days post-fracture. Dashed line indicates detection limit. (E) Histological sections of femurs 7 days post fracture stained for hematoxylin and eosin, safranin-O and fast green, and Gram. Black arrows indicate Gram-positive bacteria. Kruskal-Wallis test with Dunn's multiple comparisons test. Means ± SD. *N*=4-8, compilation of four independent experiments. **P* < 0.05, ***P* < 0.01.

Lysostaphin-delivering hydrogels should support fracture repair in the absence of infection to be an acceptable therapy for preventing staphylococcal infections. We hypothesized that the application of a lysostaphin-laden hydrogel would not impair normal (sterile) fracture healing. To test this, femoral fractures were treated with a sterile, lysostaphin-delivering hydrogel or left untreated. No bacteria were delivered in this experiment. After 5 weeks, femora were explanted and analyzed by microcomputed tomography (μCT), mechanical testing, and histology to evaluate fracture repair. μCT reconstructions revealed no gross morphologic differences in the fracture callus (Figure 11A). Similarly, no differences in fracture callus volume (P=0.26, Figure 11B) or mechanical strength (P=0.94, Figure 11C) of the repaired femora were detected between untreated and lysostaphin-delivering hydrogel-treated mice. Histological staining with hematoxylin and eosin (H&E) for tissue morphology and safranin-O and fast green (Saf-O/FG) for cartilage also showed no gross differences in healing between sterile control fractures and fractures treated with lysostaphin-delivering hydrogels (Figure 11D).

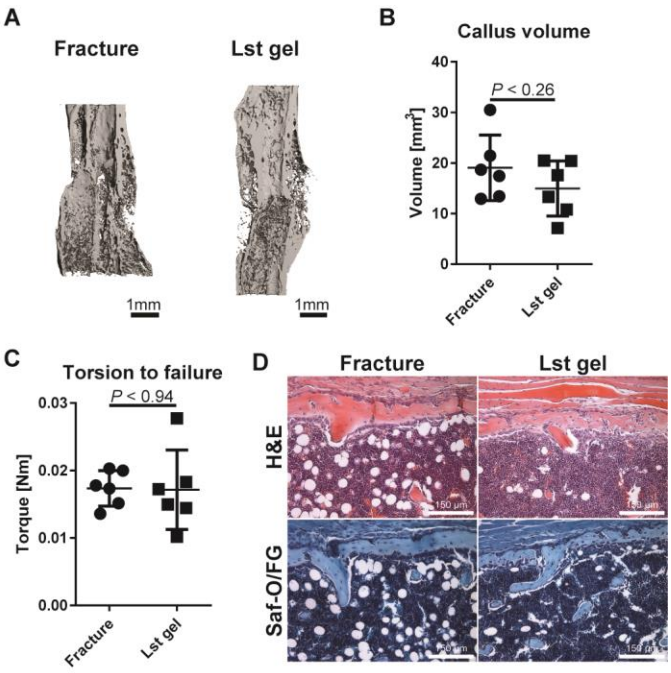

Figure 11: Lysostaphin-delivering hydrogels support fracture healing. (A) µCT reconstructions of the fracture callus 5-weeks post-operation. Quantification of (B) fracture callus volume and at 5 weeks. (C) Mechanical integrity of femurs as assessed by *ex vivo* torsion to failure testing. (D) Hematoxylin and eosin and safranin-O and fast green staining of femurs. *N*=6 per group. **P* < 0.05, Student's *t* test.

We next evaluated the ability of lysostaphin-delivering hydrogels to prevent *S. aureus* infection *in vivo* using the murine infected femur fracture model. Mouse femora were fractured and hydrogels containing methicillin-sensitive *S. aureus* UAMS-1 were polymerized *in situ* over the fracture to induce infection with or without lysostaphin. We included a group treated with soluble lysostaphin (no hydrogel) as well as an antibiotic prophylaxis group that received a single injection of oxacillin (100 mg/kg) pre-operatively to directly compare the lysostaphin-delivering hydrogel to antibiotic-based therapy. Seven days post-operation, animals were sacrificed, tissue was separated, and viable bacteria were enumerated in the tissue surrounding the femur (Figure 10B), the femur (Figure 10C), and the stabilization needle (Figure 10D). Untreated infected controls had high numbers of

recovered bacteria, indicating a persistent infection. Mice receiving prophylactic oxacillin therapy before the operation also had elevated bacteria counts, demonstrating that prophylactic antibiotic treatment did not prevent bacterial infection in this model. This result is consistent with clinical experience with systemic antibiotic regimens that do not consistently eliminate *S. aureus* infections. Treatment with lysostaphin-laden hydrogels significantly reduced the amount of recovered bacteria compared to the infection-only control and infections receiving systemic oxacillin. Importantly, the lysostaphin-laden hydrogels reduced bacteria counts to the same level as sterile controls. For the soluble lysostaphin-treated group, variable levels of bacteria were recovered and there was no difference in bacteria counts between this group and the infection-only control or the oxacillin-treated group, demonstrating that the hydrogel delivery vehicle is necessary to effectively treat these infections. The variability of infection clearance within the soluble lysostaphin group could be due to inadequate delivery of lysostaphin to the infection site since the soluble enzyme is not localized within a delivery carrier. Further, our *in vitro* data suggests the stability of the enzyme is reduced compared to lysostaphin delivered within the hydrogel. Histologic analysis demonstrated significant leukocyte infiltration for infection-only and oxacillin-treated fractures compared to sterile fractures and fractures treated with lysostaphin-laden hydrogels (Figure 10E). Safranin-O/fast green staining indicated poor collagen staining at the fracture site, characteristic of inhibited fracture repair, for the infection-only and oxacillin-treated fractures. In contrast, the lysostaphin-laden hydrogel treated samples showed collagen deposition at the fracture site, consistent with the sterile control. Gram-positive bacteria were detected in the infection-only control and oxacillin-treated groups showing that the infection persisted over the course of the

experiment. No Gram-positive bacteria were detected in the lysostaphin-treated and sterile groups. Taken together, these results demonstrate that lysostaphin-delivering hydrogels eliminate *S. aureus* infections of bone fractures and outperform systemic antibiotic and direct delivery of soluble lysostaphin.

3.3.4 Lysostaphin delivery to infections restores a sterile inflammatory environment

A major concern of bactericidal therapy is an elevated and sustained inflammatory response to bacterial degradation products that negatively impacts healing responses (*142*). Lysostaphin catalytically degrades the bacterial cell wall, leading to cell lysis and subsequent release of bacterial debris; the release of these bacterial products could cause a significant inflammatory response. To analyze this inflammatory response and assess the safety profile of lysostaphin therapy, we treated infected fractures with hydrogels containing lysostaphin or empty hydrogels. Sterile hydrogels containing lysostaphin were included as the healing control. One week post-infection, we performed a multiplexed cytokine array assay on explanted tissue. Hierarchal cluster analysis using the Ward Method revealed clear separation between the infected scaffolds and the sterile and lysostaphin-hydrogel treated gels (Figure 12A). Looking at the second tier of the cluster analysis shows two clusters containing a mix of sterile and lysostaphin-delivering hydrogel treated mice in the bottom right of the array. Closer analysis of these samples reveals that the individual cytokine levels measured are at or near the detection level of the assay and normalization by the protein content of the sample affects the values. Individual analysis of these cytokines using two-way ANOVA with Fisher's LSD test reveals no statistical differences between experimental groups. Multivariate ANOVA with a sum combination across all cytokines demonstrated significant differences ($P<0.001$) between the infection-

only group and the sterile and lysostaphin-gel treated fractures (Figure 12B). Importantly, significant overlap was observed between the sterile and lysostaphin-laden hydrogel groups, suggesting that the lysostaphin-delivering hydrogels restored the local inflammatory environment to a sterile state. Elevated levels of G-CSF, IL-1a, IL-1b, IL-6, KC, IP-10, MIP-1a, MIP-1b, and MIP-2 (Figure 12C-K), important cytokines in the inflammatory response to infection, were present in the infection-only group compared to the sterile control and lysostaphin-hydrogel treated infections. No differences were detected between the sterile and lysostaphin hydrogel-treated groups for any of the cytokines. These results provide further evidence that lysostaphin-delivering hydrogels clear infecting bacteria and restore an inflammatory environment that could support fracture repair.

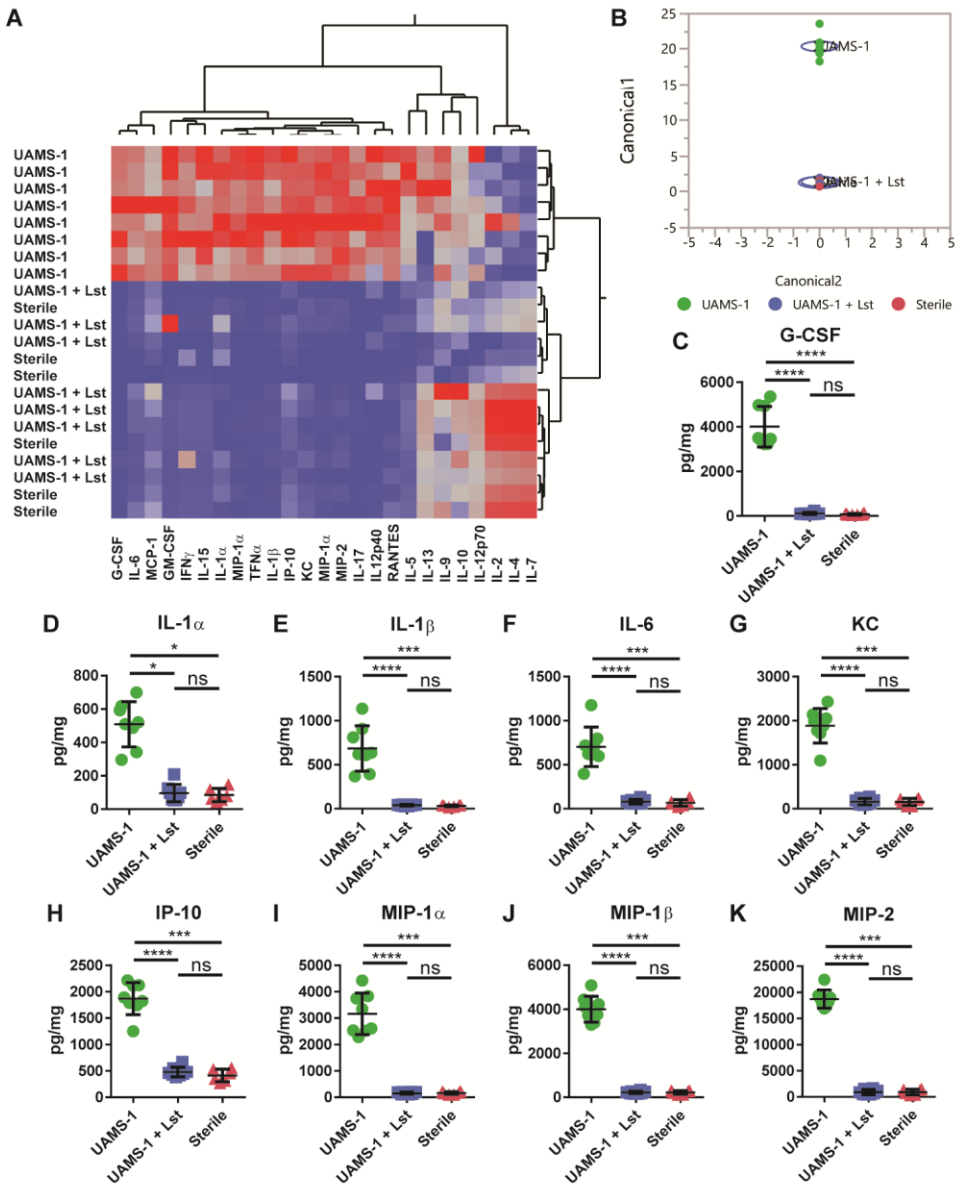

Figure 12: Lysostaphin-laden hydrogel therapy restores a sterile inflammatory environment. Femora were fractured and infected with UAMS-1 and treated with hydrogels with or without lysostaphin and the inflammatory milieu of tissue at the fracture site 7 days post-infection was assessed using multiplexed cytokine analysis. (A) Hierarchical cluster analysis of cytokine profiles using the Ward Method. (B) Multivariate-ANOVA plot using a sum combination across cytokines, $P<0.001$. (C-K) Cytokines with statistically different tissue levels as determined using two-way ANOVA with a Bonferonni Correction for multiple comparisons. Means ± SD. N=6-8 per group. *$P < 0.05$, ***$P < 0.001$, ****$P < 0.0001$, ns is not significant.

3.3.5 Lysostaphin-delivering hydrogels result in healing of infected femoral fractures

To determine whether treatment of infections with lysostaphin-delivering hydrogels effectively reduces the bacterial infection and promotes fracture repair, we assessed functional fracture healing at 5 weeks post-infection. Mouse femora were fractured and hydrogels containing *S. aureus* UAMS-1 were placed at the fracture site to induce infection. These hydrogels contained lysostaphin or were left naïve as controls. The lysostaphin-delivering hydrogels were benchmarked against soluble lysostaphin delivery. Sterile, lysostaphin-delivering hydrogels were included as the positive healing control. The fractures were allowed to heal for five weeks, and then fracture repair was analyzed using μCT imaging, torsion to failure testing was used to assess the mechanical integrity of the femora, and histologic evaluation. Reconstructions of μCT scans (Figure 13A) show no callus formation in the UAMS-1-infected control group and the presence of bone resorption and reactive bone formation around the fracture site, which is characteristic of osteomyelitis caused by bacterial infection. The sterile controls developed a robust fracture callus with evidence of bone remodeling, demonstrating fracture healing. All mice in the lysostaphin-laden hydrogel treated group showed significant fracture healing. A fracture callus was formed and the volume of the callus (Figure 13B, $P>0.99$) and bone deposition within the callus (Figure 13C, $P>0.99$) were equal to the sterile controls. Callus volume and bone volume were higher for infected fractures treated with lysostaphin-laden hydrogels compared to infection-only fractures (Figure 13B-C, $P<0.05$). Fracture repair was highly variable in the soluble lysostaphin treated group, 2/6 samples did not form a fracture callus and displayed features of osteomyelitis, including bone resorption and reaction bone formation (Figure 14A). The remaining 4/6 samples treated with soluble

lysostaphin formed a fracture callus and progressed towards fracture healing (Figure 14B).Importantly, the torsional strength of infected fractures treated with lysostaphin-laden hydrogels was significantly higher than that for the infection-only control ($P<0.001$), and these high torque values were equivalent to those for the sterile control group (Figure 13D). This result demonstrates that lysostaphin-delivering hydrogels clear the bacterial infection and support effective and complete fracture repair. No differences were observed between infected fractures treated with soluble lysostaphin and infection-only controls, again showing poor outcomes for lysostaphin therapy without the hydrogel carrier. Histologic sections of infected fractures treated with lysostaphin-delivering hydrogels and sterile fractures show no notable morphological differences (Figure 13E), providing further support of successful fracture repair. The infection-only group shows significant leukocytic infiltrate on H&E staining and the presence of Gram-positive bacteria (black arrows). This result clearly demonstrates persistent infection and inflammation for infected fractures that were not treated with lysostaphin-laden hydrogel.

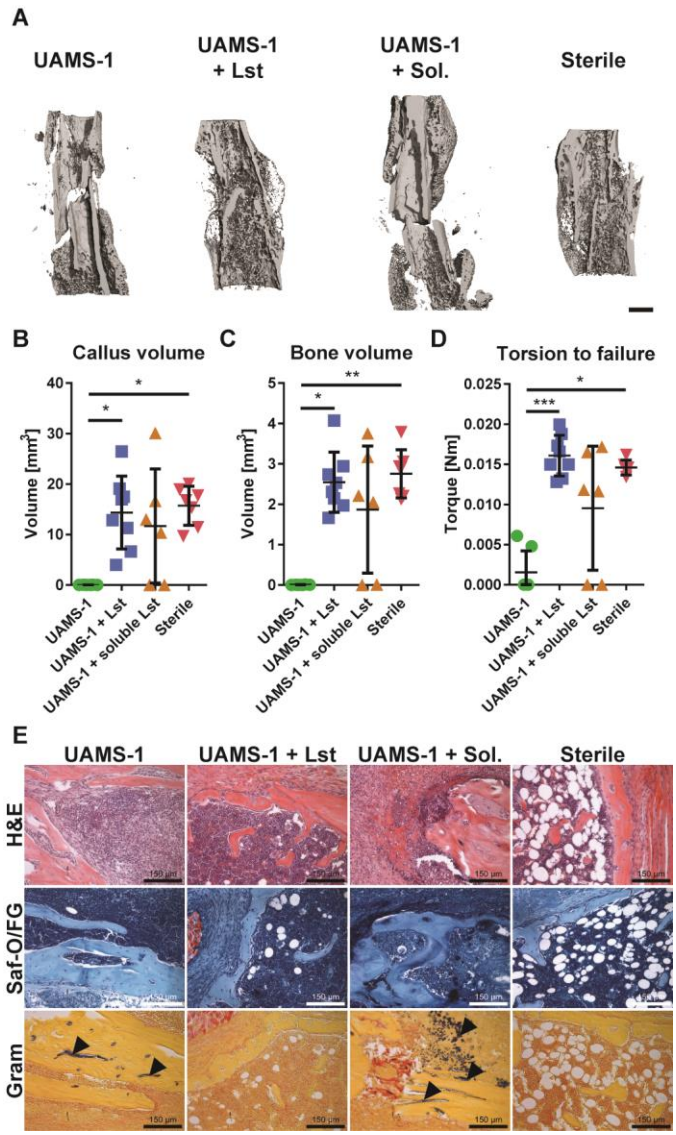

Figure 13: Lysostaphin-delivering hydrogels enable fracture healing. (A) µCT reconstructions of the fracture callus 5 weeks post-operation (scale bar 1mm). Quantification of µCT reconstructions showing the (B) fracture callus volume and (C) bone volume within the fracture callus at 5 weeks. (D) Mechanical strength of femurs as assessed by *ex vivo* torsion to failure testing. (E) Hematoxylin and eosin, safranin-O and fast green, and Gram staining of femurs. Black arrows indicate Gram-positive bacteria. Kruskal-Wallis test with Dunn's multiple comparisons test. Means ± SD. *N*=6-8, compilation of two individual experiments. **P* < 0.05, ***P* < 0.01, ****P* < 0.001.

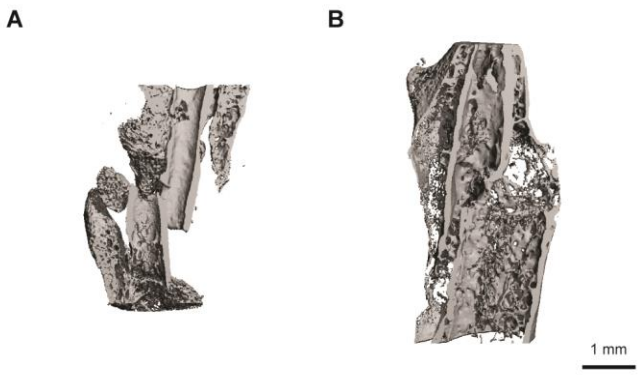

Figure 14: µCT reconstructions of non-healing and healing soluble lysostaphin treated fractures. Mice treated with soluble lysostaphin exhibited a non-healing (A) and healing (B) response.

3.3.6 Lysostaphin-delivering hydrogels clear MRSA bone infections

To test the efficacy of lysostaphin-delivery hydrogels to combat antibiotic-resistant bacteria, we measured bacterial numbers of the persistent infection 7 days post-operation with the MRSA strain USA300. Mouse femora were fractured and hydrogels containing MRSA were placed at the fracture sites to induce infection. These hydrogels contained lysostaphin or were left empty as controls. Sterile lysostaphin-delivering hydrogels were used as controls. Consistent with the results obtained with UAMS-1, lysostaphin-delivering hydrogels significantly reduced MRSA bacteria counts compared to the infection-only control for the tissue surrounding the femur (Figure 15A), the femur (Figure 15B), and the stabilization needle (Figure 15C). Notably, all of the lysostaphin hydrogel treated mice had undetectable levels of bacteria. This shows that lysostaphin-delivering hydrogels eradicate antibiotic-resistant bacteria.

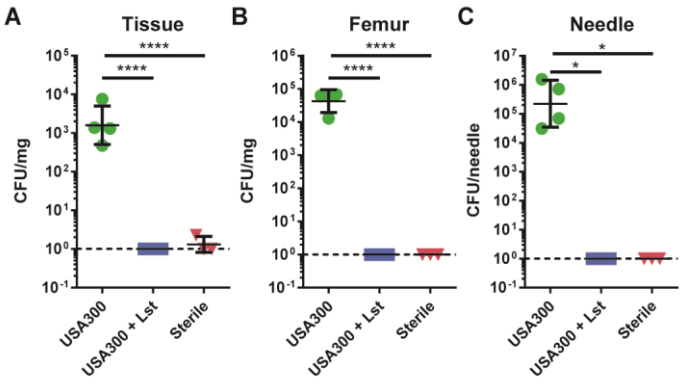

Figure 15: Lysostaphin-laden hydrogels clear MRSA infections. Quantification of MRSA USA300 recovered from the (A) tissue surrounding the femur, (B) femur, and (C) stabilization needle at 7 days post-fracture. Dashed line indicates detection limit. ANOVA with Tukey post-hoc test for (A) and (B). Kruskal-Wallis test with Dunn's multiple comparisons test for (C) Means ± SD. N=3-4. *P < 0.05, ****P < 0.0001.

3.4 Discussion

Orthopaedic hardware infections are a significant clinical problem and lack effective therapies. Current interventions are limited to long term systemic antibiotics, surgical debridement, and implant removal. Alternative therapy with antimicrobial enzymes such as lysostaphin provides for effective killing of specific bacterial species, however these approaches are limited by the lack of suitable delivery vehicles. Here, we engineered synthetic hydrogels to deliver active lysostaphin to infected bone fractures to clear the infection and promote fracture healing. The synthetic hydrogel delivery vehicle maintained lysostaphin activity over 14 days and controlled the release of active enzyme via passive and protease-triggered mechanisms. These hydrogels displayed high activity against various strains of *S. aureus*, as well as a methicillin-resistant *S. epidermidis* clinical isolate from a prosthetic joint infection *in vitro*. Importantly, lysostaphin delivery via the hydrogel carrier outperformed soluble enzyme when treating biofilms, most likely due to

the sustained release of active lysostaphin. In a murine model of fracture infection, lysostaphin-delivering hydrogels cleared the infections and supported fracture repair, with bone formation and mechanical properties equivalent to that of uninfected fractures. Lysostaphin-delivering hydrogels restored the local inflammatory environment to that of sterile fractures at 7 days. In contrast, infected fractures treated with either prophylactic antibiotics or soluble lysostaphin showed no differences in bacterial levels and impaired healing compared to the infection controls. Notably, delivery of lysostaphin with this hydrogel carrier significantly reduced MRSA infections in this fracture model. Taken together, these results show that hydrogel-mediated delivery of lysostaphin eliminates fracture infections, including antibiotic-resistant strains, allowing for the endogenous fracture repair mechanisms to progress and healing to occur.

Biomaterial strategies to deliver active lysostaphin have primarily focused on surface functionalization, either by passive adsorption (*11, 13*), covalent tethering (*155, 174*), or impregnation within a coating (*150, 175*). This is an effective way to reduce bacteria at the material surface, but may not be practical for settings where infection is already established, or not localized to a material surface (e.g., surrounding tissue). Our injectable formulation allows for *in situ* polymerization of the hydrogel at the fracture site, adhering and conforming to the injured tissue, which is an important feature for treating complex fractures. We demonstrate that lysostaphin-delivering hydrogels have greater anti-biofilm activity compared to soluble lysostaphin. This effect may be attributed to the enhanced enzyme stability and higher concentrations of lysostaphin localized to the biofilm achieved using the hydrogel carrier. Together, these material properties could allow for a

broader application of lysostaphin-delivering hydrogels to treat other types of staphylococcal infections.

We demonstrate that lysostaphin-delivering hydrogels are effective at reducing infection for both clinical osteomyelitis and MRSA isolates *in vivo*. As with any antimicrobial therapy, the development of resistance to the treatment is a potential concern. Interestingly, lysostaphin exhibits synergism with β-lactam antibiotics, and lysostaphin exposure can sensitize strains to the antibiotic they have resistance against (*5, 103*). Therefore, lysostaphin delivery together with antibiotics could broaden the activity of the enzyme, while also reducing the chance of resistance developing. A lysostaphin-based approach offers several advantages over traditional small molecule antibiotics. The bacteriospecific nature of lysostaphin provides specific targeting of the infecting organism, which may reduce complications associated with disrupting commensal bacteria (*140*). Small molecule antibiotics primarily function through disruption of bacterial metabolic processes, leading to growth inhibition and death. This reliance limits drug activity against biofilm bacteria. The enzymatic nature of lysostaphin sidesteps this requirement, as the enzyme directly disrupts and kills bacteria. This feature contributes to the low concentrations (ng/mL range) required to kill bacteria compared to antibiotics (μg/mL range) (*6*), thereby reducing the amount of enzyme needed to provide bactericidal activity to the infection site.

Lysostaphin-delivering hydrogel treatment assists in restoring a pro-healing inflammatory environment, supported by the absence of differences in cytokine secretion profiles compared to the sterile control. We attribute this effect to the kinetics of bacterial debris clearance by inflammatory cells, which is complete by 7 days after treatment. This

result also supports the translation of lysostaphin therapy, as rapid bacterial killing and clearance are critical features for materials designed to treat infections. Importantly, lysostaphin administration with the hydrogel carrier eradicates the infection while supporting fracture healing as assessed by both μCT imaging and mechanical testing. The protease degradable nature of the hydrogel carrier, in addition to protease-triggered release of lysostaphin, allows for host cells to degrade the hydrogel during repair, resulting in replacement of the gel with repair tissue. This is in contrast to non-degradable scaffolds that are either never removed, or only removed at revision surgery once the infection is cleared. A concern with lysostaphin use is the development of neutralizing antibodies. Indeed, several studies have reported antibody development (*151, 153, 176*), but bacteriolytic activity was preserved in rabbits immunized to lysostaphin before therapy (*176*). Additionally, de-immunization of lysostaphin by removing protein recognized by T-cell epitopes reduces the likelihood of antibody generation (*177, 178*), which could eliminate concerns of systemic immune response to therapeutic delivery. We found that 1/5 mice treated with lysostaphin-delivering hydrogels tested positive for anti-lysostaphin IgG antibodies five weeks after treatment, with none of the sterile or infected lysostaphin-free mice testing positive. However, pre-exposure serum was not tested for existing IgG titers, making it difficult to definitively conclude that the lysostaphin-delivering hydrogel generated an immune response. Furthermore, concerns over the development of neutralizing antibodies against lysostaphin are minimal for the bone repair application presented here as it would be exceedingly rare for a patient to have multiple independent infected or open fractures requiring lysostaphin therapy in a lifetime.

The present application focused on a biomaterial to specifically reduce *S. aureus* infections using lysostaphin. This technology could be further enhanced by broadening the antimicrobial spectrum to target other relevant pathogens in osteomyelitis cases, such as other coagulase-negative *Staphylococcus* species, *Pseudomonas,* and *Enterococcus* (*2*). Broadening the bacterial targets of the material will increase its utility as an effective prophylactic (*179, 180*). It will also be important to evaluate the ability to treat established biofilms *in vivo* (*53*). Species-specific antimicrobial therapies with activity towards bacteria growing in biofilm will help to successfully treat these complicated infections with reduced side effects to patients, such as disruption of the gut microbiota. Finally, this strategy will need to be evaluated in larger animal models for safety and efficacy to further assess its clinical potential.

3.5 Materials and Methods

Study Design

This study was designed to test whether lysostaphin-delivering hydrogels reduce *S. aureus* infection and allow for femoral fracture repair to occur. We hypothesized that a hydrogel carrier would improve the efficacy of lysostaphin's ability to kill bacteria, while allowing for the endogenous fracture healing mechanisms to occur. Lysostaphin-delivering hydrogels were first characterized and the antimicrobial activity was assessed *in vitro*. We examined the antimicrobial activity of lysostaphin *in vivo* using a mouse femur fracture infection model. The study groups included untreated UAMS-1 infections, lysostaphin-delivering gels, soluble lysostaphin (no hydrogel), pre-operative oxacillin injection, and uninfected lysostaphin-delivering gels. Male C57/B6 mice were used for all studies with

4-8 biological replicates per group with the experiment performed at least in two independent runs. Sample sizes were selected based on statistical power calculations and estimates from previous studies. The time point of one week was selected for the microbiologic assessment because it allowed for the development of a persistent infection. Colony forming units were assessed in the surrounding tissue, femur, and fixation needle. Inflammatory profiling was performed at one week to allow for a persistent infection to develop. We hypothesized that lysostaphin-delivering hydrogels would allow for infected fractures to undergo repair. Five weeks was selected based on previous studies as the endpoint for analyzing fracture repair to allow for adequate bone remodeling and mineral deposition to occur. *Ex vivo* μCT imaging and torsion to failure testing were used to evaluate fracture healing. To assess the activity of lysostaphin-delivering hydrogels to reduce antibiotic resistant infections, mice were infected with the MRSA strain USA300 and assessed for viable bacteria at seven days. Animals were randomly selected for histological examination. The experimental groups were not blinded except for the analysis μCT imaging. Excluded data was limited to animals that did not reach the pre-specified end point due to post-operative surgical complications, such as significant weight loss or destabilization of the fixation needle.

Bacteria strains and culture

The bacteria strains used in these studies were UAMS-1 (ATCC 49230 (*168*)), USA-300 (ATCC BAA-1556 (*170*)), Xen29 (Perkin-Elmer (*50*)), 49230 (CDC Clinical and Environmental Microbiology Branch Culture Collection), IDRL-8883 (Clinical isolate (*171*)) and are compiled in Table S1. All strains were cultured on trypic soy agar (TSA) plates (BD Diagnostics) at 37ºC unless otherwise specified.

Preparation of lysostaphin-delivering hydrogels

20 kDa PEG-4MAL macromer (Lysan Bio) was mixed with recombinant lysostaphin protein (AMBI Products LLC) in 100 mM MES buffer pH 5.5-6.0. Hydrogels were then cross-linked in a one-step reaction by combining PEG-lysostaphin with either the GFOGER peptide, GGYGGP$(GPP)_5$GFOGER$(GPP)_5$GPC (New England Peptide), or the RGD peptide, GRDGSPC (AAPPTEC), VPM cross-linker, GCRDVPMSMRGGDRCG (Genscript), and the bacterial suspension. Bacterial suspensions were prepared by picking individual colonies of bacteria grown on a TSA plate overnight and suspending them in Dulbecco's Phosphate Buffered Saline supplemented with calcium and magnesium (PBS) to an optical density of 0.20 at 600 nm (MicroScan Turbidity Meter, Seimens) and then diluting this suspension 100-fold. The viable count for all bacterial inocula was determined by plate count on TSA medium. Unless otherwise noted the hydrogels were 4.0% w/v 20 kDa PEG-4MAL, 1 mM GFOGER, and 424 U/mL lysostaphin. The amount of VPM cross-linker added was determined stoichiometrically by matching the remaining maleimide groups after accounting for GFOGER or RGD incorporation. After mixing, the hydrogels were allowed to gel for 15 minutes in a humidified incubator at 37ºC and 5.0% CO_2 for *in vitro* studies or polymerized over the fracture for *in vivo* studies.

Lysostaphin activity and stability assays

Lysostaphin was encapsulated within 25 µL sterile hydrogels (4.0% w/v 20 kDa PEG-MAL, 1 mM RGD, VPM, 424 U/mL lysostaphin). The soluble lysostaphin group was 424 U/mL lysostaphin in an equivalent buffer to the hydrogel formulation in 25 uL aliquots. The reference lysostaphin group was prepared fresh from frozen at each time point. At 1,

3, 7 and 14 days, samples were incubated in 50 µL of 730 U/mL collagenase for 1 hour at 37ºC and then 50 µL of each sample was assessed for activity by incubating with 150 µL UAMS-1 inoculum. The inoculum was prepared by culturing UAMS-1 overnight in brain heart infusion (BHI) broth with shaking at 37ºC, washing three times in 200 mM Tris-HCl pH 8.0 by centrifugation, and adjusting the optical density to 0.25 at 600 nm (MicroScan Turbidity Meter, Seimens). Changes in optical density at 590 nm were measured using a HTS 7000 Plus plate reader (Perkin Elmer) every minute for 1hr at 35ºC.

Lysostaphin release from PEG hydrogels

Amine groups on lysostaphin were fluorescently tagged using an AlexaFluor 488 dye conjugated to a 2 kDa PEG linker functionalized with an NHS ester (Nanocs). The reaction was performed in 100 mM $NaHCO_3$ buffer at pH of 8.3 at room temperature for one hour with continuous mixing in the dark. Excess dye was removed from labeled protein using an AKTA Pure 25 (GE Healthcare) in combination with a Superdex 75 increase size exclusion column (GE Healthcare) using PBS as the running buffer, at 4ºC. Labeled lysostaphin was incorporated in the hydrogel conditions tested: 4.0% w/v 20 kDa PEG-4MAL, 1 mM RGD, VPM; and 8.0% w/v 10 kDa PEG-4MAL, 1mM RGD, VPM. For the diffusion release study, hydrogels were polymerized, swollen in PBS, and incubated statically at 37ºC and 5.0% CO_2. For the protease-triggered release studies, 4.0% w/v 20 kDa PEG-4MAL, 1 mM RGD, VPM hydrogels were swollen in PBS supplemented with 2 U/mL, 10 U/mL, or 50 U/mL collagenase type 1 (Worthington) and incubated shaking at 200 rpm, 37ºC, and 5.0% CO_2. At each time point, the supernatant was sampled and read (488/530 excitation/emission) on a Synergy H4 (BioTek) plate reader. The measured

fluorescence values were normalized to the fluorescence of PEG-4MAL/lysostaphin mixtures of the respective hydrogel condition.

Measurement of hydrogel mechanical properties

Hydrogels with (424 U/mL) and without (0 U/mL) lysostaphin (4.0% w/v 20 kDa PEG-4MAL, 1 mM RGD, VPM) were synthesized in circular 4.5 mm diameter silicone isolators and swollen overnight in PBS at 4ºC. The loss and storage moduli were measured using a MCR 302 stress-controlled rheometer (Anton Paar) in combination with a 9 mm diameter, 2º measuring cone. The hydrogels were placed between the cone and plate and the cone was lowered to 39 µm. A strain amplitude sweep was performed at a constant frequency of 10 rad/s to identify the linear viscoelastic range. Oscillatory frequency sweeps were then performed (ω=0.5-30 rad/s) at a constant strain of 2%.

Human mesenchymal stem cell differentiation potential and calcium deposition

Bone marrow-derived human mesenchymal stem cells (Texas A&M) were cultured in growth media: αMEM (ThemoFisher) with 16.5% fetal bovine serum, 2-4 mM L-glutamine (ThermoFisher), 100 U/mL penicillin, and 100 µg/mL streptomycin at 37ºC, 5% CO_2. Media was changed every 2-3 days. Cells were seeded at 10,000 cells/cm^2 and differentiated using growth media supplemented with 10 nM dexamethasone, 20 mM β-glycerolphosphate, and 50 µM L-ascorbic acid supplemented with the indicated concentration of lysostaphin. After nine days of differentiation, alkaline phosphatase (ALP) activity was assessed. Cells were lysed and ALP activity was measured using 4-methylumbelliferyl phosphate disodium salt (MUP) substrate (*181*). Fluorescence was read at 360nm/465nm excitation/emission using a Synergy H4 plate reader (BioTek). Activity

was standardized with purified calf intestinal ALP at known dilutions, and normalized to total protein content determined using the bicinchoninic acid assay (Pierce BCA Protein Assay Kit, ThermoFisher) per the manufacturer's instructions. After 21 days of differentiation, cultures were fixed in 10% formalin, stained with alizarin red, and imaged at 4x with an EVOS Cell Imaging System (ThermoFisher). Alizarin red was then extracted and absorption was measured at 405 nm using a Synergy H4 plate reader (BioTek).

In vitro antimicrobial assessment of lysostaphin gels

The indicated bacterial strain was grown overnight on TSA at 37ºC. Bacterial cells were suspended in sterile PBS to an optical density to 0.20 measured at 600 nm (Microscan Turbidity Meter, Siemens). This suspension was then diluted 100 x in 100 mM MES buffer and used as the inoculum. Hydrogels were synthesized (4.0% w/v 20kDa PEG-MAL, 1mM RGD, VPM, 424U/mL lysostaphin), inoculated with the diluted bacterial culture, and incubated overnight in 25% trypic soy broth (TSB) at 37ºC statically. Viable bacteria were enumerated by washing the hydrogels three times in PBS and degrading them in 365 U/mL collagenase Type 1 (Worthington) for 1 hour. The degraded gels were serially diluted in PBS and 10 µL of each dilution was plated on TSA and grown overnight at 37ºC. Colony forming units (CFU) were then enumerated.

Anti-biofilm activity of lysostaphin hydrogels

Biofilms were grown by inoculating 500 µL of BHI supplemented with 1% glucose (*182*) in a 48-well tissue culture plate with 20 µL of UAMS-1 cells picked from a TSA plate and suspended in PBS to an optical density to 0.20 measured at 600 nm. The biofilm was cultured 24 hours at 37ºC statically. Biofilms were washed with PBS and 75 µL hydrogels

(4.0% w/v 20 kDa PEG-MAL, 1mM RGD, VPM, 0 U/mL, 424 U/mL, or 4240 U/mL lysostaphin) were polymerized on top of the biofilm or hydrogel buffer with a matching amount of lysostaphin added to the well, and incubated for 15 minutes at 37ºC, 5.0% CO_2 to allow for hydrogel polymerization. BHI media with 1% glucose was then added and biofilms were grown overnight, at 37ºC. Biofilms were washed, fixed with 4.0% paraformaldehyde, and stained using LIVE/DEAD BacLight Bacterial Viability Kit (ThermoFisher) per manufacturer's instructions (*183*). A Nikon-C2 laser scanning confocal microscope using a 4X objective to acquire four images per well that were subsequently stitched together was used to image the biofilms. Live bacteria stained with SYTO9 were imaged using a 488 nm excitation laser in combination with a 525/50nm filter. Live bacteria were quantified by measuring the average pixel intensity of a 2656.37µm x 2657.37µm selection of the image centered over the center of the well.

Murine femur fracture model

All animal procedures were performed in accordance with Institutional Care and Use Committee-approved protocols at the Georgia Institute of Technology. Male C57/B6 mice 10-12 weeks old were housed with 12 hour light/dark cycles and freely provided food and water. Mice were anesthetized under isofluorane and administered slow-release buprenorphine (1 mg/kg) to control pain post operatively. Fur on the right hind-leg was removed by shaving followed by the application of depilatory cream. Animals receiving antibiotic injections were administered oxacillin (100 mg/kg) intraperitoneally. The skin was disinfected by swabbing with alcohol followed by chlorohexidine. A lateral incision was made over the femur and the muscle was blunt dissected to expose the femur. The patella was then dislocated and a sterile 25-guage needle was inserted into the femur shaft

and retracted. The femur was fractured at the mid-diaphysis with a custom-made three-point bender. Following fracture, the needle was positioned through the femur to stabilize the fracture and cut to an appropriate length. For animals receiving a hydrogel, 5 µL of the hydrogel was pipetted over the fracture site and allowed to polymerize. The average inoculum of UAMS-1 used in all studies was 1.55 +/- 0.51 x 10^8 CFU/mL, which correlated to approximately 1500 CFU/mouse. The inoculum for the USA300 study was 3.43 x 10^8 CFU/mL, correlating to approximately 3400 CFU/mouse. For animals receiving soluble lysostaphin, 5 µL of lysostaphin at a concentration equal to that of the hydrogel was pipetted over the fracture after the infection was initiated with a hydrogel containing bacteria. The muscle and patella were then sutured back into place and the wound was closed using wound clips. An X-ray image (MX-20 Radiolography System – Faxitron Imaging, 23kV, 15 second scan time) was taken to confirm proper insertion of the needle and stabilization of the femur. Mice were allowed to recover under a warming lamp until ambulatory.

Recovery of bacteria from tissue samples

Mice were euthanized by CO_2 inhalation 7 days after surgery. Wound clips were removed and the skin on the right hind-leg was sterilized with alcohol. A lateral incision was made over the femur and the needle was removed from the femoral shaft and placed in PBS. The femur and surrounding tissue were separated, weighed and placed in PBS. All samples were kept on ice following dissection and removal. The tissue and femur samples were then homogenized via bead beating (Femur: MP Biomedicals lysing matrix A, 2x40sec @ 6 m/s; Tissue: OPS Diagnostics 1.4 mm zirconium beads, 5x40sec @ 6 m/s) using the FastPrep-24 (MP Biomedical). Following homogenization, single cell bacterial

suspensions were achieved by a series of water bath sonication (42 kHz, Model 2510, Branson Co., Danbury, CT) sonicating and vortexing steps (sonicate 10min, vortex 30sec, sonicate 5min, vortex 30sec, sonicate 30sec, vortex 30sec) (*93*). Homogenates were serially diluted, plated on TSA, and incubated overnight at 37˚C. Colonies were enumerated, normalized to sample weight, and transformed using the formula $CFU=\log_{10}(1+X)$ to avoid negative values. The detection limit was set to be 10 colonies in the undiluted sample to avoid false positive results.

Microcomputed tomography and mechanical testing of femurs

Five weeks post-operatively, mice were euthanized by CO_2 inhalation. The femur was dissected and the needle was removed. The femur was placed in gauze soaked in 0.9% w/v saline and frozen at -20ºC until further analysis. Samples were thawed under running deionized water and imaged using the µCT50 (Scanco Medical) at 55 kVp and 145 µA with a 0.5 mm filter and 300 ms integration time to achieve a 10 µm voxel size. 3D reconstructions were generated by segmenting the fracture callus from cortical bone and applying a Gaussian filter (sigma = 0.8, support =1) and threshold value equivalent to 50% of intact cortical bone (*173*). Immediately after imaging, samples were mounted in potting blocks filled with Wood's metal and torsion to failure was assessed with a MRTP-0.2NM force transducer (Interface) interfaced with an ELF 3200 (Bose) mechanical testing system running WinTest7. A continuous ramp function of 3 degrees/s was applied and the highest recorded torque value was reported. Femurs not able to be tested due to a lack of mechanical integrity were assigned a value of 0.

Dot blot for anti-lysostaphin antibody generation

Upon euthanization by CO_2 inhalation five weeks after fracture, blood was collected via cardiac puncture and serum was separated, frozen, and stored at -80ºC until analysis. A nitrocellulose membrane was hydrated in tris buffered saline (TBS) and lysostaphin (100 µg/mL) was bound to the membrane using a vacuum driven Manifold I Spot Blot System (Schleicher & Schuell). Samples were then blocked with TBS supplemented with 0.05% Tween-20 (TBS-T) and 1% bovine serum albumin (BSA). The spot blots were then washed in TBS-T. Serum sample were diluted 10,000 times in blocking buffer and flowed over the membrane. A polyclonal mouse anti-lysostaphin IgG (Antibody Research Corporation) was used as a positive control. Following washing with TSB-T, anti-lysostaphin antibodies were detected using an AlexaFluor-488 labeled polyclonal goat anti-mouse IgG antibody (Abcam) diluted 1,000 times in blocking buffer. The blot was then imaged using a Typhoon FLA 9500 gel imager (GE Healthcare). Blot intensity was then quantified using ImageQuant (GE Healthcare). Positive blots were determined to be twice the average intensity of serum samples from animals not exposed to lysostaphin.

Histology of femur samples

At the designated time point, mice were euthanized by CO_2 inhalation. The skin was removed and the needle was carefully extracted from the femoral canal. The entire femur and intact surrounding tissue was removed and fixed in 10% neutral buffered formalin. The samples were then decalcified in formic acid, paraffin embedded, and 5 µm sections were prepared. Samples were deparaffinized, rehydrated, and stained using H&E, Saf-O/FG, or Gram stain. Color images were acquired with a Nikon Eclipse E600 microscope using a

Plan Fluor 20x objective (Nikon), Micropublisher 5.0 RTV (Q imaging) color camera and Q-Capture software (Q imaging).

In vivo cytokine analysis

One week post-operatively, mice were euthanized via CO_2 inhalation. The femur was dissected and the fracture site with surrounding tissue was removed and placed in RIPA buffer. Samples were minced and placed on ice. Samples were sonicated for 10 s and debris was pelleted by centrifugation. The supernatant was passed through a 0.45 μm filter, snap frozen in liquid nitrogen, and stored at -80ºC until analysis. A MilliPlex 25-plex mouse cytokine kit (Millipore Sigma) was used per the manufactures instructions to assay for tissue concentrations of G-CSF, GM-CSF, IFN-γ, IL-1α, IL-1β, IL-2, IL-4, IL-5, IL-6, IL-7, IL-9, IL-10, IL-12p40, IL-12p70, IL-13, IL-15, IL-17, IP-10, KC, MCP-1, MIP-1α, MIP-1β, MIP-2, RANTES, and TNF-α. Samples with measurements below the detection limit of the assay were reported as the detection threshold. Similarly, samples with values greater than the standard cure were reported as the maximum. All cytokines were normalized to the total protein content of the individual sample, which was determined using a bicinchoninic acid (BCA) assay kit (Pierce by ThermoFisher) per manufacturer's instructions.

Statistics

Individual data points are plotted with a line representing the mean and error bars indicating the standard deviation of the mean. Statistical significance ($P < 0.05$) was determined using the student *t* test to evaluate two groups, ANOVA for multivariate groups with a Tukey post hoc test, or a Kruskal-Wallis test with Dunn's post hoc test for nonparametric data.

One-phase association curves were fit to the release data and an extra sum of squares *F* test as used to compare that *K* values were different. All calculations were performed using Prism (GraphPad). The multivariate analysis of multiplex cytokine data was performed using JMP Pro 13. Multivariate ANOVA with a sum combination was used to compare across cytokines. A two-way ANOVA with a Bonferroni correction was used to make comparisons between groups for individual cytokines with Prism (GraphPad).

LYSOSTAPHIN AND BMP-2 CO-DELIVERY REDUCES *S. AUREUS* INFECTION AND REGENERATES CRITICAL-SIZED SEGMENTAL BONE DEFECTS

4.1 Abstract

In the US, nearly 112,000 orthopedic device infections occur annually, with *Staphylococcus aureus* being the most common pathogen. These infections lead to implant failure and subsequent removal, motiving the development of bifunctional materials that both promote repair and prevent failure due to infection. Lysostaphin is an anti-staphylococcal enzyme that functions as a glycine-glycine endopeptidase cleaving the penta-glycine linkages in the peptidoglycan cell wall of Staphylococcal species leading to lysis and biofilm reduction. Lysostaphin use is limited by a lack of effective delivery methods to provide sustained, high doses of enzyme to infection sites. We engineered a BMP-2 loaded lysostaphin-delivering hydrogel that simultaneously prevents *S. aureus* infection and repairs segmental bone defects. Lysostaphin-delivering hydrogels eradicated *S. aureus* infection one week after implantation. At 8 weeks, BMP-2 loaded lysostaphin hydrogels significantly regenerated bone within the defect compared to untreated controls, which resulted in mechanically functional bone as assessed by torsion to failure testing. Lysostaphin-delivering hydrogels exhibit no hepatotoxicity and restore the local inflammatory environment to that of a sterile injury after one week, as assessed by cytokine and immune cell profiling. These data support that BMP-2 loaded lysostaphin-delivering hydrogel therapy effectively eliminates *S. aureus* infection while simultaneously regenerating functional bone resulting in segmental defect healing.

4.2 Introduction

Effective treatment of infected segmental bone defects remains a significant clinical challenge in the field of orthopaedics (*184*). Nonunion bone defects are a common clinical scenario accounting for over 600,000 hospital cases per year totaling over 5 billion dollars in costs (*185, 186*). The current standard of care includes surgical placement of bone auto- and allografts to facilitate healing (*30, 187*). However, these grafting procedures have failure rates reported as high as 13% (*188*) and donor site morbidity occurs in 20-30% of cases (*189*). Furthermore, bacterial infection of bone grafts significantly increases implant failure rates, often leading to corrective surgery, including debridement of infected tissue, and significant morbidity to the patient (*31-33, 187, 190, 191*). Up to 30% of nonunion injuries produce positive bacterial cultures, with staphylococcal species being the most common pathogen (*137-139*). This motivates the development of materials that both promote bone regeneration and prevent failure due to infection.

Lysostaphin is a metalloendopeptidase produced by *Staphylococcus simulans* (*4*). This antimicrobial enzyme is specific to staphylococcal species. Its specificity is provided by a domain that binds the *S. aureus* cell wall (*3, 192*), and the antimicrobial activity is attributed to a catalytic domain that functions by cleaving the second and third glycine residues making up the pentaglycine peptidoglycan cross bridges responsible for bacterial cell wall integrity (*5*), leading to cell lysis. The catalytic nature of lysostaphin make its antimicrobial activity independent of the bacterial metabolic state, providing activity against sessile biofilm bacteria (*6*). This in in contrast to most small molecule antibiotics that require metabolically active bacteria to be effective (*72*). Lysostaphin therapy prevents or reduces infection in several small animal models, including systemic infection (*10, 193,*

194), wound infection (*193*), endocarditis (*7, 9*), nasal colonization (*151, 195*), keratitis (*149*), catheter colonization (*11, 13*), ocular infection (*176*), and neonatal infections (*12*). A clinical case report of systemic lysostaphin therapy in an unresponsive leukemia patient with MRSA pneumonia, multiple abscesses, and cellulitis has been reported after failure of aggressive antibiotic therapy (*152*). The patient received intravenous infusion of 500 mg of lysostaphin. The reported side-effects included flushing, mild hypotension, and tachycardia, which were effectively controlled. Blood, sputum, and abscess cultures were negative following lysostaphin administration until the patient's death three days later, which was unrelated to the infection. Biomaterial carriers have been explored to increase lysostaphin stability and retention times at the site of administration, but retention times are still limited to a few hours (*196-199*). Biosynexus Corp. moved to commercialize lysostaphin cream to reduce intranasal *S. aureus* colonization. The phase I/II clinical trials demonstrated safety and efficacy; but upon completion, the current clinical standard, mupirocin, came off patent protection, making the further development of lysostaphin cream for intranasal infections economically insolvent (*200*). Taken together, it is evident that there is significant potential for the use of lysostaphin to treat staphylococcal infections.

Due to the high failure rates of bone grafting to treat segmental defects, recombinant bone morphogenetic proteins (BMPs), such as BMP-2 (*201*), BMP-7 (*202*), and BMP-14 (*203*) have been under development for use in humans. BMP-2 has been FDA approved to facilitate bone formation in anterior lumbar interbody fusion procedures (*204*). However, for effective induction of bone formation, superphysological doses are delivered, which can result in several unintended side effects, such as ectopic bone formation, nerve

damage, and significant inflammation (*205*). This motivates the development of delivery carriers for controlled BMP-2 release to improve bone healing and reduce unintended side effects.

Hydrogels are a class of materials that can be engineered to deliver a wide array of protein therapeutics. Hydrogels are water-swollen cross-linked polymer networks with characteristics that are highly desirable for protein delivery scaffolds. Our lab has engineered 4-arm poly(ethylene glycol)-maleimide (PEG-4MAL) hydrogels for the delivery of both protein and cell based therapeutics (*160-165*). This synthetic delivery platform provides a well-defined hydrogel mesh structure, mild reaction conditions that are minimally toxic to cells, precise stoichiometric incorporation of biomolecules and cell adhesive ligands, control over the polymerization kinetics for injectable or pre-cast gel delivery, and small degradation products that have low toxicity and are excreted through the urine. We have previously engineered PEG-4MAL hydrogels functionalized with the collagen-mimetic cell adhesive peptide GFOGER and loaded with BMP-2 to treat critical-sized mouse radial segmental bone defects (*164*). These BMP-2 loaded hydrogels regenerated bone of superior quality compared to the clinical standard of a BMP-2 loaded collagen sponge.

We hypothesized that BMP-2 and lysostaphin co-delivery would eradicate *S. aureus* infection, allowing for bone regeneration and functional healing. Therefore, we synthesized protease degradable PEG-4MAL hydrogels functionalized with GFOGER and loaded with BMP-2 and lysostaphin, and delivered them to mouse radial segmental defects to treat *S. aureus* infection. We then evaluated their efficacy through a combination of bacterial viability counts, μCT imaging, histology, and mechanical testing. We also

assessed the safety profile of these materials by performing liver function testing, testing for anti-lysostaphin antibody generation, and characterizing the local inflammatory environment with cytokine array profiling and cell recruitment analysis.

4.3 Results

4.3.1 Lysostaphin-delivering hydrogels eliminate S. aureus infection in a mouse radial segmental defect

Injuries resulting in a critical-sized segmental bone defects often require reparative surgery and the utilization of bone grafting or growth factor delivery to repair the injury. However, these strategies come with high rates of graft failure (*30*) and bacterial infection rates as high as 30% (*22*). Therefore, it is desirable to engineer bi-functional materials capable of eliminating infection while simultaneously repairing the bone. Our lab has previously reported that BMP-2 delivery using a PEG hydrogel functionalized with the collagen-mimetic peptide GFOGER to a mouse radial segmental defect outperforms the conventional BMP-2 loaded collagen sponge as measured by increased bone volume and superior functional healing. We set out to engineer a bone reparative hydrogel that eliminates *S. aureus* infection through the delivery of lysostaphin. To test our materials, a 2.5 mm non-healing segmental bone defect was removed from a mouse radius (Figure 16). The hydrogel is pre-cast inside of a 4.0 mm polyimide sleeve and placed over each end of the radius within the defect. Bone regeneration is then assessed over time with μCT. We synthesized lysostaphin- and BMP-2-delivering hydrogels with a one-pot reaction by mixing the protease-degradable cross-linking peptide VPM and the cell adhesive peptide GFOGER, which was covalently incorporated into the network via a peptide terminal

cysteine residue, with a 4-arm maleimide terminated PEG (PEG-4MAL) macromer (Figure 16). Both lysostaphin and BMP-2 were physically entrapped within the hydrogel mesh structure, as neither protein has free thiols available for covalent tethering into the matrix. This allows for lysostaphin to diffuse throughout the gel and kill bacteria. The hydrogel was then injected into a 4.0 mm polyimide sleeve for subsequent implantation to treat the radial segmental bone defect. To induce an infection component to the model, *S. aureus,* was added to the hydrogel. Consistency between experiments was assessed by assaying extra bacteria containing implants and comparing the bacterial counts to previous experiments.

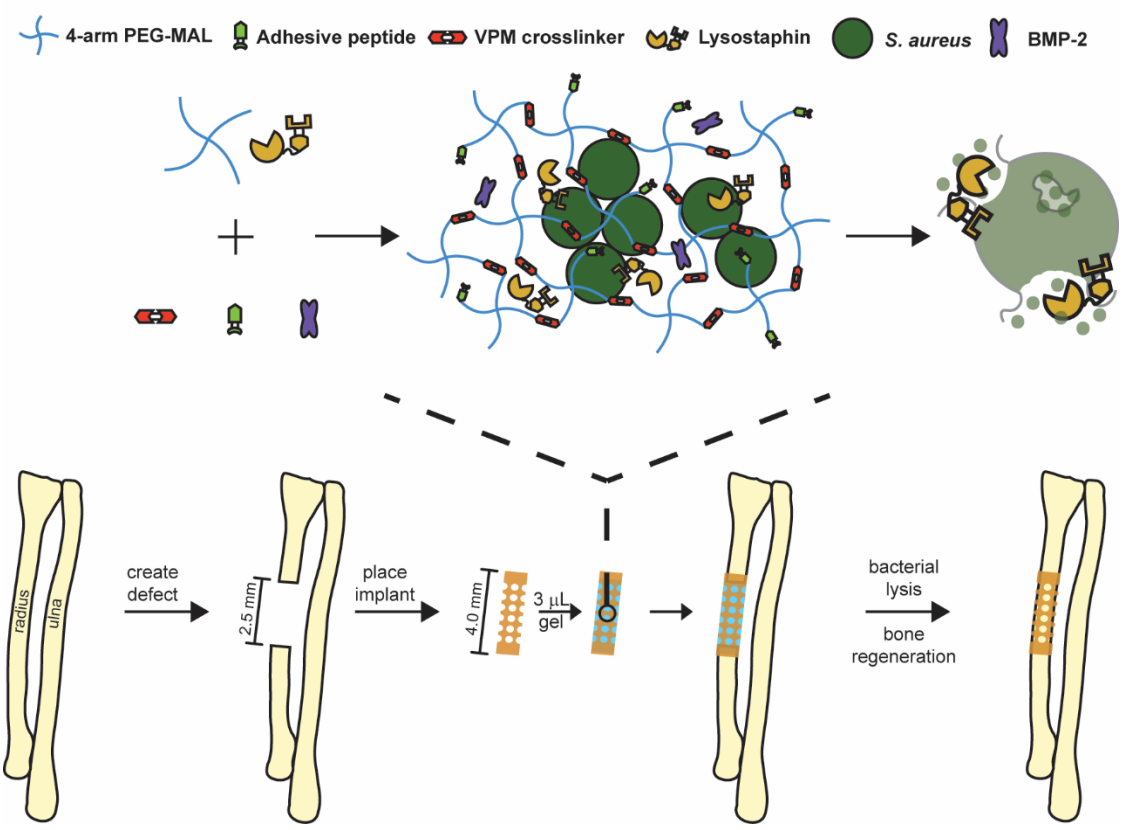

Figure 16: Lysostaphin and BMP-2 co-delivery to a critical-size segmental bone defect. A 2.5 mm segment of the radius is removed to create a critical-sized bone defect that does not spontaneously heal. A PEG-4MAL hydrogel functionalized with the adhesive ligand GFOGER and loaded with lysostaphin and BMP-2 is synthesized with *S. aureus*. Lysostaphin enzymatically creates holes in the bacterial cell wall leading to lysis. These infected hydrogel scaffolds are loaded into a 4 mm polyimide sleeve and placed over the ends of the defect. Co-delivery of BMP-2 and lysostaphin results in infection clearance followed by subsequent defect regeneration.

First, we tested the ability of lysostaphin-delivering hydrogels to eliminate *S. aureus* infection using the described mouse segmental defect infection model. *S. aureus* Xen29, a luminescent strain derived from an abdominal wound infection (ATCC 12600) that has kanamycin resistance allowing for selective growth, was chosen for the initial studies. The antimicrobial activity of the lysostaphin-delivering hydrogels was assessed by implanting hydrogels and then performing a microbiologic and histologic analysis at 7 days post-implantation (Figure 17A). The experimental groups included Xen29-containing

hydrogels with and without lysostaphin, and sterile hydrogels that were either empty, or loaded with lysostaphin. Bacteria recovered from the tissue samples were grown on both antibiotic-free agar and agar supplemented with kanamycin to selectively culture Xen29. The results showed that antibiotic selection of Xen29 did not affect bacterial viability (Figure 17B), and that there was a very strong correlation ($R^2 = 0.96$) between each culture media used (Figure 17C). With this result in mind, we used kanamycin selection for all Xen29 studies to reduce the chances of contamination in the necropsy procedure. The detection limit of this assay was set to be 100 CFU per sample (or 10 bacterial colonies in an undiluted sample). Microbiologic analysis showed significant reduction and complete eradication of *S. aureus* in the infection group treated with lysostaphin (Figure 17D). This demonstrates that lysostaphin-delivering hydrogels successfully prevent infection in radial segmental defects. Histologic analysis via hematoxylin and eosin staining (H&E) revealed significant leukocytic infiltrate in the untreated infection group, which we attribute to a robust inflammatory response to the pathogen (Figure 17E). In contrast, infections treated with lysostaphin-delivering hydrogels did not display this strong inflammatory response and had tissue morphology similar to both sterile control groups; this result suggests that the infection was cleared by the lysostaphin-containing hydrogel. Similar histologic results were observed using safranin-O/fast green (Saf-O/FG) staining. The Gram stain revealed the presence of Gram positive bacteria in the Xen29 group. No bacteria was detected using Gram staining in the lysostaphin-delivering hydrogel group, further supporting that the infection was eliminated.

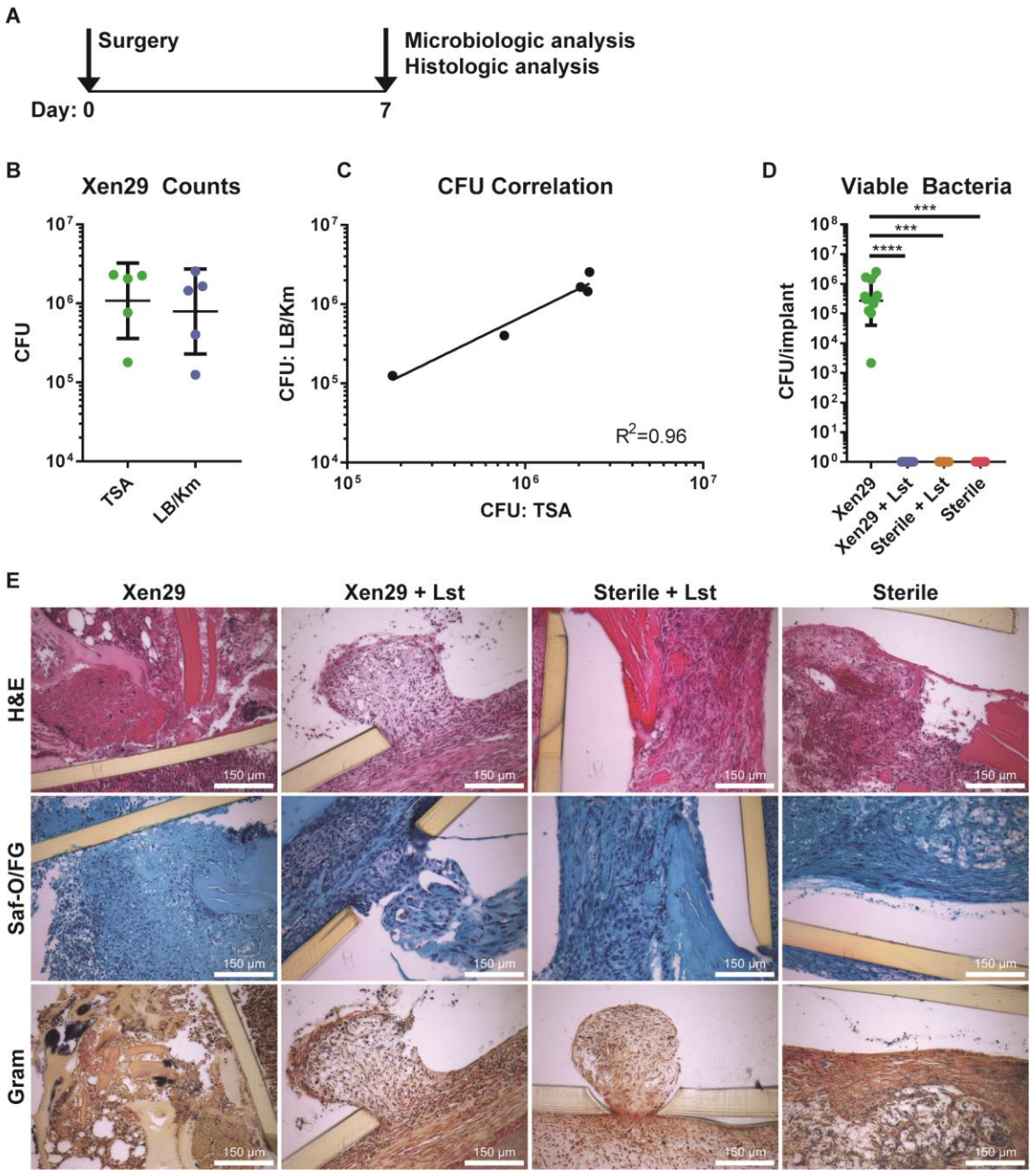

Figure 17: Lysostaphin-delivering hydrogels eliminate infection at 1 week. (A) Lysostaphin-delivering hydrogels infected with S. aureus Xen29 were implanted into mouse radial segmental defects. Viable bacteria were recovered and histologic analysis was performed one week later. (B) Viable bacteria recovered from defect sites culture on antibiotic free (TSA) and kanamycin supplemented (LB/Km) media. (C) Correlation of recovered bacteria samples from each culture media used in (C). (D) Viable bacteria recovered from the implant and surrounding tissue one week after implantation. (E) Histologic images of tissue sections stained with H&E, Saf-O/FG, and Gram stain.

Kruskal-Wallis with Dunn's post-hoc test. Means ± SD. *N*=5-11 per group combined from two independent experiments. ***$P < 0.001$, ****$P < 0.0001$.

4.3.2 BMP-2 loaded lysostaphin-delivering hydrogels eliminate infection and promote bone repair in a critical-sized segmental bone defect

Next, we tested the ability of BMP-2 loaded lysostaphin-delivering hydrogels to simultaneously kill bacteria and promote new bone formation. Radial defects were created and both sterile and infected (*S. aureus* Xen29) hydrogels, with and without lysostaphin, were assessed. All implants contained 50 ng of BMP-2. Live animal X-ray imaging and μCT analysis was performed at 0, 4, and 8 weeks and terminal microbiologic and histologic analysis was completed at 8 weeks (Figure 18). The experimental groups included hydrogels with and without lysostaphin that were synthesized sterilely or with *S. aureus* Xen29. X-ray imaging shows that infected mice, not receiving lysostaphin treatment, exhibit significant osteolysis and reactive bone formation at 4 and 8 weeks post-implantation (Figure 19). In contrast, infections treated with hydrogels containing lysostaphin have significant new bone formation, similar to defects treated with sterile hydrogels with and without lysostaphin (Figure 19). Analysis of the defect with μCT imaging corroborates these findings. Representative μCT reconstructions reveal no new bone formation in the defect site for the infection only control group, whereas infected mice treated with lysostaphin undergo progressive bone regeneration throughout the 8 week observation period (Figure 20A, C, E). At the time of surgery, all of the defects had equal amounts of bone present (Figure 20B). Subsequent longitudinal quantification of bone volume at the defect site reveals a significant increase in new bone formation for infections treated with lysostaphin-containing hydrogels and the sterile controls compared

to the infection only group at 4 weeks (Figure 20D). At 8 weeks bone volume is significantly increased in both of the sterile groups, with no differences between the infection and lysostaphin hydrogel-treated infection groups (Figure 20E).

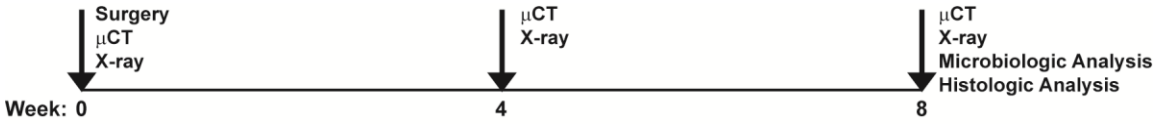

Figure 18: Experimental outline of the Xen29 bone repair study. Bone formation was assessed longitudinally with a combination of *in vivo* X-ray and μCT imaging at 0, 4, and 8 weeks after defect creation and implant placement. At 8 weeks, end point histologic and microbiologic analysis was performed.

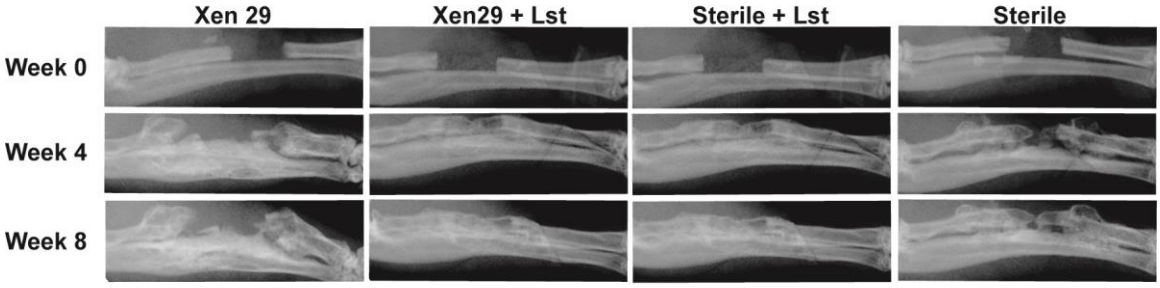

Figure 19: Longitudinal X-ray imaging of lysostaphin-delivering hydrogels to treat infection and repair bone. Representative radiographic images of the mouse radii at the time of surgery (week 0) and then 4 and 8 weeks post-op.

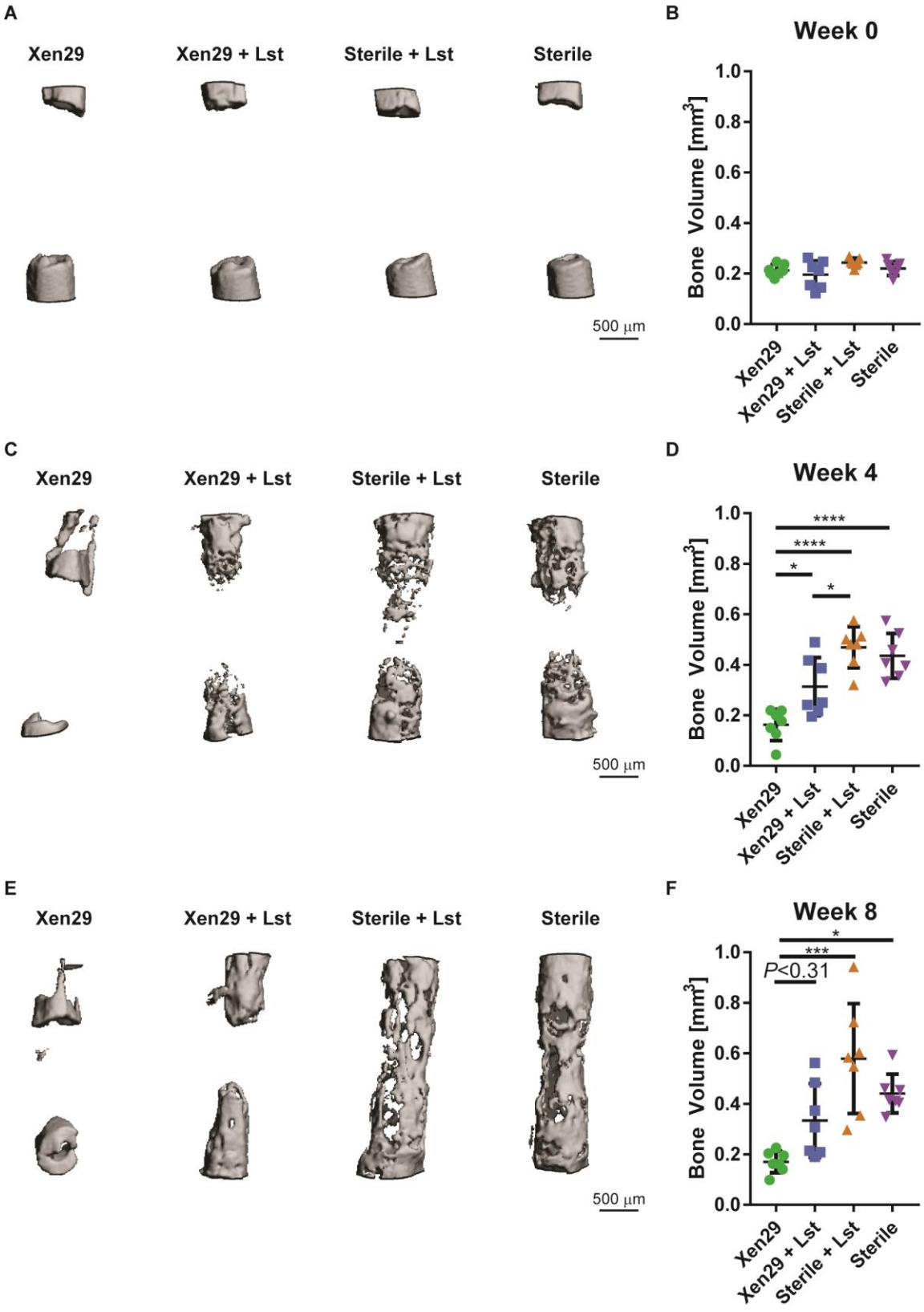
A
Xen29
Xen29 + Lst
Sterile + Lst
Sterile
500 µm
B
Week 0
Bone Volume [mm3]
1.0
0.8
0.6
0.4
0.2
0.0
Xen29
Xen29 + Lst
Sterile + Lst
Sterile
C
Xen29
Xen29 + Lst
Sterile + Lst
Sterile
500 µm
D
Week 4
Bone Volume [mm3]
****
****
*
*
1.0
0.8
0.6
0.4
0.2
0.0
Xen29
Xen29 + Lst
Sterile + Lst
Sterile
E
Xen29
Xen29 + Lst
Sterile + Lst
Sterile
500 µm
F
Week 8
Bone Volume [mm3]
*
***
P<0.31
1.0
0.8
0.6
0.4
0.2
0.0
Xen29
Xen29 + Lst
Sterile + Lst
Sterile

Figure 20: BMP-2 loaded lysostaphin-delivering hydrogels improve bone repair. Representative μCT reconstructions (A) and bone volume quantification (B) at the time of surgery. Ordinary one-way ANOVA with Tukey's post-hoc test. Representative μCT reconstructions (C) and bone volume quantification (D) 4 weeks post-operatively. Ordinary one-way ANOVA with Tukey's post-hoc test. Representative μCT reconstructions (E) and bone volume quantification (F) 8 weeks after implantation. Kruskal-Wallis with Dunn's multiple comparisons test. Means ± SD. N=7 per group. *P < 0.05, ***P < 0.001, ****P < 0.0001.

To confirm that lysostaphin-delivering hydrogel therapy eliminated the bacterial infections, the implants and surrounding tissue were processed and assayed for viable bacteria. The microbiologic analysis showed a significant reduction of viable bacteria for the lysostaphin-delivering hydrogel treatment group compared to the infection-only control (Figure 21A) demonstrating lysostaphin-delivering hydrogels eliminated the infection. Notably, high variability exists in the infection-only group, with some samples showing infection and others not. We tested for the presence of bacteria by culturing the remaining tissue sample in liquid culture media containing kanamycin, to selectively grow Xen29, overnight. All samples in the infection group were positive for Xen29, even though colonies were not detected using the quantitative assay. Importantly, the infections are localized to the radius, as no viable bacteria were recovered from the liver in any of the samples tested (Figure 21B). We also assessed if bone volume was correlated with the number of recovered CFU's in the infection only control (Figure 22). No linear correlation (R^2 = 0.073) was observed as determined by regression analysis. Pearson's correlation test also indicated no significant correlation between values (P = 0.60).

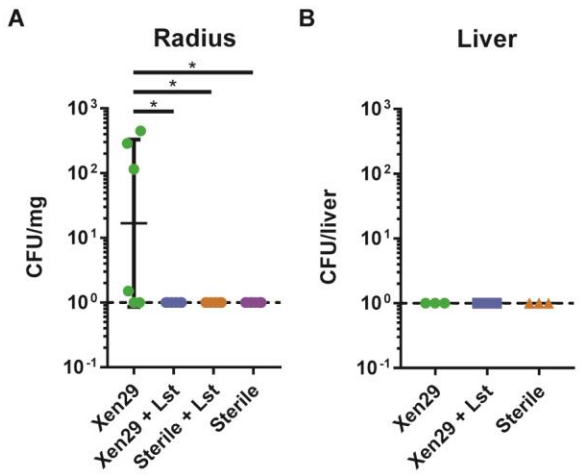

Figure 21: Lysostaphin-delivering hydrogels eliminate bacteria at 8 weeks. (A) Viable bacteria recovered from the defect and surrounding tissue after 8 weeks *in vivo*. (B) Viable bacteria recovered from the liver 8 weeks after implantation. Kruskal-Wallis with Dunn's multiple comparisons test. Means ± SD. *N*=3-6 per group. **P* < 0.05.

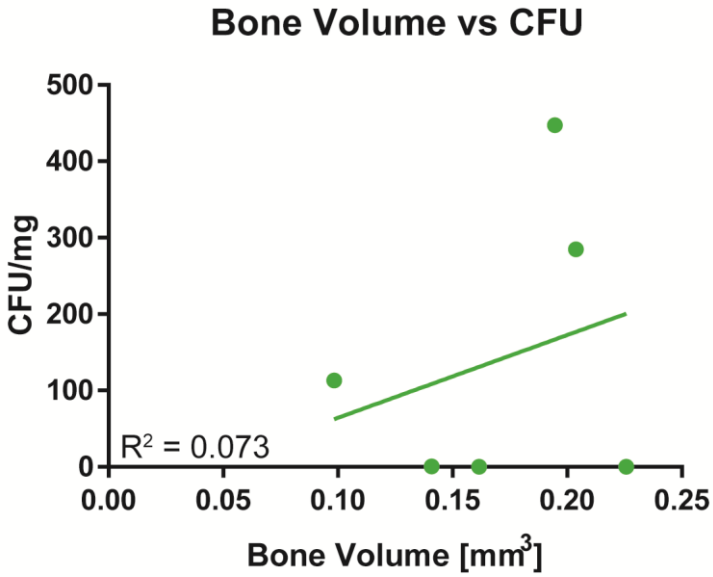

Figure 22: Bone volume and colony forming unit correlation at 8 weeks. Bone volume vs. CFU/mg was plotted for each sample from the Xen29 group. Linear regression analysis and Pearson's Correlation analysis was performed.

Finally, one sample per experimental group underwent histologic analysis (Figure 23). We sectioned and stained the radius with H&E to observe general tissue morphology, Saf-O/FG for collagen deposition, and Grams stain for the presence of bacteria. H&E staining reveals significant leukocytic infiltrate for the untreated Xen29 sample with no bone formation and the presence of Gram positive bacteria in the Gram stain. New bone is located within the defect for the Xen29 sample treated with the lysostaphin-containing hydrogel on H&E and Saf-O/FG staining. No bacteria are present on the gram stain, confirming the infection was eliminated. Both sterile groups show bone formation within the implant and a well-defined bone marrow cavity.

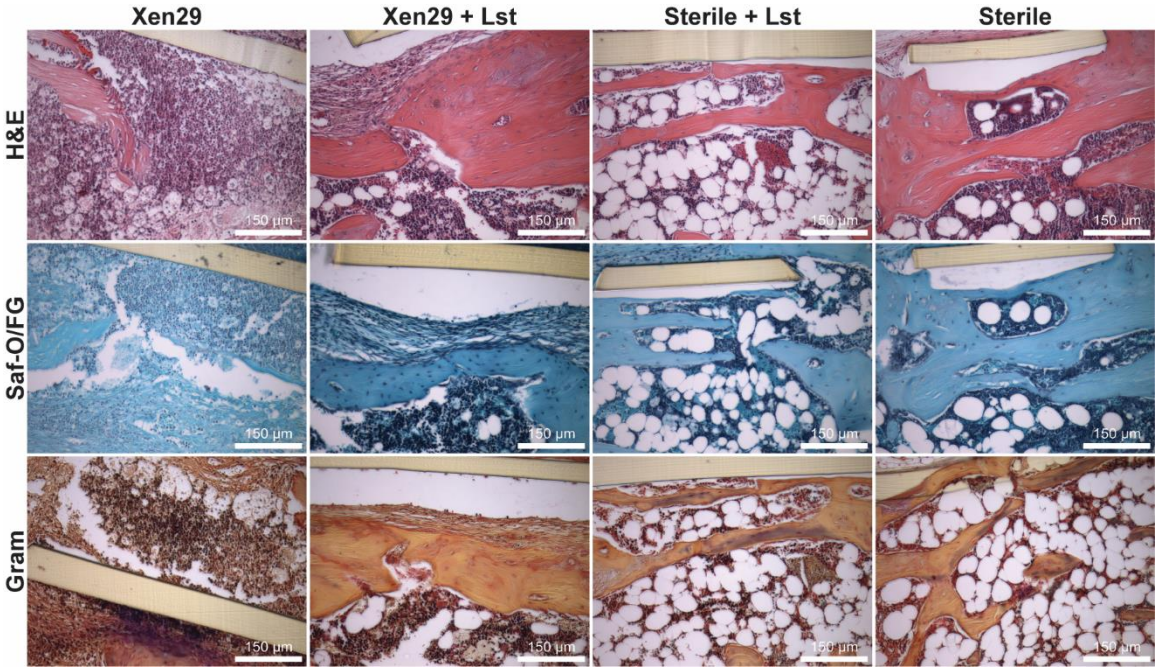

Figure 23: Histologic sections of tissue samples 8 weeks post-implantation. Mouse radii were sectioned and stained with H&E, Saf-O/FG, and Gram stain. One sample was randomly selected and prepared per experimental group. Representative images are displayed.

4.3.3 Lysostaphin-delivering hydrogels regenerate bone in a radial defect infected with a clinical isolate of S. aureus

The development of a bacterial biofilm can significantly complicate the treatment of segmental bone defects, resulting in multiple surgeries. The first to eliminate the infection, and then subsequent surgeries for repairing the bone defect. To test that the BMP-2 loaded lysostaphin-delivering hydrogels can prevent biofilm infection and regenerate bone, we utilized the *S. aureus* strain UAMS-1. UAMS-1 is a clinical isolate from a pediatric case of osteomyelitis and a prolific biofilm-former (*172*). We performed a bacterial inoculum dosing study to identify the minimum dose of UAMS-1 required to initiate a persistent infection. Hydrogels infected with UAMS-1 at varying concentrations spanning three orders of magnitude were synthesized and implanted in mouse radial segmental defects. The bacterial inoculum was confirmed by assaying the implants for viable UAMS-1 after surgery and plotting these values against the number of bacteria we expected to recover (Figure 24A). The results showed that the bacterial dose implanted was highly correlated (R^2=0.97) with the expected dose. One week later, mice were euthanized and bacteria were recovered from the defects and surrounding tissue (Figure 24B). All doses except for the lowest dose tested were above the detection limit of the assay. Therefore we selected the bacterial dose of roughly 1,000 CFU/implant UAMS-1 for all the subsequent studies.

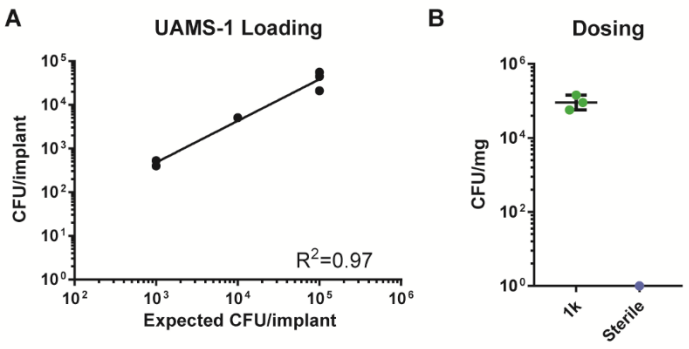

Figure 24: Identification of the minimum dose to initiate UAMS-1 infections in a radial segmental defect. (A) Three doses of UAMS-1 spanning three orders of magnitude were implanted into mouse radial segmental defects. (B) Bacterial counts at one week post implantation for the 1,000 CFU/implant group. Linear regression analysis with Goodness of Fit test. Means ± SD. *N*=7 per group.

Following the identification of an appropriate UAMS-1 dose, we tested the efficacy of BMP-2 loaded lysostaphin-delivering hydrogels to prevent infection and regenerate bone. We hypothesized that increasing the BMP-2 dose from 50 ng, used in the Xen29 study, to 100 ng would improve bone regeneration in the infected implants treated with lysostaphin. Segmental defects were created and hydrogel scaffolds were deployed (Figure 25). Longitudinal bone formation was monitored using μCT imaging at 4 and 8 weeks. At the end of the 8 week study, mechanical testing and histologic analysis was performed on the mouse forelimbs. The experimental groups included UAMS-1 infected hydrogels with and without lysostaphin, and sterile hydrogels without lysostaphin. We also included a group of UAMS-1 infected hydrogels that were dipped in gentamicin (10 mg/mL (*206, 207*)) to simulate the current therapeutic standard of antibiotic doped implants. Representative μCT reconstructions 4 weeks following implantation showed no new bone formation in the untreated, infected control group (Figure 26A). Both the lysostaphin-delivering and sterile hydrogel groups exhibited new bone formation inside the defect.

Hydrogels that were treated with gentamicin also had bone formation. However, some samples were completely devoid of new bone, suggesting not all of the infections were cleared. At 8 weeks, representative μCT images showed similar trends to the 4 week time point, but with improved bone formation in the sterile and lysostaphin-delivering hydrogel treated groups (Figure 26C). Quantification of the bone volume within the defect site at 4 weeks shows that there was significantly more bone in the sterile and lysostaphin-delivering hydrogel treated groups compared to the untreated infected control (Figure 26B). The gentamicin-treated hydrogel group was no different than the untreated infected control. Similarly, at 8 weeks, the lysostaphin-delivering hydrogel group and the sterile control had significantly more bone within the defect site than the untreated control (Figure 26D). Again, the gentamicin-treated hydrogel group was no different than the untreated control. We also quantified the extent of bridging by scoring the 8 week μCT reconstructions: 0 = no bone formation, 1 = less than half of the defect, 2 = greater than half of the defect, 3 = defect bridged. The results indicated that the sterile and lysostaphin-delivering hydrogels had higher defect bridging scores compared to the untreated control (Figure 27A). Implants dipped in gentamicin were no different than the sterile implants. Taken together, these results show that BMP-2 loaded lysostaphin-delivering hydrogels significantly improve bone regeneration compared to untreated infections and regenerate an equal amount of bone as sterile implants. Torsion to failure testing was used to determine if the regenerated bone provided functional improvements. The bregenerated bone in the lysostaphin-delivering hydrogel group, the sterile control group, and the gentamicin-treated group had significantly improved mechanical properties compared to that of the untreated infection control (Figure 27B). No differences were observed between the

samples tested in the lysostaphin-delivering hydrogel group and the antibiotic prophylaxis group. Notably, the bone regenerated in the sterile control group was of superior quality as assessed through torsion to failure testing to that of the lysostaphin-delivering hydrogel group, even though no differences were observed in the bridging score. Additionally, the sterile control groups average torsion to failure value was higher than that of normal intact bone (3.2 ± 0.3 mN·m, as reported in Shekaran *et al.*). The average torsion values measured for infections treated with lysostaphin-delivering hydrogels were slightly lower than naïve bone. Taken together, this suggests that the lysis of bacteria may have an effect on the quality of the regenerated bone, but not the total amount of bone formed. Histologic analysis revealed the presence of inflammatory cell infiltrate, no new bone formation, and the Gram positive bacteria within the defect for the untreated and gentamicin-treated infected samples, indicating a persistent infection (Figure 28). The infection treated with a lysostaphin-delivering hydrogel has similar findings to that of the sterile control. Bone was present within the defect site and a marrow cavity was formed. No bacteria are detected with Gram staining, suggesting the infection has been clearedThese data indicate that BMP-2 loaded lysostaphin-delivering hydrogels eliminate infection and drive defect repair, leading to functional bone regeneration.

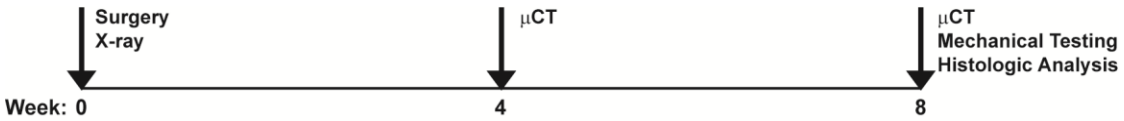

Figure 25: Experimental outline of the UAMS-1 bone repair study. Bone formation was assessed longitudinally with a combination of *in vivo* X-ray and μCT imaging at 0, 4, and 8 weeks after defect creation and implant placement. At 8 weeks, end point histologic and microbiologic analysis was performed

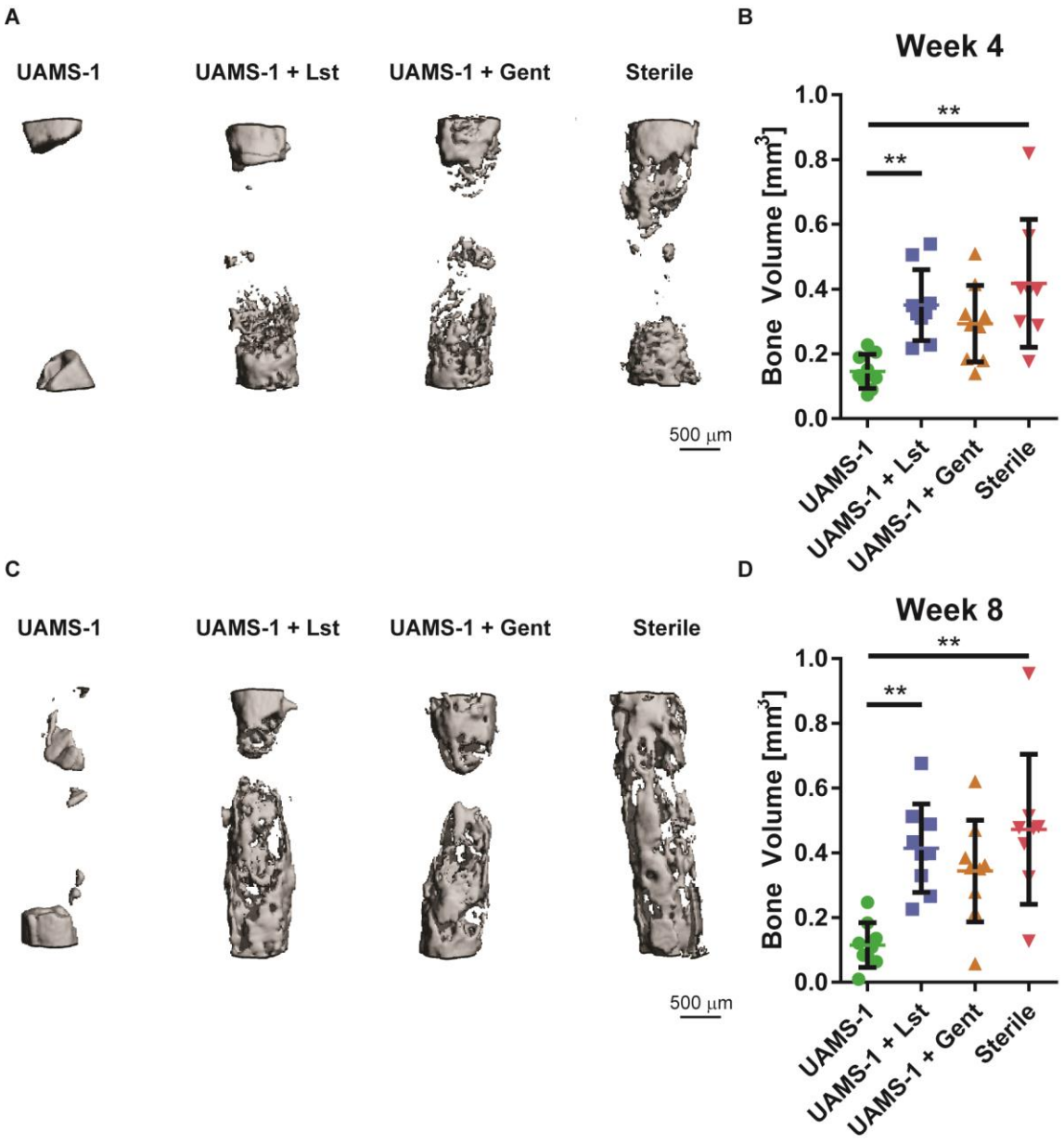

Figure 26: UAMS-1 infect defects treated with BMP-2 loaded lysostaphin-delivering hydrogels significantly improve bone repair. Representative μCT reconstructions (A) and bone volume quantification (B) 4 weeks post operatively. Representative μCT reconstructions (C) and bone volume quantification (D) 8 weeks after implantation. Kruskal-Wallis with Dunn's multiple comparisons test. Means ± SD. *N*=8-9 per group. $^{**}P < 0.01$.

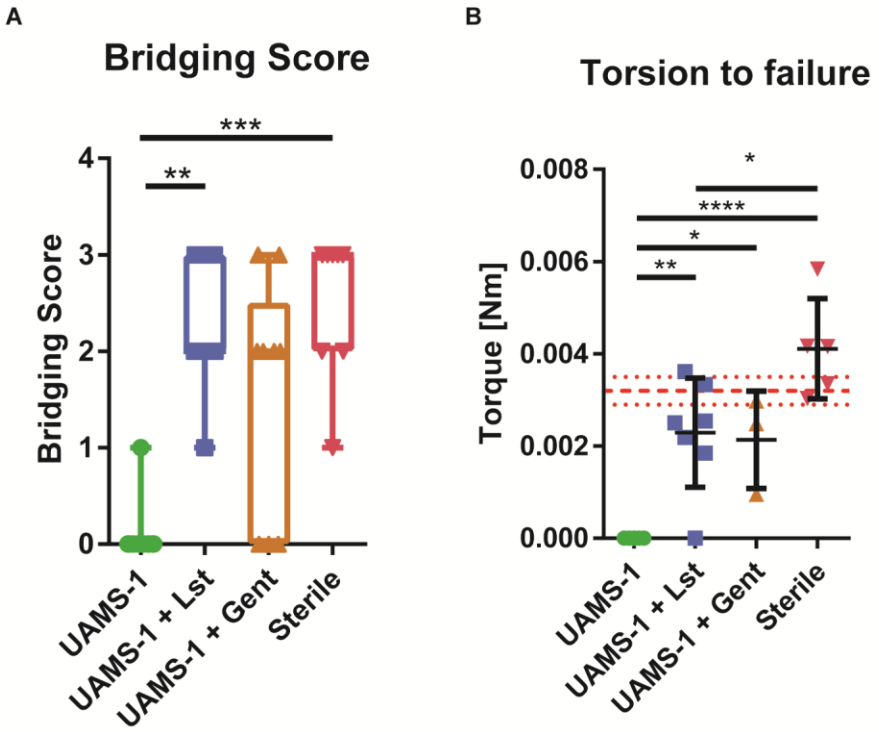

Figure 27: BMP-2 loaded lysostaphin-delivering hydrogels functionally heal defects. (A) Defect bridging was assessed semi-quantitatively using the following scale: 0 = no bone formation, 1 = less than half of the defect, 2 = greater than half of the defect, 3 = defect bridged. Kruskal-Wallis with Dunn's multiple comparisons test. *N*=3-6 per group. Whiskers represent minimum and maximum, box extends from 25th to 75th percentiles, line represents median. ***P* < 0.01. (B) Functional healing was assessed using torsion to failure testing. The average torsion to failure values for healthy mouse radii are plotted as horizontal red lines (0.0032 ± 0.0003 Nm) as reported in Shekaran *et al*. Means ± SD. *N*=3-7 per group. One-way ANOVA with Tukey's post-hoc test.

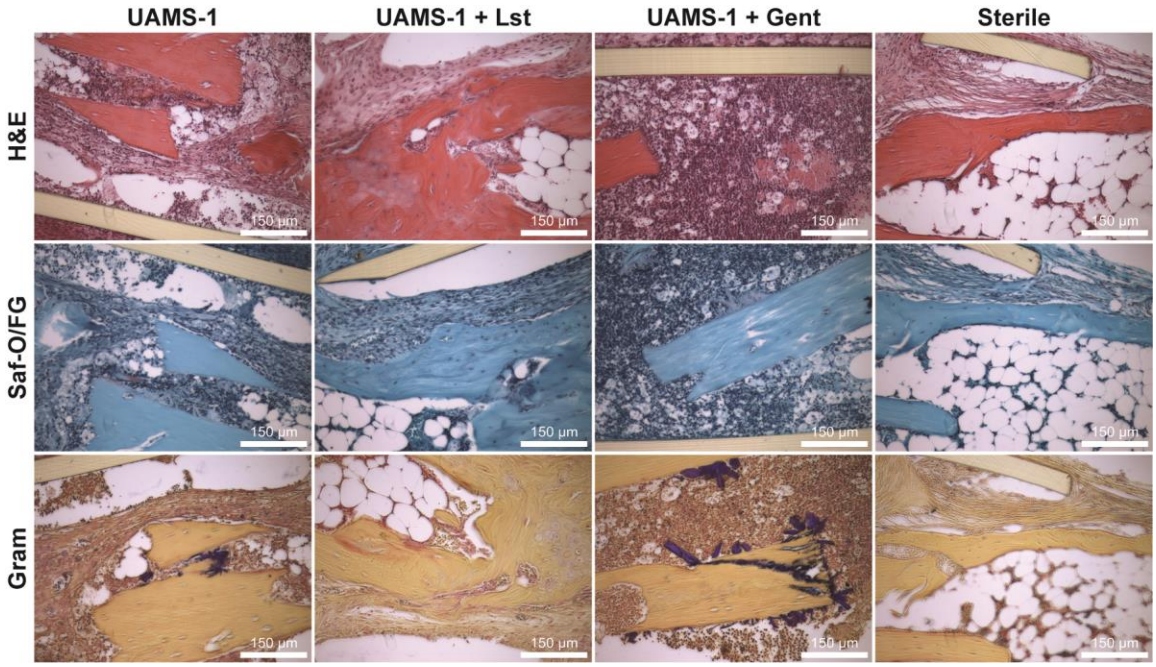

Figure 28: Histologic sections of tissue samples 8 weeks post-implantation. Mouse radii were sectioned and stained with H&E, Saf-O/FG, and Gram stain. One sample was randomly selected and prepared per experimental group. Representative images are displayed.

4.3.4 Lysostaphin-delivering hydrogels exhibit no hepatotoxicity and restore the native inflammatory environment

Lysostaphin is a protein that does not occur naturally in the human body, and could trigger an inflammatory reaction in response to administration, which could negatively impact bone formation. Furthermore, lysostaphin functions by directly lysing bacteria, which in itself could cause a significant inflammatory response. Therefore, we assessed the safety profile of lysostaphin-delivering hydrogel therapy with liver function tests, and antibody generation assays, cytokine array profiling, and cell recruitment analysis.

...1 Lysostaphin-delivering hydrogels result in minimal systemic toxicity

We performed liver function testing at 1 week post-operation to test if BMP-2 loaded lysostaphin-delivering hydrogel therapy resulted in liver toxicity. The experimental groups included lysostaphin-delivering hydrogels with and without UAMS-1 infection. Liver function was assessed by measuring total protein, albumin, aspartate aminotransferase (AST), alanine aminotransferase (ALT), and alkaline phosphatase. Normal values obtained from the literature are plotted on the graphs for male C57B/6J mice 90-135 days old with the black hashed line indicating the median values and the red lines indicated the 2.5 and 97.5 percentiles for healthy mice (*208*). Overall, no differences in total protein levels and the albumin fraction were seen between groups (Figure 29A). The albumin levels were on average higher than the reference values (Figure 29B). However, elevated albumin levels are not typically associated with liver toxicity (*209*). Acute liver toxicity is primarily identified by elevated serum AST and ALT. Upon liver injury, cells release AST and ALT into the blood stream. Our results showed that 1/5 and 2/6 animals in the infection and sterile groups had elevated AST levels (Figure 29C). ALT, a more specific indicator of acute liver toxicity, results were within normal limits (Figure 29D). Taken together, these data suggest that no acute liver injury is associated with lysostaphin-delivering hydrogel therapy. The final blood chemistry test examined was alkaline phosphatase. Elevated levels can point to liver or bone disease, which were not observed, further supporting that our therapy is not systemically toxic (Figure 29E). Finally, we screened for anti-lysostaphin antibody generation using a dot blot assay. Anti-lysostaphin antibodies were present in 1/20 animals before surgery. Four weeks following implantation, 3/7 lysostaphin-delivering hydrogel treated animals converted to being

positive for anti-lysostaphin antibodies. 1/6 animals in the infection-only control group (no lysostaphin) also converted. These data indicate that lysostaphin-delivering hydrogels do not result in liver toxicity, but can elicit an antibody response.

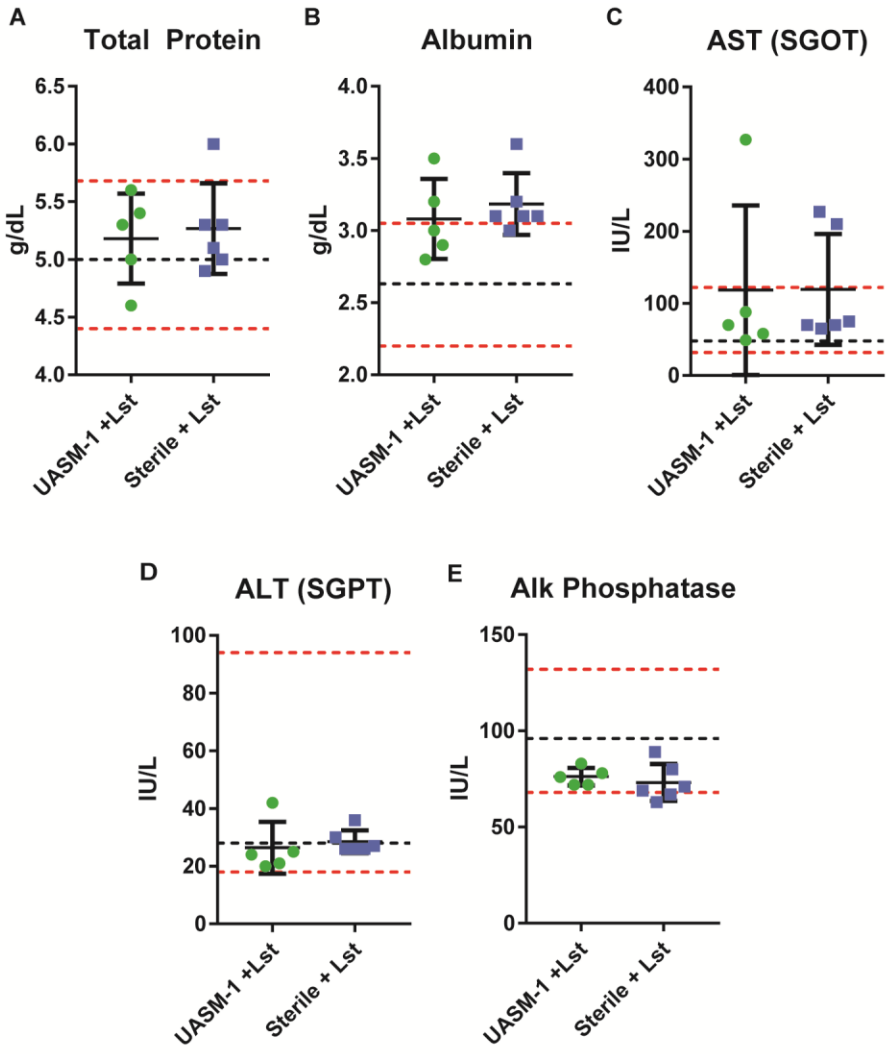

Figure 29: BMP-2 loaded lysostaphin-delivering hydrogels do not show signs of systemic toxicity. Segmental defects were created and lysostaphin-delivering hydrogels loaded were BMP-2 with and without infection were implanted. Systemic toxicity was assessed at 1 week with liver function testing. Serum samples were tested for total protein (A), albumin (B), aspartate aminotransferase (AST) (C), alanine aminotransferase (ALT) (D), and alkaline phosphatase (Alk phosphatase) (E) levels. Means ± SD. *N*=5-6 per group. One-way ANOVA with Tukey's post-hoc test. No differences were detected between groups.

...2 Lysostaphin-delivering hydrogels restore the cytokine milieu to a pro-regenerative state

We characterized the local cytokine milieu generated in response to BMP-2 loaded lysostaphin-delivering hydrogel therapy. Hydrogels were placed, and 1 and 4 weeks post implantation, the implant tube and surrounding tissue was isolated and analyzed using a multiplexed cytokine array assay. The experimental groups included UAMS-1 containing hydrogels with and without lysostaphin and lysostaphin-free sterile controls. All implants contained 100 ng of BMP-2. At the one week time point, hierarchical cluster analysis reveals clear segregation of the untreated infection group from the sterile control and lysostaphin-delivering hydrogel group (Figure 30A). Notably, no obvious clustering of the sterile and lysostaphin hydrogel-treated group is apparent, suggesting the infection has been cleared and the local inflammatory environment has been restored to that of a sterile wound environment. Several individual cytokines were significantly elevated in the infection only control group, including G-CSF, IL-1β, KC, IL-6, MIP-1α, MIP-1β, MIP-2, and IP-10 (Figure 30B-I). These cytokines are primarily associated with the acute inflammatory response and are responsible for inflammatory cell recruitment. No significant differences were detected between infections treated with lysostaphin-delivering hydrogels and the sterile controls. Principal component analysis was performed, which confirmed that the infection only group had a significantly cytokine milieu than the sterile and lysostaphin-delivering hydrogel treated mice (Figure 31). These same trends continued at the four week time point. Hierarchical cluster analysis delineates the infection group from both the sterile and lysostaphin-delivering hydrogel treated groups, which are indistinguishable from each other (Figure 32A). This is further illustrated through

individual cytokine analysis. Significantly elevated levels of G-CSF, KC, MIP-2, MIP-1 α, and MIP-1β in the UAMS-1 infection mice were detected (Figure 32B-F). Principal component analysis revealed similar global cytokine levels for the sterile and lysostaphin-delivering hydrogel treated mice, which were significantly different that the infection only controls as captured by component 1 (Figure 33). Again, these cytokines are primarily associated with inflammatory cell recruitment, showing a continued immune response to the infection. Fewer differences in individual cytokine expression levels were detected at the 4 week time point, which may be attributed to the local inflammatory profile changing from an acute to a chronic state (*210*). Again, no differences were detected between the sterile and lysostaphin-delivering hydrogel treated mice.

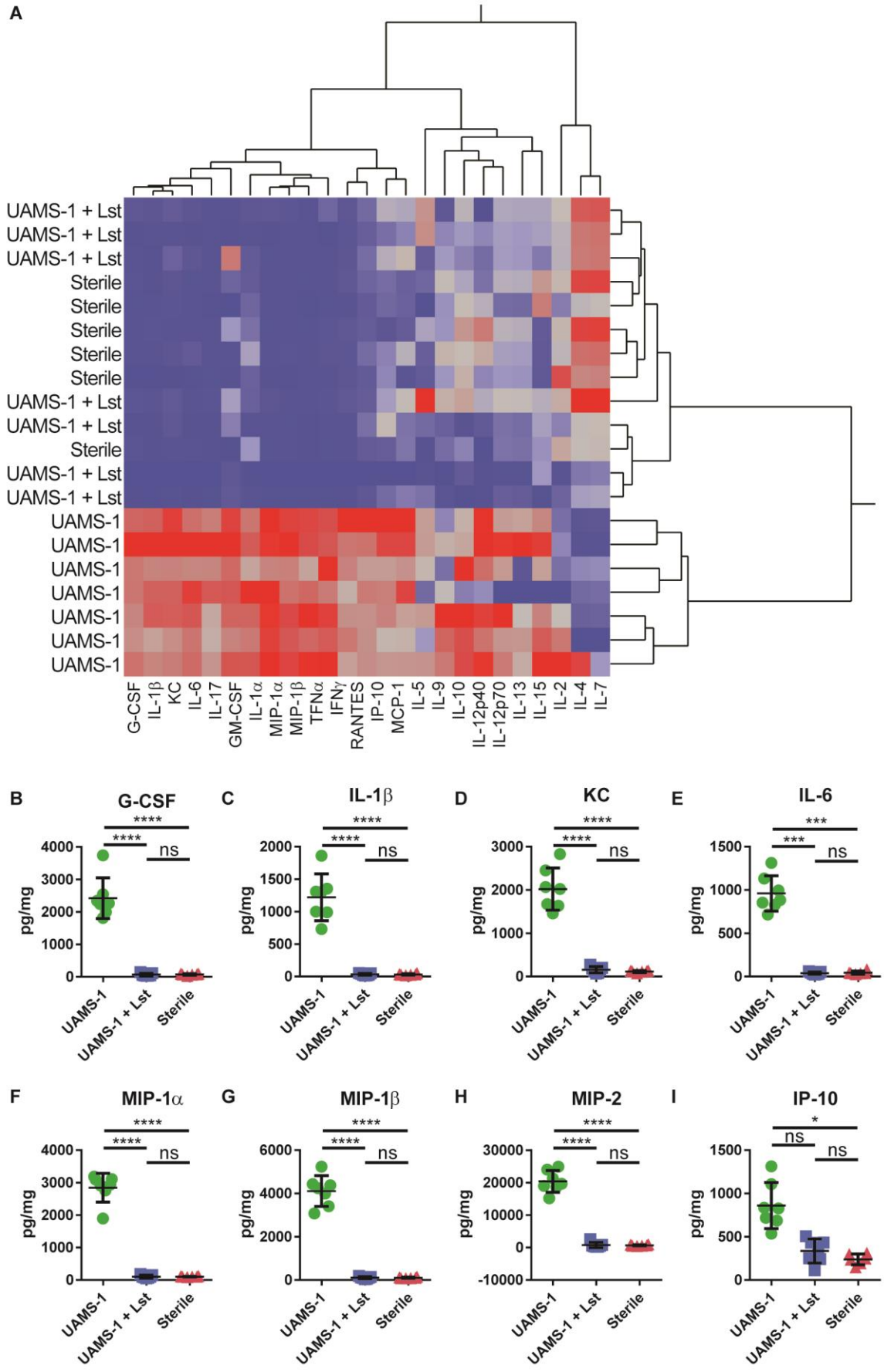
A
UAMS-1 + Lst
UAMS-1 + Lst
UAMS-1 + Lst
Sterile
Sterile
Sterile
Sterile
Sterile
UAMS-1 + Lst
UAMS-1 + Lst
Sterile
UAMS-1 + Lst
UAMS-1 + Lst
UAMS-1
UAMS-1
UAMS-1
UAMS-1
UAMS-1
UAMS-1
UAMS-1
G-CSF
IL-1β
KC
IL-6
IL-17
GM-CSF
IL-1α
MIP-1α
MIP-1β
TFNα
IFNγ
RANTES
IP-10
MCP-1
IL-5
IL-9
IL-10
IL-12p40
IL-12p70
IL-13
IL-15
IL-2
IL-4
IL-7
B
G-CSF
C
IL-1β
D
KC
E
IL-6
F
MIP-1α
G
MIP-1β
H
MIP-2
I
IP-10
pg/mg
****
ns
***
*
UAMS-1
UAMS-1 + Lst
Sterile

Figure 30: BMP-2 loaded lysostaphin-delivering hydrogels restore the local inflammatory environment to a regenerative state one week after implantation. Segmental defects were created and hydrogel scaffolds infected with UAMS-1 with or without lysostaphin as well as sterile gels were implanted and the inflammatory response was assessed using a multiplexed cytokine array assay 1 week later. (A) Hierarchical cluster analysis of cytokine profiles using the Ward Method. (B-I) Cytokines with statistically different tissue levels as determined using two-way ANOVA with a Bonferonni Correction for multiple comparisons. Means ± SD. *N*=6-7 per group. **P* < 0.05, ****P* < 0.001, *****P* < 0.0001, ns is not significant.

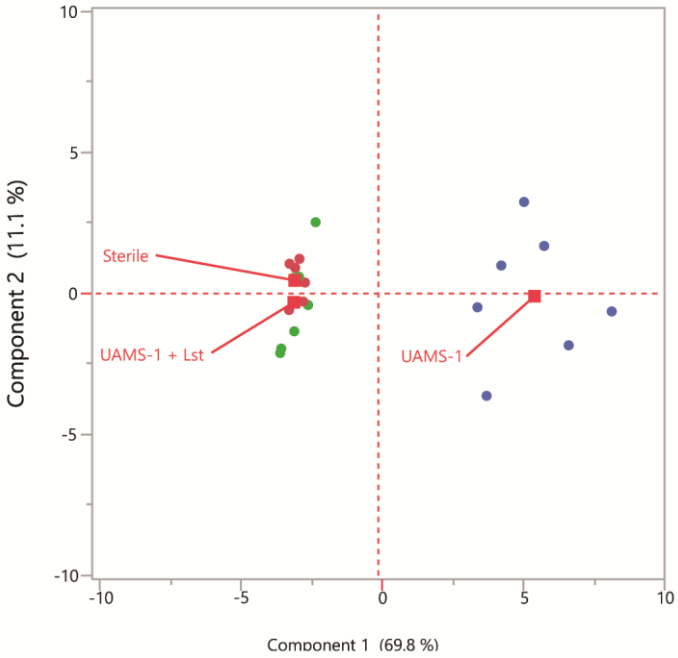

Figure 31: Principal component analysis of the local cytokine levels one week post-implantation.

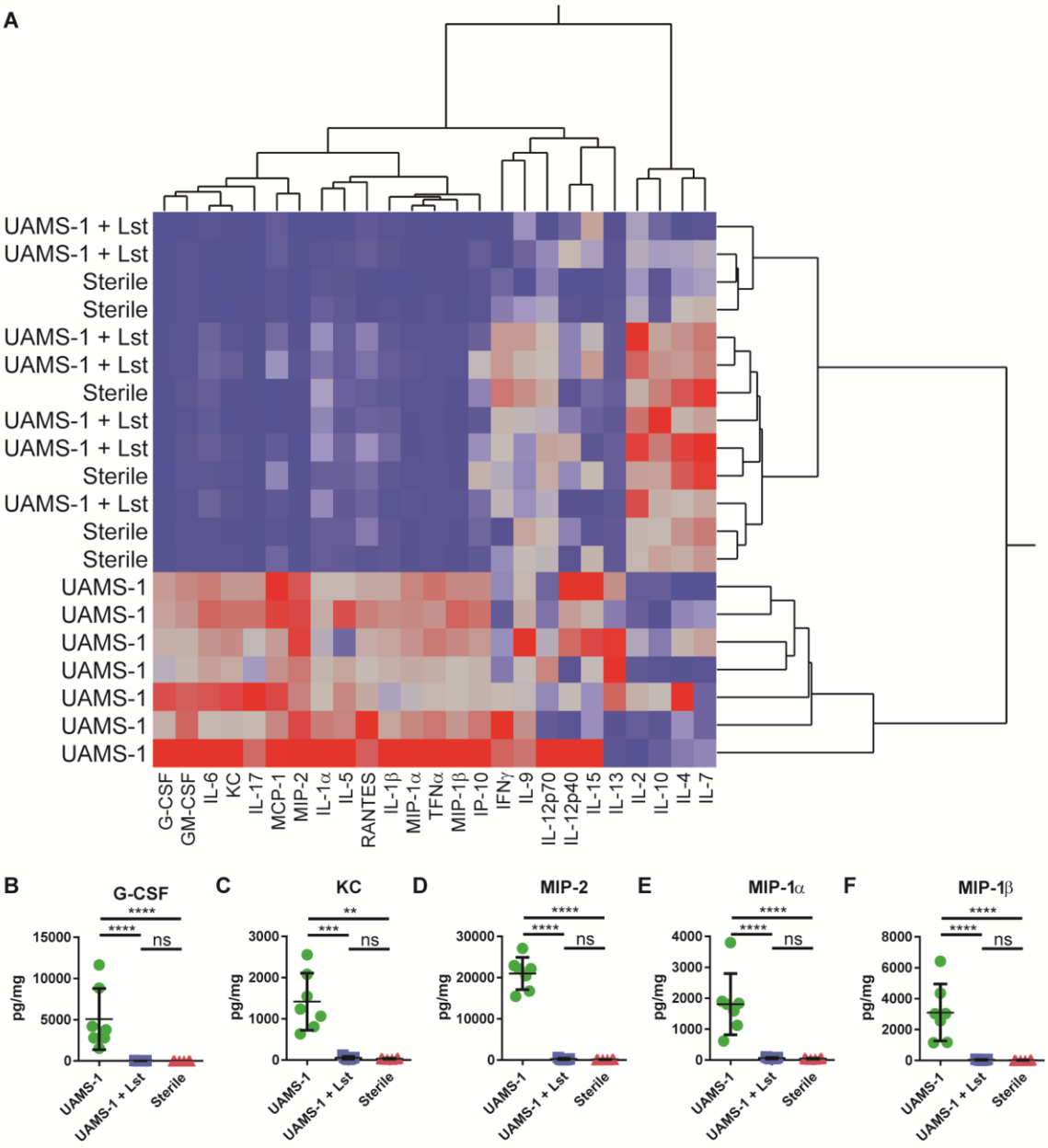

Figure 32: Cytokine profile of BMP-2 loaded lysostaphin-delivering hydrogels 4 weeks post-operatively. Segmental defects were created and hydrogel scaffolds infected with UAMS-1 with or without lysostaphin as well as sterile gels were implanted and the inflammatory response was assessed using a multiplexed cytokine array assay 4 week later. (A) Hierarchical cluster analysis of cytokine profiles using the Ward Method. (B-F) Cytokines with statistically different tissue levels as determined using two-way ANOVA with a Bonferonni Correction for multiple comparisons. Means ± SD. *N*=6-7 per group. **P* < 0.05, ****P* < 0.001, *****P* < 0.0001, ns is not significant.

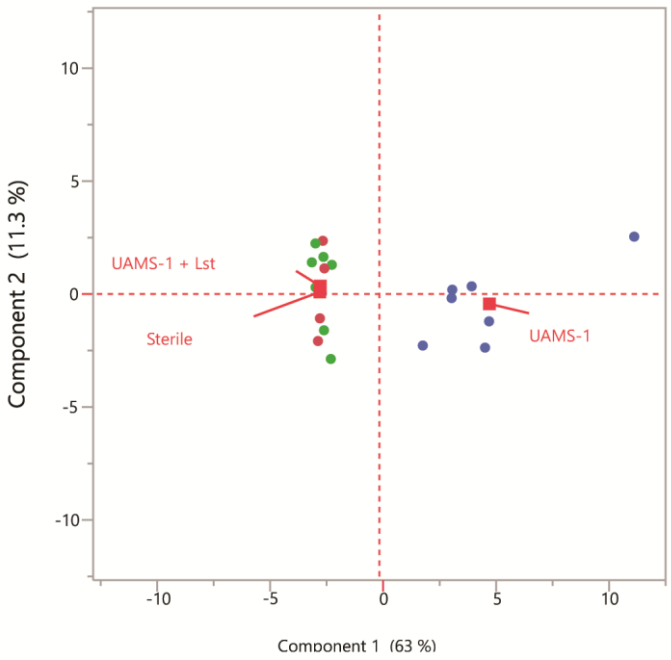

Figure 33: Principal component analysis of the local cytokine levels four weeks post-implantation.

...3 Lysostaphin-delivering hydrogel therapy does not alter the native inflammatory cell profile

To further characterize the host response to BMP-2-loaded lysostaphin-delivering hydrogel therapy to treat *S. aureus* infection, we profiled the inflammatory cell makeup at the defect site via flow cytometry one week after surgery. Segmental defects were made and lysostaphin-delivering hydrogels loaded with 100 ng of BMP-2 were implanted. The experimental groups included hydrogels with and without lysostaphin that were implanted with and without UAMS-1. One week following implantation, mice were euthanized, tissue was isolated, and single cell suspensions were stained for inflammatory cell markers. The gating strategy used to identify the individual cells types is outlined in Figure 34. All analysis was performed on live cells. T cells were identified as being low side scatter CD3

positive events and where then separated into CD4 positive helper T cells and CD8 positive cytotoxic T cell subsets (*211*). Low side scatter CD19 positive events made up the B cell population (*212, 213*). Myeloid cells were identified as being CD11b positive and were sorted using F4/80 staining to separate macrophages (F4/80 positive) from monocytes and neutrophils (F4/80 negative). Macrophages were split into the classically activated CD86 positive M1 macrophage and alternatively activated CD206 positive M2 macrophage subsets (*214*). Similarly, monocytes were split into inflammatory $Ly6C^{Hi}$ monocyte (IM) and anti-inflammatory $Ly6C^{Lo}$ monocyte (AM) subsets (*215, 216*). Neutrophils were classified as the Ly6G positive myeloid cells (*217*). Sorted cells were then analyzed as both the total number of cells per tissue weight and the percent of the parent cell population.

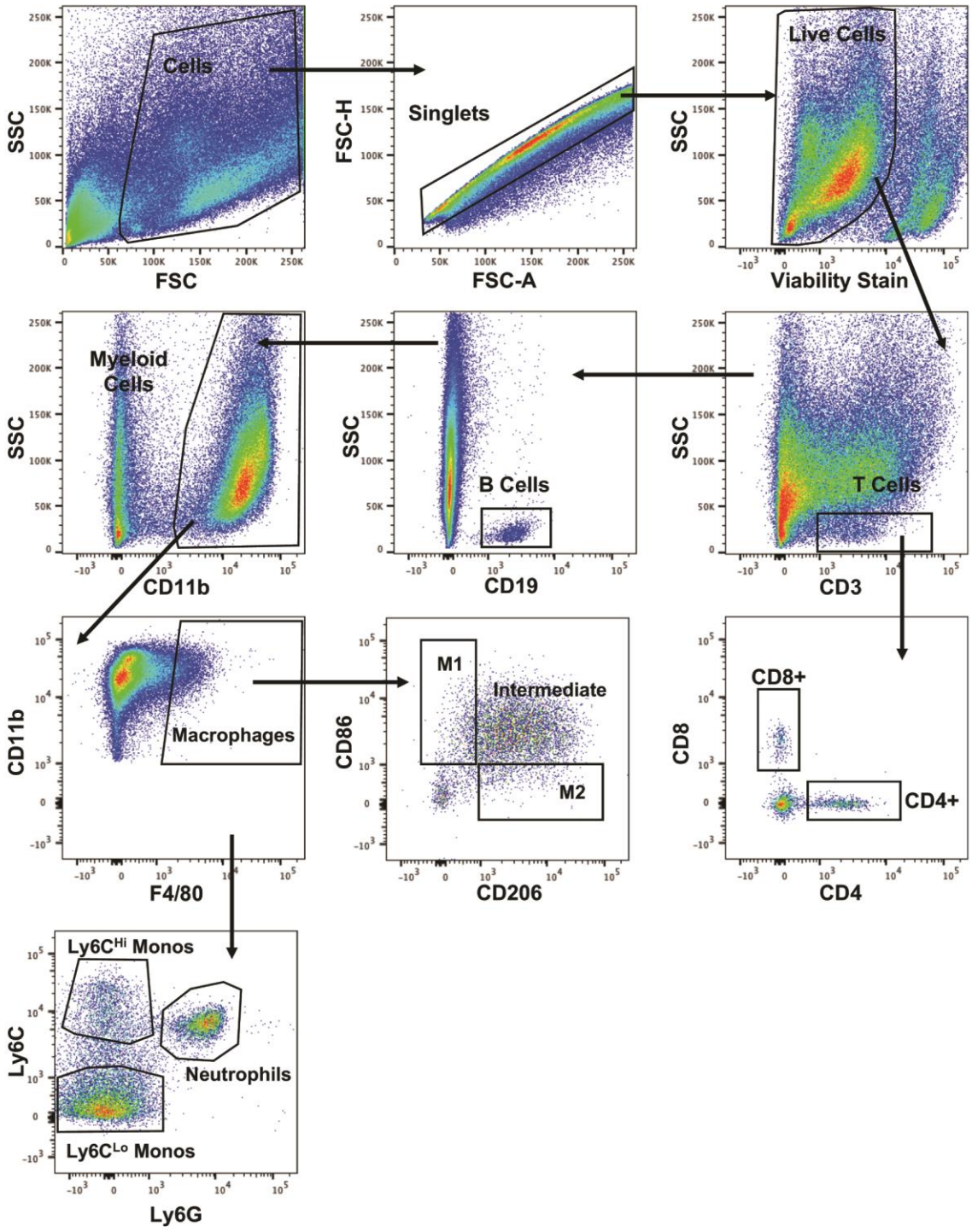

Figure 34: Gating strategy for inflammatory cell profiling analysis. Single cell suspension of tissue samples were created and stained for subsequent flow cytometry analysis. Single cells were identified and live cells were selected. T cells were identified by selecting as low side scatter CD3 positive events and then sorted into CD8 positive cytotoxic T cells and CD4 positive helper T cells. B cells were low side scatter CD19

positive events. Myeloid cells were identified as being CD11b positive. Macrophages were identified as CD11b and F4/80 positive events then split into CD86 positive M1 and CD206 positive M2 subsets. Neutrophils are identified as Ly6G positive myeloid cells. Monocytes are classified as Ly6G negative myeloid cells and split into $Ly6C^{Hi}$ IM monocytes and $Ly6C^{Lo}$ AM monocytes.

Analysis of the total number of cells at the defect site revealed a significantly higher number of total cells (Figure 35A), T cells (Figure 35B), helper T cells (Figure 35C), cytotoxic T cells (Figure 35D), myeloid cells (Figure 35I), neutrophils (Figure 35J), and IM monocytes (Figure 35L) for the infection-only group compared to the lysostaphin-delivering hydrogel-treated infections and both sterile control groups. Significantly higher levels of AM monocytes were observed in the lysostaphin-delivering hydrogel-treated infections and the sterile lysostaphin hydrogel group compared to the infection-only control (Figure 35K). Overall, the higher numbers of inflammatory cells observed in the infection control group is not surprising as all animals analyzed had visible tissue abscesses present at necropsy. This is also the most likely explanation for the significantly elevated levels of myeloid cells, but more specifically neutrophils in the group, as abscesses are primarily composed of neutrophilic infiltrate. Remarkably, for all cell types identified, no differences were observed between the lysostaphin-delivering hydrogel-treated infections and both sterile control groups (Figure 35A-L), showing that lysostaphin-delivering hydrogels do not alter the inflammatory cell populations at the defect site both with and without infection. No differences in the number of B cells (Figure 35E), total macrophages (Figure 35F), M1 macrophages (Figure 35G), or M2 macrophages (Figure 35H) among any of the groups were detected, even though the total number of cells present was elevated in the infection-only groups. For this reason, we posit that these cell populations are tissue resident cells. It may also be that the elevated levels of monocytes observed in the infection-

only group have been recruited at higher number due to the infection, but have not yet become fully differentiated macrophages. In an attempt to remove the confounder of increased total cells being present in the infection control group, we also analyzed the data as percent of parent cell. The infection-only group had significantly higher proportions of helper T cells (Figure 36A) and neutrophils (Figure 36F) and a significantly lower proportion of macrophages (Figure 36C), IM monocytes (Figure 36G) and AM monocytes (Figure 36H) compared to all other experimental groups. No differences were observed between the lysostaphin-delivering hydrogel groups with and without infection or the empty sterile group, providing more evidence that lysostaphin-delivering hydrogel therapy does not affect the inflammatory cell profile compared to empty uninfected controls. The percent of cytotoxic T cells (Figure 36B) and M1 (Figure 36D) and M2 (Figure 36E) macrophages were equivalent among all groups. Taken together, these data indicate that infections treated with BMP-2 loaded lysostaphin-delivering hydrogels return the inflammatory cell profile to that of empty BMP-2 hydrogel controls, which subsequently allows for bone regeneration within the defect site.

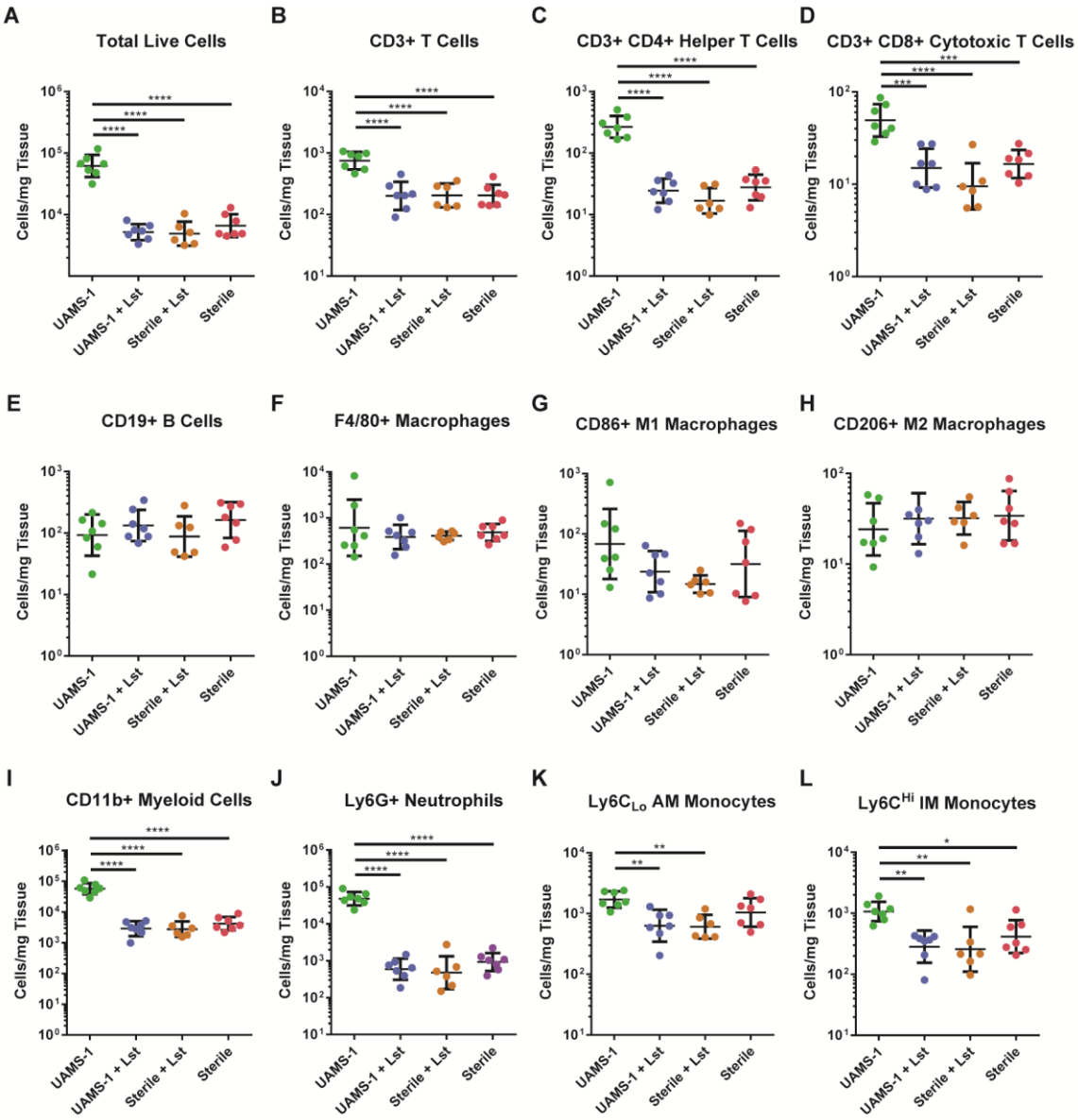

Figure 35: Total number of inflammatory cells 1 week post implantation of BMP-2 loaded lysostaphin-delivering hydrogels. One week following segmental defect creation and implant placement, mice were euthanized and the implant and surrounding tissue were recovered and flow cytometry was performed to enumerate the total number of inflammatory cells present. (A) Total cells, (B) CD3+ T cells, (C) CD3+CD4+ helper T cells, (D) CD3+CD8+ cytotoxic T cells, (E) CD19+ B cells, (F) F4/80+ macrophages, (G) CD86+ M1 macrophages, (H) CD206+ M2 macrophages, (I) CD11b+ myeloid cells, (J) Ly6G+ neutrophils, (K) $Ly6C_{low}$ AM monocytes, and (L) $Ly6C^{high}$ IM monocytes were enumerated. Data were log transformed and ordinary one-way ANOVA with a Tukey post hoc test was used. Means ± SD. N=6-7 per group. *$P < 0.05$, **$P < 0.01$, ***$P < 0.001$, ****$P < 0.0001$.

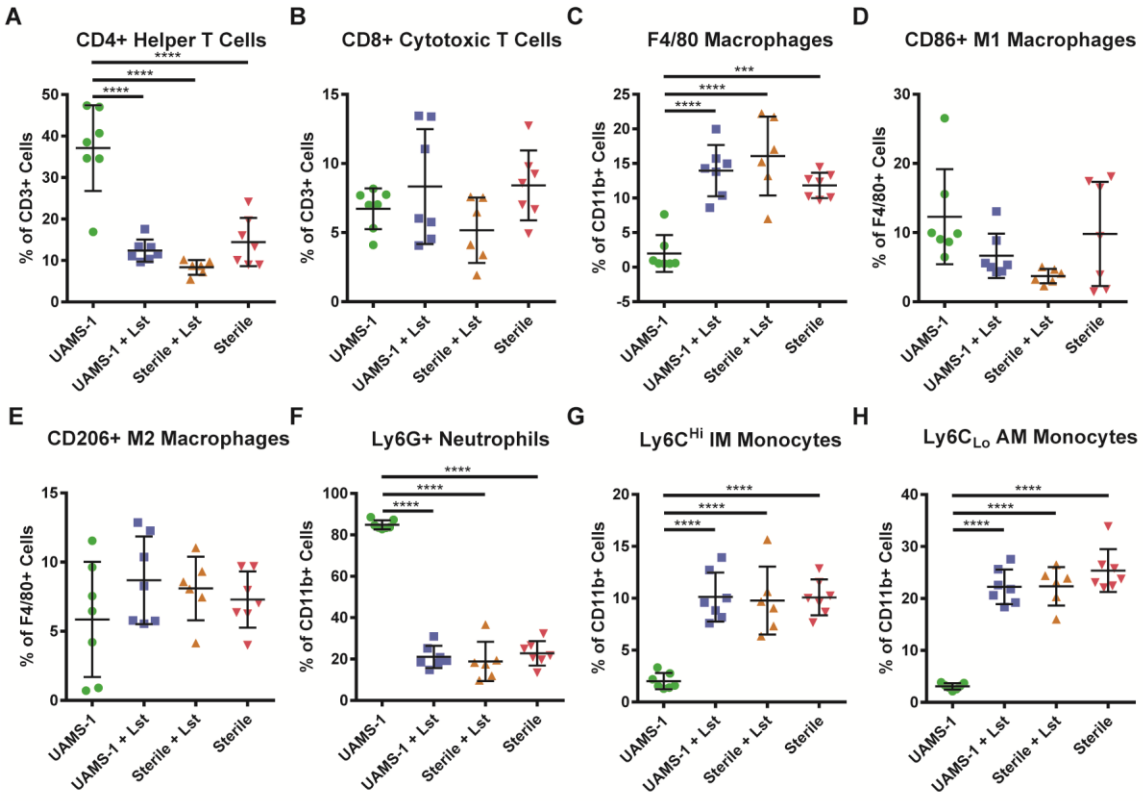

Figure 36: Percent of parent inflammatory cells 1 week post implantation of BMP-2 loaded lysostaphin-delivering hydrogels. One week following segmental defect creation and implant placement, mice were euthanized and the implant and surrounding tissue were recovered and flow cytometry was performed to enumerate the total number of inflammatory cells present. (A) CD4+ helper T cells as a percent of CD3+ cells, (B) CD8+ cytotoxic T cells as a percent of CD3+ cells, (C) F480+ macrophages as a percent of CD11b+ cells, (D) CD86+ M1 macrophages as a percent of F480+ cells, (E) CD206+ M2 macrophages as a percent of F4/80+ cells, (F) Ly6G+ neutrophils as a percent of CD11b+ cells, (G) $Ly6C^{Lo}$ AM monocytes as a percent of CD11b+ cells, and (H) $Ly6C^{Hi}$ IM monocytes as a percent of CD11b+ cells were analyzed. Ordinary one-way ANOVA with a Tukey post hoc test, or Kurskall-Wallis with Dunn's test for non-parametric data was used. Means ± SD. *N*=6-7 per group. ***$P < 0.001$, ****$P < 0.0001$.

4.4 Discussion

Non-healing segmental bone defects often require the placement of a bone auto- or allograft, or the use of BMP-2 to induce osteogensis and cause defect healing. However, these injuries carry rates of infection reported as high as 30%, making it critically important that infection is prevented, in order to facilitate healing (*138, 139*). We engineered an injectable PEG hydrogel that both induces bone regeneration and fights infection through the delivery of BMP-2 and lysostaphin respectively. We showed that BMP-2 loaded lysostaphin-delivering hydrogels eradicate infection and regenerate bone. Liver function testing revealed no signs of toxicity even though anti-lysostaphin antibodies were generated. Locally, lysostaphin-delivering hydrogels returned the inflammatory environment to that of an uninfected defect as measured by both cytokine secretion and immune cell profiling. These results support the development of BMP-2 loaded lysostaphin-delivering hydrogels to prevent *S. aureus* infection and promote segmental bone defect regeneration.

Infection prevention is critical to the success of segmental bone defect repair (*218, 219*). Injuries resulting in segmental bone defects carry a disproportionately high infection rate compared to other orthopaedic injuries, often due to the complexity of the injury, such as exposed bone fragments (*22*). Treatment requires extensive surgical debridement to remove necrotic bone and tissue, followed by the placement of an antibiotic impregnated spacer. A second procedure is performed at a later time, once the infection has cleared, to remove the spacer and place the bone graft (*220*). Even with proper surgical intervention, infection remains one of the primary causes of non-union (*139*). Interventions that fight infection while also being osteoinductive have the potential to significantly reduce the

incidence of non-union, leading to improved patient outcomes. Current strategies have centered on adding broad spectrum antimicrobial therapy to an already osteoinductive scaffold (*221*). Alternatives to broad spectrum antimicrobials, such as silver (*43*) and D-amino acids (*129, 222*), have also been shown to be effective at reducing infection and promoting bone repair.

Antimicrobial prophylaxis is a critical component to treating segmental bone defects (*138, 139*). Lysostaphin provides potent bacteriospecific antimicrobial activity. This targeted approach ensures that only the pathogen of interest is eliminated, but may not be an ideal approach to prevent infection, when the target is often unknown and broad spectrum agents are desirable (*179*). Further, it is possible that prevention of a single pathogen may allow other opportunistic pathogens to colonize the injury site, such as with a less common gram negative pathogen like *Pseudomonas aeruginosa*. In orthopaedics, roughly two thirds of all infections are staphylococcal in nature (*2*), providing lysostaphin therapy significant prophylactic coverage using an extremely targeted approach. Our strategy could be expanded to include other species specific antimicrobial agents, such as bacteriophage lysins (*71*) or antimicrobial peptides (*223*), thereby enhancing its translational potential as a prophylactic agent (*179*).

Infections treated with BMP-2 loaded lysostaphin-delivering hydrogels induced bone volume equal to sterile hydrogels. However, the mechanical strength of the regenerated bone was reduced. This may be due to the bacterial by-products released by lysostaphin during bacterial lysis. The bacterial debris may negatively affect the repair process, leading to lower quality bone. Bacterial debris may acutely activate local immune cells, causing changes to the local wound environment that affect bone regeneration, but

are resolved within the first week, since we observed no differences in either the cytokine or cell profile at that time compared to uninfected controls. Increased immune cell activation at very early time points may cause a more rapid release of BMP-2, which could also be responsible for the reduced bone quality. Modification of the release rate of BMP-2 though changes to hydrogel mesh structure may improve bone formation through optimized BMP-2 presentation. Studies investigating lysostaphin-delivering hydrogel BMP-2 release and hydrogel degradation *in vivo* in combination with further cytokine and cellular analysis at earlier time points may be required to more fully understand how to improve the functionality of regenerated bone.

The synthetic nature of our PEG-4MAL hydrogels functionalized with the GFOGER peptide and loaded with recombinant BMP-2 protein has several advantages over traditional bone grafting procedures. Synthetic scaffolds do not require graft procurement, which will eliminate donor site morbidity. Removing this aspect of the procedure could reduce the opportunity for intraoperative infection by shortening the procedure times (*224, 225*). Additionally, the "off the shelf" nature of this synthetic delivery vehicle is scalable to any defect size. Lysostaphin-delivering hydrogels are inherently adhesive and can be delivered via injection, allowing for the material to coat and fill any gaps within the injury for easy administration to orthopaedic injuries that may be very anatomically complex and heterogeneous. However, further studies will need to be performed in larger animal models to confirm that larger BMP-2 loaded lysostaphin-delivering hydrogels can regenerate bone in larger defects.

In these studies, the scaffold and the bacteria are delivered together, effectively modeling infection prevention. Clinically, injuries occur and then intervention follows

some time later, allowing for bacteria to begin colonizing the injury before treatment. This motivates further development of a delayed treatment model (*115*). To more accurately simulate infection prevention, defects could be created and inoculated with bacteria and then several hours/days later lysostaphin-delivering hydrogels would be administered.

Bacterial infection triggers a robust inflammatory response in an effort to clear the pathogen from the body. Our histologic analysis supported that *S. aureus* infection resulted in the development of significant leukocytic infiltrate. Importantly, both the cytokine and immune cell profiling supported this data. One week post infection, several cytokines responsible for immune cell recruitment were significantly upregulated, including G-CSF, MIP-1a, MIP-1b, MIP-2, KC, IP-10, IL-6, and IL-1b. G-CSF, MIP-2, and KC contribute to neutrophil recruitment (*226, 227*), which was directly supported by the flow cytometry results, showing significant increases in both the total number and percent of myeloid cells at the implant site in the infection-only group compared to the sterile control. This result clearly supports a robust innate immune response to the infection, and that lysostaphin-delivering hydrogels are able to either prevent this response to infection from occurring or restore the inflammatory environment to normal levels through the elimination of bacteria. Notably, no differences in the cellular response to the material were observed between sterile empty hydrogels and sterile lysostaphin-delivering hydrogels, supporting that lysostaphin delivery does not, in itself, trigger a significant inflammatory response. In terms of the adaptive immune response, we observed significantly elevated levels of T cells including both helper and cytotoxic T cells in the untreated infection animals. Interestingly, the percentage of cytotoxic T cells remained constant in the infection-only group compared to both sterile controls, but both the number and proportion of helper T cells was

significantly elevated. Helper T cells are required for B cell antibody affinity maturation and class switching (*228*). They are also involved in the recruitment of neutrophils and macrophages from the bone marrow, thereby promoting phagocytosis (*229*), supporting that this increase is evidence of a typical adaptive immune response to infection. Other groups have characterized the inflammatory cells at present in bone infection sites for a limited number of cell types, such as myeloid derived suppressor cells (MDSCs) (*230*-*232*) and B cells (*233*) as well as T cell subsets located at the draining lymph node and in spleen (*234*). Vidlak and Kielian have also reported MDSC, monocyte, macrophage, and CD3+ T cell compositions (*235*) in the context of prosthetic joint infections. To our knowledge, this is the most comprehensive report of immune cell subtypes for bone-associated *S. aureus* infections.

In conclusion, we have engineered a lysostaphin- and BMP-2-delivering hydrogel that simultaneously eradicates *S. aureus* infection and repairs critical-sized mouse radial segmental bone defects. This bacteriospecific strategy is limited in that it is only effective against *Staphylococcus* species. However, future studies could investigate the incorporation of antimicrobial agents that could expand the activity spectrum. These hydrogels show no signs of systemic or local toxicity, supporting further investigation using higher order animal models.

4.5 Materials and Methods

Bacterial strains and culture

S. aureus strains UAMS-1 (ATCC 49230) and Xen29 (Perkin-Elmer) were grown at 37ºC on TSA or Luria-Burtani (LB) agar supplemented with 50 µg/mL kanamycin respectively.

Lysostaphin and BMP-2 co-delivering hydrogel synthesis

Hydrogels were synthesized using 20 kDa PEG-MAL (Lysan Bio) functionalized with the collagen-mimetic peptide GFOGER (New England Peptide), lysostaphin (AMBI), *S. aureus* UAMS-1 or Xen29, and then cross-linked using the cysteine-flanked protease degradable peptide VPM. All components were suspended in 100 mM MES buffered PBS at a pH of 5.5 – 6.0. Single colonies of UAMS-1 or Xen29 were picked from agar plates and suspended in PBS to an optical density of 0.20 measured at 600 nm using a benchtop spectrophotometer (Microscan Turbidity Meter, Siemens). The bacteria suspension was diluted 100 fold for UAMS-1 studies and 10 fold for Xen29 studies. BMP-2 (R&D Systems) was prepared at 333 ng/mL in 4 mM HCl. For hydrogels with lysostaphin, the enzyme was added to PEG-MAL. Hydrogels were synthesized by mixing 4:2:2:1:1 parts PEG-MAL, 1.0 mM GFOGER, VPM, BMP-2, and bacteria, followed by injection into a polyimide tube with 300 μm laser machined holes (Microlumen). The final hydrogel composition was 4.0% w/v 20 kDa PEG-MAL, 1 mM GFOGER, (412 ± 85) UAMS-1, 100 ng BMP-2, with or without 1 U lysostaphin. Hydrogels were polymerized at 37ºC and 5% CO_2 for 15 minutes and then swollen in PBS cut into 4 mm segments, and kept in PBS until implantation.

Murine radial segmental defect infection model

All live animal experiments were performed in accordance with the Institutional Animal Care and Use Committee at Georgia Institute of Technology under veterinary supervision. Male C57/B6 mice (Jackson Laboratories) 10-12 weeks old were anesthetized via isoflurane inhalation. Depilatory cream was used to remove fur from the right forelimb.

The limb was surface disinfected by applying 70% isopropyl alcohol followed by chlorohexidine solution. 1 mg/kg slow release buprenorphine was injected intraperitoneally before surgery as an analgesic. A 1 cm incision was made on the right forelimb over the radius, followed by blunt dissection of the radius. A 2.5 mm section of the radius was then excised using a custom made double-bladed bone cutting device. A 4 mm polyimide implant tube containing the hydrogel was then fitted over each end of the radius. For mice receiving local gentamicin therapy, infected UAMS-1 containing implants were dipped in 10 mg/mL gentamicin (*206, 207*) followed by dipping in 0.9% w/v sodium chloride prior to implantation. The wound was sutured closed and a X-ray image (MX-20 Radiography System, Faxitron) was taken of the radius to confirm a successful surgery. Mice placed under and warming lamp and monitored until ambulatory.

Recovery of bacteria from tissue samples

Mice were euthanized via CO_2 inhalation and the right forelimb was sterilized with 70% isopropyl alcohol and the skin was removed. The implant tube and surrounding tissue and bone were removed, weighed, and kept on ice. Tissue samples from the mouse forelimb were homogenized using bead beating tubes (1.4 mm zirconium beads, OPS Diagnostics) in combination with the FastPrep 24 (MP Biomedicals) set to 6 m/s for a total of 5 successive runs, 40 s in duration. Liver samples were homogenized for 10 sec using a Lab Gen 7 (Cole Plamer) tissue homogenizer. Single cell bacterial suspensions were then prepared by a series of sonication and vortexing steps (10 min sonication, 30 sec vortex, 5 min sonication, 30 sec vortex, 30 sec sonication, 30 sec vortex). These single cell suspensions were then serially diluted in PBS, plated on agar plates, incubated overnight

at 37ºC, and enumerated. Bacterial counts were normalized to tissue weight and reported as CFU/mg or CFU/implant if tissue weights were not recorded.

Microcomputed tomography and bone volume quantification

Microcomputed tomography of mouse radii was performed as previously described with modifications (*164, 236*). Animals were anesthetized via isoflurane inhalation and a 3.2 mm length sectioned centered over the radial defect was imaged using a VivaCT system (Scano Medical) with the following imaging parameters: 145 μA intensity, 55 kVp energy, 200 ms integration time, and 15 μm resolution. Contours of the radius within the implant tube were drawn on each 2D section and a Gaussian filter was applied (sigma = 1, support = 1, threshold = 540 mg HA/ccm) to quantify bone volume.

Mechanical testing of radii

Mechanical testing was performed as described in Shekaran et. al. Briefly, mice were euthanized via CO_2 inhalation and the right forelimb was dissected, wrapped in saline soaked gauze, and frozen at -20ºC until the time of analysis. Samples were thawed under running deionized water and the radius and surrounding tissue was removed from the radius and ulna. The ulna was then cut at its midpoint using a scalpel blade to ensure the mechanical integrity of the radius was evaluated. Samples were potted in woods metal containing blocks. Torsion to failure testing was performed using a Bose Electroforce ELF 3200 system in conjunction with a 0.07 Nm torque sensor (Transducer Techniques) by applying a constant rotation of 3 degree per second. The maximum recorded torque value was reported.

Dot blot for anti-lysostaphin antibody generation

Pre-exposure blood samples were collected at the time of surgery via cheek bleed. Post-exposure blood samples were collected 4 weeks after surgery by cardiac puncture after CO_2 euthanasia. Blood samples were clotted, centrifuged, and serum was collected and stored at -80ºC until analysis. The dot blot assay was performed using a vacuum driven Manifold I Spot Blot System (Schleicher & Schuell). The nitrocellulose membrane was coated with lysostaphin (AMBI, 100 µg/mL), blocked, washed, and then 10,000 fold diluted serum samples were exposed to the membrane. A mouse anti-lysostaphin polyclonal IgG (Antibody Research Corporation) was used as a positive control. Anti-lysostaphin antibodies were detected using an AlexaFluor 488 conjugated polyclonal goat anti-mouse IgG antibody (Abcam). A Typhoon FLA 9500 gel imager (GE Healthcare) was used to image the membrane. ImageQuant (GE Healthcare) was used to quantify blot intensity. Positive results were determined to be five times the average intensity of serum samples from animals that were not exposed to lysostaphin.

Liver function analysis

Mice were euthanized by CO_2 inhalation and blood was taken via cardiac puncture. Serum was separated and samples were sent for blood chemistry testing at Antech Diagnostics.

Histology of tissue samples

Mice were euthanized via CO_2 asphyxiation and the right forelimb was dissected, fixed in 10% neutral buffered formalin, and decalcified in formic acid. Sampled were then processed and embedding in paraffin. 5 µm sections of the radius and implant tube were

cut, and stained with either hematoxylin and eosin, safranin-O and fast green, or gram stain using standard methods. Color images of the tissue sections were taken with a Nikon Eclipse E600 microscope using a Plan Fluor 20x objective (Nikon), Micropublisher 5.0 RTV (Q imaging) color camera, and Q-Capture software (Q imaging).

In vivo flow cytometry analysis

Flow cytometry analysis of tissue samples was performed as previously described (*237*). Briefly, mice were euthanized via CO_2 asphyxiation and the right forelimb was dissected. The implant tube and surrounding tissue were removed, weighed, and digested in collagenase type 1-A (1 mg/mL, Sigma) at 37ºC for 45 min. Following digestion, samples were separated using a cell strainer to form a single cell suspension. The single cell suspensions were stained for flow cytometry using standard methods. The samples were analyzed on a FACS-Aria IIIu flow cytometer (BD Biosciences). The antibodies used for cell staining were: AlexaFluor 488 conjugated anti-CD206 (BioLegend), BV421 conjugated anti-CD19 (BioLegend), BV605 conjugated anti-CD4 (BioLegend), BV785 anti-CD8a (BioLegend), PE/Cy7 conjugated anti-CD3ε (BioLegend), BV510 conjugated anti-Ly-6C (BioLegend), APC conjugated anti-F4/80 (BioLegend), APC/Cy7 conjugated anti-Ly-6G (BioLegend), and PE conjugated anti-CD86 (BioLegend). Live/dead staining was performed using the Zombie Red fixable viability kit per manufacturer's instructions (BioLegend). Precision Counting Beads (BioLegend) were used to report cell numbers.

In vivo cytokine array analysis

Following euthanasia via CO_2 inhalation, the right forelimb was dissected and the implant tube and surrounding tissue was removed for processing. The samples were placed in RIPA

buffer, minced, and sonicated. The homogenate was centrifuged at 10,000 g for 5 minutes and the supernatant was filtered using a 0.45 μm spin filter, snap frozen in liquid nitrogen, and stored at -80ºC until the time of analysis. A MilliPlex 25-plex mouse cytokine array kit (Millipore Sigma) was used to quantify tissue concentrations of G-CSF, GM-CSF, IFN-γ, IL-1α, IL-1β, IL-2, IL-4, IL-5, IL-6, IL-7, IL-9, IL-10, IL-12p40, IL-12p70, IL-13, IL-15, IL-17, IP-10, KC, MCP-1, MIP-1α, MIP-1β, MIP-2, RANTES, and TNF-α per the manufacturer's instructions. Results were read using a Luminex system (Luminex Corporation) and normalized to total protein content of the sample measured with a bicinchoninic acid (BCA) assay kit (Pierce by ThermoFisher). Samples below or above the detection limit of the assay were reported as the minimum or maximum value respectively.

Statistics

All data is plotted as individual data points with a line indicating the mean and the error bars representing the standard deviation of the mean. A *P* value less than 0.05 was deemed statistically significant. Statistical comparisons between two groups were made with the Student's *t* Test. Multivariate parametric data was analyzed using ANOVA with Tukey's post-hoc test and non-parametric data was analyzed using the Kruskall-Wallis test with Dunn's multiple comparison test. A two-way ANOVA with a Bonferroni correction was used to identify statistically significant cytokines. All calculations were performed using Prism (GraphPad). Hierarchal cluster analysis was performed on the cytokine data using JMP Pro 13.

LYSOSTPAHIN-DELIVERING HYDROGELS TO TREAT ESTABLISHED INFECTIONS

5.1 Abstract

Traumatic injuries resulting in complex open fractures are associated with high infection rates, with reports of up to 30%. These infections are treated with a combination of systemic antibiotic therapy, extensive surgical debridement, followed by a second surgery to repair the bone, resulting in significant patient morbidity. Lysostaphin is a bacteriolytic enzyme that specifically kills *S. aureus,* but translation has been impeded by the lack of an effective delivery vehicle. We engineered an injectable lysostaphin-delivering hydrogel capable of conforming and adhering to the infected injury. We investigated the ability of lysostaphin-delivering hydrogels to treat established segmental bone defect infections. Lysostaphin-delivering hydrogels alone modestly reduced bacterial counts at one week post implantation. Long term, lysostaphin laden hydrogels preserved bone volume compared to untreated controls. Importantly, the combination of lysostaphin-delivering hydrogel treatment and systemic antibiotic therapy to established bone infections resulted in an enhanced antibacterial effect, resulting in a nearly two log reduction in bacteria numbers. Taken together, lysostaphin-delivering hydrogels have the potential to significantly reduce established bacterial infections.

5.2 Introduction

Traumatic injuries resulting in complex open fractures are associated with the highest infection rates, with reports of up to 30% (*137-139, 238*). Additionally, orthopaedic injuries account for 65% of all military combat casualties, and carry infection rates as high as 50% (*218*). Staphylococcal species are the most common pathogens, responsible for over two thirds of cases (*2*). Successful clinical management of these complex injuries is focused on preventing infections through a combination of extensive and early surgical debridement of the affected bone, fracture stabilization, and aggressive antibiotic therapy (*218*). Even with the employment of optimal care, infection rates remain high. The placement of biomaterials, such as fixation hardware, reduces the number of bacteria required to initiate an infection by up to 10,000 fold or more (*239*). Colonization of orthopaedic hardware leads to bacterial biofilm formation and the subsequent development of osteomyelitis (inflammation of the bone), characterized by osteolysis and reactive bone formation (*17, 18*).

Bacterial biofilms play a significant role in the pathogenesis of orthopaedic infections and subsequent progression to osteomyelitis. Biofilms are communities of bacteria encased within a secreted matrix composed of DNA, protein, and polysaccharides (*143*). They form in a stepwise manner: the implant is coated with host proteins, bacteria then adhere to these proteins and subsequently begin to grow, leading to colonization, and finally biofilm formation (*239*). The biofilm matrix then acts as a defense mechanism against the host immune response to infection, and a diffusion barrier to antibiotics (*144, 240*).

Clinical management of hardware-associated biofilm infections is limited to surgical debridement, antibiotic therapy, and implant removal and replacement. Recently, employment of the Masquelet technique, a two stage reconstruction protocol for segmental bone defects, has become popular in treating these infections (*220*). The first stage consists of extensive tissue debridement, limb stabilization followed by the placement of an antibiotic eluting space maintainer, and ensuring soft tissue coverage and wound healing. The second stage of the procedure commences once the infection has been eradicated, often 4-8 weeks later. In this surgery, the cement spacer is removed, permanent fixation hardware is placed, and an autogenous bone graft is harvested and deployed (*241*). The development of treatment protocols that simultaneously eradicate the bacterial infection and promote bone healing would effectively eliminate a surgery, having the potential to reduce patient morbidity and healthcare costs. The elimination of a surgical procedure will significantly reduce the recovery time for patients, which may result in reduced complications and improved outcomes. However, preclinical studies have focused primarily on evaluating prophylactic therapies and do not address these established infection scenarios.

Lysostaphin is an endopeptidase produced by *Staphylococcus simulans* as a defense mechanism against *Staphylococcus aureus (4).* It is specific to, and highly active against, staphylococcal species (*4, 103*). Lysostaphin is composed of a SH3B targeting domain, providing its specificity, and a catalytic domain that cleaves the glycine-glycine peptidoglycan linkages present in the cell wall (*3, 242*). Bacterial lysis is achieved by rapid catalytic degradation of the cell wall. The catalytic nature of lysostaphin allows for it to have activity against biofilm infections *in vivo,* in models of endocarditis (*7, 9, 103*), jugular vein catheterization (*11*), and nasal colonization (*151, 195*).

Further development of lysostaphin as a therapeutic to treat biofilm infections has been severely limited by a lack of effective delivery vehicles. Biomaterial-based strategies for lysostaphin delivery have been primarily centered around preventing infections (*150, 154-156*) as opposed to treating established infections. Local delivery of antibacterials provides high, sustained, local doses, to infection sites (*157, 158*). We have previously engineered PEG hydrogels for the delivery of cell and protein based therapeutics to treat a variety of disease pathologies (*160-165*). This hydrogel system consists of a 4-arm PEG macromer with maleimide functionalized end groups that react specifically with thiols, allowing for covalent incorporation of cell adhesive peptides, and cross-linking with protease degradable cysteine-terminated peptides.

In this study, we engineered an injectable PEG hydrogel for local lysostaphin delivery to treat established bone infections. We extended the mouse radial segmental defect infection model to assess treatments for established infections, by first initiating an infection, and then in a second procedure, providing therapy to the infection site. We showed that lysostaphin-delivering hydrogels alone reduce bacteria counts at one week after treatment, and that this infection reduction translated to a preservation of bone volume. Next, we investigated the effect of administering systemic antibiotic therapy in conjunction with lysostaphin-delivering hydrogels and showed that there was a combined effect provided by combination therapy. These proof-of-concept studies provide a platform for further optimization of lysostaphin-delivering hydrogels and simultaneous antibiotic therapy to treat established *S. aureus* bone infections.

5.3 Results

5.3.1 Lysostaphin-delivering hydrogels reduce bacteria in an established biofilm infection model

Few mouse models exist to study the treatment of established biofilm infections. Therefore, we first set out to develop and validate an established biofilm infection model by adapting the murine radial segmental defect infection model. We first initiate an infection, allowing for implant colonization, and then treat the established infection at a later time, in a two-stage surgical model (Figure 37). The infection is initiated by implanting hydrogels containing *S. aureus* UAMS-1 into a radial segmental defect. The infection is allowed to become established over the course of 7 days. Then, a second revision surgery is performed to remove the contaminated implant, debride surrounding dead tissue, and place a sterile implant with additional gel polymerized *in situ* to provide extra lysostaphin therapy. This model mimics current therapeutic strategies where infected hardware is removed and the wound bed is cleaned and treated locally.

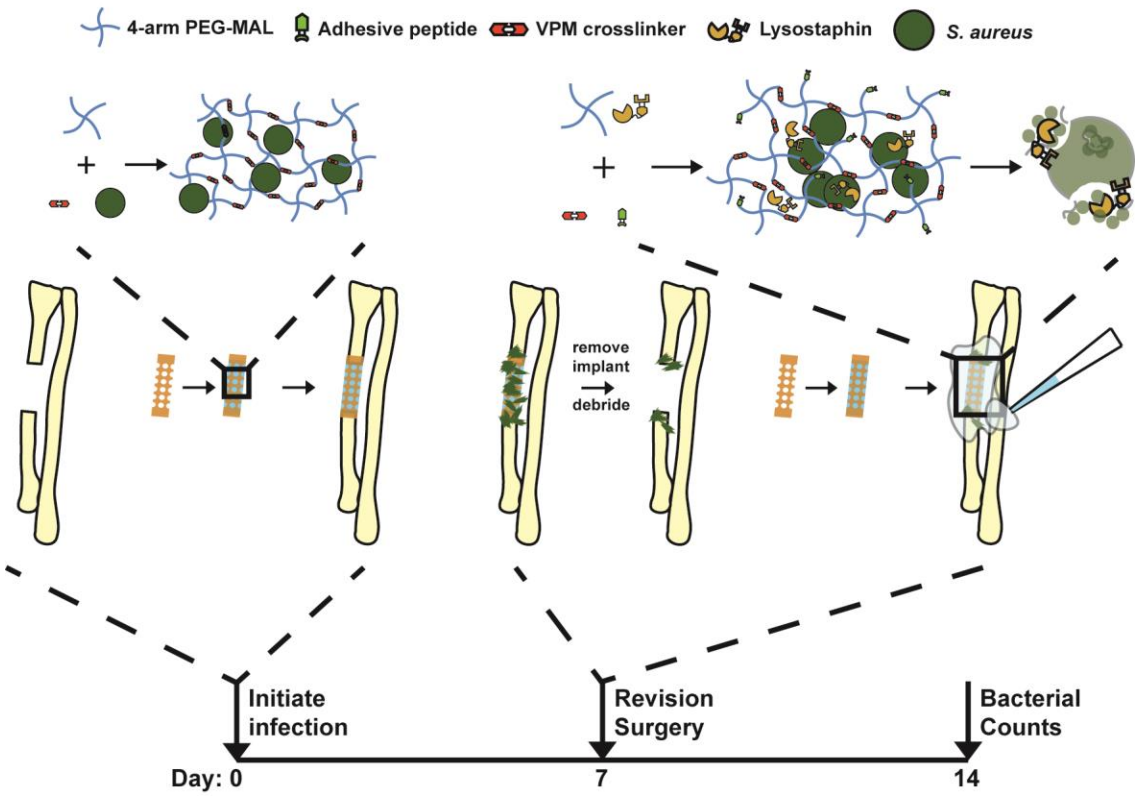

Figure 37: In vivo established S. aureus biofilm infection model. *In vivo* biofilms were established by implanting hydrogel scaffolds containing *S. aureus* UAMS-1. A 2.5 mm segment of the radius was removed and a 4.0 mm perforated polyimide tube filled with a hydrogel is fitted over the ends of the radius, filling the defect. Seven days following infection initiation, revision surgery was performed to remove the infected implant and surrounding dead tissue, irrigate the wound, place a sterile scaffold, and an additional wound filling gel, polymerized *in situ*, to deliver additional lysostaphin. Seven days following revision surgery, mice were assayed for viable bacteria within the defect site.

To establish a working model, we tested two different doses of *S. aureus* UAMS-1 (low dose = 55 ± 24 CFU/implant; high dose = 613 ± 117 CFU/implant) to identify the lowest bacterial dose that reliably initiates the infection (Figure 38A). At the time of revision surgery, sterile implants were placed and an additional 10 µL of gel was polymerized *in situ* in the wound bed over the implant. Both empty and lysostaphin-containing hydrogels were evaluated for each bacterial dose. Seven days following revision surgery, mice were euthanized and assayed for viable bacteria at the infection site. There

was a statistically significant reduction in recovered bacteria in the lysostaphin-delivering hydrogel-treated group compared to the untreated control for the low dose of UAMS-1 of roughly 50% (Figure 38B). This shows that lysostaphin-delivering hydrogels are modestly effective against bacteria growing in an established infection. No differences were detected in the high dose group between the treated and untreated groups ($P < 0.053$). Notably, there were no differences in the number of bacteria recovered from untreated mice in the low and high bacterial inoculum groups (Figure 38C). For this reason, we selected the lower dose to initiate infections for all the following studies.

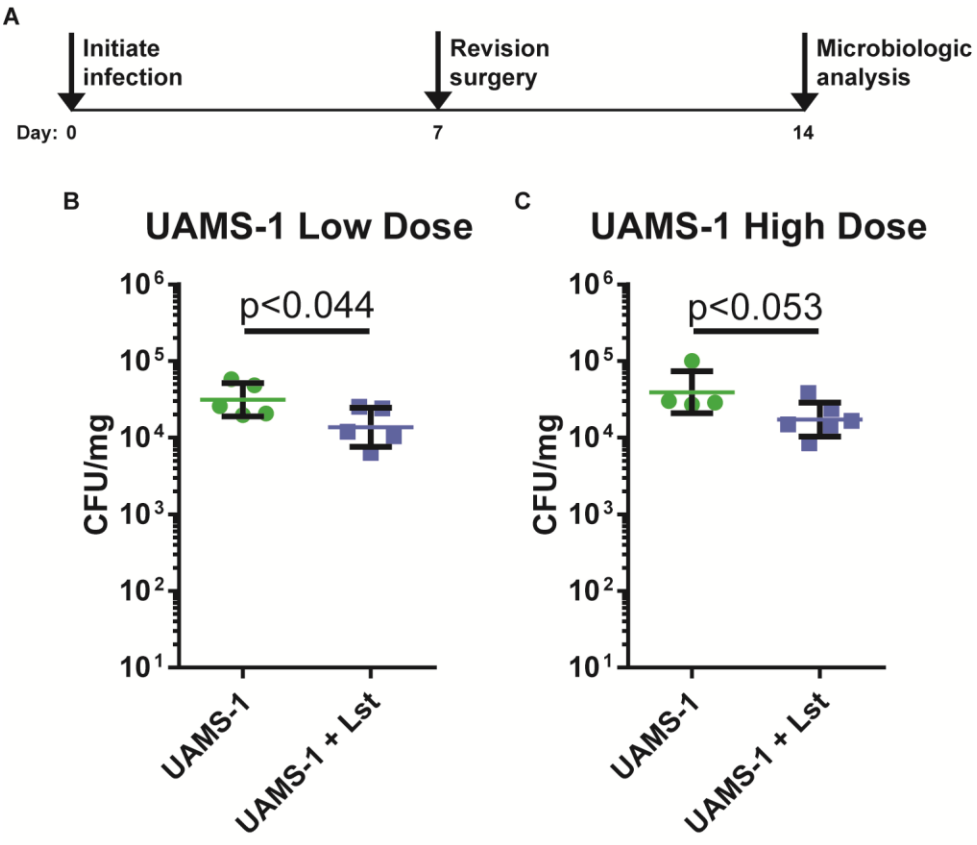

Figure 38: Lysostaphin-delivering hydrogels reduce in vivo biofilm. (A) Biofilms were initiated and 7 days later revision surgery was performed. 7 days following revision

surgery bacteria from the implant and surrounding tissue was quantified. (B) Bacterial counts 7 days after revision surgery recovered from mice receiving the low initial dose of *S. aureus* UAMS-1. (C) Bacterial counts 7 days after revision surgery recovered from mice receiving the high initial dose of *S. aureus* UAMS-1. Means ± SD. *N*=4-6 per group. **P* < 0.05, Student's *t* test.

To determine if this reduction of bacteria translated to differences in bone within the defect, we assessed bone volume at 4 and 8 weeks following revision surgery via μCT imaging (Figure 39A). Representative μCT reconstructions of radii scanned at 4 weeks post-revision surgery show no gross morphological differences between groups (Figure 39B). However, at 8 weeks, no bone is present in the untreated infection control group, with minimal bone loss observed in the lysostaphin-delivering hydrogel group. Quantification of the μCT imaging at 5 weeks revealed no differences in bone volume between empty and lysostaphin-delivering hydrogel treated mice (Figure 39C). However, at 9 weeks, significantly more bone was present within the defect for mice treated with lysostaphin-delivering hydrogels compared to the untreated control group (Figure 39D). This result suggests that treatment with lysostaphin-delivering hydrogels reduces bone resorption in our mouse model, since no apparent new bone formation was present in the lysostaphin-delivering hydrogel group.

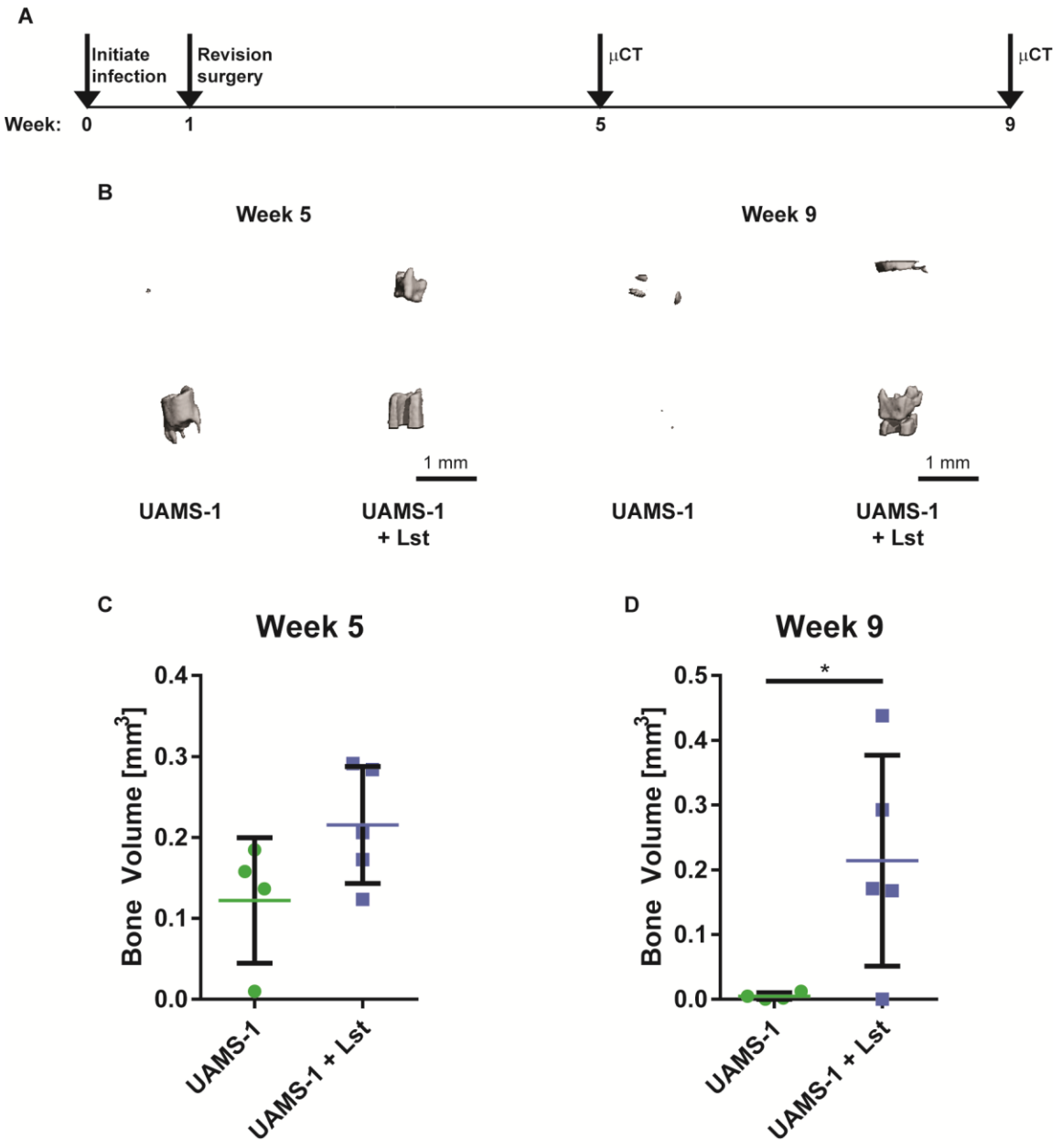

Figure 39: Lysostaphin-delivering hydrogels preserve bone volume. (A) *S. aureus* infections were initiated for one week and then treated with lysostaphin-delivering hydrogels. Bone formation was assessed using µCT imaging at 5 and 9 weeks. Representative µCT reconstructions at 5 weeks **(B)** and 9 weeks **(C)** post infection initiation. Bone volume within the implant site quantified at 5 weeks **(C)** and 9 weeks **(D)** post-revision surgery. Means ± SD. *N*=3-5 per group. **P* < 0.05. Student's *t* test.

5.3.2 Lysostaphin-delivering hydrogels act in combination with systemic antibiotic therapy to reduce infection

The previous studies demonstrated that lysostaphin-delivering hydrogels modestly reduce bacteria compared to untreated controls at one week following revision surgery, and that there is less apparent bone loss 8 weeks after revision surgery. These reductions were promising, but may not be clinically relevant, since the infections are not close to being eliminated. With this observation in mind, we hypothesized that optimization of bacterial clearance will be critical to developing a wound environment that can support new bone formation. We set out to further reduce the viable bacteria recovered at 7 days post-revision surgery by testing the effect of systemic antibiotic therapy in combination with lysostaphin-delivering hydrogels. We initiated biofilm growth and then, at revision surgery, treated mice with lysostaphin-delivering hydrogels or lysostaphin-delivering hydrogels paired with twice daily injections of tobramycin for 4 days, totaling 8 injections (Figure 40A). The control groups included mice treated with empty hydrogels, with and without tobramycin therapy. Mice were then assessed for viable bacteria one week following revision surgery. The microbiologic assessment of the implants and surrounding tissue showed a significant reduction in bacteria for the lysostaphin-delivering hydrogel with tobramycin group compared to the untreated infection control (Figure 40B). No effect was observed in mice treated with systemic tobramycin alone compared to control. Notably, 2/5 mice treated with lysostaphin-delivering hydrogels in combination with systemic antibiotics responded robustly to the therapy with bacterial reductions of 2 and 5 orders of magnitude compared to untreated controls. This result shows that the addition of

tobramycin to lysostaphin-delivering hydrogel therapy provides a combined effect, potentiating the antimicrobial capacity of the material.

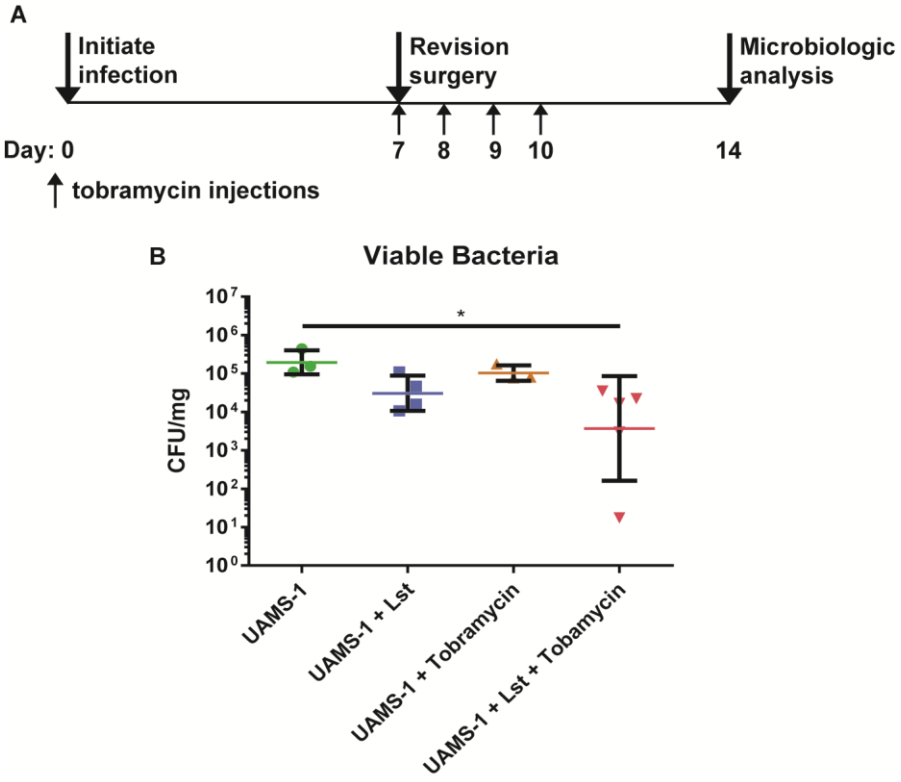

Figure 40: Systemic tobramycin administration provides a combined antimicrobial effect. (A) *In vivo* biofilms were established for seven days. At the time of revision surgery, tobramycin was administered twice daily for 4 days. 7 days following revision surgery, mice were assayed for bacteria. (B) Viable bacteria recovered from mouse radii 7 days following revision surgery. Means ± SD. *N*=3-5 per group. **P* < 0.05. Kruskall-Wallis with Dunn's post hoc test for.

It has been reported that lysostaphin acts synergistically with oxacillin *in vitro* (*5*, *103*). Therefore, we hypothesized that systemic oxacillin therapy would potentiate the antimicrobial activity of lysostaphin-delivering hydrogels. Infections of UAMS-1 were initiated in the defect site. Twice daily oxacillin injections (100 mg/kg) began at day 6, 1 day prior to revision surgery, and continued until microbiologic assessment at day 14 for

animals receiving antibiotics (Figure 41A). At day 7, revision surgery was performed and mice were treated with empty hydrogels or lysostaphin-delivering hydrogels. At day 14, mice were euthanized and both the implant and surrounded tissue were separately assayed for viable bacteria. A significant reduction in bacteria recovered from the surrounding tissue was observed in the lysostaphin-delivering hydrogel with oxacillin group compared to both the infection-only control and the systemic oxacillin-treated group (Figure 41B). Bacteria counts of the implant tube revealed significantly more bacteria in the lysostaphin-delivering hydrogel group compared to the untreated control (Figure 41C). However, lysostaphin-delivering hydrogels combined with antibiotic therapy significantly reduced bacteria compared to the untreated infection control and the hydrogel only group (Figure 41D). Analysis of the total bacteria recovered from both the tissue and implant tube showed that combing lysostaphin-delivering hydrogels with oxacillin therapy was superior in reducing bacterial counts compared to the untreated control and lysostaphin-delivering hydrogels alone. Taken together, the efficacy of lysostaphin-delivering hydrogels is potentiated when paired with systemic oxacillin therapy, suggesting that to effectively reduce infection in our mouse model, both lysostaphin and antibiotics need to be delivered in combination.

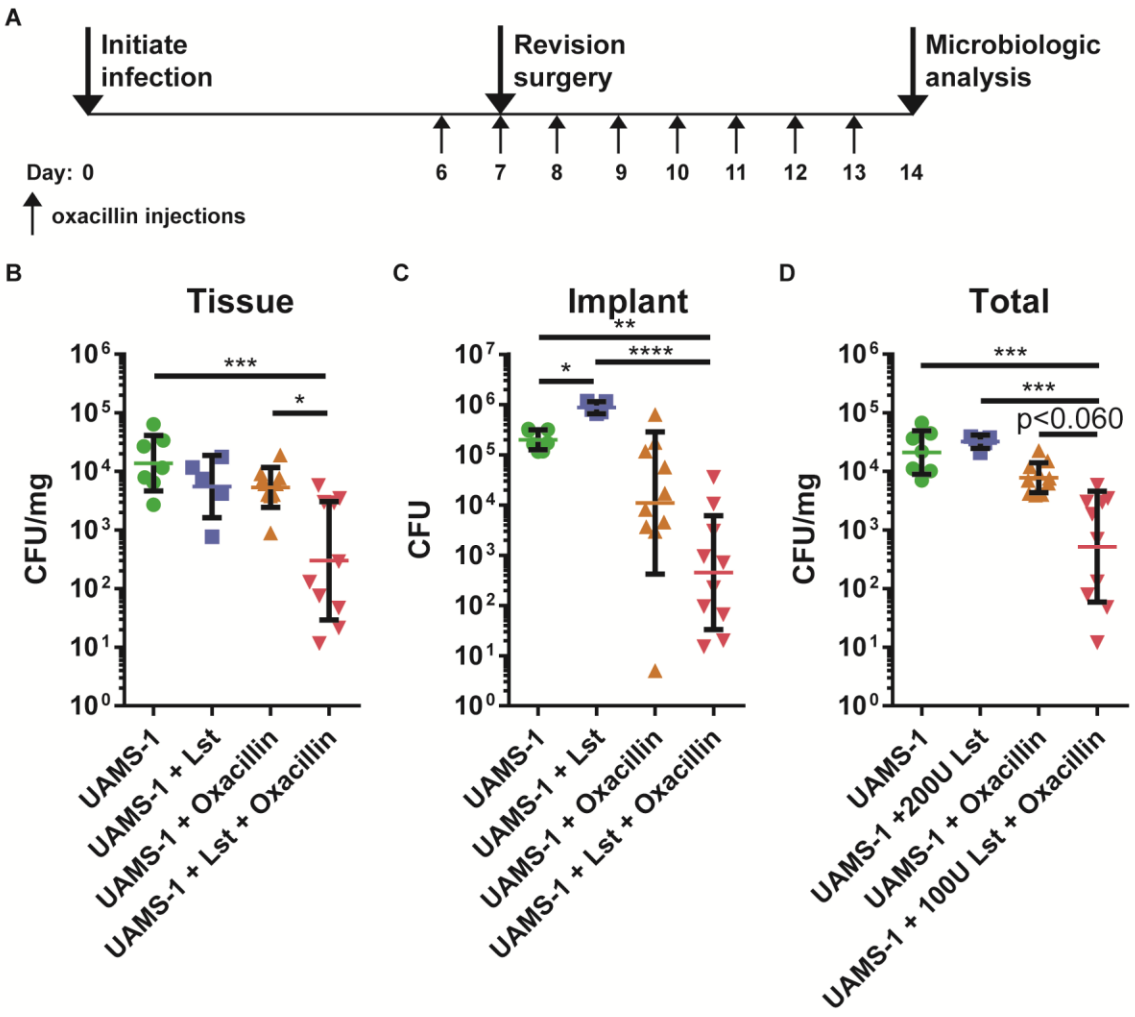

Figure 41: Systemic oxacillin administration enhances lysostaphin-delivering hydrogel efficacy. (A) *S. aureus* infections were initiated and after seven days, revision surgery was performed to remove the implant and place lysostaphin-delivering hydrogels. Animals undergoing systemic oxacillin therapy received twice daily injections beginning one day before revision surgery and continued until necropsy. At 7 days post-revision surgery, the (B) tissue surrounding the implant and the (C) implant were assayed for viable bacteria. (D) indicates the sum of all bacteria recovered. Means ± SD. N=5-10 per group combined from two independent experiments. *P < 0.05, ***P < 0.001, ****P < 0.0001, Kruskal-Wallis with Dunn's multiple comparisons test.

5.4 Discussion

In this study, we developed a novel mouse model to study orthopaedic hardware-associated established infections in the context of segmental bone defects, and then used this model to test the efficacy of lysostaphin-delivering hydrogels. We identified the minimal bacterial dose required to reliably establish an infection in a mouse radial segmental defect. After 7 days of infection, we performed a second revision surgery to clean the wound bed, remove infected hardware, replace the hardware, and apply the specified hydrogel treatment. Our results showed that lysostaphin-delivering hydrogels by themselves reduce infection compared to the untreated controls and that this effect reduces infection-associated bone loss. Importantly, we showed that lysostaphin-delivering hydrogel therapy in combination with either systemic tobramycin or oxacillin further potentiates the antimicrobial effect.

Treating orthopaedic hardware-associated established infections remains a very complicated and challenging clinical scenario (*158*). Successful therapy typically requires extended antibiotic regimens, multiple surgeries, and significant patient morbidity. Progress remains slow in the development of experimental therapies that address these infections. Several animal models exist to study established orthopaedic infections. However, until recently, these have been limited to rats and larger animals, which are expensive to work with and require significant ethical justification, limiting their use. These issues motivate the development of murine established infection models for rapid screening of experimental therapies. One murine established infection mouse model first initiates a tibial infection by injection of bacteria into the medullary canal, and then 2 weeks later, necrotic bone is debrided from the tibial canal using a needle (*243*). This model has

been used to compare systemic antibiotic therapy to tissue debridement as well as characterize the inflammatory response of tissue debridement in osteomyelitis (*244*). However, this approach is limited in that there is no bone fracture or hardware placement, two critical components to treating most orthopaedic injuries. To date, only a single murine model has been published involving established orthopaedic hardware infections (*53*). In this femoral fracture model, the authors first initiate an infection and then perform a revision surgery seven days later, where necrotic tissue and bone are debrided and an antibiotic spacer is placed in the expanded osteotomy site. Our approach differs in that we are investigating segmental bone defect infections and our procedure does not require a fixation device, as the radius is self-stabilized by the ulna. This is advantageous in that the model is simplified by not including fixation hardware, which eliminates the possibility of hardware failure. Furthermore, the use of a segmental defect will enable the evaluation of bifunctional therapies that simultaneously eradicate infection and repair bone. However, further characterization of the model should be performed, including analyzing if biofilm and osteomyelitis are present at 1 week, both in the debrided tissue and at the defect site. The amount of bacteria present at the time of revision should also be quantified, along with the amount of bacteria removed during the debridement procedure. This analysis will provide better characterization of the contribution of tissue debridement and how the hydrogel treatment potentiates the affect.

Our results clearly demonstrate that systemic antibiotics potentiate the efficacy of lysostaphin-delivering hydrogel therapy. However, even with combination therapy, we do not consistently eradicate the infection. This could be due to a variety of factors including, improper lysostaphin release kinetics, ineffective intracellular killing of *S. aureus*, or poor

penetration into the biofilm. Bacterial regrowth after the cessation of systemic antibiotic therapy cannot be ruled out, and furthermore, the surviving bacteria could be resistant to both the given antibiotic and lysostaphin. Bacterial infection causes a significant upregulation in inflammatory cytokines, that recruit inflammatory cells and trigger protease production (*169*). The lysostaphin-delivering hydrogel responds to this by degrading, and more rapidly releasing lysostaphin. Modification of the hydrogel structure by reducing the mesh size or utilizing a cross-linking peptide that is less responsive to proteases should extend the release of lysostaphin, increasing the time that bactericidal concentrations of lysostaphin are present at the infection. The elimination of intracellular bacteria is a significant challenge when treating bone infections (*245*). Although *S. aureus* was primarily thought of as an extracellular pathogen, this is no longer the case (*246*). *S. aureus* invades both phagocytic and non-phagocytic cells, which can persist and eventually lead to the generation of small colony variants exhibiting high levels of antibiotic resistance (*246*). Lysostaphin exhibits variable activity against intracellular bacteria, limiting its efficacy treating these infections (*247*). Additionally, both oxacillin and tobramycin have very poor intracellular antimicrobial activity (*248*). Other antibiotics may also be considered, such as macrolides, vancomycin, or fluoroquinolones, to see if they further potentiate the effect of lysostaphin-delivering hydrogels. However, reports of the effectiveness of monotherapy in the context of osteomyelitis are variable (*249*). With some classes, such as macrolides, being recommended against due to low bioavailability in bone (*249*). Although we observed significant reductions in bacteria, it may be possible to further reduce bacterial numbers through the addition of antibiotics with high activity against intracellular pathogens. Checkerboard assays could be performed to identify antibiotics

that act synergistically with lysostaphin-delivering hydrogels. Rifampin is a critical therapeutic component when treating orthopaedic infections where the hardware is retained. Moreover, it has relatively high activity against bacteria growing in biofilm and is highly effective against intracellular bacteria. However, rifampin must be given in combination with another antibiotic to avoid the rapid development of resistance against it (*250, 251*). For these reasons, the addition of systemic rifampin therapy to our antibiotic regimen and lysostaphin-delivering hydrogel may be a way to further reduce the infection. Another option could be to expand the defect to simulate more extensive debridement. This modification may improve therapeutic efficacy, as extensive debridement is a more effective treatment than antibiotics alone (*243*).

Eradication of the biofilm will be critical to successfully engineering an implant that is also capable of regenerating bone to repair a segmental defect. Our results indicate that lysostaphin-delivering hydrogels alone do not promote new bone formation, but do preserve some bone mass compared to untreated controls. Multiple groups have shown that increasing the BMP-2 dose, even with infection still present, increases new bone formation within the defect (*40, 115*). Further optimization of the hydrogel formulation, including BMP-2 dosing, will be required to simultaneously eliminate the infection and regenerate bone. This dual function strategy may allow for the elimination of a revision surgery to repair the fracture after mitigation of the infection, thereby reducing patient morbidity and associated health care costs, having the potential to significantly transform how these complex clinical scenarios are managed.

Lysostaphin therapy provides bacteriospecific targeting of staphylococcal species. This is particularly advantageous when treating established bacterial infections, where the

pathogen can be identified prior to administering therapy. A targeted approach will ensure patients have the best chance of recovery, while also reducing unwanted side effects associated with broad spectrum strategies aimed at eliminated all bacteria. The incorporation of other bacteriospecific antimicrobial strategies, such as phage lysins, bacteriophage, or antimicrobial peptides, will provide personalized treatment approaches for successfully treating infections. Furthermore, the development of targeted bacteriospecfic approaches as either primary or adjuvant therapies will help to reduce the spread of antibiotic resistance associated with long term systemic antibiotic therapy.

5.5 Materials and Methods

Bacterial strains and culture

S. aureus UAMS-1 (ATCC 49230) was grown on trypic soy agar (TSA) plates at 37ºC.

Lysostaphin-delivering hydrogel synthesis

Hydrogels were synthesized by reacting a20 kDa 4-arm PEG macromer with end functional maleimide units (PEG-4MAL) (Lysan Bio) with the collagen mimetic GFOGER peptide ($GGYGGP(GPP)_5GFOGER(GPP)_5GPC$; New England Peptide) and the cysteine-flanked protease degradable cross-linking peptide VPM (GCRDVPMSMRGGDRCG; Genscript). The individual hydrogel components, lysostpahin (AMBI Products LLC), and *S. aureus* UAMS-1 were suspended in 100 mM MES in PBS and pH adjusted to a final pH of 5.5-6.0 and the VPM cross-linker in 100 mM MES in PBS at a pH of 5.5-6.0.

For hydrogels used to initiate the bacterial infection, single colonies of *S. aureus* UAMS-1 were picked from a TSA plate and suspended in PBS to an optical density of 0.20

at 600 nm measured using a spectrophotometer (MicroScan Turbidity Meter, Siemens), and then diluted 1,000 fold in PBS. Hydrogels were synthesized by mixing PEG-4MAL, VPM, and the bacterial suspension at a volume ratio of 2:2:1. Following mixing, hydrogels wereinjected into a polyimide tube with 300 μm laser machined holes (Microlumen). The final hydrogel composition was 4.0% w/v 20 kDa PEG-4MAL and containing 55 ± 24 CFU of *S. aureus* UAMS-1. The hydrogel was allowed to fully polymerize in a humidified incubator at 37ºC at 5% CO_2 for 15 minutes before being swollen in PBS. Individual implants were created by cutting the hydrogel containing implant to into 4 mm long segments. The implants were kept in PBS until implantation.

The hydrogels placed at the revision surgery were synthesized in a similar fashion with slight modifications. Individual hydrogel components were suspended in 100 mM MES in PBS and pH adjusted to 5.5-60. Hydrogels components, 20 kDa PEG-4MAL, GFOGER, lysostaphin, and VPM, were then mixed at volume ratios of 2:1:1:1 to produce hydrogels with a final compositions of 4.0% w/v 20 kDa PEG-4MAL, 1.0 mM GFOGER, with or without 25 U of lysostaphin. These hydrogels were injected into polyimide tubes, allowed to polymerize for 15 min at 5.0% CO_2 in a humidified incubator, cut into 4 mm segments, and swollen in PBS until implantation. After placement of this sterile implant at revision surgery, a second hydrogel was polymerized *in situ* over the implant tube. This hydrogel was the same composition as the hydrogel in the implant tube. It was prepared by mixing a 3:2 volume ratio of 2:1 20 kDa PEG-4MAL:lysostaphin (42400 U/mL) solution with a 1:1 GFOGER:VPM solution and then pipetting this hydrogel over the wound bed for a final hydrogel composition of 4.0% w/v 20 kDa PEG-4MAL, 1.0 mM GFOGER, with or without 85 U of lysostaphin polymerizing in the wound bed.

Murine radial segmental defect established biofilm infection model

All live animal experiments were performed under protocols approved by the Institutional Animal Care and Use Committee at Georgia Institute of Technology with veterinary supervision. Male C57/B6 mice 10-12 weeks old (Jackson Laboratories) were anesthetized via isoflurane inhalation. Slow release buprenorphine was administered (1 mg/kg) intraperitoneally as an analgesic. Right forepaw fur war removed with depilatory cream and the area was sterilized with 70% isopropyl alcohol and the subsequent application of cholorhexidine. A 1.5mm incision was made on the right forepaw and the radius was blunt dissected. A 2.5 mm segment of the radius was then removed using custom made bone cutters. A 3 µL hydrogel (4.0% w/v 20 kDa PEG, VPM) containing *S. aureus* UAMS-1 loaded inside of a 4 mm polyimide tube was then slipped over the ends of the radial defect. The wound was sutured closed and an X-ray image was taken to confirm proper defect formation and implant placement using the MX-20 Radiography System (Faxitron) (*164*). Mice were then monitored under a warming lamp until ambulatory. 7 days following infection initiation surgery, mice were anesthetized under isoflurane, slow release buprenorphine was injected (1 mg/kg) intraperitoneally, fur was removed from the right forepaw with depilatory cream, and the skin was sterilized with 70% isopropyl alcohol followed by chlorohexidine. The incision site was reopened, and the wound was debrided by removing the original implant and surrounding dead tissue. The wound was irrigated with 0.9% w/v saline. A 4 mm perforated polyimide tube containing a 3 µL hydrogel scaffold (4.0% w/v 20 kDa PEG, 1 mM GFOGER, VPM) with or without lysostaphin was placed over the ends of the radial defect. A 10 µL (4.0% w/v 20 kDa PEG, 1 mM GFOGER, VPM) hydrogel with or without lysostaphin was polymerized *in situ* over

the implant tube. The incision was sutured closed and mice were monitored under a warming lamp until ambulatory.

µCT imaging and analysis

µCT imaging was performed as previously described with slight modification (*164*, *236*). Animals were anesthetized under isoflurane and 3.2 mm of the radius was scanned using the VivaCT system (Scanco Medical, 145 mA intensity, 55 kVp energy, 200 ms integration time, and 15 µm resolution). Bone volume was determined by contouring 2D slices of the radius and implant tube at the defect area for a total of 3.2 mm radial length. A Gaussian filter was applied and bone volume was quantified.

Recovery of bacteria from tissue samples

At the designated experimental end point, mice were euthanized via CO_2 inhalation. The right forepaw was sterilized with 70% ethanol and the radius was dissected. The polyimide tube containing the hydrogel and other surrounding tissue was removed, placed in a bead beating tube containing 1.4 mm zirconium beads (OPS Diagnostic), weighed, and stored in PBS on ice. Tissue samples were homogenized with 5 successive runs at 6 m/s for 40 s using a FastPrep 24 (MP Biomedicals). Samples then underwent a series of sonication followed by vortexing (10 min sonication, 30 sec vortex, 5 min sonication, 30 sec vortex, 30 sec sonication, 30 sec vortex) to disperse the biofilm and create a single cell bacterial suspension. Bacteria were enumerated by serially diluting the samples and culturing the dilutions on TSA plates overnight at 37ºC. Bacterial colony forming units (CFU) were enumerated, normalized to tissue weight, and reported as CFU/mg.

Statistics

Individual data points are plotted with bars representing the mean ± standard deviation. A student *t* test was used to compare two individual groups. Multiple groups were compared with ANOVA in combination with a Tukey post-hoc test. Non-parametric data was analyzed using a Kruskall-Wallis test with Dunn's multiple comparison test.

FUTURE CONSIDERATIONS

The overarching objective of this thesis was to engineer a synthetic hydrogel serving as a controlled delivery vehicle for lysostaphin to treat orthopaedic *S. aureus* infections and promote bone repair. We have demonstrated that lysostaphin-delivering hydrogels prevent infection while simultaneous supporting fracture healing and segmental bone defect regeneration. Additionally, lysostaphin-delivering hydrogels reduce *in vivo* established orthopaedic infections, and this effect is potentiated by the additional of systemic antibiotic therapy.

In Aim 1, we engineered injectable lysostaphin-delivering hydrogels for controlled release of lysostaphin to eradicate *S. aureus* femur fracture infections. We showed that hydrogel encapsulation of lysostaphin retains the enzyme activity, stability, and that modulation of the material parameters directly modulates the enzyme release rate. Lysostaphin-delivering hydrogels were effective against several strains of bacteria, including bacteria growing in biofilm. *In vivo,* lysostaphin-delivering hydrogels eliminate bacteria and support bone repair, outperforming both soluble enzyme delivery and systemic antibiotic prophylaxis. Cytokine analysis showed that the inflammatory environment of lysostaphin treated infections is no different than untreated controls.

In Aim 2, we demonstrated that the addition of BMP-2 to lysostaphin-delivering hydrogels supports bone regeneration in a *S. aureus* infected mouse radial segmental defect model. Lysostaphin-delivering hydrogels were used to treat both Xen29 and UAMS-1 infections. Bacteria was eliminated 1 week after implantation, and at 8 weeks, significantly more bone was regenerated within the defect. Radii treated with lysostaphin-delivering hydrogels demonstrated improved mechanical properties compared to untreated controls.

Safety profiling revealed no systemic toxicity and that infections treated with lysostaphin-delivering hydrogels had no effect on the local cytokine and inflammatory cell milieu.

In Aim 3, we created a model of established biofilm infection by initiating infections in a mouse radial defect and then performing a second operation to remove necrotic tissue and deliver lysostaphin-delivering hydrogel therapy. Established infections treated with lysostaphin-delivering hydrogels had significantly reduced bacteria and retained significantly more bone that untreated controls. The addition of systemic antibiotics potentiated the antimicrobial effect of lysostaphin-delivering hydrogels.

Translation of this technology to the human scale will require significantly more validation. This will include evaluation of the antimicrobial efficacy in larger animal models of orthopaedic implant infection. Additionally, significantly more material safety analysis will have to be performed. The synthetic, well defined composition of the material may increase the probability of successful scaling. Each component can be synthesized in scalable amounts at very high purity, which allows for consistent and repeatable material synthesis. However, a major limitation to human translation will be navigation through the FDA regulations regarding combination products. Since the hydrogel is composed of several different biologically active components, safety will need to be demonstrated for each one in order to reach market approval.

Future studies as a follow up to this work should include further developing strategies to treat established biofilm infections. Successful eradication of bacteria growing in an established biofilm may require further controlling the lysostaphin release rate through modification of the hydrogel material properties. It is likely that lysostaphin-delivering hydrogels degrade faster when implanted to established infection sites due to the body's response to bacteria recruiting inflammatory cells, leading to higher protease levels and faster hydrogel degradation (*169*). Synthesizing hydrogels with a higher cross-

link density, or utilizing cross-linking peptides that are less sensitive to proteolytic cleavage would be one way to extend lysostaphin release. This could also be accomplished by engineering a free cysteine residue into lysostaphin, allowing for covalent incorporation into the hydrogel. We have shown that encapsulation of lysostaphin within the hydrogel improves enzyme stability. A combination of stable lysostaphin and a slower release rate may further increase the time bactericidal concentrations of lysostaphin are in contact with the biofilm.

Optimization of the antibiotic regimen may also be critical to eliminating established infections. Lysostaphin and oxacillin cannot cross mammalian cell membranes and are therefore not effective at killing intracellular bacteria. The addition of antibiotic adjuvants such as rifampin, which is highly active against both intracellular bacteria and bacteria growing in biofilm, may be critical to achieve total infection clearance (*250*, *251*).

The extension of the femur fracture model to include an established biofilm infection will also be important to more fully evaluate the translational potential of lysostaphin-delivering hydrogel therapy. Currently, only one mouse model of an established femur infection has been published (*53*). The authors stabilize the femur using a fixation plate and then perform a small osteotomy to create a defect. Upon revision, the osteotomy is expanded allowing for necrotic bone to be removed. A similar approach may be ideal to further test lysostaphin-delivering hydrogels, since the infection would be more localized to the injury site and in direct contact with an *in situ* polymerized hydrogel. A similar approach could be used for either the radial segmental defect model or the femur fracture model.

Recently, there has been increasing interest in the immune response to infection (*252*). Using the mouse radial segmental defect infection model, we characterized the immune cells involved in the local inflammatory response to infection. Extending our

immune cell analysis to established infections treated with lysostaphin-delivering hydrogels may offer insight into how the host response to infection affects bacterial clearance, as our current results have shown significant variability in the animal's ability to clear bacteria. Chronic *S. aureus* infection can lead to a suppressed immune response to the infection (*252, 253*). It would be interesting to test if similar immunomodulatory effects are occurring, and if lysostaphin-delivering hydrogel therapy alters the immune response in an established infection setting.

This work was focused on treating *S. aureus* infections. However, *S. epidermidis* plays an equally important role in orthopaedic infections (*2*). We have shown that lysostaphin-delivering hydrogels are effective at killing *S. epidermidis in vitro*, but did not validate these results *in vivo.* The models developed and described herein should be extended to *S. epidermidis* strains. *S. epidermidis* orthopaedic hardware infections typically include a biofilm component, as biofilm formation is the primary virulence factor (*254*). We have shown lysostaphin-delivering hydrogels are efficacious in reducing *in vivo* established *S. aureus* biofilm infections. This strategy should be testes using established *S. epidermidis* biofilms as well.

Staphylococcal species account for roughly two thirds of all orthopaedic infections (*35*). Therefore, lysostaphin-delivering hydrogels will need to be expanded to target other organisms. Bacteriophage lysins are another type of bacteriolytic enzyme currently under development (*71*). Lysins that specifically target non-staphylococcal bacteria have been identified, which may make them good candidates to expand the target range of lysostaphin-delivering hydrogels, making them a more effective prophylactic therapy.

Overall, these studies begin to address the major unmet clinical need of preventing and treating *S. aureus* orthopaedic hardware associated infections, which will only worsen with the continued emergence of antibiotic-resistant bacteria. Lysostaphin kills bacteria

using mechanisms separate to those of small molecule antibiotics, making it effective against antibiotic-resistant strains. These data show our simple, injectable, biomaterial based delivery carrier outperforms systemic antibiotic therapy and restores a local pro-healing inflammatory environment. Overall, we have engineered and characterized lysostaphin-delivering hydrogels to treat *S. aureus* infections while simultaneously repairing bone fractures and defects in small animal models of orthopaedic implant infections.

APPENDIX A. PUBLICATIONS

6.1 Johnson CT and García AJ. Scaffold-based Anti-infection Strategies in Bone Repair. *Annals of Biomedical Engineering.* 2015 Mar;43(3):515-28. DOI: 10.1007/s10439-014-1205-3

Annals of Biomedical Engineering, Vol. 43, No. 3, March 2015 *(© 2014)* pp. 515–528
DOI: 10.1007/s10439-014-1205-3

BMES BIOMEDICAL ENGINEERING SOCIETY™ www.bmes.org

Scaffold-based Anti-infection Strategies in Bone Repair

CHRISTOPHER T. JOHNSON[1,2,3] and ANDRÉS J. GARCÍA[1,4]

[1]Petit Institute for Bioengineering and Bioscience, Georgia Institute of Technology, Atlanta, GA, USA; [2]Coulter Department of Biomedical Engineering, Georgia Institute of Technology and Emory University, Atlanta, GA, USA; [3]School of Medicine, Emory University, Atlanta, GA, USA; and [4]Woodruff School of Mechanical Engineering, Georgia Institute of Technology, Atlanta, GA, USA

(Received 15 July 2014; accepted 26 November 2014; published online 5 December 2014)

Associate Editor Fei Wang oversaw the review of this article.

Abstract—Bone fractures and non-union defects often require surgical intervention where biomaterials are used to correct the defect, and approximately 10% of these procedures are compromised by bacterial infection. Currently, treatment options are limited to sustained, high doses of antibiotics and surgical debridement of affected tissue, leaving a significant, unmet need for the development of therapies to combat device-associated biofilm and infections. Engineering implants to prevent infection is a desirable material characteristic. Tissue engineered scaffolds for bone repair provide a means to both regenerate bone and serve as a base for adding antimicrobial agents. Incorporating anti-infection properties into regenerative medicine therapies could improve clinical outcomes and reduce the morbidity and mortality associated with biomaterial implant-associated infections. This review focuses on current animal models and technologies available to assess bone repair in the context of infection, antimicrobial agents to fight infection, the current state of antimicrobial scaffolds, and future directions in the field.

Keywords—Biomaterial, Scaffold, Bone repair, Regeneration, Infection.

Implant-associated infection is a significant clinical problem.[23] Bacterial colonization of implants is associated with surgical sites, central line access points, ventilators, surgical drains and shunts, urinary and central venous catheters, and others. Current strategies used to prevent such infections include, but are not limited to, antibiotic therapy, healthcare-provider hygiene, environmental controls such as isolation or negative pressure rooms, surface coatings and modifications, sterilization, and the use of sterile technique during procedures. Nearly all types of bacteria and fungi are capable of infecting implanted devices.[23] Some of the most common pathogens include *Staphylococcus aureus*, *Staphylococcus epidermis*, *Pseudomonas aeruginosa, Propionibacterium acnes*, beta-hemolytic *Streptococcus*, *Proteus mirabilis*, and *Escherichia coli*.[37,77] The development of biomaterials with antimicrobial properties to prevent device-associated infection is a rapidly expanding field.

Address correspondence to Andrés J. García, Petit Institute for Bioengineering and Bioscience, Georgia Institute of Technology, Atlanta, GA, USA. Electronic mail: andres.garcia@me.gatech.edu

DEVICE-ASSOCIATED INFECTIONS IN BONE RECONSTRUCTION

In the field of orthopedics alone, 2–5% of all procedures involving implants are complicated by infection.[23] This number can be as high as 30% when open fractures are present.[93] Significant morbidity and even death are associated with implant-related infections, with outcomes often leading to complete implant removal, surgical debridement of the affected tissue, and long-term antibiotic therapy.[55,56] Device-associated infections not only occur from direct implantation of bacteria, but also develop post-operatively following hematogenous bacteremia, or direct spreading from a nearby infection site.[55,56] Further complicating treatment is the emergence of antibiotic-resistant bacteria.[34] Choosing the correct antibiotic for initial treatment is directly correlated with successful infection management and becomes more difficult in the case of nosocomial infections, due to the inherent resistance that these organisms possess.[75] The above circumstances motivate the development of implantable materials with antibacterial properties to significantly improve surgical outcomes and reduced patient morbidity and mortality. Engineered scaffolds for regenerative medicine applications provide a framework for tissue repair as well as a substrate for the inclusion of antimicrobial properties.

BIOFILM AND NONUNION DEFECTS

Device-associated infection is characterized by bacterial adhesion, colonization, and biofilm development, which is outlined in Fig. 1.[9,94] The most common organisms associated with orthopedic implant infections include the gram positive strains *Staphylococcus epidermis*, *Staphylococcus aureus*, and *Propionibacterium acnes*, as well as the gram negative *Pseudomonas aeruginosa*.[94] Osteomyelitis is inflammation of the bone, which can be due to biofilm formation, causing increased bone resorption and reactive bone formation.[55,56] These biofilms are composed of secreted bacterial components, such as protein, lipid, lipopolysaccharide, and DNA,[9] forming a matrix around the bacteria that provides protection from antibiotic therapy and immune defenses.[21,57] Bacteria in a biofilm have higher mutation rates,[30] and can display increased virulence[73] than if growing planktonically. When exposed to antibiotics, mutation rates increase further, allowing for accelerated development of a drug-resistant phenotype.[64] Moreover, incomplete resolution following therapy leads to highly resistant cells, or persistors, that then replenish the biofilm.[58] These characteristics paired with availability of only semi-effective treatment options leave a significant, unmet need for the development of therapies to combat device-associated biofilm and infection.[9,63]

Non-union bone defects are fracture injuries that cannot heal without intervention. Currently, standard medical therapies include the use of bone auto- and allografts, or delivering high doses of therapeutic protein, such as bone morphogenetic protein 2 (BMP-2), to facilitate healing. However, there are unacceptably high failure and complication rates associated with these interventions,[25] which are significantly increased when an infection develops.[47,60,66] Advances in biomaterials and regenerative therapies have led to the development of engineered scaffolds capable of correcting non-union defects without the need for bone grafting procedures.[27] These strategies for bone repair often rely on biomaterial-based scaffolds to bridge the defect. This provides a convenient framework to introduce antibacterial agents to prevent and treat infection after surgical intervention.

Engineering regenerative medicine implants to overcome bacterial contamination is a critical and emerging area of biomaterials research. These technologies require rigorous *in vitro* and *in vivo* evaluation, bringing together the fields of microbiology and biomaterials engineering. Significant progress has been made in the design of infection-resistant surfaces, as recently reviewed by Campoccia *et al.*[14,15] Therefore this review will focus on relevant animal models and techniques to assess antimicrobial tissue scaffolds in the context of bone repair, potential therapeutic additives to fight infection, and the current and future of scaffolds with infection resistant properties to promote bone repair.

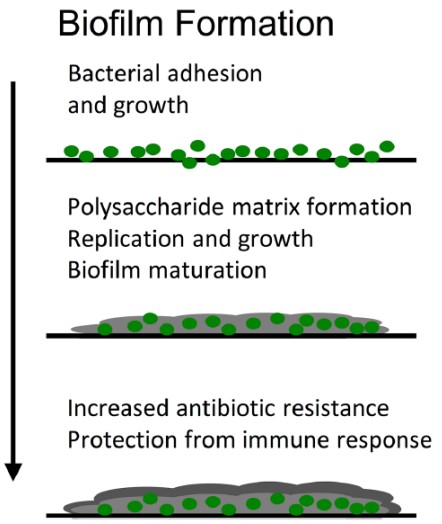

FIGURE 1. Bacterial adhesion and biofilm development. Biofilm formation begins by bacteria adhering and growing on a surface. As the pathogen continues to replicate, a polysaccharide matrix is deposited. This matrix protects the pathogen from the host immune system and increases the development of antibiotic resistance.

ANIMAL MODELS TO ASSESS INFECTION AND BONE REPAIR

Successful evaluation of antimicrobial scaffolds for bone regeneration requires the development of reliable and robust infection models. This proves to be a very challenging task, as pathogenic bacteria are required to induce the infection without causing overly adverse harm to the host. Furthermore, the model should provide a sustained infection over a prolonged period of time to have increased relevance to human health. Several animal models to assess fracture therapy exist, and appropriate model selection was discussed in depth by Mills and Simpson.[69] Bone regeneration is most frequently evaluated using critical-sized, segmental defect models. Critical-sized segmental defects are bone injuries that do not spontaneously heal, allowing for assessment of bone regeneration due to the therapy, such as implantation of a scaffold.

Few validated models exist to evaluate bone regeneration in infected defects. These models introduce

TABLE 1. Infection-based segmental defect models.

Ref.	Animal	Procedure	Advantages	Disadvantages
17–20,103	Rat	Femoral segmental defect, debridement following 2 weeks later	Evaluates long weight bearing bone, widely validated, not self healing	Failure if infection extends to fixation pins, two surgical procedures required
74,103	Rat	Femoral segmental defect, contaminated scaffold	Evaluates long weight bearing bone, widely validated, not self healing, single operation	Failure if infection extends to fixation pins, complicated procedure
88	Rabbit	Femoral segmental defect	Evaluates long weight bearing bone, not self healing	Failure if infection extends to fixation pins
8	Rabbit	Radial segmental defect	No fixation device required, evaluates long bone, not self healing, single procedure, simulates intraoperative contamination	Non-weight bearing bone

infection to bone repair models. Table 1 summarizes validated models developed to characterize the efficacy of antimicrobial bone repair scaffolds. The most common repair model extends the rat femoral segmental defect[102] to include pathogenic bacteria.[17] Femoral segmental defects have been widely used in regenerative medicine studies, and allow for the evaluation of a long, weight-bearing bone, that will not spontaneously heal. This procedure requires bone fixation hardware and effectively tests the reparative capacity of regenerative scaffolds. To introduce infection, two distinct inoculation techniques exist. In one, a segment of the femur is excised, the bone is stabilized, bacteria is introduced, and the surgical site is closed. Once enough time has elapsed for the infection to become established, reoperation occurs, the infected tissue is debrided, and a sterile regenerative scaffold is placed.[17] This method has been used to evaluate osteogenic protein-1[17] as well as systemic antibiotic therapy paired with recombinant human BMP-2[8] and recombinant human osteogenic protein-1[9] in the presence of infection. This technique provides clinical relevance, as it mimics how implant infections are treated, but two surgical procedures may increase variability and add more stress to the animal. The second approach requires a single procedure, where the defect is created and stabilized and the implant is placed. Following implant placement, the pathogen is injected into the implant (or the implant is inoculated prior to implantation), simulating intraoperative contamination.[103] This technique is advantageous because it only requires a single procedure, which may reduce variability associated with surgery. This model was later adapted to realize a 50% overall infection rate in order to reduce the chances of observing false-negative (type II error) *in vivo* results.[74] An infected femoral segmental defect model in the rabbit has also been reported where infection was induced 48 h after bone excision and defect stabilization by a percutaneous injection of a bacterial suspension.[88] These models provide an economical way to assess bone-healing strategies, but are complicated by requiring defect fixation with plates and wires. Stabilization can pose a problem when assessing the antimicrobial abilities of regenerative scaffolds if the stabilization pins become infected and cause failure.[17]

Self-stabilizing segmental defects could be a means to avoid complications associated with infected stabilization hardware. Self-stabilization is achieved by removing a segment of a non-weight bearing bone, such as the radius. This allows for the study of regenerative implants in critically sized defects of long bones that will not self-heal, but may not be as clinically relevant since many orthopedic procedures require fixation of long bones. Bi *et al.* developed a lapine radial segmental defect infection model to assess localized antibiotic release compared to systemic therapy.[8] In this model, a defect was created and a bacterial suspension was placed in the wound. After 30 min, the area was washed, the implant was placed and the wound was closed. This model only requires a single procedure and also simulates intraoperative contamination. Although several different animal models have been developed to assess bone repair, to our knowledge a validated murine model has not yet been published, even though murine models have been used extensively throughout the osteomyelitis literature.[78]

The advent of *in vivo* imaging systems has significantly improved the analysis of biomaterial-associated infections.[87] Genetic engineering of bioluminescence genes into clinically relevant bacterial strains allows for *in vivo* monitoring of infection. Commercially available gram positive (Xen29 *S. aureus*) and gram negative (Xen5 *P. aeruginosa*) strains contain a stable luminescence reporter, and can be tracked over time *in vivo*, providing the assessment of infection progression,[48] and treatment efficacy.[49] However, limitations do exist.

For example, the luminescence signal detected is not a direct marker of the number of bacteria, but of the metabolic activity of the colony.[32,48,49] The population of bacteria making up a biofilm is composed of both rapidly dividing and quiescent cells. This heterogeneity may be a possible explanation for the large variability between bacterial counts and bioluminescent signal. The use of bioluminescent bacteria has been successfully established *in vivo* in the context of osteomyelitis,[36,42] suggesting that this technology could be adaptable to monitoring scaffold-associated infections in bone repair. Nevertheless, genetic modification of bacteria through bioluminescent gene insertion could reduce the virulence of the clinically isolated strains, which could complicate the evaluation of infection resistant materials.

In addition to bioluminescent bacteria, several *in vivo* probes utilizing fluorescent, magnetic, and radioactive tracers have been developed. Near infrared (near-IR) imaging probes that specifically identify bacteria have received heightened interest as a viable alternative to luminescent bacteria. Discrimination between infection and inflammation is the key challenge associated with their development.[31] Eggleston and Panizzi provide an extensive review on this topic.[31] Our lab has recently developed near-IR probes that specifically discriminate between infection and inflammation through targeting the products produced by the inflammatory response.[91] Reactive oxygen species (ROS) are characteristic of the body's response to biomaterials implants, whereas large quantities of nitric oxide (NO) are produced by macrophages and neutrophils in a direct response to bacteria. Dual administration of ROS- and NO-selective probes allows for the simultaneous *in vivo* observation of infection and inflammation with high specificity.[91] Furthermore, we have shown these fluorescent probes exhibit increased sensitivity compared to bioluminescent strains. Fluorescent probes also have a dose dependent response to the number of bacteria regardless of metabolic activity, in a strain independent manner.[28] Other strategies to achieve specificity include utilizing antimicrobial peptides that have been labeled with radioactive isotopes and paired with clinically available imaging systems, such as single photon emission computed tomography (SPECT),[12] and labeling the antibiotic vancomycin with a near-IR fluorophore to identify gram positive infections.[96] The technologies described above provide a real-time, *in vivo* means to monitor infection initiation, progression, and resolution, and could provide an indispensable tool in the development of infection-resistant scaffolds.

Although significant effort has been made to develop finely tuned animal models for the assessment of antibacterial material properties as described above, ethical concerns do exist surrounding these methods. This is especially relevant when evaluating infection resistant properties of scaffolds after a sterile implantation, which is the most clinically realistic scenario. These types of studies require large animal numbers to adequately power the analysis, due to the relatively low rates of spontaneous infection developing (less than 7%) and that both the control and treatment groups will require large animal numbers to resolve a difference.[54] Concerns also exist surrounding animal welfare. Many infection models are highly variable and it can be challenging defining a sub-lethal bacterial dose that does not cause animal suffering. This is particularly difficult, as simply increasing the bacterial dose could result in sepsis and termination before the desired experimental end point.

ANTIMICROBIAL AGENTS TO FIGHT INFECTION

Several different strategies exist to combat bacterial infection. Table 2 provides a list of major antimicrobial strategies.[2,24,39,40,67] Brief overviews of the major antibacterial classes, including the advantages and limitations of each follow.

Clinically, antibiotics are the most common agents used to clear bacterial infections. They are widely used throughout clinical medicine as treatment and prophylaxis. However, over the past decades, the emergence of antibiotic-resistant bacteria, such as methicillin resistant *Staphylococcus aureus* (MRSA), have become more common.[24] Sub-inhibitory aminoglycoside antibiotic treatment can induce biofilm formation.[41] The development of biofilm can potentiate the emergence of resistant cells, further complicating the infection.[89] Biofilm requires higher doses and longer trials of therapy to eradicate infection, thereby prolonging the patient's exposure to drug side effects. Moreover, it has been shown that bactericidal antibiotics are toxic to mammalian cells, causing mitochondrial dysfunction.[50] However, the benefits of treatment far outweigh the risks, and until viable alternatives are available, antibiotics will remain the standard of care. For a comprehensive review of antibiotic therapy including drug mechanisms, specificities, and the development of resistance, refer to Davies and Davies.[24]

Silver is a broad-spectrum antimicrobial agent used clinically, and in research. Silver exerts bactericidal activity on both gram positives and gram negatives through several mechanisms. Silver ions enter the bacterium and generate ROS capable of damaging DNA, they interact with membrane proteins affecting their function, and alter membrane permeability lead-

TABLE 2. Review articles detailing various antimicrobial strategies.

Ref.	Antimicrobial	Topics covered
4	Antibiotics	Mechanisms of action, and how resistance has emerged
67	Silver	Antimicrobial properties of silver nanomaterials and effects on human health and the environment
2	Host defense peptides	Host defense peptides as therapeutics for antibiotic resistant infections
40	Host defense peptides	Immunomodulatory aspects of host defense peptides
39	Bacteriophage	Bacteriophages and how they can be used to treat infection

ing to cell death.[67] It is believed that silver resistance is widespread, but not realized since it is not widely tested for. A Chicago hospital revealed that over 10% of enteric bacteria exhibit silver resistance,[86] and overuse could potentiate the problem. Furthermore, the bactericidal mechanisms of silver ions are not specific to bacterial cells, and also disrupt mammalian cell function placing significant concern on toxicity.[5,10] However, it has been reported that silver can be effective against antibiotic-resistant bacterial strains, and even induce susceptibility towards antibiotics that were ineffective in the absence of silver.[71] Silver can also be adapted to reduce bacterial adherence to orthopedic implants by killing adherent pathogens.[95] For a more detailed discussion, the reader is referred to Marambio-Jones and Hoek.[67] Clinically, silver has translated to several applications, including wound dressings, creams, urinary catheters and endotracheal tubes. However, little if any data has demonstrated efficacy. An analysis of 2066 patients enrolled in several clinical trials failed to show any benefits to silver-doped wound dressings.[90] Silver-coated endotracheal tubes[53] have exhibited modest efficacy in preventing bacterial colonization, whereas silver-coated urinary catheters have shown mixed results.[6]

Host defense peptides or antimicrobial peptides (AMPs) have activity against bacteria, viruses, and fungi.[45] Defensins, cathelicidins and histatins are AMPs produced by many mammalian cells.[26] AMPs are amphiphilic peptides characterized by a several cationic and hydrophobic residues and exhibit broad-spectrum activity against both gram positive and gram negative bacteria.[26,40,45] The cationic residues associate with the negatively charged bacterial membrane. The hydrophobic and hydrophilic residues cause membrane penetration, leading to instability, pore formation, osmotic changes, and bacterial lysis.[45] As with all antimicrobial strategies, the development of resistance is a concern. This could be especially problematic since AMPs are part of the natural host response to pathogens and resistance could make simple infections dangerous.[2,72] Another drawback is the observation that AMPs are not stable over long periods of time in an *in vivo* environment. However, AMPs are easily engineered, and several synthetic peptides have been developed in an attempt to overcome these shortcomings.[11] It has been well documented that AMPs possess immunomodulatory activity in addition to being antipathogenic.[26,40,45] AMPs modulate both the innate and adaptive immune responses to control infection and stimulate regenerative processes.[40] These attributes make AMPs an enticing candidate for antimicrobial regenerative scaffolds. However, there are no reports of human safety or efficacy trials for AMPs.

Bacteriophage therapy has gained renewed interest with the increased prevalence of antibiotic resistance.[62] Bacteriophages are viruses that specifically infect bacteria. The phage binds to a membrane receptor, introducing phage DNA into the cell. This DNA is replicated and translated by the host bacterium, leading to phage replication, progeny assembly, bacterial lysis, release of progeny, and phage propagation to surviving bacteria. Following eradication of the infecting organism, phage replication ceases, allowing for resolution of the affected tissue. Bacteriophage DNA can also code for lysins, lytic enzymes that destroy the bacterial cell wall,[84] as well as polysaccharide depolymerases, enzymes that break down the biofilm matrix created by bacteria.[44,61] This allows bacteriophages to disperse biofilm as well as eradicate infection. In addition, synergism between phage therapy and antibiotics has been demonstrated.[81] Host bacterial strains can develop resistance to phage infection, which can be reduced using several different phages at once.[35] There are also concerns surrounding the immunogenicity of *in vivo* phage administration, even though adverse events have not been reported in the literature.[4,70] Currently, the safety of bacteriophage therapy administered orally[13] and cutaneously[79] has been evaluated in humans in phase I clinical trials. Preliminary results of the first controlled trial to evaluate bacteriophage efficacy in chronic otitis to treat antibiotic-resistant *P. aeruginosa* have been positive, demonstrating therapeutic value in humans.[99]

ANTIMICROBIAL SCAFFOLDS FOR BONE REPAIR

Recently, tissue engineered scaffolds for bone repair have started to include antimicrobial agents to prevent or fight infection. These scaffolds provide a substrate

for sustained, localized drug release, tunable degradation properties to promote tissue integration, and support for cell delivery. Rigorous evaluation of the antimicrobial efficacy exhibited by these scaffolds has proven difficult, and requires expertise in both microbiology techniques as well as biomaterials engineering. Antimicrobial scaffolds are required to be toxic to bacterial cells, while promoting local tissue regeneration and minimizing the adverse inflammatory events. Figure 2 is a schematic diagram illustrating how engineering antimicrobial properties into scaffolds for bone repair can improve outcomes associated with bacterial infection. Bacterial contamination is introduced into a model used to evaluate regenerative implants. If the contaminate is not cleared by the immune system or an infection-resistant scaffold, the infection becomes established, which may lead to the development of osteomyelitis. Infection fighting scaffolds can be implanted into defects with ongoing infection or osteomyelitis to remove the existing pathogen and facilitate repair. Further development of these technologies will allow for bone repair to occur in both sterile and contaminated conditions.

Antibiotic-Releasing Scaffolds

Antibiotic delivery scaffolds are the most well developed area in the literature. In orthopedics, antibiotic-loaded fillers and bone cements have been used clinically for a number of years. Zilberman and Elsner published an extensive review on antibiotic-releasing materials.[104] We will focus on advances in tissue engineering scaffolds that incorporate antibiotics.

Scaffolds provide an ideal substrate to deliver long-term bactericidal doses of antibiotics to the injury site. This is accomplished by modifying drug release characteristics through encapsulation within degradable matrices. Antibiotic releasing matrices have been used as coatings for orthopedic implants prone to infection. Sol–gel thin films have been engineered to provide sustained release of vancomycin and protect against implant associated infection of titanium rods. The addition of the thin film minimized bacterial adherence to the implant, and protected against the development of osteomyelitis *in vivo*.[1] A similar has also been applied to stainless steel K-wires.[7]

Antimicrobial activity can also be engineered into scaffolds for tissue regeneration. Poly (L-lactic acid) (PLLA) nanofiber scaffolds were synthesized with poly (lactic-co-glycolic acid) (PLGA) nanospheres to provide extended release of the antibiotic doxycycline.[33] These scaffolds provided sustained antimicrobial activity against *S. aureus* and *E. coli* over 42 days in bacterial culture, demonstrating an approach to provide extended, localized antibiotic release, which would reduce the systemic side effects associated with antibiotic therapy. This is especially important when treating osteomyelitis, which typically involves extended courses of high dose antibiotics. Poly(caprolactone) (PCL) scaffolds were synthesized by electrospinning PCL using 10 and 20% (w/w) rifampin.[80] These scaffolds exhibited extended rifampin release over 8 h and were bactericidal towards *S. epidermis* and *P. aeruginosa in vitro*. Shi *et al.* demonstrated the addition of lecithin can increase the encapsulation efficiency of gentamicin and protein into PLGA microsphere-based scaffolds.[85] After an initial burst release, gentamicin release occurred for 60 days, and protein was released for 18 days. The material was active against *E. coli* while still supporting mesenchymal stem cell (MSC) viability, proliferation, and mineralization. These observations suggest that this scaffold is a viable candidate for delivering protein therapeutics as well as antibiotics, and supporting bone

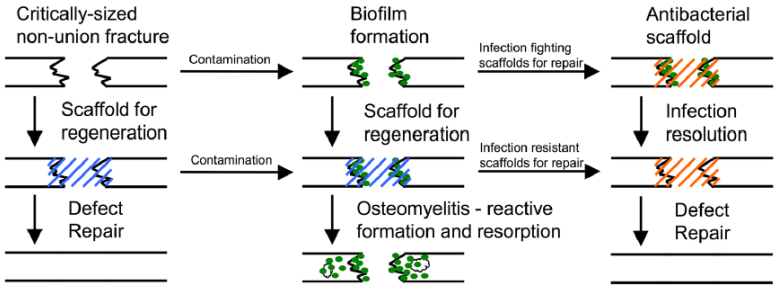

FIGURE 2. Critically-sized non-union bone defects are used to assess the therapeutic efficacy of regenerative scaffolds. Contamination of these defects can be introduced before or after the scaffold is placed to establish the infection. Absence of antimicrobial agents will lead to the development of osteomyelitis, which is characterized by bone resorption and reactive bone formation. Infection resistant scaffolds are designed to prevent initial bacterial colonization whereas infection fighting scaffolds can be used to resolve an established biofilm and promote defect repair.

formation for the treatment of infected bone defects. The encapsulation of growth factors has also been paired with antibiotic encapsulation. Calcium sulfate scaffolds with chitosan microspheres containing vancomycin, recombinant human BMP-2 (rhBMP-2), or both were developed and assessed *in vitro* for bactericidal activity and regenerative properties.[29] It was shown that these scaffolds are bactericidal against *S. aureus* for 18 days and release rhBMP-2 over 6 weeks, causing increased alkaline phosphatase (a marker of osteoblast differentiation) expression. These investigators found that an optimal balance between antibiotic and growth factor release is required for optimal osteoblastic differentiation, as high antibiotic concentrations can lead to inhibition of osteoblastic differentiation. However, these techniques have not yet been extended to *in vivo* models.

As mentioned above, the current standard of care for critically sized bone defects is bone grafting. Infection is one of the most significant side effects associated with grafting procedures. Bi *et al.* engineered bone xenografts (grafts from a different animal species) composed of antigen-free calf cancellous bone combined with calf cortical bone extract and bovine BMP impregnated with clindamycin to treat critically sized defects contaminated with *S. aureus*.[8] This scaffold was evaluated *in vivo* within a rabbit radial segmental defect. After the graft was implanted, 1×10^6 colony forming units (CFU) of *S. aureus* were administered to the injury. All animals in the clindamycin-impregnated graft group healed completely. Defect repair was observed in the clindamycin-graft group including recanalization of the medullary cavity. Systemic clindamycin therapy resulted in either nonunion, or delayed union after the 16 week period, whereas the non-treatment control developed osteomyelitis characterized by reactive bone formation and resorption. This study shows that local, sustained delivery of antibiotics can overcome an infection, while still providing regenerative properties.

The bone graft substitute calcium sulfate has also been combined with antibiotics and assessed *in vivo*. The antibiotic moxifloxacin has been evaluated with commercially available Stimulan®, a synthetic semihydrate form of calcium sulfate.[51] In this study, osteomyelitis was induced in a rabbit tibia by injection of 2×10^7 CFU of a clinical osteomyelitis isolate of MRSA into the intramedullary cavity. After the infection was allowed to develop for 3 weeks, the rabbits underwent surgical debridement of all necrotic bone tissue and implant placement. The results showed a significant reduction in viable bacteria throughout the 6 week observation period. *In vitro* assessment of the delivery system showed sustained moxifloxacin release over 35 days. However, this study did not evaluate whether the regenerative properties of the moxifoxacin doped Stimulan® are still intact in the presence of sustained antibiotic release. Xie *et al.* compared bioactive borate glass to the clinically used calcium sulfate as a carrier for vacomycin to treat MRSA-induced osteomyelitis in rabbits.[101] Bioactive borate glass provided sustained vancomycin release over 28 days *in vitro* and improved mechanical properties compared to calcium sulfate. The scaffold was assessed *in vivo* using a rabbit model for osteomyelitis. After 3 weeks of infection, surgical debridement was performed and scaffolds were placed within the defect. Both the vancomycin-loaded calcium sulfate and vancomycin-loaded borate glass significantly reduced the number of bacteria, improved the radiographic score and improved the histopathologic score at the end of the eight-week observation period. This study further illustrates that scaffolds serve as an effective mechanism to provide sustained antibiotic therapy to eradicate osteomyelitis.

Polyurethane scaffolds have also received interest as a substrate to deliver antibiotics and growth factors for bone repair. Polyurethane scaffolds designed for prolonged release of vancomycin were compared to the clinically used vancomycin-loaded PMMA- beads.[59] Extended vancomycin release from polyurethane scaffolds could be controlled by changing the solubility of vancomycin. *In vivo* evaluation of the vancomycin-loaded polyurethane scaffolds in a contaminated rat femoral segmental defect reduced viable bacterial counts as well as the clinical standard of vancomycin-loaded PMMA beads. Importantly, nearly 10 times less antibiotic was loaded to the polyurethane scaffolds. Dual delivery of vancomycin and the growth factor BMP-2 to a *S. aureus* infected rat femoral segmental defect using a biodegradable polyurethane scaffold demonstrated increased bone formation as determined by microCT and histological analysis.[38] The addition of vancomycin to the scaffold reduced the clinical signs of infection while not affecting bone regeneration. Together, these studies illustrate that extended release of vancomycin can eradicate infection and the addition of BMP-2 can enhance regeneration in contaminated defects.

Clearly there has been significant progress towards the development of antibiotic releasing materials for bone repair. However, as mentioned before, biofilm can offer protection to the microorganisms against antibiotic therapy, leading to the development of resistance. In a study evaluating the efficacy of gentamicin-loaded bone cement against the well-known biofilm former *S. epidermis* in rats, it was shown that even though the number of bacteria was reduced, there was a significant increase in the number of gentamicin-resistant bacteria.[92] In another study evaluating van-

comycin-releasing polyurethane scaffolds in an infected rat segmental defect, significantly fewer bacteria were recovered at 2 weeks.[99] Nonetheless, this was only a roughly three-fold reduction, leaving over 1×10^5 CFU/g of bone tissue, demonstrating a significant limitation in effectively treating infections.

Silver-Presenting Scaffolds

Silver can be easily incorporated into materials through various manufacturing techniques such as reduction or the addition of silver nanoparticles. This ease of incorporation combined with silver's broad spectrum antimicrobial activity has led to the development of several silver-containing antimicrobial scaffolds. Several designs have demonstrated *in vitro* efficacy, but success *in vivo* has been limited.

Naturally derived tissue engineered scaffolds have been used for a multitude of applications, including bone repair. These materials can be modified to present silver and exhibit infection resistance. Collagen scaffolds were fabricated to include silver nanoparticles coated with poly(ethylene glycol) (PEG) and Triton X-100.[65] The scaffolds had increased elasticity and antimicrobial effects against both gram positives (*B. cereus* and *S. aureus*) and gram negatives (*E. coli* and *P. mirabilis*). Silver nanoparticles have also been incorporated into type I collagen scaffolds synthesized using UV initiation of a non-toxic, water-soluble benzoin to facilitate polymerization.[3] The collagen scaffolds served to stabilize the nanoparticles and supported fibroblast and keratinocyte viability at silver concentrations less than or equal to 100 μM. Bactericidal activity (*E. coli*, *B. megaterium* and *S. epidermis*) was determined using a modified minimum inhibitory concentration assay. These studies show that collagen-based scaffolds that include silver nanoparticles can prevent bacterial growth *in vitro*, while also supporting mammalian cell viability. Further development of these technologies and evaluation in *in vivo* models is necessary to establish the feasibility of silver nanoparticle-containing collagen scaffolds for infection prevention and bone repair. Bioactive glass containing silver has been incorporated into extracellular matrix-derived hydrogels to exhibit sustained antimicrobial effects and bone regenerative properites.[16] These materials show sustained silver ion release over 25 days and is bactericidal against *E. coli* and *E. faecalis*. The composite hydrogels support dental pulp cell viability, making them a plausible candidate for tooth or bone regeneration. Silver ions have been added to composite chitosan/nano-hydroxyapatite scaffolds to add antimicrobial properties.[83] The chitosan/nano-hydroxyapatite scaffolds were immersed in silver nitrate, allowing for an ion-exchange and reduction to occur between the scaffold and silver. The scaffolds support osteoprogenitor and osteosarcoma cell viability and demonstrate antimicrobial effects against both gram positive and gram negative bacteria (*S. aureus* and *E. coli*).

PLGA has been of particular interest for bone repair due to its biocompatibility, degradable properties, and being used in FDA-approved devices. Silver was incorporated into tricalcium phosphate (TCP) nanocomposite, mixed with PLGA and then electrospun to form a fibrous scaffold. These scaffolds provided sustained silver release at bactericidal levels *in vitro* against *E. coli*, a frequent contaminator of dental implants. The scaffolds were equally as effective as the clinical standard of tetracycline-soaked cotton swabs. However, upon media exchange in the assay, the silver scaffolds maintained antimicrobial ability due to sustained release characteristics. This study demonstrates the importance of sustained antimicrobial release, and that scaffolds for tissue engineering provide a convenient avenue to accomplish this. Zheng *et al*. reported a promising antimicrobial regenerative scaffold.[103] In this study, microporous PLGA scaffolds were fabricated to contain silver nanoparticles. Interestingly, 1.0% silver containing grafts supported increased osteoblastic differentiation and increased alkaline phosphatase activity compared to the 2.0% silver grafts *in vitro*. These scaffolds were evaluated using a rat femoral segmental defect. After implantation, 1×10^8 CFUs of vancomycin-resistant MRSA was injected into the implant. Radiographic and histological analysis showed that the 2.0% silver implants completely eliminated infection and supported defect bridging, whereas the 1.0% silver implants only reduced the number of bacteria present, but supported some bone regeneration. Control scaffolds that did not contain silver were grossly infected, demonstrating bone resorption and reactive bone formation, indicative of osteomyelitis. The *in vitro* analysis paired with the *in vivo* data show that although high concentrations of silver can inhibit osteoblast differentiation, it is more important to eliminate the contaminating bacteria to facilitate bone formation. This is a clear demonstration that developing implants capable of resisting infection while providing functional cues to facilitate bone repair is possible.

As an alternative to silver, copper ions loaded into microporous bioactive glass scaffolds reduce bacterial growth and support MSC viability and differentiation.[100] These scaffolds significantly reduced *E. coli* growth, and promoted human MSC differentiation towards osteoblasts in a dose dependent manner. Vascular endothelial growth factor levels were also elevated, suggesting the scaffold could promote vascularization.

Antimicrobial Peptides, Bacteriophage, and Other Antimicrobial Strategies

Interest has been building surrounding technologies that take advantage of alternative antimicrobial therapies. These alternatives to silver and antibiotics could expand the arsenal against infection, while also reducing the chances of bacteria developing resistance to our most efficacious treatments. Scaffolds provide a means to extend the activity of these agents by providing sustained release characteristics. Antimicrobial peptides have been introduced into scaffolds designed for orthopedic regeneration. Poly(caprolactone) (PCL)-chitosan nanofiber scaffolds were synthesized and PEG-microgels containing the cationic antimicrobial peptide L5 were electrostatically associated with the nanofibers.[98] These novel scaffolds demonstrated antimicrobial activity against *S. epidermis*, and maintained L5 stability and activity. The scaffolds supported osteoblast adhesion, spreading, and proliferation.

Stainless steel K wires used in orthopedic procedures coated with a hydroxypropylmethlycellulose (HPMC) hydrogel containing bacteriophage, the antibiotic linezolid, or both were developed to prevent MRSA infection.[52] The coated wires showed sustained phage and linezolid release over several days, as well as inhibiting MRSA adherence in a dose dependent manner. The bacteriophage and linezolid group exhibited the greatest efficacy toward inhibiting MRSA attachment and growth, suggesting synergism exists between the co-delivery of antibiotics and bacteriophage. This claim was further supported by analysis of recovered MRSA after treatment showing reduced mutation rates in the dual treatment group suggesting lower drug resistance. This *in vitro* evaluation of scaffolds presenting bacteriophage and antibiotics suggests the treatment could be extended to an *in vivo* environment to prevent infection associated with stainless steel implants. Bacteriophage has also been evaluated in a regenerative context. In one study, the *E. coli* bacteriophage λ was loaded into microporous hydroxyapatite or beta-tricalcium phosphate scaffolds with various porosities by passive adsorption.[68] Bactericidal activity against *E. coli* K12 was observed *in vitro,* demonstrating the prophylactic potential bacteriophage loaded materials could provide.

Polyelectrolyte scaffolds assembled by electrostatic interactions of chitosan gamma-polyglutamic acid and carboxy-methylcellulose were developed for treating dental bone defects. These scaffolds supported pre-osteoblast cell adhesion and viability *in vitro*, and antimicrobial activity against *S. aureus* and *E. coli*. Scaffold biocompatibility was assessed by extracting the second pre-molars of beagle dogs and replacing them with the material. The scaffolds were explanted after 10 weeks and histology revealed no adverse foreign body reaction.

Neutrophils and macrophages produce peroxide and other free radicals to kill invading pathogens. This mechanism was extended to electrospun polycaprolactone (PCL) scaffolds with different concentrations of calcium peroxide to exhibit antimicrobial activity by releasing a significant initial burst of peroxide.[97] This short-term antimicrobial response was effective in controlling *E. coli* and *S. epidermis in vitro*, illustrating broad applicability. The nanowires supported osteoblast viability for 4 days of culture despite the cells being exposed to toxic peroxide levels for the first 24 h. This novel method of direct peroxide generation from a PLC scaffold shows that burst release from materials can be toxic to bacteria but still provide a means to promote bone growth.

Berberine is a natural antimicrobial agent that exhibits activity against several different organisms and is non-toxic to mammalian cells. For these reasons,

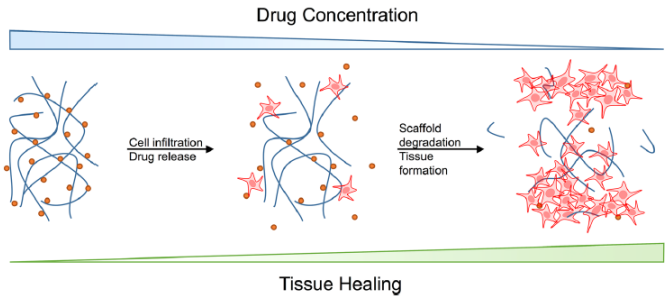

FIGURE 3. Scaffold based drug delivery for tissue repair. Current regenerative medicine strategies focus on delivering therapeutics to drive cell recruitment and tissue repair. As cells are recruited, the scaffold degrades, releasing therapeutics, and promoting integration. Next generation biomaterials will include abilities to prevent or eliminate pathogens and provide regenerative cues.

Huang *et al*. incorporated it into a chitosan coating on a nano-hydroxyapatite/polyamide66 scaffold developed for bone regeneration.[43] These scaffolds provided a continuous release of berberine over 150 h and were bactericidal to *S. aureus*. Furthermore, the scaffolds supported MG63 cell adhesion, proliferation, and spreading, supporting that berberine is nontoxic. However, this material has not been evaluated *in vivo*. These data provided preliminary evidence that berberine may be suitable for *in vivo* evaluation to provide antimicrobial and regenerative properties in a bone repair setting.

Preventing biofilm formation may be another way to protect against chronic osteomyelitis. Sanchez *et al*. demonstrated biofilm dispersal agents reduce infection *in vivo*.[82] A polyurethane scaffold containing D-amino acids was contaminated with *S. aureus* and implanted into a rat femoral segmental defect. The treated scaffolds significantly reduced the number of contaminating bacteria, showing that preventing biofilm formation can improve post-operative outcomes, by preventing the biofilm from shielding the bacteria from endogenous antimicrobial defenses.

CONCLUSIONS AND OUTLOOK

Preventing infection in the presence of biomaterials implants is a major unmet need and will significantly improve patient outcomes. Currently, implant infection leads to removal, and significant medical costs from reoperations and extended antibiotic therapy. Moreover, after an initial infection, patients are at a much higher risk for relapse, further complicating management and causing increased patient morbidity. As medicine advances, we have become more and more reliant on implantable devices to more effectively correct patient problems, which increases the risk of implant-associated infections.[23] Demand exists for the prevention of orthopedic implant infections due to the frequency of their occurrence, as well the challenges associated with combating osteomyelitis. Despite improvements in intraoperative techniques and the invention of antibiotic-doped cements and fillers, infection continues to be a significant issue associated with non-union defects. Furthermore, the increased prevalence of antibiotic resistant bacteria raises concern over widespread use of antibiotic presenting materials. This suggests alternative antimicrobials such as silver, antimicrobial peptides or bacteriophage could help to preserve the efficacy of our most potent weapons against infection. These alternative strategies to fight infection offer exciting opportunities to introduce new properties into scaffolds. For example, the rapid expansion, but self-limiting characteristics of a bacteriophage infection provide a way to engineer materials that respond only when a pathogen is present. Scaffolds can shield the phage from the host response, while providing activity only in the presence of offending bacteria. Antimicrobial peptides can enhance the body's defenses against pathogens, and even promote wound healing. Scaffolds can serve a means to extend the stability of these peptides and enhance their utility.

In addition to extending the stability of antimicrobial agents, scaffolds provide a highly controlled means to release therapeutics. Modulation of scaffold degradation typically correlates with therapeutic drug release. Traditionally, bone repair is driven by scaffold degradation leading to therapeutic release. The drug release recruits cells and further promotes scaffold degradation, leading to tissue healing. This process is outlined in Fig. 3. Degradable scaffolds are also advantageous from an *in vivo* infection resolution point of view. Implanted biomaterials are prone to infection after implantation by transient bacteremia causing colonization and direct bacterial spreading from infection sites.[55,56] Degradable scaffolds provide the benefit of controlled therapeutic release while facilitating integration into the native tissue.

Degradable scaffolds to treat infection and regenerate bone have been primarily investigated in the bioactive glass literature.[76] These studies are mostly centered on extending the release of antibiotics to provide continuous antimicrobial activity.[22,46,101] However, a significant gap exists in understanding how the degradation properties of scaffolds influence antimicrobial efficacy *in vivo*. Future studies could focus on optimizing scaffold degradation properties to efficiently eliminate pathogens and guide the bone repair process. These studies can then be extended to characterize and understand how engineering extended release of antimicrobial therapies affects drug activity though drug-scaffold interactions. However, modifications of scaffolds to provide continuous release may negatively impact the efficacy of the loaded therapeutic.

The next generation of antimicrobial scaffolds for bone repair will optimally balance antimicrobial delivery with regenerative therapeutics. This could be achieved by tuning material properties such as porosity, charge, degradation speed, density, antimicrobial agent, growth factors, and the bulk material. Understanding how material design choices prevent bacterial contamination, biofilm development, eradication of existing osteomyelitis, while simultaneously regenerating bone, will lead to optimized scaffold designs.

In order for these new technologies to translate into the clinic, several challenges need to be overcome. The

development of robust, controlled, and reproducible animal models of infected scaffolds is a critical need for the success of this fast emerging field. Animal models that utilize bioluminescent bacteria allow for real time monitoring of infection progression without animal sacrifice, which addresses some of the ethical concerns of biomaterial infection research. Reproducible, controlled infections that accurately simulates clinical scenarios are required to effectively evaluate experimental materials to prevent infection and facilitate bone regeneration.

Scaffolds provide an ideal substrate for designing regenerative therapies due to the exquisite engineering control we have over them. They provide a platform for controlled drug release, a substrate for therapeutic cell delivery, tunable degradation characteristics that facilitate replacement by regenerating tissue, reduced immunogenicity, and response to the surrounding environment. It is clear that progress is being made towards the development of infection-resistant bone repair implants. However, the *in vivo* validation of these technologies is still in its infancy. The advancement of *in vivo* imaging techniques, paired with robust bone repair models will facilitate the translation from the bench to the bedside.

ACKNOWLEDGMENTS

The authors gratefully acknowledge funding from the National Institutes of Health (R01 AR062920, R01 AR062368).

REFERENCES

[1]Adams, C. S., V. Antoci, Jr., G. Harrison, P. Patal, T. A. Freeman, I. M. Shapiro, J. Parvizi, N. J. Hickok, S. Radin, and P. Ducheyne. Controlled release of vancomycin from thin sol-gel films on implant surfaces successfully controls osteomyelitis. *J. Orthop. Res.* 27:701–709, 2009.

[2]Afacan, N. J., A. T. Yeung, O. M. Pena, and R. E. Hancock. Therapeutic potential of host defense peptides in antibiotic-resistant infections. *Curr. Pharm. Des.* 18:807–819, 2012.

[3]Alarcon, E. I., K. Udekwu, M. Skog, N. L. Pacioni, K. G. Stamplecoskie, M. Gonzalez-Bejar, N. Polisetti, A. Wickham, A. Richter-Dahlfors, M. Griffith, and J. C. Scaiano. The biocompatibility and antibacterial properties of collagen-stabilized, photochemically prepared silver nanoparticles. *Biomaterials* 33:4947–4956, 2012.

[4]Alemayehu, D., P. G. Casey, O. McAuliffe, C. M. Guinane, J. G. Martin, F. Shanahan, A. Coffey, R. P. Ross, and C. Hill. Bacteriophages phimr299-2 and phinh-4 can eliminate *Pseudomonas aeruginosa* in the murine lung and on cystic fibrosis lung airway cells. *MBio* 3:e00029–00012, 2012.

[5]AshaRani, P. V., G. Low Kah Mun, M. P. Hande, and S. Valiyaveettil. Cytotoxicity and genotoxicity of silver nanoparticles in human cells. *ACS Nano*. 3:279–290, 2009.

[6]Beattie, M., and J. Taylor. Silver alloy vs. uncoated urinary catheters: a systematic review of the literature. *J. Clin. Nurs*. 20:2098–2108, 2011.

[7]Bhattacharyya, S., A. Agrawal, C. Knabe, and P. Ducheyne. Sol–gel silica controlled release thin films for the inhibition of methicillin-resistant *Staphylococcus aureus*. *Biomaterials* 35:509–517, 2014.

[8]Bi, L., Y. Hu, H. Fan, G. Meng, J. Liu, D. Li, and R. Lv. Treatment of contaminated bone defects with clindamycin-reconstituted bone xenograft-composites. *J. Biomed. Mater. Res. B Appl. Biomater*. 82:418–427, 2007.

[9]Bjarnsholt, T., O. Ciofu, S. Molin, M. Givskov, and N. Hoiby. Applying insights from biofilm biology to drug development—can a new approach be developed? *Nat. Rev. Drug Discov*. 12:791–808, 2013.

[10]Braydich-Stolle, L., S. Hussain, J. J. Schlager, and M. C. Hofmann. In vitro cytotoxicity of nanoparticles in mammalian germline stem cells. *Toxicol. Sci*. 88:412–419, 2005.

[11]Brogden, N. K., and K. A. Brogden. Will new generations of modified antimicrobial peptides improve their potential as pharmaceuticals? *Int. J. Antimicrob. Agents* 38:217–225, 2011.

[12]Brouwer, C. P., L. Sarda-Mantel, A. Meulemans, D. Le Guludec, and M. M. Welling. The use of technetium-99 m radiolabeled human antimicrobial peptides for infection specific imaging. *Mini. Rev. Med. Chem*. 8:1039–1052, 2008.

[13]Bruttin, A., and H. Brussow. Human volunteers receiving escherichia coli phage t4 orally: a safety test of phage therapy. *Antimicrob. Agents Chemother*. 49:2874–2878, 2005.

[14]Campoccia, D., L. Montanaro, and C. R. Arciola. A review of the biomaterials technologies for infection-resistant surfaces. *Biomaterials* 34:8533–8554, 2013.

[15]Campoccia, D., L. Montanaro, and C. R. Arciola. A review of the clinical implications of anti-infective biomaterials and infection-resistant surfaces. *Biomaterials* 34:8018–8029, 2013.

[16]Chatzistavrou, X., J. C. Fenno, D. Faulk, S. Badylak, T. Kasuga, A. R. Boccaccini, and P. Papagerakis. Fabrication and characterization of bioactive and antibacterial composites for dental applications. *Acta Biomater*. 10:3723–3732, 2014.

[17]Chen, X., L. S. Kidder, and W. D. Lew. Osteogenic protein-1 induced bone formation in an infected segmental defect in the rat femur. *J. Orthop. Res*. 20:142–150, 2002.

[18]Chen, X., D. T. Tsukayama, L. S. Kidder, C. A. Bourgeault, A. H. Schmidt, and W. D. Lew. Characterization of a chronic infection in an internally-stabilized segmental defect in the rat femur. *J. Orthop. Res*. 23:816–823, 2005.

[19]Chen, X., A. H. Schmidt, D. T. Tsukayama, C. A. Bourgeault, and W. D. Lew. Recombinant human osteogenic protein-1 induces bone formation in a chronically infected, internally stabilized segmental defect in the rat femur. *J. Bone Joint Surg. Am*. 88:1510–1523, 2006.

[20]Chen, X., A. H. Schmidt, S. Mahjouri, D. W. Polly, Jr., and W. D. Lew. Union of a chronically infected internally stabilized segmental defect in the rat femur after debridement and application of rhbmp-2 and systemic antibiotic. *J. Orthop. Trauma*. 21:693–700, 2007.

[21]Costerton, J. W., Z. Lewandowski, D. E. Caldwell, D. R. Korber, and H. M. Lappin-Scott. Microbial biofilms. *Annu. Rev. Microbiol.* 49:711–745, 1995.
[22]Cui, X., C. Zhao, Y. Gu, L. Li, H. Wang, W. Huang, N. Zhou, D. Wang, Y. Zhu, J. Xu, S. Luo, C. Zhang, and M. N. Rahaman. A novel injectable borate bioactive glass cement for local delivery of vancomycin to cure osteomyelitis and regenerate bone. *J. Mater. Sci. Mater. Med.* 25:733–745, 2014.
[23]Darouiche, R. O. Treatment of infections associated with surgical implants. *N. Engl. J. Med.* 350:1422–1429, 2004.
[24]Davies, J., and D. Davies. Origins and evolution of antibiotic resistance. *Microbiol. Mol. Biol. Rev.* 74:417–433, 2010.
[25]De Long, Jr., W. G., T. A. Einhorn, K. Koval, M. McKee, W. Smith, R. Sanders, and T. Watson. Bone grafts and bone graft substitutes in orthopaedic trauma surgery. A critical analysis. *J. Bone Joint Surg. Am.* 89:649–658, 2007.
[26]De Smet, K., and R. Contreras. Human antimicrobial peptides: defensins, cathelicidins and histatins. *Biotechnol. Lett.* 27:1337–1347, 2005.
[27]Dimitriou, R., E. Jones, D. McGonagle, and P. V. Giannoudis. Bone regeneration: current concepts and future directions. *BMC Med.* 9:66, 2011.
[28]Dinjaski, N., S. Suri, J. Valle, S. M. Lehman, I. Lasa, M. A. Prieto, and A. J. Garcia. Near-infrared fluorescence imaging as an alternative to bioluminescent bacteria to monitor biomaterial-associated infections. *Acta Biomater.* 10:2935–2944, 2014.
[29]Doty, H. A., M. R. Leedy, H. S. Courtney, W. O. Haggard, and J. D. Bumgardner. Composite chitosan and calcium sulfate scaffold for dual delivery of vancomycin and recombinant human bone morphogenetic protein-2. *J. Mater. Sci. Mater. Med.* 25:1449–1459, 2014.
[30]Driffield, K., K. Miller, J. M. Bostock, A. J. O'Neill, and I. Chopra. Increased mutability of *Pseudomonas aeruginosa* in biofilms. *J. Antimicrob. Chemother.* 61:1053–1056, 2008.
[31]Eggleston, H., and P. Panizzi. Molecular imaging of bacterial infections *in vivo*: the discrimination between infection and inflammation. *Informatics* 1:72–99, 2014.
[32]Engelsman, A. F., H. C. van der Mei, K. P. Francis, H. J. Busscher, R. J. Ploeg, and G. M. van Dam. Real time noninvasive monitoring of contaminating bacteria in a soft tissue implant infection model. *J. Biomed. Mater. Res. B Appl. Biomater.* 88:123–129, 2009.
[33]Feng, K., H. Sun, M. A. Bradley, E. J. Dupler, W. V. Giannobile, and P. X. Ma. Novel antibacterial nanofibrous plla scaffolds. *J. Control Release* 146:363–369, 2010.
[34]Fridkin, S. K. Increasing prevalence of antimicrobial resistance in intensive care units. *Crit. Care Med.* 29:N64–N68, 2001.
[35]Fu, W., T. Forster, O. Mayer, J. J. Curtin, S. M. Lehman, and R. M. Donlan. Bacteriophage cocktail for the prevention of biofilm formation by *Pseudomonas aeruginosa* on catheters in an in vitro model system. *Antimicrob. Agents Chemother.* 54:397–404, 2010.
[36]Funao, H., K. Ishii, S. Nagai, A. Sasaki, T. Hoshikawa, M. Aizawa, Y. Okada, K. Chiba, S. Koyasu, Y. Toyama, and M. Matsumoto. Establishment of a real-time, quantitative, and reproducible mouse model of staphylococcus osteomyelitis using bioluminescence imaging. *Infect Immun.* 80:733–741, 2012.
[37]Gristina, A. G. Biomaterial-centered infection: microbial adhesion versus tissue integration. *Science* 237:1588–1595, 1987.
[38]Guelcher, S. A., K. V. Brown, B. Li, T. Guda, B. H. Lee, and J. C. Wenke. Dual-purpose bone grafts improve healing and reduce infection. *J. Orthop. Trauma* 25:477–482, 2011.
[39]Hanlon, G. W. Bacteriophages: an appraisal of their role in the treatment of bacterial infections. *Int. J. Antimicrob. Agents* 30:118–128, 2007.
[40]Hilchie, A. L., K. Wuerth, and R. E. Hancock. Immune modulation by multifaceted cationic host defense (antimicrobial) peptides. *Nat. Chem. Biol.* 9:761–768, 2013.
[41]Hoffman, L. R., D. A. D'Argenio, M. J. MacCoss, Z. Zhang, R. A. Jones, and S. I. Miller. Aminoglycoside antibiotics induce bacterial biofilm formation. *Nature* 436:1171–1175, 2005.
[42]Horst, S. A., V. Hoerr, A. Beineke, C. Kreis, L. Tuchscherr, J. Kalinka, S. Lehne, I. Schleicher, G. Kohler, T. Fuchs, M. J. Raschke, M. Rohde, G. Peters, C. Faber, B. Loffler, and E. Medina. A novel mouse model of *Staphylococcus aureus* chronic osteomyelitis that closely mimics the human infection: an integrated view of disease pathogenesis. *Am. J. Pathol.* 181:1206–1214, 2012.
[43]Huang, D., Y. Zuo, Q. Zou, L. Zhang, J. Li, L. Cheng, J. Shen, and Y. Li. Antibacterial chitosan coating on nanohydroxyapatite/polyamide66 porous bone scaffold for drug delivery. *J. Biomater. Sci. Polym. Ed.* 22:931–944, 2011.
[44]Hughes, K. A., I. W. Sutherland, and M. V. Jones. Biofilm susceptibility to bacteriophage attack: the role of phage-borne polysaccharide depolymerase. *Microbiology* 144(Pt 11):3039–3047, 1998.
[45]Izadpanah, A., and R. L. Gallo. Antimicrobial peptides. *J. Am. Acad. Dermatol.* 52:381–390, 2005; (quiz 391-382).
[46]Jia, W. T., X. Zhang, C. Q. Zhang, X. Liu, W. H. Huang, M. N. Rahaman, and D. E. Day. Elution characteristics of teicoplanin-loaded biodegradable borate glass/chitosan composite. *Int. J. Pharm.* 387:184–186, 2010.
[47]Journeaux, S. F., N. Johnson, S. L. Bryce, S. J. Friedman, S. M. Sommerville, and D. A. Morgan. Bacterial contamination rates during bone allograft retrieval. *J. Arthroplasty.* 14:677–681, 1999.
[48]Kadurugamuwa, J. L., L. Sin, E. Albert, J. Yu, K. Francis, M. DeBoer, M. Rubin, C. Bellinger-Kawahara, T. R. Parr, and P. R. Contag. Direct continuous method for monitoring biofilm infection in a mouse model. *Infect. Immun.* 71:882–890, 2003.
[49]Kadurugamuwa, J. L., L. V. Sin, J. Yu, K. P. Francis, R. Kimura, T. Purchio, and P. R. Contag. Rapid direct method for monitoring antibiotics in a mouse model of bacterial biofilm infection. *Antimicrob. Agents Chemother.* 47:3130–3137, 2003.
[50]Kalghatgi, S., C. S. Spina, J. C. Costello, M. Liesa, J. R. Morones-Ramirez, S. Slomovic, A. Molina, O. S. Shirihai, and J. J. Collins. Bactericidal antibiotics induce mitochondrial dysfunction and oxidative damage in mammalian cells. *Sci Transl Med.* 5:192ra185, 2013.
[51]Kanellakopoulou, K., I. Galanopoulos, V. Soranoglou, T. Tsaganos, V. Tziortzioti, I. Maris, A. Papalois, H. Giamarellou, and E. J. Giamarellos-Bourboulis. Treatment of experimental osteomyelitis caused by methicillin-resistant *Staphylococcus aureus* with a synthetic carrier of calcium sulphate (stimulan) releasing moxifloxacin. *Int. J. Antimicrob. Agents.* 33:354–359, 2009.
[52]Kaur, S., K. Harjai, and S. Chhibber. Bacteriophage mediated killing of *Staphylococcus aureus* in vitro on orthopaedic k wires in presence of linezolid prevents implant colonization. *PLoS ONE* 9:e90411, 2014.

[53]Kollef, M. H., B. Afessa, A. Anzueto, C. Veremakis, K. M. Kerr, B. D. Margolis, D. E. Craven, P. R. Roberts, A. C. Arroliga, R. D. Hubmayr, M. I. Restrepo, W. R. Auger, R. Schinner, and N. I. Group. Silver-coated endotracheal tubes and incidence of ventilator-associated pneumonia: the nascent randomized trial. *JAMA* 300:805–813, 2008.

[54]Kuijer, R., E. J. Jansen, P. J. Emans, S. K. Bulstra, J. Riesle, J. Pieper, D. W. Grainger, and H. J. Busscher. Assessing infection risk in implanted tissue-engineered devices. *Biomaterials* 28:5148–5154, 2007.

[55]Lazzarini, L., J. T. Mader, and J. H. Calhoun. Osteomyelitis in long bones. *J. Bone Joint Surg. Am.* 86A:2305–2318, 2004.

[56]Lew, D. P., and F. A. Waldvogel. Osteomyelitis. *Lancet* 364:369–379, 2004.

[57]Lewis, K. Riddle of biofilm resistance. *Antimicrob. Agents Chemother.* 45:999–1007, 2001.

[58]Lewis, K. Persister cells. *Annu. Rev. Microbiol.* 64:357–372, 2010.

[59]Li, B., K. V. Brown, J. C. Wenke, and S. A. Guelcher. Sustained release of vancomycin from polyurethane scaffolds inhibits infection of bone wounds in a rat femoral segmental defect model. *J. Control Release* 145:221–230, 2010.

[60]Lord, C. F., M. C. Gebhardt, W. W. Tomford, and H. J. Mankin. Infection in bone allografts. Incidence, nature, and treatment. *J. Bone Joint Surg. Am.* 70:369–376, 1988.

[61]Lu, T. K., and J. J. Collins. Dispersing biofilms with engineered enzymatic bacteriophage. *Proc. Natl. Acad Sci. USA* 104:11197–11202, 2007.

[62]Lu, T. K., and M. S. Koeris. The next generation of bacteriophage therapy. *Curr. Opin. Microbiol.* 14:524–531, 2011.

[63]Ma, H., E. T. Darmawan, M. Zhang, L. Zhang, and J. D. Bryers. Development of a poly(ether urethane) system for the controlled release of two novel anti-biofilm agents based on gallium or zinc and its efficacy to prevent bacterial biofilm formation. *J. Control Release* 172:1035–1044, 2013.

[64]Macia, M. D., J. L. Perez, S. Molin, and A. Oliver. Dynamics of mutator and antibiotic-resistant populations in a pharmacokinetic/pharmacodynamic model of *Pseudomonas aeruginosa* biofilm treatment. *Antimicrob. Agents Chemother.* 55:5230–5237, 2011.

[65]Mandal, A., V. Meda, W. J. Zhang, K. M. Farhan, and A. Gnanamani. Synthesis, characterization and comparison of antimicrobial activity of peg/tritonx-100 capped silver nanoparticles on collagen scaffold. *Colloids Surf. B Biointerfaces* 90:191–196, 2012.

[66]Mankin, H. J., F. J. Hornicek, and K. A. Raskin. Infection in massive bone allografts. *Clin. Orthop. Relat. Res.* 432:210–216, 2005.

[67]Marambio-Jones, C., and E. M. V. Hoek. A review of the antibacterial effects of silver nanomaterials and potential implications for human health and the environment. *J. Nanoparticle Res.* 12:1531–1551, 2010.

[68]Meurice, E., E. Rguiti, A. Brutel, J. C. Hornez, A. Leriche, M. Descamps, and F. Bouchart. New antibacterial microporous cap materials loaded with phages for prophylactic treatment in bone surgery. *J. Mater. Sci. Mater. Med.* 23:2445–2452, 2012.

[69]Mills, L. A., and A. H. Simpson. *In vivo* models of bone repair. *J. Bone Joint Surg. Br.* 94:865–874, 2012.

[70]Morello, E., E. Saussereau, D. Maura, M. Huerre, L. Touqui, and L. Debarbieux. Pulmonary bacteriophage therapy on *Pseudomonas aeruginosa* cystic fibrosis strains: first steps towards treatment and prevention. *PLoS ONE* 6:e16963, 2011.

[71]Morones-Ramirez, J. R., J. A. Winkler, C. S. Spina, and J. J. Collins. Silver enhances antibiotic activity against gram-negative bacteria. *Sci. Transl. Med.* 5:190ra181, 2013.

[72]Nijnik, A., and R. Hancock. Host defence peptides: antimicrobial and immunomodulatory activity and potential applications for tackling antibiotic-resistant infections. *Emerg. Health Threats J.* 2:e1, 2009.

[73]O'Loughlin, C. T., L. C. Miller, A. Siryaporn, K. Drescher, M. F. Semmelhack, and B. L. Bassler. A quorum-sensing inhibitor blocks *Pseudomonas aeruginosa* virulence and biofilm formation. *Proc. Natl. Acad. Sci. USA* 110:17981–17986, 2013.

[74]Penn-Barwell, J. G., B. C. Rand, K. V. Brown, and J. C. Wenke. A versatile model of open-fracture infection : a contaminated segmental rat femur defect. *Bone Joint Res.* 3:187–192, 2014.

[75]Pierce, G. E. *Pseudomonas aeruginosa*, candida albicans, and device-related nosocomial infections: implications, trends, and potential approaches for control. *J. Ind. Microbiol. Biotechnol.* 32:309–318, 2005.

[76]Rahaman, M. N., B. S. Bal, and W. Huang. Review: emerging developments in the use of bioactive glasses for treating infected prosthetic joints. *Mater. Sci. Eng. C Mater. Biol. Appl.* 41:224–231, 2014.

[77]Ramage, G., M. M. Tunney, S. Patrick, S. P. Gorman, and J. R. Nixon. Formation of propionibacterium acnes biofilms on orthopaedic biomaterials and their susceptibility to antimicrobials. *Biomaterials* 24:3221–3227, 2003.

[78]Reizner, W., J. G. Hunter, N. T. O'Malley, R. D. Southgate, E. M. Schwarz, and S. L. Kates. A systematic review of animal models for *Staphylococcus aureus* osteomyelitis. *Eur. Cell Mater.* 27:196–212, 2014.

[79]Rhoads, D. D., R. D. Wolcott, M. A. Kuskowski, B. M. Wolcott, L. S. Ward, and A. Sulakvelidze. Bacteriophage therapy of venous leg ulcers in humans: results of a phase I safety trial. *J. Wound Care.* 18:237–238, 2009.

[80]Ruckh, T. T., R. A. Oldinski, D. A. Carroll, K. Mikhova, J. D. Bryers, and K. C. Popat. Antimicrobial effects of nanofiber poly(caprolactone) tissue scaffolds releasing rifampicin. *J. Mater. Sci. Mater. Med.* 23:1411–1420, 2012.

[81]Ryan, E. M., M. Y. Alkawareek, R. F. Donnelly, and B. F. Gilmore. Synergistic phage-antibiotic combinations for the control of escherichia coli biofilms in vitro. *FEMS Immunol. Med. Microbiol.* 65:395–398, 2012.

[82]Sanchez, Jr., C. J., E. M. Prieto, E. M. Prieto, C. A. Krueger, K. J. Zienkiewicz, D. R. Romano, C. L. Ward, K. S. Akers, K. S. Guelcher, and J. C. Wenke. Effects of local delivery of d-amino acids from biofilm-dispersive scaffolds on infection in contaminated rat segmental defects. *Biomaterials* 34:7533–7543, 2013.

[83]Saravanan, S., S. Nethala, S. Pattnaik, A. Tripathi, A. Moorthi, and N. Selvamurugan. Preparation, characterization and antimicrobial activity of a bio-composite scaffold containing chitosan/nano-hydroxyapatite/nano-silver for bone tissue engineering. *Int. J. Biol. Macromol.* 49:188–193, 2011.

[84]Schuch, R., H. M. Lee, B. C. Schneider, K. L. Sauve, C. Law, B. K. Khan, J. A. Rotolo, Y. Horiuchi, D. E. Couto, A. Raz, V. A. Fischetti, D. B. Huang, R. C. Nowinski, and M. Wittekind. Combination therapy with lysin cf-301

and antibiotic is superior to antibiotic alone for treating methicillin-resistant *Staphylococcus aureus*-induced murine bacteremia. *J. Infect Dis.* 209:1469–1478, 2014.

[85]Shi, X., Y. Wang, L. Ren, W. Huang, and D. A. Wang. A protein/antibiotic releasing poly(lactic-co-glycolic acid)/lecithin scaffold for bone repair applications. *Int. J. Pharm.* 373:85–92, 2009.

[86]Silver, S. Bacterial silver resistance: molecular biology and uses and misuses of silver compounds. *FEMS Microbiol. Rev.* 27:341–353, 2003.

[87]Sjollema, J., P. K. Sharma, R. J. Dijkstra, G. M. van Dam, H. C. van der Mei, A. F. Engelsman, and H. J. Busscher. The potential for bio-optical imaging of biomaterial-associated infection *in vivo*. *Biomaterials* 31:1984–1995, 2010.

[88]Southwood, L. L., D. D. Frisbie, C. E. Kawcak, S. C. Ghivizzani, C. H. Evans, and C. W. McIlwraith. Evaluation of ad-bmp-2 for enhancing fracture healing in an infected defect fracture rabbit model. *J. Orthop. Res.* 22:66–72, 2004.

[89]Stewart, P. S., and J. W. Costerton. Antibiotic resistance of bacteria in biofilms. *Lancet* 358:135–138, 2001.

[90]Storm-Versloot, M. N., C. G. Vos, D. T. Ubbink, and H. Vermeulen. Topical silver for preventing wound infection. *Cochrane Database Syst. Rev.* 3:CD006478, 2010.

[91]Suri, S., S. M. Lehman, S. Selvam, K. Reddie, S. Maity, N. Murthy, and A. J. Garcia. *In vivo* fluorescence imaging of biomaterial-associated inflammation and infection in a minimally invasive manner. *J. Biomed. Mater. Res. A.*, 2014.

[92]Thomes, B., P. Murray, and D. Bouchier-Hayes. Development of resistant strains of staphylococcus epidermidis on gentamicin-loaded bone cement *in vivo*. *J. Bone Joint Surg. Br.* 84:758–760, 2002.

[93]Trampuz, A., and A. F. Widmer. Infections associated with orthopedic implants. *Curr. Opin. Infect. Dis.* 19:349–356, 2006.

[94]Trampuz, A., and W. Zimmerli. Diagnosis and treatment of infections associated with fracture-fixation devices. *Injury* 37(Suppl 2):S59–S66, 2006.

[95]Trujillo, N. A., R. A. Oldinski, H. Y. Ma, J. D. Bryers, J. D. Williams, and K. C. Popat. Antibacterial effects of silver-doped hydroxyapatite thin films sputter deposited on titanium. *Mater. Sci. Eng.* 32:2135–2144, 2012.

[96]van Oosten, M., T. Schafer, J. A. Gazendam, K. Ohlsen, E. Tsompanidou, M. C. de Goffau, H. J. Harmsen, L. M. Crane, E. Lim, K. P. Francis, L. Cheung, M. Olive, V. Ntziachristos, J. M. van Dijl, and G. M. van Dam. Real-time *in vivo* imaging of invasive- and biomaterial-associated bacterial infections using fluorescently labelled vancomycin. *Nat. Commun.* 4:2584, 2013.

[97]Wang, J., Y. Zhu, H. K. Bawa, G. Ng, Y. Wu, M. Libera, H. C. van der Mei, H. J. Busscher, and X. Yu. Oxygen-generating nanofiber cell scaffolds with antimicrobial properties. *ACS Appl. Mater. Interfaces* 3:67–73, 2011.

[98]Wang, Q., X. Yu, and M. Libera. Reducing bacterial colonization of 3-d nanofiber cell scaffolds by hierarchical assembly of microgels and an antimicrobial peptide. *Adv. Healthcare Mater.* 2:687–691, 2013.

[99]Wright, A., C. H. Hawkins, E. E. Anggard, and D. R. Harper. A controlled clinical trial of a therapeutic bacteriophage preparation in chronic otitis due to antibiotic-resistant *Pseudomonas aeruginosa*; a preliminary report of efficacy. *Clin. Otolaryngol.* 34:349–357, 2009.

[100]Wu, C., Y. Zhou, M. Xu, P. Han, L. Chen, J. Chang, and Y. Xiao. Copper-containing mesoporous bioactive glass scaffolds with multifunctional properties of angiogenesis capacity, osteostimulation and antibacterial activity. *Biomaterials* 34:422–433, 2013.

[101]Xie, Z., X. Liu, W. Jia, C. Zhang, W. Huang, and J. Wang. Treatment of osteomyelitis and repair of bone defect by degradable bioactive borate glass releasing vancomycin. *J. Control Release* 139:118–126, 2009.

[102]Yasko, A. W., J. M. Lane, E. J. Fellinger, V. Rosen, J. M. Wozney, and E. A. Wang. The healing of segmental bone defects, induced by recombinant human bone morphogenetic protein (rhbmp-2). A radiographic, histological, and biomechanical study in rats. *J. Bone Joint Surg. Am.* 74:659–670, 1992.

[103]Zheng, Z., W. Yin, J. N. Zara, W. Li, J. Kwak, R. Mamidi, M. Lee, R. K. Siu, R. Ngo, J. Wang, D. Carpenter, X. Zhang, B. Wu, K. Ting, and C. Soo. The use of bmp-2 coupled—nanosilver-plga composite grafts to induce bone repair in grossly infected segmental defects. *Biomaterials* 31:9293–9300, 2010.

[104]Zilberman, M., and J. J. Elsner. Antibiotic-eluting medical devices for various applications. *J. Control Release* 130:202–215, 2008.

6.2 Enemchukwu NO, Cruz-Acuña R, Bongiorno T, Johnson CT, García JR, Sulchek T, and García AJ. Synthetic Matrices Reveal Contributions of ECM Biophysical and Biochemical Properties to Epithelial Morphogenesis. *Journal of Cell Biology.* 2016 Jan 4;212(1):113-24. DOI: 10.1083/jcb.201506055

JCB: Tools

Synthetic matrices reveal contributions of ECM biophysical and biochemical properties to epithelial morphogenesis

Nduka O. Enemchukwu,[1,2] Ricardo Cruz-Acuña,[2,3] Tom Bongiorno,[1,2] Christopher T. Johnson,[2,3] José R. García,[1,2] Todd Sulchek,[1,2] and Andrés J. García[1,2]

[1]Woodruff School of Mechanical Engineering, [2]Petit Institute for Bioengineering and Bioscience, and [3]Coulter Department of Biomedical Engineering, Georgia Institute of Technology, Atlanta, GA 30332

Epithelial cells cultured within collagen and laminin gels proliferate to form hollow and polarized spherical structures, recapitulating the formation of a rudimentary epithelial organ. However, the contributions of extracellular matrix (ECM) biochemical and biophysical properties to morphogenesis are poorly understood because of uncontrolled presentation of multiple adhesive ligands, limited control over mechanical properties, and lot-to-lot compositional variability in these natural ECMs. We engineered synthetic ECM-mimetic hydrogels with independent control over adhesive ligand density, mechanical properties, and proteolytic degradation to study the impact of ECM properties on epithelial morphogenesis. Normal cyst growth, polarization, and lumen formation were restricted to a narrow range of ECM elasticity, whereas abnormal morphogenesis was observed at lower and higher elastic moduli. Adhesive ligand density dramatically regulated apicobasal polarity and lumenogenesis independently of cell proliferation. Finally, a threshold level of ECM protease degradability was required for apicobasal polarity and lumen formation. This synthetic ECM technology provides new insights into how cells transduce ECM properties into complex morphogenetic behaviors.

Introduction

Cell–ECM adhesion transduces mechanical and biochemical signals that regulate epithelial morphogenesis (Klinowska et al., 1999; Lubarsky and Krasnow, 2003; Wozniak et al., 2003; Paszek et al., 2005; Yu et al., 2005; Nelson et al., 2006; Bryant and Mostov, 2008; Zhang et al., 2009, 2011). Bissell, Mostov, and others have pioneered the use of 3D collagen and laminin (i.e., Matrigel) gels in organotypic cultures that recreate the epithelial morphogenetic developmental program (O'Brien et al., 2002; Mroue and Bissell, 2013). In these natural matrices, epithelial cells, such as MDCK cells, proliferate from single cells to form multicellular, hollow spherical monolayer structures (cysts) within 10 d that bear the hallmarks of epithelial polarity, recapitulating the morphogenetic program for the formation of a rudimentary epithelial organ (McAteer et al., 1986). These 3D cultures have revealed that interactions between integrin adhesion receptors and secreted laminin and the density of ECM, which impacts the gel mechanical properties, regulate the establishment of cell polarity and morphogenesis as well as tumorigenesis (Barcellos-Hoff et al., 1989; O'Brien et al., 2001; Wozniak et al., 2003; Levental et al., 2009; Provenzano et al., 2009). Nevertheless, these natural matrices are inherently limited by the inability to decouple mechanical properties from matrix and ligand density and lot-to-lot compositional and structural variability (Yu et al., 2005; Hughes et al., 2010). Additionally, tumor-derived matrices such as Matrigel have limited clinical translational potential in regenerative medicine applications. In the work presented here, we describe a modular, synthetic ECM-mimetic hydrogel platform with controlled presentation of cell-adhesive ligands, tunable mechanical properties, and protease-dependent degradation to direct epithelial morphogenesis. Whereas previous work has established synthetic polymer hydrogels as engineered ECMs to investigate single cell behaviors (Lutolf et al., 2003; Kloxin et al., 2009; Huebsch et al., 2010; Khetan et al., 2013) and multicellular assemblies of cancer cell lines with a focus on tumorigenesis (Gill et al., 2012; Weiss et al., 2012; Beck et al., 2013; Raza et al., 2013), we analyze the contributions of ECM mechanical and biochemical properties to the coordinated multicellular epithelial morphogenesis developmental program. Understanding how cells transduce ECM properties into complex morphogenetic behaviors is paramount to developmental biology, pathogenesis, and materials-based regenerative medicine. Finally,

Correspondence to Andrés J. García: andres.garcia@me.gatech.edu

Abbreviations used in this paper: EdU, 5-ethynyl-2′-deoxyuridine; EMEM, Eagle's minimal essential media; MMP, matrix metalloproteinase; PEG, polyethylene glycol; PEG-4MAL, 4-arm PEG-maleimide; TEA, triethanolamine.

Supplemental material can be found at:
http://doi.org/10.1083/jcb.201506055

The Rockefeller University Press $30.00
J. Cell Biol.
www.jcb.org/cgi/doi/10.1083/jcb.201506055

THE JOURNAL OF CELL BIOLOGY

this platform technology is straightforward to implement and uses commercially available reagents, allowing for facile and broad adoption by the community.

Results

Synthetic PEG hydrogels as ECM mimics with tunable biophysical and biochemical properties

To overcome the inability to tune the mechanical, structural, and biochemical characteristics and lot-to-lot compositional variability of natural ECMs, we engineered synthetic ECM-mimetic hydrogels with independent control over the presentation of cell-adhesive ligand type/density, mechanical and structural properties, and protease-dependent degradation to study the impact of ECM biophysical and biochemical properties on epithelial morphogenesis. These polyethylene glycol (PEG) hydrogels are based on a four-arm PEG macromer with maleimide groups at each terminus (PEG-4MAL; Fig. 1 A). The PEG-4MAL platform outperforms other synthetic chemistries in generating structurally defined hydrogels with stoichiometric incorporation of ligands and improved cross-linking efficiency (Phelps et al., 2012), providing an ideal material platform for the systematic and rigorous evaluation of the effects of ECM biochemical and biophysical properties on cell functions. Furthermore, these hydrogels exhibit superior in vitro and in vivo biocompatibility for several cell types including mesenchymal stem cells, skeletal myoblasts, and pancreatic islets (Phelps et al., 2012, 2013; Salimath et al., 2012). In a rapid reaction with quantitative yields, thiol-containing ligands such as cysteine-containing peptides can be conjugated to the PEG-4MAL macromer via reaction with the maleimide group to yield a functionalized macromer (Fig. 1 A). In this fashion, PEG-4MAL macromers presenting GRGDSPC (RGD) peptide that binds to integrin adhesion receptors were prepared (Fig. 1 A). RGD peptides were tethered onto the PEG-4MAL macromer with high yield (Fig. 1 B), demonstrating precise control over adhesive ligand density. Cysteine-flanked, protease-degradable peptide was then reacted with RGD-functionalized PEG-4MAL macromers in the presence of cells to cross-link macromers into a hydrogel network encapsulating the cells (Fig. 1 A). Importantly, in this synthetic platform, macromer size, polymer density, adhesive ligand type and density, and cross-linker type and density can be independently controlled to tune hydrogel structure (mesh size), mechanical properties, ECM ligand presentation, and protease-dependent degradation. For example, for a given macromer size (e.g., 20 kD PEG-4MAL), hydrogel elastic modulus increases, whereas equilibrium swelling (which is related to hydrogel structure) decreases as a function of polymer density as a tighter network is formed (Fig. 1 C), in excellent agreement with Flory-Rehner theory (Flory and Rehner, 1943; Canal and Peppas, 1989).

A major limitation for natural matrices such as collagen gels and Matrigel is that changes in protein concentration to vary mechanical properties invariably alter adhesive site local density and organization through changes to fiber structure and density. In contrast, for this modular synthetic system, mechanics, degradation, and adhesive ligand presentation can be independently tuned (Fig. 1 D). Because the PEG-4MAL macromers are symmetric and, when cross-linked into a hydrogel, form a regular mesh structure that is fully swollen, the adhesive peptide is uniformly distributed throughout the hydrogel network within the "statistical mean" of the mesh size. For the 20-kD macromer hydrogel system described here, the mesh size is 30–40 nm. Because of the small size of the PEG macromer arms and the swollen state of the gel, the mobility of the adhesive peptide is very limited. FRAP experiments with fluorescently labeled RGD peptide within hydrogels showed negligible fluorescence recovery, indicating very limited mobility of the adhesive peptide and uniform distribution throughout the hydrogel (Fig. S1 A). We also examined whether the spatial distribution of RGD peptide changes at the cell–hydrogel interface because of cell contractility. Using hydrogels presenting labeled RGD peptide and confocal microscopy, we monitored signal intensity at the cell–hydrogel interface as a function of time for cell cysts (Fig. S1 B). We observed no differences in signal intensity over time for either Y-27632–treated (10 µM) or control cysts, indicating no changes in local ligand density (i.e., clustering) with cell contractility. Taken together, these results demonstrate uniform spatial presentation of the adhesive peptide in a length scale relevant to the cell. Using this modular and well-controlled hydrogel platform, we analyzed the effects of ECM biochemical and biophysical properties on epithelial morphogenesis.

Normal epithelial morphogenesis requires an optimal range of ECM elasticity

We first investigated the influence of hydrogel polymer density, which is analogous to ECM concentration, on epithelial morphogenesis. Single MDCK cells were embedded in PEG-4MAL hydrogels formulated over a range of polymer densities (3.5%–5.0%, wt/vol). This range of polymer densities results in hydrogels with varying mechanical properties (0.85–8.0 kPa elastic modulus) and swelling behavior (Fig. 1 C). All these hydrogels were engineered to present the same density of RGD peptide (2,000 µM) and cross-linked by a fast-degrading, collagen-derived peptide (GPQ-W). This RGD density was chosen based on pilot experiments demonstrating cell attachment and robust spreading on top of such gels (unpublished data). Type I collagen gels (2.0 mg/ml) were used as a reference, because this natural ECM supports epithelial morphogenesis. Single cells embedded in hydrogels formulated at 3.5%, 4.0%, and 4.5% PEG-4MAL remained rounded and maintained high viability at 24 h and, after 48 h, formed multicellular clusters (Fig. 2, A and B; and Fig. S2 A). Formation of these cell clusters did not result from individual cells migrating toward each other, and 5-ethynyl-2′-deoxyuridine (EdU) incorporation confirmed that clusters arose from robust cell proliferation (Fig. 2, A and C). In contrast, cells encapsulated in 5.0% and higher-density PEG-4MAL gels had high viability at 24 h but remained as single and rounded cells at 48 h, with dramatically diminished viability and a complete abrogation of proliferation and formation of multicellular clusters (Fig. 2, A and C). These results demonstrate polymer density–dependent effects on epithelial cell survival and proliferation within PEG-4MAL hydrogels with a nonpermissive barrier at polymer densities of 5.0% and higher.

Columnar epithelia are characterized by polarized distribution of membrane complexes and morphological features between an apical domain facing a lumen/free space and a continuous basolateral domain interfacing with ECM and neighboring cells. This apicobasal polarity is critical for transport, secretion, and barrier functions in several organ systems (Roignot et al., 2013). Furthermore, in morphogenesis of 3D epithelial tissues such as ducts and sacs, establishment of a central

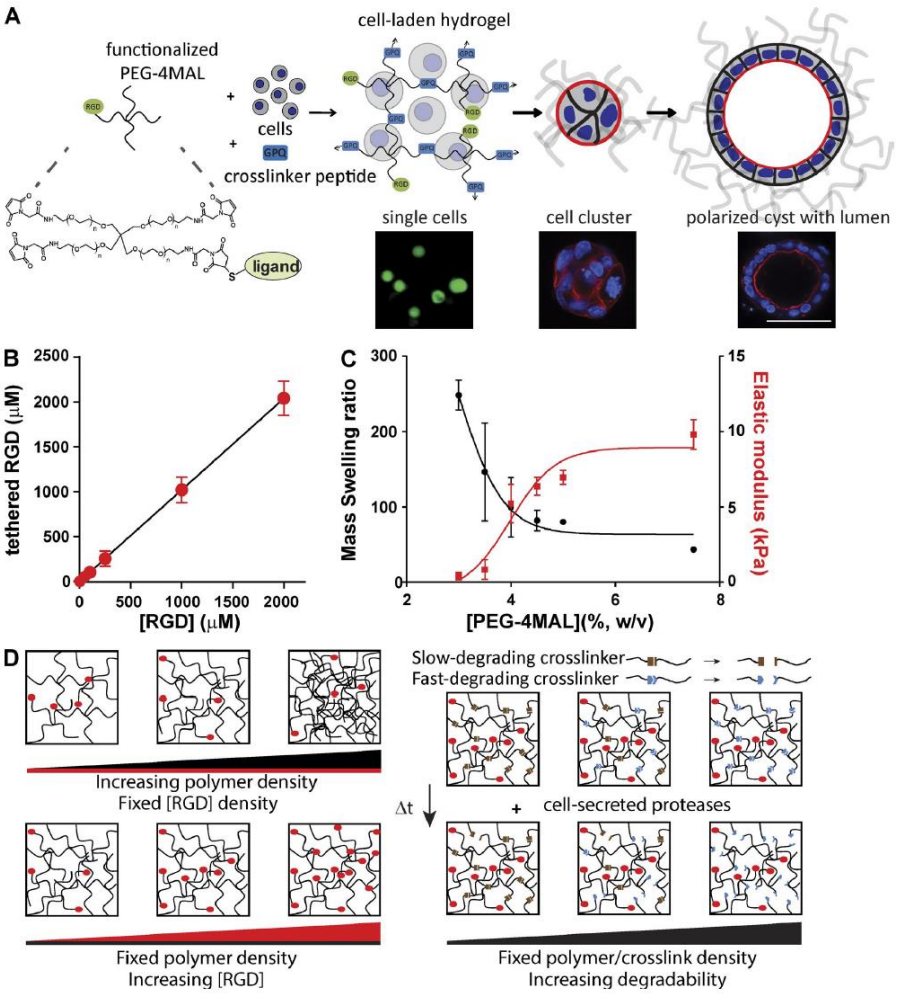

Figure 1. **Synthetic ECMs with tunable biophysical and biochemical properties.** (A) Schematic of cell-encapsulating hydrogel. Adhesive ligand-functionalized 4-arm PEG (PEG-4MAL) is reacted with a thiol-flanked protease-degradable peptide in the presence of cells to form a hydrogel network. Hydrogels support epithelial morphogenesis program. Bar, 50 µm. (B) Tethered RGD density (mean ± SEM) in hydrogel as a function of input RGD concentration. Linear regression: $y = 1.02x + 0.55$, $P < 0.0001$. (C) Relationship between polymer density (wt%) and hydrogel equilibrium mass swelling ratio (Q_m; left axis, mean ± SEM) and elastic modulus (right axis, mean ± SEM). (D) Cartoon illustrating independent control of polymer density, adhesive ligand density, and cross-link density/network degradation rate in PEG-4MAL hydrogels.

lumen is a critical phase in sculpting tissue architecture (Bryant and Mostov, 2008). For cell proliferation–permissive hydrogel polymer densities, hollowing of the multicellular clusters was visible after 4 d in culture (Fig. S2, A and B). Cleaved caspase-3 labeling indicated the presence of apoptotic cells in developing cysts (Fig. 3, A and B), demonstrating a mode of lumen clearance in permissive hydrogels similar to that observed in collagen gels (Martín-Belmonte et al., 2008). Moreover, MDCK cells in permissive PEG-4MAL hydrogels formed differentiated epithelial cysts after 10 d in culture consisting of spherical (50- to 100-µm diameter, Fig. 3 C) cellular assemblies with lumens and apicobasal polarity (Fig. 2 D). These well-defined spherical cell structures exhibited canonical markers of apicobasal polarity, including podocalyxin/gp135, actin, ZO-1, GM130, and β-catenin (O'Brien et al., 2006; Fig. S3 A). Cysts in different hydrogel formulations were analyzed for apicobasal polarity and lumen formation using a scoring system (Fig. S3 B). Remarkably, hydrogel polymer density modulated apicobasal

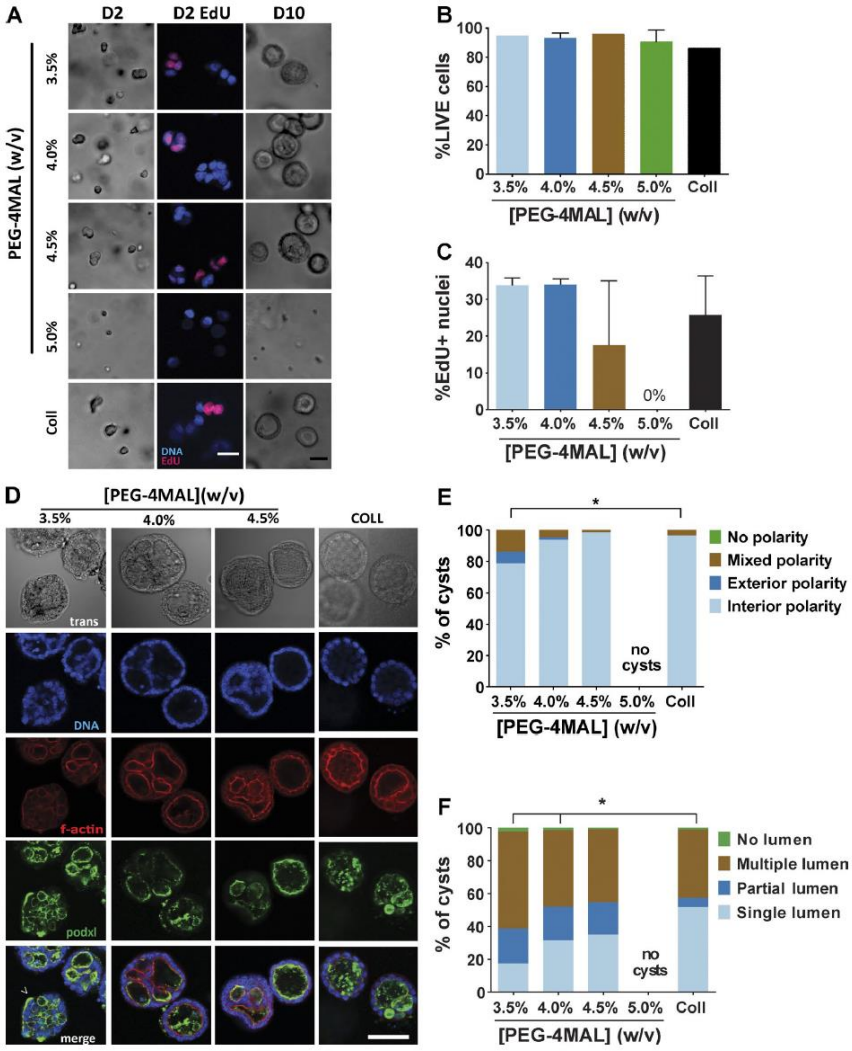

Figure 2. **PEG-4MAL polymer density regulates epithelial morphogenesis.** (A) Transmitted light and fluorescence microscopy images of single MDCK cells cultured in PEG-4MAL hydrogels of different polymer weight percentages over 10 d. At day 2, newly synthesized DNA was labeled by EdU incorporation. Bar, 50 µm. (B) Cell viability (mean ± range in two independent experiments) assessed by calcein-AM (live) and TOTO-3 iodide (dead) labeling at day 1 (>500 cells counted per condition). (C) Proliferation (mean ± range in two independent experiments) as determined by EdU labeling (>590 nuclei counted per condition). (D) Transmitted light and fluorescence microscopy images for MDCK cultures at day 10 and labeled for apical polarity marker gp135/podocalyxin (podxl) and filamentous actin. No cysts were detected in 5.0% PEG-4MAL gels. Bar, 50 µm. (E) Distribution of apical polarity phenotypes at day 10 (>90 cysts analyzed per condition). χ^2 test with Bonferroni's correction; *, $P < 0.014$, 3.5% versus collagen. (F) Distribution of lumen phenotypes at day 10 (>90 cysts scored per condition). χ^2 test with Bonferroni's correction; *, $P < 3 \times 10^{-6}$, 3.5% versus collage; $P < 0.02$, 4.0% versus collagen.

polarity (Fig. 2 E) and lumen formation (Fig. 2 F). Epithelial cysts grown in 4.0% and 4.5% PEG-4MAL gels exhibited normal, internal apical polarity and partial or fully formed single lumens. The frequencies of internal apical polarity and single lumen formation in 4.0% and 4.5% PEG-4MAL gels were equivalent to those for cysts formed in collagen gels (Fig. 2 D–F). In contrast, epithelial cysts grown in 3.5% PEG-4MAL gels exhibited aberrant polarity, with >20% of the cysts

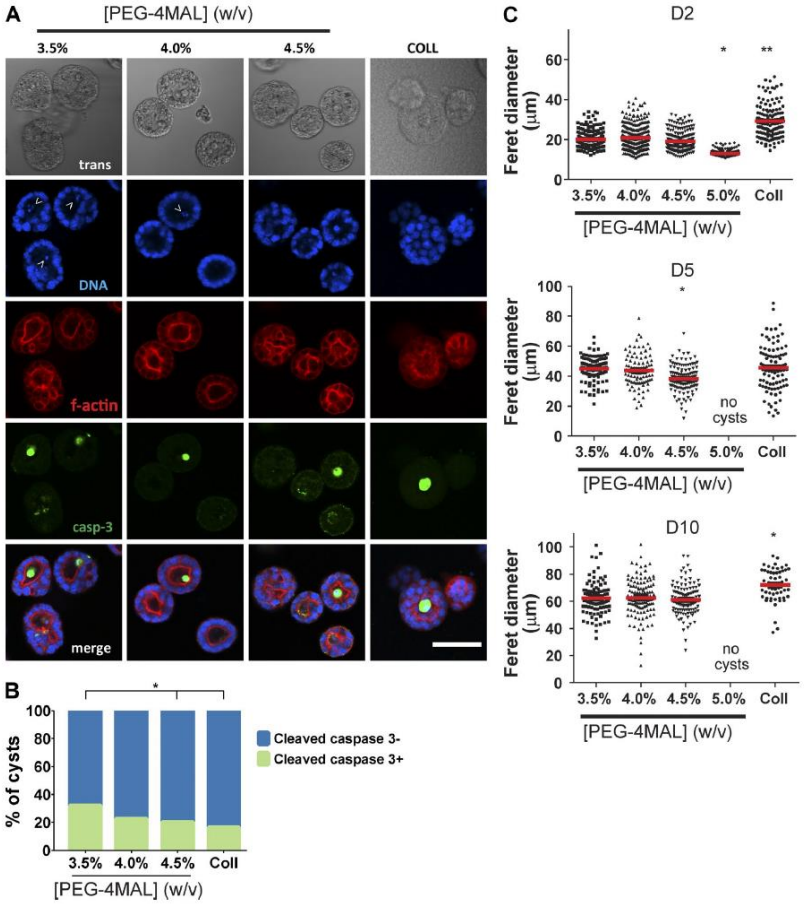

Figure 3. **Lumen formation for epithelial cysts within PEG-4MAL hydrogels involves cell apoptosis.** (A) Transmitted light and fluorescence microscopy images of MDCK cells cultured within PEG-4MAL hydrogels. Samples were stained for filamentous actin and caspase-3. (B) Distribution of cysts staining positive for caspase-3 (>103 cysts analyzed per condition). χ^2 test with Bonferroni's correction *, $P < 0.005$, 3.5% versus 4.5% and collagen. (C) Epithelial cyst size (median shown as red line) as a function of PEG-4MAL hydrogel polymer density (>62 cysts analyzed per condition). χ^2 test with Bonferroni's correction. Day 2: *, $P < 0.05$, 5.0% versus all other polymer densities; **, $P < 0.01$, 5.0% versus collagen. Day 5: *, $P < 0.05$, 4.5% versus collagen. Day 10: *, $P < 0.05$, collagen versus PEG-4MAL groups.

exhibiting mixed or exclusively external (or inverted) polarity (Fig. 2, D and E). Furthermore, only 17% of cysts grown in 3.5% PEG-4MAL exhibited a well-defined single lumen versus 31% and 35% for 4.0% and 4.5% PEG-4MAL gels, respectively (Fig. 2, D and F). Although polymer density regulated polarization and lumen formation, there were no differences in cyst diameter among these permissive hydrogel formulations (Fig. 3 C). No epithelial cysts formed in PEG-4MAL hydrogels with polymer densities of 5.0% and higher.

Normal cyst development, polarization and lumen formation were restricted to a narrow range of hydrogel polymer density, whereas abnormal epithelial morphogenesis and complete abrogation of this developmental program were observed at lower and higher polymer densities, respectively. Because polymer density strongly dictates the mechanical properties of the hydrogel (Fig. 1 C), these results suggest that normal epithelial morphogenesis requires an optimal range of ECM elasticity (E, ~4 kPa). This conclusion is consistent with previous studies reporting changes in epithelial morphogenesis with collagen concentration (Wozniak et al., 2003; Paszek et al., 2005). However, polymer density (as well as collagen concentration) also controls hydrogel structure, as evidenced by changes in swelling behavior (Fig. 1 C), which impacts other important hydrogel properties such as permeability that can influence cell behaviors (Ghajar et al., 2008). To assess whether the polymer density–dependent effects on epithelial morphogenesis were

caused by changes in hydrogel elasticity, we compared cyst polarization and lumen formation in RGD-functionalized hydrogels generated from different macromer sizes (20 vs. 40 kD) but different polymer densities (4.0% vs. 8.0%) engineered to have equivalent mean cross-link densities. Measurements for diffusion of labeled protein (α-bungarotoxin, 8 kD) through these hydrogels demonstrated differences in permeability caused by the differences in macromer arm length (Fig. S4 A). Nevertheless, as expected for gels with equivalent mean cross-link densities, these two gel formulations had equivalent mechanical properties (Fig. S4 B). MDCK cell cyst development proceeded normally in both hydrogel formulations, and there were no differences in polarization or lumen formation between these two formulations (Fig. S4, C and D). This result demonstrates that the effects of polymer density on epithelial morphogenesis are related to hydrogel mechanical properties. Taken together, these results show that normal epithelial morphogenesis requires an optimal range of ECM elasticity.

Adhesive ligand density regulates polarization and lumen formation independently of cell proliferation

We next examined the effects of RGD adhesive ligand density on epithelial morphogenesis within synthetic ECM hydrogels. A constant total density (2,000 µM) of a mixture of cell-adhesive RGD peptide and scrambled inactive RDG peptide was used to vary RGD density (0–2,000 µM) while maintaining identical structures among hydrogel formulations of 4.0% polymer density and constant GPQ-W cross-linking peptide density. Cell proliferation and assembly into multicellular structures was insensitive to RGD peptide density (Fig. 4, A and B). However, epithelial cyst polarity and lumen phenotypes showed a dramatic dependence on RGD density (Fig. 4 C). Hydrogels presenting low (≤100 µM) RGD densities supported the formation of very few cysts with internal apical polarity (<14%), in striking contrast to hydrogels presenting high (≥250 µM) RGD density in which >60% of cysts had internal apical polarity (Fig. 4, C and D). A similarly dramatic shift in the distribution of lumen phenotypes occurred at 250 µM RGD density. Nearly all (>90%) cysts in hydrogels presenting high densities of RGD peptide contained lumens, whereas the majority of cysts in low-density RGD gels lacked lumens (Fig. 4, C and E). The extent of cyst polarization and lumen formation was not different between PEG-4MAL hydrogels presenting 2,000 µM RGD peptide and collagen gels. These results show that although RGD peptide is not required for initial proliferation and generation of cell aggregates, differentiation of polarized cysts with lumens requires a threshold density of RGD in the matrix.

To explore the role of integrins in the RGD density–dependent effects on cyst phenotype within the synthetic hydrogel system, we cultured MDCK cells in PEG-4MAL hydrogels presenting 2,000 µM RGD peptide in the presence of LM609, an antibody that blocks binding of the αVβ3 integrin to RGD peptides, or AIIB2, an antibody that blocks the function of the β1 integrin that binds and assembles secreted laminin during cyst morphogenesis (Yu et al., 2005). Nearly all (>98%) cysts that developed in the presence AIIB2 or control isotype antibodies had normal, interior apical polarity (Fig. 4, F–H). In contrast, only 80% of epithelial cysts grown in the presence of LM609 exhibited interior apical polarity. Similarly, ∼18% of cysts grown with AIIB2 or control antibodies exhibited a well-developed single lumen, whereas none of the cysts grown in the presence of LM609 had well-formed, single lumens. These results demonstrate that the RGD-dependent effects on epithelial morphogenesis within PEG-4MAL are mediated by the αVβ3 integrin. Although statistically significant, the cyst phenotype shifts observed in RGD-presenting PEG-4MAL hydrogels in the presence of LM609 were considerably less than those seen in the absence of RGD. We attribute this discrepancy to the presence of other integrin heterodimers that bind RGD and provide significant signaling in the presence of LM609 (Teräväinen et al., 2013). The absence of a cyst phenotype shift in the presence of AIIB2 suggests that β1 integrin function is dispensable for polarized cyst morphogenesis in the RGD-functionalized synthetic hydrogel.

To demonstrate the versatility of the synthetic platform to study different adhesive ligands, we performed additional experiments for apicobasal polarization and lumen formation with other cysteine-terminated cell-adhesive peptides: laminin α1 chain–derived AG73 peptide (CGGRKRLQVQLSIRT; Hoffman et al., 1998), EF1zz peptide (CGGATLQLQEGRLHFXFD LGKGR, X: Nle; Suzuki et al., 2003), and collagen IV–derived peptide (CGGGEFYFDLRLKGDKY; Miles et al., 1994). This study showed peptide-specific differences in epithelial morphogenesis for MDCK cells (Fig. S5, A and B). We note that synthetic hydrogels presenting full-length proteins such as laminin and collagen can be prepared by blending the matrix protein with the PEG components during cross-linking, and these hydrogels also support lumen formation and polarization (Fig. S5 C). However, this approach has limitations, as these full-length proteins are considerable larger than the PEG macromer and will disrupt the local structure and cross-linking of the hydrogel, potentially resulting in ill-defined local mechanical and biochemical properties. At high concentrations of protein, these effects may be large enough such that performing dose-dependent studies as shown here for RGD peptide will be difficult.

A threshold level of ECM protease degradability is required for apicobasal polarity and lumen formation without alterations in cyst size

Epithelial morphogenesis requires local, cell-mediated matrix degradation to create space for expansion of cellular aggregates or extension of cellular processes (Weaver et al., 2014). We used two different experimental approaches to examine the effects of cross-link degradation on epithelial cyst development in PEG-4MAL hydrogels. First, we directly tuned the degradability of the hydrogel matrix by titrating a slower-degrading variant peptide (GPQ-A; Patterson and Hubbell, 2010) of the GPQ-W cross-linker in hydrogel formulations (4% polymer density, 2,000 µM RGD) that typically support high proliferation and formation of cell aggregates. Whereas 5% and 10% substitution of GPQ-A had no effect on cyst morphogenesis, GPQ-A content of 20% increased the incidence of abnormal polarity and altered lumen phenotypes (Fig. 5, A–C). GPQ-A content of >20% resulted in complete abrogation of cell proliferation and multicellular cyst precursor formation (Fig. 5 A). This result is consistent with the observation that cells did not proliferate or form cysts in PEG-4MAL gels of ≥5.0% polymer density with GPQ-W (Fig. 2).

We also incubated MDCK cells embedded in 4.0% PEG-4MAL hydrogels functionalized with RGD (2,000 µM) and cross-linked with GPQ-W in the broad-range matrix metalloproteinase (MMP) inhibitors GM6001 and MMPII. Interestingly,

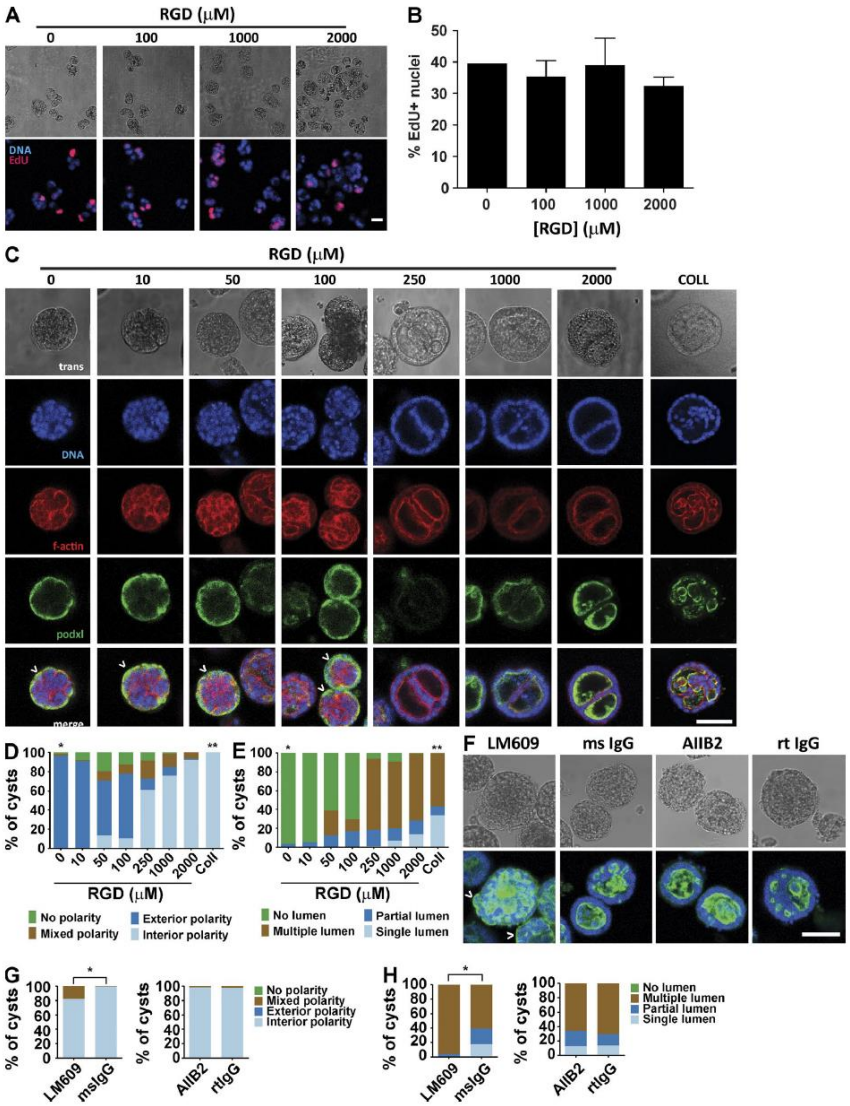

Figure 4. **Adhesive ligand density in PEG-4MAL hydrogel modulates cyst phenotype and apical polarity.** (A) Transmitted light and fluorescence microscopy images for MDCK cells cultured for 2 d in 4.0% PEG-4MAL hydrogels incorporating different amounts of RGD. Newly synthesized DNA was labeled by EdU. Bar, 20 μm. (B) Cell proliferation (mean ± SEM) at day 2 as assessed by EdU incorporation (>374 nuclei counted per condition). (C) Transmitted light and fluorescence microscopy images for MDCK cells cultured in 4.0% PEG-4MAL for 10 d and labeled for apical polarity marker gp135/podocalyxin (podxl). Inverted apical polarity indicated by ^. Bar, 50 μm. F-actin, filamentous actin. (D) Distribution of apical polarity phenotypes at day 10 (>78 cysts counted per condition). χ^2 test with Bonferroni's correction; *, $P < 0.0001$, 0 μM RGD versus every other condition except 10 μM RGD; **, $P < 0.0001$, collagen versus every other condition except 2,000 μM RGD. (E) Distribution of lumen phenotypes at day 10 (>78 cysts counted per condition). χ^2 test with Bonferroni's correction; *, $P < 0.0001$, 0 μM RGD versus every other condition except 10 μM RGD; **, $P < 0.0001$, collagen versus every other group. (F) MDCK cultured for 10 d in 4.0% PEG-4MAL gels with 2,000 μM RGD in the presence of function-blocking antibodies against integrin αVβ3 (LM609) or integrin β1 (AIIB2) or isotype control antibodies (mouse [ms] or rat [rt] IgG). Cysts were labeled with antibodies against gp135/podocalyxin (podxl). Bar, 50 μm. (G) Distribution of lumen phenotypes in F at day 10 (>100 cysts counted per condition). χ^2 test; *, $P < 0.0001$, mouse IgG versus LM609. (H) Distribution of apical polarity phenotypes in F at day 10 (>100 cysts counted per condition). χ^2 test; *, $P < 0.0001$, mouse IgG versus LM609.

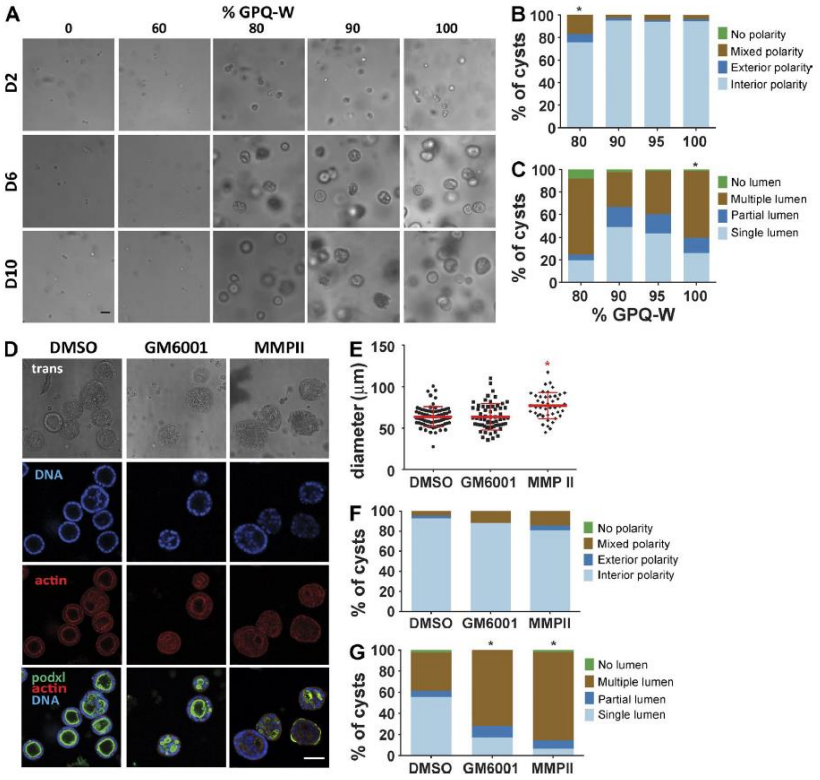

Figure 5. **Hydrogel cross-link degradation rate regulates cyst growth, lumen formation, and polarity.** (A) Transmitted light microscope images of MDCK cells cultures for 10 d in 4.0% PEG-4MAL hydrogels with 2,000 µM RGD cross-linked with either fast-degrading (GPQ-W) or slow-degrading (GPQ-A) cross-linking peptides titrated from 0% GPQ-W (100% GPQ-A) to 100% GPQ-W (0% GPQ-A). Bar, 50 µm. (B) Distribution of apical polarity phenotypes at day 10 (>135 cysts counted per condition). χ^2 test with Bonferroni's correction; *, $P < 0.0001$, 80% GPQ-W versus 100% GPQ-W. (C) Distribution of lumen phenotypes at day 10 (>135 cysts counted per condition). χ^2 test with Bonferroni's correction; *, $P < 0.005$, 100% GPQ-W versus all other conditions. (D) MDCK cells cultured for 10 d in PEG-4MAL hydrogels with 2,000 µM RGD and incubated with MMP inhibitors MMPII or GM6001 or control. Cysts were labeled with rhodamine phalloidin (filamentous actin), Hoechst 3342 (DNA), and an antibody against apical polarity marker gp135/podocalyxin (podxl; green). Bar, 50 µm. (E) Cyst size at day 10 (>44 cysts counted per condition). χ^2 test with Bonferroni's correction; *, $P < 0.05$, MMPII versus all other conditions. (F) Distribution of apical polarity phenotypes at day 10 (>108 cysts counted per condition). (G) Distribution of lumen phenotypes at day 10 (>108 cysts counted per condition). χ^2 test with Bonferroni's correction; *, $P < 0.0001$, GM6001 versus DMSO and MMPII versus DMSO.

these MMP inhibitors had modest effects on cyst size at day 10 (Fig. 5, D and E). However, both MMP inhibitors reduced the proportion of cysts with internal apical polarity and well-defined single lumen compared with the vehicle-only (DMSO) control (Fig. 5, D, F, and G). These alterations in cyst polarization and lumen formation mirror the effects of incorporating 20% of the slower-degrading GPQ-A cross-linking peptide in the permissive hydrogel formulation (Fig. 5 B). Taken together, these results show that MMP-dependent degradation of the PEG-4MAL hydrogel network is essential for normal epithelial morphogenesis within these synthetic ECM.

Synthetic ECM platform is applicable to study other epithelial cell models

We performed additional experiments with Caco-2 colon epithelial cells to demonstrate that the synthetic ECM platform can be used to study epithelial morphogenesis with other cell systems. This study demonstrated that specific hydrogel formulations supported multicellular cyst assembly, lumen formation, and polarization with this epithelial cell line (Fig. 6). Interestingly, for Caco-2 cells, RGD adhesive peptide was required for multicellular cyst formation, as scrambled RDG-presenting gels supported poorly organized cell clusters with fewer cells. In addition, the range of permissive formulations for cyst formation occurred at higher polymer densities (6.0–8.0%) for Caco-2 cells compared with MDCK cells. Even though the hydrogel of 8.0% polymer density supported lumen formation and polarization, the resulting cysts were smaller than those developed in the formulation with 6.0% polymer density. These results show differences on the effects of ECM biochemical and biophysical cues on the morphogenetic program for different epithelial cell lines.

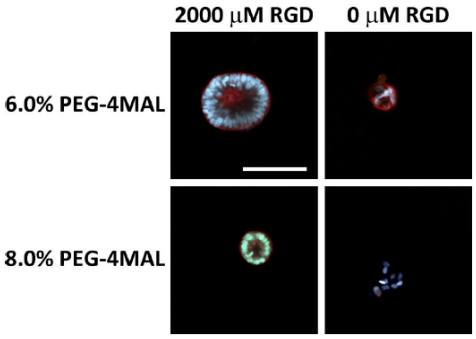

Figure 6. **Hydrogel polymer density and RGD adhesive ligand regulate epithelial morphogenesis in Caco-2 cells.** Fluorescence microscopy images of Caco-2 cells grown within PEG-4MAL hydrogels for 10 d. Bar, 100 µm. Cysts were labeled with rhodamine phalloidin (filamentous actin) and Hoechst 3342 (DNA). Cyst formation, lumen formation, and polarization required RGD adhesive peptide. Hydrogel polymer density influences the size of the resulting epithelial cyst.

Discussion

This study establishes a modular synthetic ECM-mimetic hydrogel platform with controlled presentation of cell-adhesive ligands, tunable mechanical properties, and protease-dependent degradation that can be precisely engineered to study the contributions of ECM biophysical and biochemical properties on the epithelial morphogenetic program. Systematic changes in hydrogel formulation to independently tune hydrogel polymer density, elasticity, adhesive ligand density, and protease-dependent degradation revealed that each of these properties has profound effects on specific stages of this coordinated morphogenetic process, including proliferation, multicellular cyst development, polarization, and lumen formation. Importantly, these effects occur via mechanisms that parallel development in natural matrices. Because of their inherent complexity, these new insights into the contributions of ECM biochemical and mechanical properties to the regulation of epithelial morphogenesis are simply not tractable using natural collagen and laminin ECMs. Remarkably, a spectrum of developmental outcomes including cell apoptosis, normal cyst development comprising a spherical polarized cell monolayer enclosing a single lumen, and abnormal cellular assemblies consisting of solid spheres with no lumen or structures with inverted polarity and multiple lumens reminiscent of pathological states could be engineered within the same synthetic hydrogel platform.

We identified synthetic hydrogel formulations that supported the epithelial morphogenesis program to the same extent as type I collagen matrices. Interestingly, the collagen gels used as a reference in the experiments presented here have a fibrillar architecture with micrometer-sized pores, whereas the PEG-4MAL gels have an amorphous structure with a nanoscale mesh size. Our results suggest that the epithelial morphogenesis program is insensitive to these differences in matrix architecture. However, because of the complex nature of the collagen gels, it is difficult to determine whether other important parameters (e.g., adhesive ligand density) regulating epithelial morphogenesis are equivalent between the optimal synthetic analog and the natural ECM.

Our results for the effects of ECM properties on the normal epithelial morphogenetic program are fundamentally different from those reported for cancer cells in synthetic gels, most likely reflecting central differences between developmental morphogenesis and tumorigenesis. For instance, MDCK cell proliferation and assembly into multicellular structures was insensitive to RGD peptide density, whereas cyst polarity and lumen phenotypes showed a dramatic dependence on RGD density. Additionally, the literature has major inconsistencies regarding the effects of polymer density (equated in these papers to stiffness) on the organization of cancer cells into aggregates of varying size (Gill et al., 2012; Beck et al., 2013; Raza et al., 2013). We observe different responses for normal epithelial cells. Multicellular cysts formed at polymer densities below a threshold that supported cell proliferation; above this threshold, no cell aggregates were formed owing to inhibited proliferation and apoptosis. Moreover, for permissive formulations, we report polymer density-dependent differences in the establishment of apicobasal polarity and the formation of cysts with no lumen, a single lumen, and multiple lumens, which are hallmarks of normal epithelial morphogenesis and formation of a rudimentary epithelial organ. Yet all these cysts had equivalent size. Raza et al. reported that hydrogels that were not protease-degradable did not support formation of larger cell aggregates (Raza et al., 2013). This result is the expected consequence of a tight hydrogel network encapsulating the cells. In the present study, we show this effect for a hydrogel with 100% nondegradable cross-links. However, we also find that intermediate levels of protease-degradability regulate apicobasal polarity and lumen phenotypes without alterations in cyst size, demonstrating that protease-degradability of the ECM regulates these critical epithelial characteristics independently of simply constraining cells from forming cell aggregates.

We expect that this biomaterial platform will find widespread adoption in developmental cell and tumor biology fields to study ECM-regulated morphogenetic processes. Furthermore, this technology enables the engineering of instructive epithelial synthetic niches for cell expansion and controlled differentiation as well as delivery vehicles for regenerative medicine applications that overcome the limitations of natural matrices such as lot-to-lot variability and regulatory and translational constraints.

Materials and methods

Antibodies and labeling reagents

Primary antibodies used were mouse anti-gp135/podocalyxin (clone 3F21D8; provided by G. Ojakian, SUNY Downstate Medical Center, Brooklyn, NY), rabbit anti-laminin (Sigma-Aldrich), mouse anti-αvβ3 integrin (LM609; EMD Millipore), rat anti–β1 integrin (AIIB2; Developmental Studies Hybridoma Bank), mouse anti-GM130 (BD Transduction Laboratories), mouse anti-ZO-1 (Life Technologies), and rabbit anti–β-catenin (H-102; Santa Cruz Biotechnology). The following secondary antibodies were used: goat anti–mouse IgG Alexa Fluor 488, goat anti–rat IgG Alexa Fluor 555, goat anti–rabbit IgG Alexa Fluor 488 (Life Technologies), and donkey anti–rabbit IgG Dylight649 (Thermo Fisher Scientific). Nuclei were stained with Hoechst 33342, and filamentous actin was stained with rhodamine phalloidin (Life Technologies).

Cell culture and hydrogel formation

MDCK strain II epithelial cells (Sigma-Aldrich) were maintained in Eagle's minimal essential media (EMEM; ATCC) supplemented with fetal bovine serum (Life Technologies) at 10% (vol/vol), penicillin (100 IU/ml) and streptomycin (100 µg/ml), and fungizone.

To prepare PEG hydrogels, PEG-4MAL (MW 22,000; Laysan Bio) was dissolved in a triethanolamine (TEA) buffer (4 mM in DPBS, pH 7.4). Adhesive and cross-linking peptides were custom-synthesized by AAPPTec. Adhesive peptide (GRGDSPC) or nonadhesive peptide (GRDGSPC) or combination was dissolved in TEA to generate functionalized PEG-4MAL precursor. Bis-cysteine cross-linking peptide GCRDGPQG↓IWGQDRCG (GPQ-W; ↓ denotes enzymatic cleavage site) or GCRDGPQG↓IAGQDRCG (GPQ-A) was dissolved in TEA at 1:1 maleimide/cysteine ratio after accounting for maleimide groups reacted with adhesive peptide. MDCK cells were resuspended at 5× final cell density in ice-cold serum-free EMEM and kept on ice. To form gels, adhesive peptide-functionalized PEG-4MAL macromer, cells, and cross-linking peptides were polymerized under serum-free conditions for 20 min before addition of complete medium. For studies with integrin-blocking antibodies, cells were preincubated (30 min, gentle rocking, at 22°C) in 0.1% bovine serum albumin in serum-free EMEM containing antibodies. For collagen gels, type I collagen from bovine tendon (3 mg/ml; Sigma-Aldrich) was mixed with cell suspension in serum-free media to achieve a 2.0 mg/ml type I collagen gels cast onto polyester permeable supports (0.4-µm pore; Corning) in a 24-well plate.

Hydrogel characterization

Hydrogel elastic modulus measurements were obtained by atomic force microscopy as described previously (Phelps et al., 2012) with cantilever spring constants of 10 mN/m, indentation speed of ∼2.0 µm/s, and force trigger set point of 1.25 nN. Using an MFP-3D-BIO atomic force microscope (Asylum Research), samples were probed under fluid conditions (ultrapure H_2O) using a pyramidal-tipped silicon nitride cantilever (Bruker). The force–indentation curve was obtained for each measurement and then analyzed with a Hertzian model for a pyramidal tip (Wavemetrics; IgorPro software routines), from which the Young's modulus values were calculated. The sample Poisson's ratio was assumed as 0.33, and a power law of 2.0 for the sample indentation distance was used to model tip geometry. Hydrogel mass swelling ratio and ligand tethering were measured as described previously (Phelps et al., 2012). The storage and loss moduli of hydrogels were assessed by dynamic oscillatory strain and frequency sweeps performed on a MCR 302 stress-controlled rheometer (Anton Paar) with a 9-mm diameter, 2° cone, and plate geometry. Oscillatory frequency sweeps were used to examine the storage and loss moduli ($\omega = 0.5–100$ rad s^{-1}) at a strain of 1%. For permeability experiments, hydrogels were incubated in FITC-labeled α-bungarotoxin (500 µg/ml), and signal intensity at the center of the gel sample was measured over time via confocal microscopy. Intensity profiles were fit to Fick's second law to obtain diffusion coefficients (Koutsopoulos et al., 2009). For ligand mobility studies, a Ti-E inverted microscope (Nikon) with Perfect Focus System and C2-Plus Confocal System with a Plan Fluor 40× (NA 0.75) objective was used for FRAP. Hydrogels were prepared with Alexa Fluor 594–labeled RGD peptide and allowed to equilibrate. Initial fluorescence intensity was measured using low laser power followed by photobleaching of a 0.20-mm-diameter circle within the hydrogel at 38 mW with 561-nm laser for 10 s. The recovery of fluorescence was monitored for up to 5.8 h. Image series were imported into MATLAB, where background subtraction and correction for incidental bleaching during image acquisition were applied to data extracted from the bleached region. For analysis of cell-dependent RGD peptide clustering, MDCK cells were cultured within hydrogels presenting a mixture of Alexa Fluor 594–labeled and control RGD peptide for 8 d. Fluorescence signal intensity was measured for 35 min at different radial positions from the cell–hydrogel interface in the presence or absence of 10 µM Y-27632.

RGD labeling

RGD peptide was labeled using Alexa Fluor 594 NHS-ester dye (Life Technologies). To quantify labeling efficiency, size-exclusion chromatography was performed using a HiPrep Sephacryl S-100 HR gel filtration column on an AKTA Pure 25 chromatography system (GE Healthcare). DPBS supplemented with 0.15 M NaCl was used as the elution buffer to separate conjugated from unconjugated dye at a volumetric rate of 0.5 ml/min. Onboard absorbance readings of the eluted sample at 280/594 nm yielded a set of curves with peaks that corresponded to labeled and unlabeled peptide. Quantification of the area under the peaks was determined, and the ratio of the areas was used as the labeling efficiency.

Viability and proliferation assays

PEG-4MAL gels were incubated in 0.5% collagenase I (Worthington Biochemical), 2 µM calcein-AM (live), and 1 µM TOTO-3 iodide (dead; Life Technologies) in serum-free EMEM media until hydrogel was completely dissolved and cells settled at bottom of well. For collagen gels, gel was incubated in 2 µM calcein-AM and 1 µM TOTO-3 for 30 min and placed in chambered coverglass for imaging. Proliferation was assayed using the Click-iT EdU Imaging Kit (Life Technologies). Samples were imaged with Nikon Plan Fluor 10× (NA 0.30) or Plan Fluor 20× (NA 0.45) objectives in a Nikon Eclipse TE2000 inverted microscope and C1 Confocal System (EZ-C1 acquisition software) or Ti-E inverted microscope with Perfect Focus System and C2-Plus Confocal System (NIS Elements acquisition software). Cells were counted with ImageJ macros.

Immunofluorescence labeling of cysts

Gels were washed extensively in DPBS and fixed in 4% formaldehyde in DPBS for 15 min. Gels were incubated for 30 min in blocking buffer (1% bovine serum albumin, 1% goat serum, 0.1% fish skin gelatin, 0.5% Triton X-100, and 0.05% sodium azide in PBS). Samples were incubated in primary antibodies diluted in blocking buffer on an orbital shaker at 4°C overnight. Secondary antibodies and nuclear stain were diluted in blocking buffer and incubated on an orbital shaker at 4°C overnight. After immunostaining, cysts were recovered by collagenase digestion and mounted in 2% low-melt agarose. Fluorescent images for cyst scoring were captured with Nikon Plan Fluor 20× (NA 0.45) or Plan Apo 60× (NA 1.40) objectives in a Nikon Eclipse TE2000 inverted microscope and C1 Confocal System (EZ-C1 acquisition software) or Ti-E inverted microscope with Perfect Focus System and C2-Plus Confocal System (NIS Elements acquisition software). Cyst size was measured from fluorescent images of cyst cross sections using ImageJ FIJI package. The following scoring system was used for polarity: (1) interior apical polarity: a cyst cross section in which the interior of one or more lumens is lined with gp135 staining and the exterior of cyst lacks gp135 staining; (2) exterior apical polarity: a cyst cross section in which the interior of one or more lumens lacks gp135 staining and the exterior of cyst is lined with gp135 staining; (3) mixed apical polarity: a cyst cross section in which the interior of one or more lumens and the exterior of cysts show staining for gp135; and (4) no apical polarity: a cyst cross section with no staining for gp135. The following scoring system was used for lumen phenotypes: (1) single lumen: a cyst cross section having a single hollow space and outlined by a monolayer of cells; (2) partial lumen: a cyst cross section having a single hollow space bounded by multiple layers or groups of cells; (3) multiple lumens: a cyst cross section having multiple hollow spaces; and (4) no lumen: a cyst cross section having no hollow spaces. Fig. S3 presents exemplary cysts for each scoring category.

Statistical analyses

Results are presented either as mean ± SEM or percentages of population. Statistical analyses were performed using GraphPad Prism 6.0. For normally distributed data with equal variances, one-way analysis of variance with Tukey's multiple comparison test was used. For categorical data such as polarity and lumen phenotypes, χ^2 test with Bonferroni's test for multiple comparisons was used. A p-value <0.05 was considered significant.

Online supplemental material

Fig. S1 shows adhesive ligand mobility within PEG hydrogels. Fig. S2 shows epithelial cyst polarization and lumen formation. Fig. S3 shows that epithelial cysts within PEG-4MAL hydrogels exhibit canonical markers of apicobasal polarity and lumen phenotypes. Fig. S4 shows biophysical characterization and epithelial cyst phenotypes for PEG-4MAL hydrogel formulations generated with different macromer sizes. Fig. S5 shows epithelial cyst phenotypes for PEG-4MAL hydrogels presenting different adhesive peptides. Online supplemental material is available at http://www.jcb.org/cgi/content/full/jcb.201506055/DC1. Additional data are available in the JCB DataViewer at http://dx.doi.org/10.1083/jcb.201506055.dv.

Acknowledgments

We thank George Ojakian for the gp135/podocalyxin antibody as well as Asma Nusrat, Thomas Barker, and David Collard for helpful discussions.

This work was supported by National Institutes of Health grants R01-EB004496, R01-AR062368, and R01-AR062920. N.O. Enemchukwu was supported by the GEM graduate fellowship, Ford Foundation fellowship, NASA Harriet G. Jenkins predoctoral fellowship, and United Negro College Fund/Merck dissertation fellowship. T. Bongiorno and J.R. García are supported by the Cell and Tissue Engineering National Institutes of Health Biotechnology training grant (T32-GM008433). R. Cruz-Acuña is supported by a National Science Foundation graduate fellowship.

The authors declare no competing financial interests.

Submitted: 10 June 2015
Accepted: 2 December 2015

References

Barcellos-Hoff, M.H., J. Aggeler, T.G. Ram, and M.J. Bissell. 1989. Functional differentiation and alveolar morphogenesis of primary mammary cultures on reconstituted basement membrane. *Development.* 105:223–235.

Beck, J.N., A. Singh, A.R. Rothenberg, J.H. Elisseeff, and A.J. Ewald. 2013. The independent roles of mechanical, structural and adhesion characteristics of 3D hydrogels on the regulation of cancer invasion and dissemination. *Biomaterials.* 34:9486–9495. http://dx.doi.org/10.1016/j.biomaterials.2013.08.077

Bryant, D.M., and K.E. Mostov. 2008. From cells to organs: building polarized tissue. *Nat. Rev. Mol. Cell Biol.* 9:887–901. http://dx.doi.org/10.1038/nrm2523

Canal, T., and N.A. Peppas. 1989. Correlation between mesh size and equilibrium degree of swelling of polymeric networks. *J. Biomed. Mater. Res.* 23:1183–1193. http://dx.doi.org/10.1002/jbm.820231007

Flory, P.J., and J. Rehner. 1943. Statistical mechanics of cross-linked polymer networks II. Swelling. *J. Chem. Phys.* 11:1183–1193.

Ghajar, C.M., X. Chen, J.W. Harris, V. Suresh, C.C. Hughes, N.L. Jeon, A.J. Putnam, and S.C. George. 2008. The effect of matrix density on the regulation of 3-D capillary morphogenesis. *Biophys. J.* 94:1930–1941. http://dx.doi.org/10.1529/biophysj.107.120774

Gill, B.J., D.L. Gibbons, L.C. Roudsari, J.E. Saik, Z.H. Rizvi, J.D. Roybal, J.M. Kurie, and J.L. West. 2012. A synthetic matrix with independently tunable biochemistry and mechanical properties to study epithelial morphogenesis and EMT in a lung adenocarcinoma model. *Cancer Res.* 72:6013–6023. http://dx.doi.org/10.1158/0008-5472.CAN-12-0895

Hoffman, M.P., M. Nomizu, E. Roque, S. Lee, D.W. Jung, Y. Yamada, and H.K. Kleinman. 1998. Laminin-1 and laminin-2 G-domain synthetic peptides bind syndecan-1 and are involved in acinar formation of a human submandibular gland cell line. *J. Biol. Chem.* 273:28633–28641. http://dx.doi.org/10.1074/jbc.273.44.28633

Huebsch, N., P.R. Arany, A.S. Mao, D. Shvartsman, O.A. Ali, S.A. Bencherif, J. Rivera-Feliciano, and D.J. Mooney. 2010. Harnessing traction-mediated manipulation of the cell/matrix interface to control stem-cell fate. *Nat. Mater.* 9:518–526. http://dx.doi.org/10.1038/nmat2732

Hughes, C.S., L.M. Postovit, and G.A. Lajoie. 2010. Matrigel: a complex protein mixture required for optimal growth of cell culture. *Proteomics.* 10:1886–1890. http://dx.doi.org/10.1002/pmic.200900758

Khetan, S., M. Guvendiren, W.R. Legant, D.M. Cohen, C.S. Chen, and J.A. Burdick. 2013. Degradation-mediated cellular traction directs stem cell fate in covalently crosslinked three-dimensional hydrogels. *Nat. Mater.* 12:458–465. http://dx.doi.org/10.1038/nmat3586

Klinowska, T.C., J.V. Soriano, G.M. Edwards, J.M. Oliver, A.J. Valentijn, R. Montesano, and C.H. Streuli. 1999. Laminin and beta1 integrins are crucial for normal mammary gland development in the mouse. *Dev. Biol.* 215:13–32. http://dx.doi.org/10.1006/dbio.1999.9435

Kloxin, A.M., A.M. Kasko, C.N. Salinas, and K.S. Anseth. 2009. Photodegradable hydrogels for dynamic tuning of physical and chemical properties. *Science.* 324:59–63. http://dx.doi.org/10.1126/science.1169494

Koutsopoulos, S., L.D. Unsworth, Y. Nagai, and S. Zhang. 2009. Controlled release of functional proteins through designer self-assembling peptide nanofiber hydrogel scaffold. *Proc. Natl. Acad. Sci. USA.* 106:4623–4628. http://dx.doi.org/10.1073/pnas.0807506106

Levental, K.R., H. Yu, L. Kass, J.N. Lakins, M. Egeblad, J.T. Erler, S.F. Fong, K. Csiszar, A. Giaccia, W. Weninger, et al. 2009. Matrix crosslinking forces tumor progression by enhancing integrin signaling. *Cell.* 139:891–906. http://dx.doi.org/10.1016/j.cell.2009.10.027

Lubarsky, B., and M.A. Krasnow. 2003. Tube morphogenesis: making and shaping biological tubes. *Cell.* 112:19–28. http://dx.doi.org/10.1016/S0092-8674(02)01283-7

Lutolf, M.P., G.P. Raeber, A.H. Zisch, N. Tirelli, and J.A. Hubbell. 2003. Cell-responsive synthetic hydrogels. *Adv. Mater.* 15:888–892. http://dx.doi.org/10.1002/adma.200304621

Martín-Belmonte, F., W. Yu, A.E. Rodríguez-Fraticelli, A.J. Ewald, Z. Werb, M.A. Alonso, and K. Mostov. 2008. Cell-polarity dynamics controls the mechanism of lumen formation in epithelial morphogenesis. *Curr. Biol.* 18:507–513. http://dx.doi.org/10.1016/j.cub.2008.02.076

McAteer, J.A., A.P. Evan, E.E. Vance, and K.D. Gardner. 1986. MDCK cysts: An in vitro model of epithelial cyst formation and growth. *Methods Cell Sci.* 10:245–248.

Miles, A.J., A.P. Skubitz, L.T. Furcht, and G.B. Fields. 1994. Promotion of cell adhesion by single-stranded and triple-helical peptide models of basement membrane collagen alpha 1(IV)531-543. Evidence for conformationally dependent and conformationally independent type IV collagen cell adhesion sites. *J. Biol. Chem.* 269:30939–30945.

Mroue, R., and M.J. Bissell. 2013. Three-dimensional cultures of mouse mammary epithelial cells. *Methods Mol. Biol.* 945:221–250. http://dx.doi.org/10.1007/978-1-62703-125-7_14

Nelson, C.M., M.M. Vanduijn, J.L. Inman, D.A. Fletcher, and M.J. Bissell. 2006. Tissue geometry determines sites of mammary branching morphogenesis in organotypic cultures. *Science.* 314:298–300. http://dx.doi.org/10.1126/science.1131000

O'Brien, L.E., T.S. Jou, A.L. Pollack, Q. Zhang, S.H. Hansen, P. Yurchenco, and K.E. Mostov. 2001. Rac1 orientates epithelial apical polarity through effects on basolateral laminin assembly. *Nat. Cell Biol.* 3:831–838. http://dx.doi.org/10.1038/ncb0901-831

O'Brien, L.E., M.M. Zegers, and K.E. Mostov. 2002. Opinion: Building epithelial architecture: insights from three-dimensional culture models. *Nat. Rev. Mol. Cell Biol.* 3:531–537. http://dx.doi.org/10.1038/nrm859

O'Brien, L.E., W. Yu, K. Tang, T.S. Jou, M.M. Zegers, and K.E. Mostov. 2006. Morphological and biochemical analysis of Rac1 in three-dimensional epithelial cell cultures. *Methods Enzymol.* 406:676–691. http://dx.doi.org/10.1016/S0076-6879(06)06053-8

Paszek, M.J., N. Zahir, K.R. Johnson, J.N. Lakins, G.I. Rozenberg, A. Gefen, C.A. Reinhart-King, S.S. Margulies, M. Dembo, D. Boettiger, et al. 2005. Tensional homeostasis and the malignant phenotype. *Cancer Cell.* 8:241–254. http://dx.doi.org/10.1016/j.ccr.2005.08.010

Patterson, J., and J.A. Hubbell. 2010. Enhanced proteolytic degradation of molecularly engineered PEG hydrogels in response to MMP-1 and MMP-2. *Biomaterials.* 31:7836–7845. http://dx.doi.org/10.1016/j.biomaterials.2010.06.061

Phelps, E.A., N.O. Enemchukwu, V.F. Fiore, J.C. Sy, N. Murthy, T.A. Sulchek, T.H. Barker, and A.J. García. 2012. Maleimide cross-linked bioactive PEG hydrogel exhibits improved reaction kinetics and cross-linking for cell encapsulation and in situ delivery. *Adv. Mater.* 24:64–70: 2. http://dx.doi.org/10.1002/adma.201103574

Phelps, E.A., D.M. Headen, W.R. Taylor, P.M. Thulé, and A.J. García. 2013. Vasculogenic bio-synthetic hydrogel for enhancement of pancreatic islet engraftment and function in type 1 diabetes. *Biomaterials.* 34:4602–4611. http://dx.doi.org/10.1016/j.biomaterials.2013.03.012

Provenzano, P.P., D.R. Inman, K.W. Eliceiri, and P.J. Keely. 2009. Matrix density-induced mechanoregulation of breast cell phenotype, signaling and gene expression through a FAK-ERK linkage. *Oncogene.* 28:4326–4343. http://dx.doi.org/10.1038/onc.2009.299

Raza, A., C.S. Ki, and C.C. Lin. 2013. The influence of matrix properties on growth and morphogenesis of human pancreatic ductal epithelial cells in 3D. *Biomaterials.* 34:5117–5127. http://dx.doi.org/10.1016/j.biomaterials.2013.03.086

Roignot, J., X. Peng, and K. Mostov. 2013. Polarity in mammalian epithelial morphogenesis. *Cold Spring Harb. Perspect. Biol.* 5:a013789. http://dx.doi.org/10.1101/cshperspect.a013789

Salimath, A.S., E.A. Phelps, A.V. Boopathy, P.L. Che, M. Brown, A.J. García, and M.E. Davis. 2012. Dual delivery of hepatocyte and vascular endothelial growth factors via a protease-degradable hydrogel improves cardiac function in rats. *PLoS One.* 7:e50980. http://dx.doi.org/10.1371/journal.pone.0050980

Suzuki, N., H. Nakatsuka, M. Mochizuki, N. Nishi, Y. Kadoya, A. Utani, S. Oishi, N. Fujii, H.K. Kleinman, and M. Nomizu. 2003. Biological activities of homologous loop regions in the laminin alpha chain G domains. *J. Biol. Chem.* 278:45697–45705. http://dx.doi.org/10.1074/jbc.M304667200

Teräväinen, T.P., S.M. Myllymäki, J. Friedrichs, N. Strohmeyer, J.V. Moyano, C. Wu, K.S. Matlin, D.J. Muller, and A. Manninen. 2013. αV-integrins are required for mechanotransduction in MDCK epithelial cells. *PLoS One.* 8:e71485. http://dx.doi.org/10.1371/journal.pone.0071485

Weaver, S.A., B. Wolters, N. Ito, A.M. Woskowicz, K. Kaneko, Y. Shitomi, M. Seiki, and Y. Itoh. 2014. Basal localization of MT1-MMP is essential for epithelial cell morphogenesis in 3D collagen matrix. *J. Cell Sci.* 127:1203–1213. http://dx.doi.org/10.1242/jcs.135236

Weiss, M.S., B.P. Bernabé, A. Shikanov, D.A. Bluver, M.D. Mui, S. Shin, L.J. Broadbelt, and L.D. Shea. 2012. The impact of adhesion peptides within hydrogels on the phenotype and signaling of normal and cancerous mammary epithelial cells. *Biomaterials.* 33:3548–3559. http://dx.doi.org/10.1016/j.biomaterials.2012.01.055

Wozniak, M.A., R. Desai, P.A. Solski, C.J. Der, and P.J. Keely. 2003. ROCK-generated contractility regulates breast epithelial cell differentiation in response to the physical properties of a three-dimensional collagen matrix. *J. Cell Biol.* 163:583–595. http://dx.doi.org/10.1083/jcb.200305010

Yu, W., A. Datta, P. Leroy, L.E. O'Brien, G. Mak, T.S. Jou, K.S. Matlin, K.E. Mostov, and M.M. Zegers. 2005. Beta1-integrin orients epithelial polarity via Rac1 and laminin. *Mol. Biol. Cell.* 16:433–445. http://dx.doi.org/10.1091/mbc.E04-05-0435

Zhang, H., F. Landmann, H. Zahreddine, D. Rodriguez, M. Koch, and M. Labouesse. 2011. A tension-induced mechanotransduction pathway promotes epithelial morphogenesis. *Nature.* 471:99–103. http://dx.doi.org/10.1038/nature09765

Zhang, X., G. Mernaugh, D.H. Yang, L. Gewin, M.B. Srichai, R.C. Harris, J.M. Iturregui, R.D. Nelson, D.E. Kohan, D. Abrahamson, et al. 2009. beta1 integrin is necessary for ureteric bud branching morphogenesis and maintenance of collecting duct structural integrity. *Development.* 136:3357–3366. http://dx.doi.org/10.1242/dev.036269

6.3 Weaver JD, Headen DM, Aquart J, Johnson CT, Shea LD, Shirwan J, and García AJ. Vasculogenic hydrogel enhances marginal islet mass engraftment and function in extrahepatic transplant sites. *Science Advances.* 2017 Jun 2. DOI: 10.1126/sciadv.1700184

SCIENCE ADVANCES | RESEARCH ARTICLE

BIOENGINEERING

Vasculogenic hydrogel enhances islet survival, engraftment, and function in leading extrahepatic sites

Jessica D. Weaver,[1,2] Devon M. Headen,[1,2] Jahizreal Aquart,[2] Christopher T. Johnson,[2,3] Lonnie D. Shea,[4,5] Haval Shirwan,[6,7] Andrés J. García[1,2]*

Islet transplantation is a promising alternative therapy for insulin-dependent patients, with the potential to eliminate life-threatening hypoglycemic episodes and secondary complications of long-term diabetes. However, widespread application of this therapy has been limited by inadequate graft function and longevity, in part due to the loss of up to 60% of the graft in the hostile intrahepatic transplant site. We report a proteolytically degradable synthetic hydrogel, functionalized with vasculogenic factors for localized delivery, engineered to deliver islet grafts to extrahepatic transplant sites via in situ gelation under physiological conditions. Hydrogels induced differences in vascularization and innate immune responses among subcutaneous, small bowel mesentery, and epididymal fat pad transplant sites with improved vascularization and reduced inflammation at the epididymal fat pad site. This biomaterial-based strategy improved the survival, engraftment, and function of a single pancreatic donor islet mass graft compared to the current clinical intraportal delivery technique. This biomaterial strategy has the potential to improve clinical outcomes in islet autotransplantation after pancreatectomy and reduce the burden on donor organ availability by maximizing graft survival in clinical islet transplantation for type 1 diabetes patients.

INTRODUCTION

Type 1 diabetes mellitus, a chronic condition characterized by the autoimmune destruction of pancreatic islets and an inability to regulate blood glucose, affects millions of patients worldwide (*1*). Exogenous insulin administration does not accurately recapitulate normal glucose dynamics, and diabetic patients face recurrent and life-threatening hypoglycemic episodes and serious secondary complications, such as retinopathy, neuropathy, and nephropathy (*2*). Islet transplantation is a promising cell therapy for the treatment of type 1 diabetes mellitus, with the potential to restore normal blood glucose regulation and eliminate secondary complications (*3*). Clinical trials with intrahepatic allogeneic islet transplantation have demonstrated insulin independence in diabetic patients, but the median duration of insulin independence is only 35 months and requires multiple donor pancreata (*4*). Although clinically accessible for islet delivery, the hepatic vasculature is an inhospitable transplant site, as evidenced by suboptimal performance of grafts in islet autotransplantation after total pancreatectomy (*5*, *6*). Instant blood-mediated inflammatory responses to intraportally infused islets contribute to rapid graft destruction (*7*–*9*), resulting in an immediate loss of 50 to 60% of the graft (*10*), a substantial barrier to the translation of this therapy. Further graft destruction is mediated by both innate and acquired immune responses, even with chronic immunosuppressive regimens (*11*).

Various extrahepatic transplant sites have been explored to avoid instant blood-mediated inflammatory response–instigated graft loss, including the subcutaneous (SUBQ) space (*12*–*16*) and laparoscopically accessible intraperitoneal locations, such as the small bowel mesentery (SBM) (*17*, *18*) and omentum (*19*–*22*) or the murine omentum equivalent, the epididymal fat pad (EFP) (*23*–*25*). Although the accessibility of these extrahepatic sites is appealing, these tissues present varying degrees of vascular supply and inflammatory responses, which influence islet survival, engraftment, and function (*26*–*28*). Preclinical models using intraportal, renal subcapsular, or splenic subcapsular transplant sites have demonstrated that reestablishment of blood flow to islets requires days to weeks (*29*–*31*), resulting in ischemic conditions during the revascularization period and a vascular bed with lower vessel density and oxygen tension than in the native pancreas (*32*, *33*). This inadequate revascularization of transplanted islets is a major cause of reduced islet viability, function, and engraftment (*34*–*36*). Delivery of provascularization factors via genetic manipulation of islets or biomaterials has shown improved vascularization and islet function (*24*, *37*–*42*). However, these strategies are hindered by suboptimal pharmacokinetics, inadequate delivery matrices, and technical and safety considerations, and evaluate impracticably large islet masses in a limited diversity of sites.

Here, we report a synthetic hydrogel vehicle engineered to enhance extrahepatic site vascularization. We evaluate the impact of this vasculogenic hydrogel on islet engraftment and function in three extrahepatic sites: SUBQ, SBM, and EFP. This versatile hydrogel facilitates minimally invasive and facile cell delivery to extrahepatic sites and enhances islet survival compared to the suboptimal clinical intrahepatic site. Furthermore, this biomaterial-based strategy enables the restoration of euglycemia via the islet yield from a single pancreatic donor, which is a clinical limitation in diabetes reversal due to limited donor availability and increased rejection risk posed by multiple donors, suggesting that its implementation could improve clinical outcomes in islet autotransplantation after total pancreatectomy and reduce the burden on donor organ availability in clinical islet transplantation for type 1 diabetes mellitus patients.

[1]Woodruff School of Mechanical Engineering, Georgia Institute of Technology, Atlanta, GA, 30332, USA. [2]Petit Institute for Bioengineering and Bioscience, Georgia Institute of Technology, Atlanta, GA, 30332, USA. [3]Coulter Department of Biomedical Engineering, Georgia Tech and Emory University, Atlanta, GA, 30332, USA. [4]Department of Biomedical Engineering and Department of Chemical Engineering, University of Michigan, Ann Arbor, MI, 48109, USA. [5]Department of Obstetrics and Gynecology, Feinberg School of Medicine, Northwestern University, Suite 03-2303, 250 East Superior Street, Chicago, IL 60611, USA. [6]Institute of Cellular Therapeutics, Department of Microbiology and Immunology, University of Louisville School of Medicine, Louisville, KY, 40202, USA. [7]FasCure Therapeutics LLC, 300 East Market Street, Louisville, KY 40202, USA.
*Corresponding author. Email: andres.garcia@me.gatech.edu

RESULTS

Localized vascular endothelial growth factor delivery via synthetic hydrogel induces vascularization to different degrees among extrahepatic transplant sites

We explored the ability of a synthetic hydrogel to promote localized vascularization in extrahepatic transplant sites via controlled delivery of vascular endothelial growth factor (VEGF) (Fig. 1). This poly(ethylene glycol) (PEG) hydrogel consists of maleimide-functionalized, four-arm macromers cross-linked into a network using protease-degradable peptides (*17*, *43*). The hydrogel is functionalized with RGD adhesive peptide to promote cell adhesion and ingrowth; VEGF is tethered into the hydrogel network and released in a sustained, on-demand fashion, as infiltrating host cells remodel the gel via proteolytic degradation within a 2- to 4-week period (*17*). VEGF-containing (PEG-VEGF) and control (PEG) hydrogels (50 μl) were polymerized in situ within the SUBQ space or onto SBM or EFP tissue in C57BL/6J recipient mice (fig. S1). Two or 4 weeks after implantation, mice were perfused with fluorescently labeled lectin to identify functional vasculature. Explanted grafts were whole mount–imaged using confocal microscopy (Fig. 2A); the pancreas, liver, and kidney were imaged for reference to native tissue, the current clinical site, and a common preclinical implant site, respectively. Several parameters characterizing the resulting vascularization were evaluated for PEG-VEGF (purple box plot) and control PEG hydrogels (blue box plot) at weeks 2 (open box plots) and 4 (filled box plots) (Fig. 2, B to E) and compared to pancreatic vasculature (dashed line). Differences in vascularization responses to PEG-VEGF hydrogels were observed among alternative transplant sites, particularly by the fractional area metric (Fig. 2B and table S1). By week 4, the SUBQ site exhibited minimal vascularization compared to the pancreas reference ($P < 0.002$ and $P < 0.01$ for PEG and PEG-VEGF, respectively), and vascularization at this site was relatively insensitive to VEGF delivery; the SBM site had comparable vessel fractional area to the pancreas reference for PEG-VEGF groups and little evident improvement over PEG within the same site. Notably, by week 4, PEG-VEGF hydrogels delivered to the EFP enhanced vascularization fractional area, total branch length, junction number, and branch number to significantly greater levels than the SUBQ/PEG-VEGF site (table S1). Together, this analysis demonstrates transplant site–dependent differences in vasculogenesis in response to VEGF-delivering synthetic hydrogels.

Extrahepatic sites exhibit varying leukocyte densities in response to synthetic gels

We examined transplant site inflammatory cell densities 4 weeks after hydrogel delivery as site-specific innate immune responses may influence islet engraftment and survival (*44*). PEG-VEGF and control PEG hydrogels were delivered to the three transplant sites, and inflammatory cell recruitment was evaluated by immunostaining (Fig. 3A). Significant differences in CD45-positive leukocyte percent area were observed among extrahepatic transplant sites (Fig. 3B and table S2), with high leukocyte presence in the SUBQ site (2.0 and 1.1% for PEG and PEG-VEGF, respectively) and decreasing densities for SBM (0.3% for both PEG and PEG-VEGF) and EFP sites (0.2 and 0.03% for PEG and PEG-VEGF, respectively), with the SUBQ site exhibiting an 80-fold ($P < 0.001$) and 40-fold higher ($P < 0.05$) leukocyte expression than EFP/PEG-VEGF for PEG and PEG-VEGF groups, respectively. This trend was also observed for the leukocyte myeloid marker CD11b. These site-specific differences in inflammatory cell recruitment are inversely proportional, by linear nonparametric correlation, to the trends in vascular fractional area for both CD11b ($P = 0.0583$) and CD45 ($P = 0.0167$) markers (fig. S2), where PEG-VEGF recipient sites exhibited reduced resident leukocyte density over PEG controls. Overall, these results show transplant site–dependent responses to vasculogenic hydrogels, with the EFP site demonstrating the lowest degree of inflammatory cell recruitment and equivalent levels of vascularization as native pancreatic tissue.

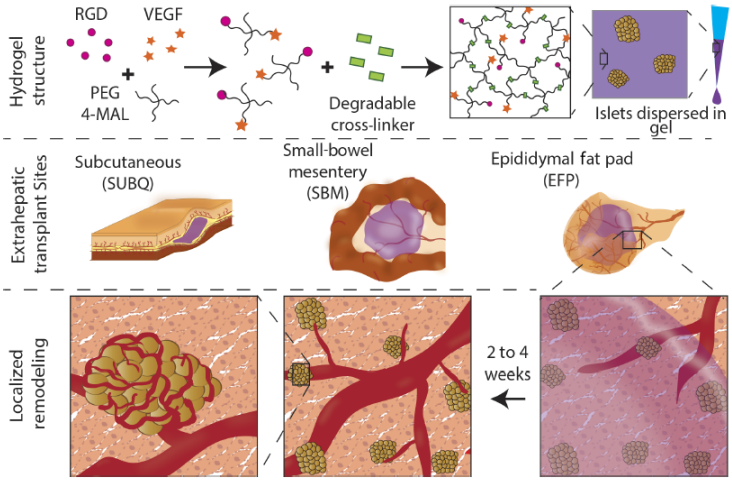

Fig. 1. Schematic demonstrating vasculogenic, proteolytically degradable synthetic hydrogel structure, islet delivery strategy, and localized gel remodeling within extrahepatic transplant sites.

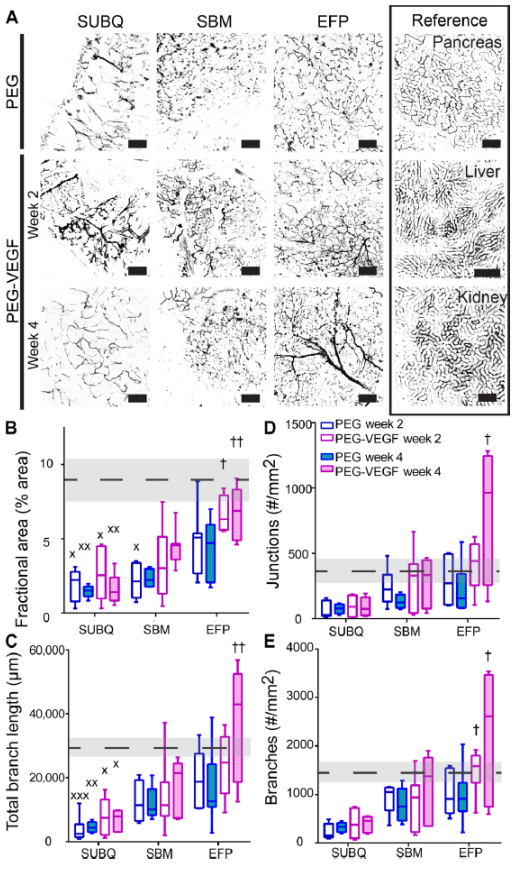

Fig. 2. Localized VEGF enhances vascularization in extrahepatic transplant sites. (**A**) Recipients of PEG-only or VEGF-presenting hydrogels were lectin-perfused at 2 or 4 weeks, and excised grafts were whole mount–imaged. Scale bars, 200 μm. Vascular characteristics of blood vessel fractional area (**B**), total branch length (**C**), junction number (**D**), and branch number per field of view (FOV) (**E**). Dashed line and shaded region represent average and SEM for pancreas reference, respectively. Minimum to maximum box-and-whisker plots, $n = 5$ to 7 per group. † versus SUBQ within the same time point ($^{\dagger\dagger}P < 0.01$ and $^{\dagger}P < 0.05$); × versus pancreas control ($^{\times\times\times}P < 0.001$, $^{\times\times}P < 0.01$, and $^{\times}P < 0.05$); evaluated by Kruskal-Wallis nonparametric tests with Dunn's multiple comparison.

VEGF hydrogel enhances islet engraftment and function in extrahepatic sites

We next examined the effects of vasculogenic hydrogels on the engraftment and function of a single pancreatic donor islet mass in extrahepatic transplant sites, a clinical limitation for diabetes reversal in islet autotransplantation after pancreatectomy and clinical islet transplantation for type 1 diabetes mellitus. We delivered 600 syngeneic islet equivalents (IEQs), the yield from a single C57BL/6J donor mouse, to the SUBQ, SBM, and EFP sites in streptozotocin-induced diabetic mice using PEG-VEGF and control PEG hydrogels. Nonfasting blood glucose (Fig. 4A) was continuously monitored for 5 weeks. Blood glucose values stabilized in most of the individuals by day 15 postoperatively (fig. S3). Average blood glucose levels for islets transplanted with PEG-VEGF to EFP (EFP/PEG-VEGF) were significantly lower than those for islets delivered to SUBQ and SBM using VEGF hydrogels ($P < 0.0001$ and $P < 0.005$ for SUBQ/PEG-VEGF and SBM/PEG-VEGF, respectively) (Fig. 4A). A separate study demonstrated stable, long-term euglycemia out to 100 days for islets delivered to EFP with PEG-VEGF gels (fig. S4A), and islet graft removal ($n = 1$) resulted in a return to hyperglycemia, confirming islet graft–dependent function. Additionally, robust insulin staining and proximal CD31-positive blood vessels (fig. S4, B and C) further confirmed long-term EFP/PEG-VEGF islet engraftment and function. Islets transplanted via hydrogel to the EFP outperformed islets transplanted into SUBQ and SBM sites, with 60 and 75% diabetes reversal within 30 days for EFP/PEG and EFP/PEG-VEGF groups, respectively (Fig. 4C), compared to 0% in the same period for intrahepatic controls (fig. S5, A and B). An intraperitoneal glucose tolerance test (IPGTT) evaluated graft responsiveness to bolus glucose 35 days after transplantation (Fig. 4D). Islets delivered via PEG-VEGF and PEG control hydrogels to EFP and SBM sites performed similarly to glucose bolus, indicating sufficient islet engraftment to respond to a single glucose challenge, whereas subjects receiving islets in PEG-VEGF to the SUBQ site exhibited minimal glucose responsiveness, evidencing limited islet engraftment. An insufficient number of SUBQ/PEG subjects survived to the 35-day time point to include in IPGTT and body weight analysis (fig. S6). Subject body weight was monitored continuously for the duration of the study as an additional metric of graft performance (Fig. 4E), and only the SUBQ/PEG-VEGF group exhibited substantial weight loss (5%) by the end point, further illustrating the poorest islet engraftment in this site among all groups.

To examine functional vascular remodeling of islet grafts delivered with hydrogels, we perfused subjects with labeled lectin at the end point of the study, and whole-mount graft imaging enabled three-dimensional (3D) visualization of functional vasculature (green) and insulin-positive (magenta) transplanted islets (Fig. 4F). Engrafted islets were easily locatable, as the islet organoid vasculature presents as a tight, organized, glomerular-like grouping of dense, lectin-positive blood vessels. The observed density of engrafted islets varied between extrahepatic transplant sites, where the EFP site exhibited numerous vascularized islets, the SBM site displayed intermediate numbers of vascularized islets, and very few vascularized islets were observed in the SUBQ site (fig. S7). Notably, insulin staining for grafts excised at day 35 was exclusively limited to vascularized islets, and no lectin-negative islets were observed. In addition, a higher density of vascularized islets was observed for PEG-VEGF gels, especially for the EFP site (fig. S7). Finally, analysis of normoglycemic subjects transplanted with islets in the EFP via PEG-VEGF gels also showed vascularized islets 100 days after transplantation (fig. S4C). These patterns of islet engraftment and vascularization mirror the functional performance of the grafts, indicating that islet survival, engraftment, and functionality are dependent on integration with transplant site vasculature.

The SUBQ/PEG group experienced the poorest survival ($P < 0.05$; fig. S6), due to hypoglycemic events occurring within the first week after transplant, which may be partly attributable to an elevated innate immune response and corresponding acute loss of transplanted islets, resulting in rapid insulin release, also referred to as insulin "dumping" (Figs. 3 and 4) (*45*). Together, these results demonstrate transplant site–specific differences in vascularization and inflammatory responses

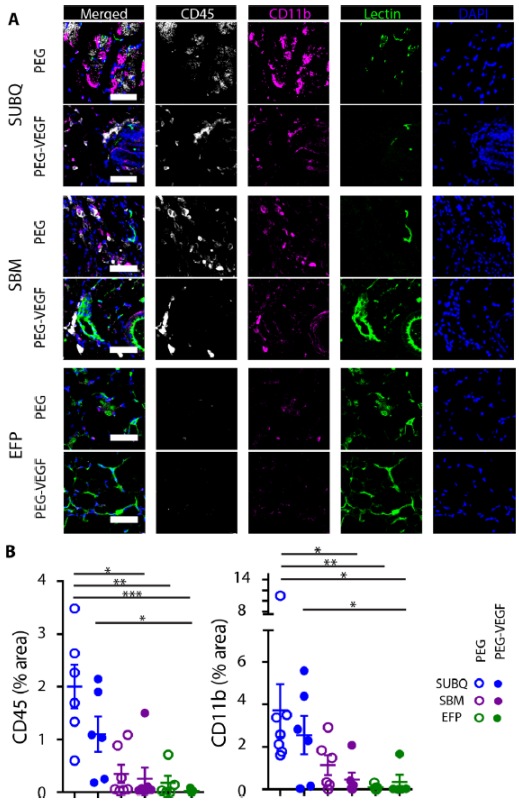

Fig. 3. Leukocyte density varies within extrahepatic transplant sites 4 weeks after hydrogel transplantation. (**A**) Extrahepatic transplant site tissue explanted at week 4 after implantation was stained for CD45 (white) and CD11b (magenta) and was imaged for functional vasculature [lectin (green)] and cell nuclei [DAPI (4′,6-diamidino-2-phenylindole) (blue)]. Scale bars, 50 μm. (**B**) CD11b and CD45 staining was quantified and normalized to FOV area. $n = 4$ to 7 subjects per group. *$P < 0.05$, **$P < 0.01$, and ***$P < 0.001$, evaluated by Kruskal-Wallis nonparametric tests with Dunn's multiple comparison.

to the hydrogel vehicle and a strong correlation between these responses and islet graft function. Hydrogel-based delivery of a single pancreatic donor mass of islets to the EFP via PEG-VEGF gels resulted in the most consistent and accelerated return to euglycemia in this nonfasting murine diabetic model.

In vivo tracking demonstrates vasculogenic hydrogel–dependent islet survival in extrahepatic sites

The immediate loss of a large proportion of donor islets during intrahepatic infusion requires multiple donors per recipient and presents a significant barrier to the effective and widespread application of islet replacement therapy (*34*, *46*). To directly assess transplanted islet survival in extrahepatic sites following hydrogel-based delivery, we transplanted islets constitutively expressing luciferase (Luc) and green fluorescent protein (GFP) using PEG hydrogels to the SUBQ and EFP sites and tracked them over time using in vivo bioluminescent imaging. NOD-SCID (nonobese diabetic–severe combined immunodeficient) recipients were chosen to prevent immune rejection of Luc^+GFP^+ islets from a C57BL/6J;FVB background. Pilot studies with various ratios of Luc^+GFP^+/unlabeled islets (a total of 600 IEQs) in immunocompetent C57BL/6J (B6) recipients determined that an optimal loading of 200-IEQ Luc^+GFP^+ islets provided sufficient signal to track islet graft survival and loss and confirmed the expected loss in luminescence signal upon immune rejection beginning 21 days after transplantation (fig. S8). To replicate the graft conditions of our syngeneic studies, 400-IEQ B6 islets were codelivered with 200-IEQ Luc^+GFP^+ islets to achieve a single pancreatic donor islet mass of 600 IEQs. The islets were delivered to extrahepatic sites in PEG-VEGF or control PEG hydrogels and imaged weekly following intraperitoneal luciferin injection (Fig. 5A). An intrahepatic control group was included to compare extrahepatic hydrogel delivery against the clinical standard for islet transplantation, where islets are infused through the portal vein via a saline solution and become entrapped in hepatic vasculature. Because of the possibility of thrombosis and loss of blood flow within the liver upon injection of hydrogel within the vasculature, no PEG or PEG-VEGF was delivered to the intraportal reference site.

Within 1 week after transplant, we observed a moderate increase in luciferase signal of Luc^+GFP^+ islets delivered to the EFP via PEG-VEGF (Fig. 5, B and C), and the signal remained elevated throughout the 35-day imaging window. The signal increase over day 0 readings is attributed to improved metabolic activity of islets after integration with host vasculature (see below). For islets delivered to the EFP using control PEG hydrogel, the luciferase signal remained constant over time but was twofold lower than the corresponding signal from islets delivered using PEG-VEGF hydrogel ($P < 0.01$; Fig. 5C). Islets delivered to the SUBQ site using PEG-VEGF hydrogel displayed a 16-fold lower signal than EFP/PEG at early time points and a 6-fold lower signal at later time points. Finally, islets transplanted in SUBQ using control gel showed loss in bioluminescence signal over time, reaching background levels after 21 days. Overall, the PEG-VEGF hydrogel vehicle enhanced islet bioluminescence signal compared to the control hydrogel for both transplant sites, and the EFP/PEG-VEGF group showed higher and sustained bioluminescence signal compared to all other groups (Fig. 5C), demonstrating that delivery of islets to EFP via PEG-VEGF provides superior islet survival compared to hydrogel control vehicle and other extrahepatic sites. To further support that this effect is because of improved islet integration, we perfused subjects with labeled lectin at day 35 to examine Luc^+GFP^+/B6 islet vascularization (Fig. 5D). Consistent with the syngeneic study, a high density of well-vascularized B6 (GFP-negative) and Luc^+GFP^+ islets was observed for islets transplanted into the EFP with PEG-VEGF. In contrast, fewer and poorly vascularized islets were detected in the SUBQ site.

We observed poor bioluminescence signal from intraportally infused islets (Fig. 5C), with a rapid loss in signal by week 2 after infusion. As with extrahepatic sites, an increase in signal was observed at week 1 after infusion and is likely due to a period of improved metabolic activity (fig. S9A). This rapid loss in bioluminescence signal is consistent with the well-documented instant blood-mediated inflammatory response–instigated intrahepatic islet graft destruction (*46*) and highlights the significant advantage of extrahepatic sites over intraportal delivery for islet survival. Intrahepatic islet loss was confirmed by whole-mount imaging of lectin and GFP at week 6 after infusion (fig. S9B), where only small, fragmented islets were found within the hepatic vasculature.

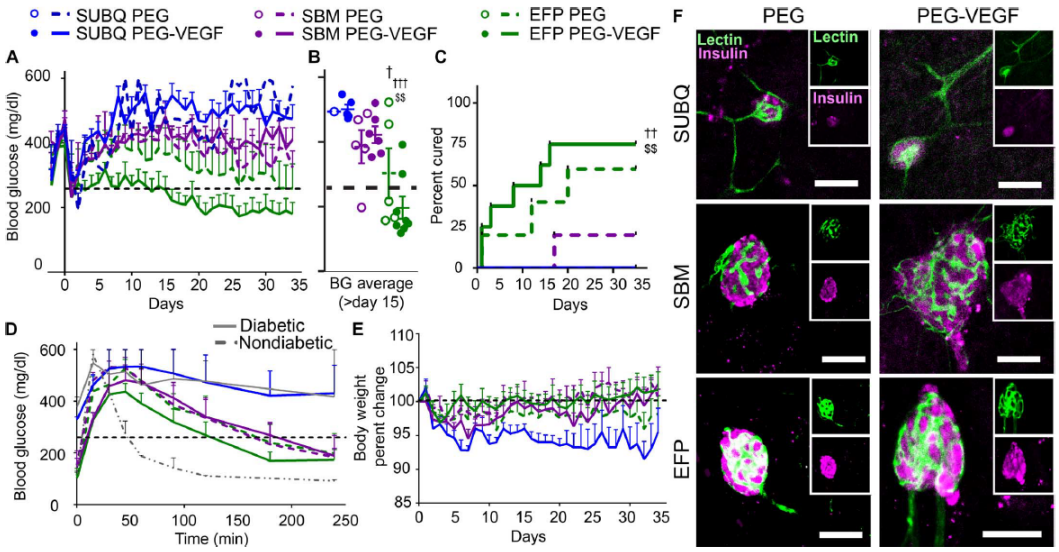

Fig. 4. Vasculogenic hydrogels promote engraftment and function of single pancreatic donor islet graft. Gels containing islets, either with or without VEGF, were delivered to extrahepatic sites. (**A**) Recipients were monitored daily for nonfasting blood glucose values for calculation of average blood glucose (beyond postoperative day 15) (**B**) and survival curve of diabetes reversal (**C**). Graft function was further evaluated by IPGTT on day 35 (**D**) and by monitoring of recipient body weight (**E**). (**F**) Whole-mount imaging of lectin (green)–perfused grafts enabled 3D visualization of engrafted islet vascular network. Error bars represent SEM. Scale bars, 100 μm. $n = 5$ to 8 per group. † versus SUBQ ($^{†††}P < 0.001$, $^{††}P < 0.01$, and $^{†}P < 0.05$); $ versus SBM within the same group (control or VEGF) ($^{\$\$}P < 0.01$). Blood glucose averages were evaluated by one-way analysis of variance (ANOVA), and survival curve analysis was performed using log-rank (Mantel-Cox) test.

We also analyzed the time-to-peak bioluminescence signal after luciferin injection for each imaging time point (Fig. 5E and fig. S10). The rate of bioluminescence signal production serves as an indirect metric of islet vascularization as faster bioluminescence signal kinetics can be attributed to greater islet integration with host vasculature. The EFP/PEG and EFP/PEG-VEGF groups showed a comparable decrease in time-to-peak signal to stable values within 7 days after transplant, suggesting establishment of islet vascularization within this time frame. The SUBQ/PEG-VEGF group decreased to a stable time-to-peak signal by week 2, whereas the SUBQ/PEG group maintained an elevated time-to-peak signal until week 5, providing further evidence that localized VEGF delivery accelerates and enhances site vascularization. Additionally, poor SUBQ site vascularization and subsequent luciferin transport kinetics may explain the 16-fold lower bioluminescence signal observed on day 0. As expected, intraportally infused islets demonstrated rapid times to bioluminescence signal peak throughout the study period due to direct exposure to systemic blood supply within the hepatic vasculature. The EFP/PEG, EFP/PEG-VEGF, and intraportal group demonstrated consistent reduced time-to-peak signal through the study period, significantly less than SUBQ/PEG ($P < 0.05$, $P < 0.005$, and $P < 0.001$, respectively), further evidencing superior islet vascularization within the EFP.

DISCUSSION

Here, we investigated the potential of three extrahepatic sites to sustain islet engraftment and function when delivered in a synthetic hydrogel carrier with or without VEGF and to improve graft survival over the current clinical technique. Although the islet transplantation field broadly recognizes that intrahepatic islet delivery is incompatible with establishing consistent insulin independence, there is a lack of consensus on the optimal extrahepatic site (*21*). A unique advantage of this hydrogel platform is the capacity to directly evaluate leading extrahepatic sites in parallel, and the use of a clinically relevant islet loading shows the feasibility of these sites for translation.

The SUBQ site has been repeatedly explored because it is readily accessible, potentially retrievable, and minimally invasive (*12*, *13*, *15*). However, the low degree of vascularization and heightened immune response in the SUBQ space demonstrated here and in a previous study (*13*) indicate that the SUBQ site is poorly suited for islet engraftment. Whereas the use of the SUBQ site is ubiquitous for the evaluation of vascularization strategies for tissue engineering applications, it is evident that the suitability of this site is application- and context-dependent. The SBM has a large, vascularized surface area to potentially accommodate large transplant volumes; however, this site is not readily retrievable without disturbance of the bowel, and the open nature of the site lends itself to potential islet loss into the peritoneal space. By contrast, the murine EFP, and equivalent human omentum, is a highly vascularized and easily manipulated tissue that can enclose delivered islets to create an isolated, retrievable islet graft. Additionally, the omentum is a nonvital organ that can be manipulated laparoscopically, and previous studies support our findings of reduced immune response, despite enhanced islet vascularization, which points to the omentum's superiority over alternative locations (*21*, *27*). These factors, combined with the omentum's high inherent vascularization and advantageous portal drainage (*18*, *47*), support this site's potential

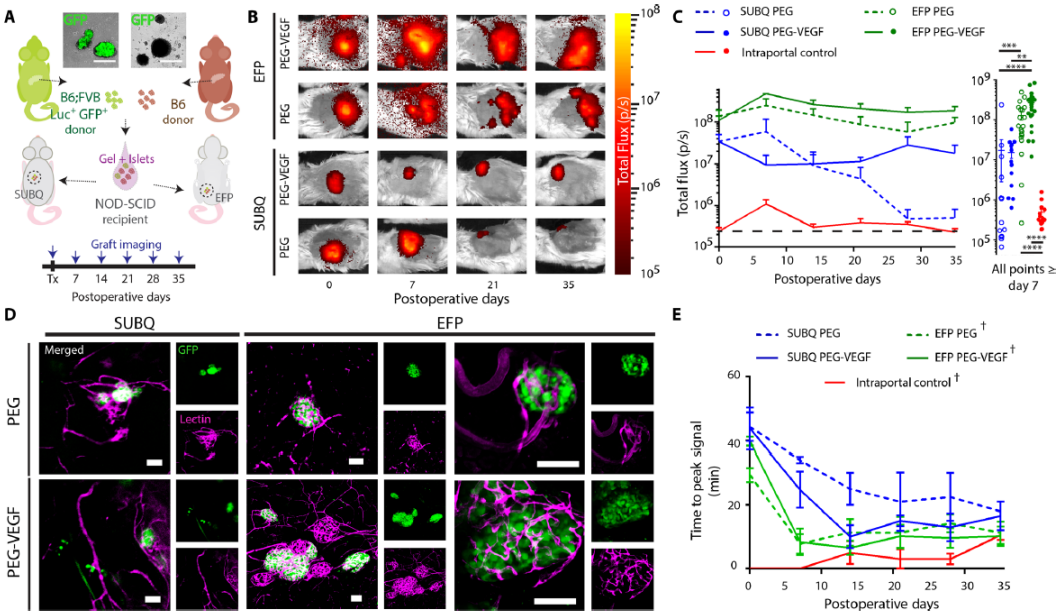

Fig. 5. In vivo bioluminescent islet tracking allows real-time monitoring of islet survival. (**A**) Gels containing Luc$^+$GFP$^+$/B6 hybrid islet grafts, either with or without VEGF, were delivered to extrahepatic sites as demonstrated in the schematic. (**B**) Representative in vivo bioluminescence images. (**C**) Recipients were monitored weekly for bioluminescent signal (left) by intraperitoneal luciferin injection, and cumulative bioluminescent data after day 7 demonstrate significantly enhanced survival in EFP-VEGF group. (**D**) Lectin perfusion at experimental end point allowed visualization of Luc$^+$GFP$^+$/B6 islet graft [GFP (green)] integration with host vasculature [lectin (magenta)]. High-magnification images of EFP/PEG and EFP/PEG-VEGF islets illustrate integration of vasculature with islet organoid structure. (**E**) Time-to-peak bioluminescent signal serves as an additional measure of graft vascularization over time. Error bars represent SEM. $n = 3$ to 4 per group. ****$P < 0.0001$, ***$P < 0.005$, and **$P < 0.01$, evaluated by Kruskal-Wallis nonparametric tests with Dunn's multiple comparison. $^{\dagger}P < 0.05$ versus SUBQ-PEG, evaluated by one-way ANOVA with repeated measures and Dunnett's multiple comparisons test. Scale bars, 100 μm.

for clinically relevant single pancreatic donor islet mass transplantation. This study highlights that careful consideration of transplant site microenvironments, particularly capacity for vasculogenesis and immune milieu, should inform islet graft transplant site selection in the clinical setting.

Our studies demonstrate that VEGF delivery using this synthetic hydrogel enhances islet survival, vascularization, and function. Early preclinical and clinical models exploring bolus or systemic VEGF delivery demonstrated poor outcomes as a therapeutic effect required large doses and resulted in temporary and leaky/dysfunctional vessels (*48*). In contrast, we and others (*49*–*52*) have shown that sustained VEGF delivery from appropriate biomaterial carriers results in stable, mature, and functional vessels. Furthermore, islets themselves secrete VEGF after transplantation (*53*), supported by our findings of functional organoid vasculature in PEG-only groups within this study.

Islet autotransplantation after total pancreatectomy uses the intrahepatic site for islet mass delivery from a single pancreatic source, and poor outcomes in the absence of the substantial complications of autoimmunity and immune rejection point to the hostility of the hepatic site (*54*). Although the use of syngeneic and immunodeficient mouse models in this study enabled evaluation of islet engraftment and survival in the context of islet autotransplantation after total pancreatectomy, it is unclear how systemic immunosuppression and autoimmunity may contribute to extrahepatic allogeneic islet graft survival and engraftment. The enhanced survival of extrahepatic syngeneic islet grafts observed in our study could translate to greater insulin independence for single pancreatic donor procedures in the context of clinical allogeneic islet transplantation for type 1 diabetes mellitus patients. Further investigations are required to fully elucidate the benefits of extrahepatic allogeneic islet transplantation with the added complexity of autoimmunity and/or systemic immunosuppression. Whereas systemic immunosuppressive agents have been shown to counteract islet revascularization to some degree (*55*), it is possible that this VEGF delivery system may counteract this effect by supplementing native islet VEGF expression and thereby potentially enhance islet revascularization in clinical islet transplantation for type 1 diabetes mellitus patients.

In summary, this study demonstrates that the degree of vascularization of an extrahepatic transplant site in response to a biomaterial vehicle plays a key role in islet engraftment, survival, and function and that VEGF delivery via synthetic hydrogels promotes sufficient engraftment of a single pancreatic donor islet mass to restore nonfasting euglycemia in a syngeneic murine model. These results suggest that islet delivery to the omentum within PEG-VEGF hydrogels may improve rates of insulin independence in patients receiving islet

autotransplantation after pancreatectomy and may greatly reduce the burden on donor organ availability in allogeneic islet transplantation to treat type 1 diabetes mellitus.

MATERIALS AND METHODS

Materials

Chemical reagents were purchased from Sigma-Aldrich, cell culture materials were obtained from Invitrogen, and peptides were synthesized by AAPPTec, unless otherwise noted.

Animals

Animal experiments were performed with the approval of the Georgia Tech Animal Care and Use Committee with veterinary supervision and within the guidelines of the *Guide for the Care and Use of Laboratory Animals*. In syngeneic studies, C57BL/6J male mice (10 to 14 weeks old) were used as recipients, and diabetes was induced by intraperitoneal injection of single-dose streptozotocin (200 mg/kg) on preoperative day 5. C57BL/6J female mice (10 to 14 weeks old) were used as islet donors. For the luciferase islet study, B6;FVB-Ptprc^{a} Tg(CAG-luc,-GFP)L2G85Chco Thy1^{a}/J female mice (8 to 12 weeks old) were used as donors. NOD-SCID male mice (10 to 14 weeks old) were used as recipients, and diabetes was induced by single-dose streptozotocin injection (180 mg/kg) on preoperative day 5. All mice were obtained from the Jackson Laboratory.

Vasculogenic hydrogels

A sterile 5% (final, w/v) solution of a four-arm PEG-maleimide monomer (20 kDa; Laysan Bio) was functionalized with 1.0 mM RGD peptide and VEGF (10 μg/ml) (where applicable) at 37°C for a minimum period of 15 min in gel buffer [phosphate-buffered saline (PBS), 25 mM Hepes; CellGro]. A separate cross-linking solution of VPM peptide was prepared in gel buffer. The pH for all solutions was adjusted to 7.0 to 7.5. To generate gels, functional macromers were rapidly mixed with VPM cross-linker at the site of transplant. The peptide sequences are GCRDVPMSMRGGDRCG for VPM and GRGDSPC for RGD.

Vascularization analyses

For SUBQ grafts, a small incision was made and sufficient connective tissue was cleared to accommodate a 50-μl gel, and the PEG-RGD and VPM cross-linking components were mixed in situ and allowed to polymerize for 10 min before closure with wound clips. For SBM grafts, a small amount of mesentery adjacent to the cecum was exposed. SBM location was chosen to avoid proximity to pancreatic tissue and for ease of graft location postoperatively. EFP tissue was gently exteriorized on a sterile gauze and spread with saline. Gel components were mixed directly on the surface of the SBM or EFP and allowed to cross-link for 10 min before reinsertion into the peritoneal space. For lectin perfusion, anesthetized mice were given an intravenous lectin injection (200 μl; DyLight 488–labeled lectin, Vector Laboratories) and sacrificed after 15 min; the vasculature was flushed with saline before graft removal and fixation in 10% buffered formalin. Grafts were stabilized between glass slides before whole mount–imaging on a confocal microscope. *Z* stacks of each sample were acquired at 4 to 6 FOV, within five to seven grafts per group. Vascular characteristics were analyzed using ImageJ/FIJI and were calculated to obtain an FOV of 1.59×10^{6} μm^{2} (objective, 10×; numerical aperture, 0.3).

Islet engraftment and function in extrahepatic transplant sites

Islets were isolated by pancreatic perfusion with Liberase TL (Roche), for 10 min of digestion at 37°C with gentle shaking and ultrapure (80 to 90%) islet separation from acinar using standard Ficoll gradients (1.108, 1.096, 1.069, and 1.037; Mercodia). Islets were counted using the standard IEQ method and dithizone staining. Two to 3 days after isolation, 600 IEQs were aliquoted in 10 μl of medium and mixed with PEG-RGD gel component just before in situ gelation at the site of transplant. Transplant recipients were monitored for nonfasting blood glucose levels. An IPGTT was performed before sacrifice. At sacrifice, graft recipients were lectin-perfused, as described above. Grafts were additionally stained for insulin (DAKO) using traditional histological techniques with incubation times for permeabilization [Triton X-100 (1 μl/ml) in PBS], blocking (goat serum; BioGenex), and antibody staining extended to 24 hours each to allow whole-graft infiltration.

Histological evaluation

Formalin-fixed grafts were paraffin-embedded and sectioned for staining. Standard antigen retrieval in citrate buffer was used before sequential blocking with Power Block (BioGenex) and goat serum (BioGenex). Primary antibodies (CD31, Thermo Scientific; CD11b, Novus Biologicals; CD45, BioLegend; insulin, DAKO) and isotype control antibodies were incubated overnight at 4°C, and secondary antibodies (Invitrogen) were incubated for 2 hours at room temperature with DAPI before mounting. Quantification of markers was performed using FIJI, where CD11b and CD45 staining was evaluated in four to seven subjects per group, where a minimum of three images per subject were averaged.

In vivo islet tracking

Islets were isolated from B6;FVB Luc^{+}GFP^{+} transgenic (200 IEQs per recipient) and wild-type C57BL/6J mice (400 IEQs per recipient) and transplanted in the SUBQ and EFP sites of NOD-SCID or C57BL/6J recipients. Because of an incomplete backcross in the B6;FVB Luc^{+}GFP^{+} transgenic strain, as well as the expression of xenogeneic GFP and luciferase proteins, NOD-SCID recipients were used to prevent islet rejection. Intraportal islets were slowly infused using 200 μl of saline through the duodenum mesenteric vein, which drains to the hepatic portal vein. Bioluminescence was detected by kinetic monitoring of signal (3-min intervals) after beetle luciferin (Promega) injection under anesthesia, until peak signal was reached, on an IVIS SpectrumCT (PerkinElmer) every week until the end point of the study. Hyperglycemic mice received 4 U of insulin (NovoLog) before imaging. Total flux per graft was measured over a 2-cm-diameter circular region of interest drawn around each graft for quantitative measurements. At sacrifice, graft recipients were lectin-perfused (200 μl; DyLight 649–labeled lectin, Vector Laboratories), as described above, with the exception of formalin fixation. Grafts were placed in saline on ice for immediate whole-mount imaging by confocal microscopy to preserve native GFP expression.

Statistics

All statistical analyses were performed in Prism software (GraphPad). Vascularization metrics, blood glucose data (temporal, >15 day average, and IPGTT), body weights, and bioluminescence data are presented as means ± SEM. For characterization of vascularization metrics, leukocyte quantification, and bioluminescence quantification,

Kruskal-Wallis nonparametric tests with Dunn's multiple comparison of select groups were used for all analyses. Nonparametric two-tailed Spearman correlation analysis for CD11b and CD45 markers plotted against vascular fractional area. Syngeneic blood glucose averages (>15 day) were analyzed by one-way ANOVA. Blood glucose comparison between EFP/PEG-VEGF and intraportal graft performance by two-tailed unpaired *t* test. Time-to-peak curves were analyzed by one-way ANOVA with repeated measures and by Dunnett's multiple-comparisons test against SUBQ/PEG. Survival curve analysis was performed using log-rank (Mantel-Cox) test.

SUPPLEMENTARY MATERIALS

Supplementary material for this article is available at http://advances.sciencemag.org/cgi/content/full/3/6/e1700184/DC1

fig. S1. Gross morphology of extrahepatic transplant sites during gel casting.
fig. S2. Correlation between site vascularization fractional area and site leukocyte density.
fig. S3. Blood glucose traces demonstrating individual recipient graft performance in extrahepatic islet transplant sites.
fig. S4. Long-term engraftment of marginal islet mass in EFP with PEG-VEGF.
fig. S5. Comparison of reversal in intraportal control islet transplant site and EFP/PEG-VEGF transplant site syngeneic diabetes reversal.
fig. S6. Survival curve for SUBQ groups.
fig. S7. Density of vascularized islets by site as demonstrated by lectin labeling.
fig. S8. Dose-dependent response of $Luc^{+}GFP^{+}$ islet signal in B6 recipients in EFP site over a 3-week period.
fig. S9. In vivo imaging of intraportally infused islets.
fig. S10. Bioluminescence signal kinetics by time point.
table S1. Exact *P* values for select comparisons between groups in vascularization metrics analyses.
table S2. Exact *P* values for select comparisons between groups in leukocyte presence analyses.

REFERENCES AND NOTES

1. S. Wild, G. Roglic, A. Green, R. Sicree, H. King, Global prevalence of diabetes estimates for the year 2000 and projections for 2030. *Diabetes Care* **27**, 1047–1053 (2004).
2. Center for Disease Control, "National diabetes fact sheet: National estimates and general information on diabetes and prediabetes in the United States, 2011" (CDC, 2011); https://www.cdc.gov/diabetes/pubs/pdf/ndfs_2011.pdf.
3. R. Calafiore, Perspectives in pancreatic and islet cell transplantation for the therapy of IDDM. *Diabetes Care* **20**, 889–896 (1997).
4. A. Bruni, B. Gala-Lopez, A. R. Pepper, N. S. Abualhassan, A. J. Shapiro, Islet cell transplantation for the treatment of type 1 diabetes: Recent advances and future challenges. *Diabetes Metab. Syndr. Obes. Target Ther.* **7**, 211 (2014).
5. M. D. Bellin, D. E. Sutherland, R. P. Robertson, Pancreatectomy and autologous islet transplantation for painful chronic pancreatitis: Indications and outcomes. *Hosp. Pract.* **40**, 80–87 (2012).
6. A. Balamurugan, T. L. Pruett, Trying to prevent the clogged drain: Optimizing the yield and function of portal vein-infused islets. *Dig. Dis. Sci.* **58**, 1170–1172 (2013).
7. D. B. Kaufman, P. F. Gores, M. J. Field, A. C. Farney, S. A. Gruber, E. Stephanian, D. E. R. Sutherland, Effect of 15-deoxyspergualin on immediate function and long-term survival of transplanted islets in murine recipients of a marginal islet mass. *Diabetes* **43**, 778–783 (1994).
8. R. Bottino, L. A. Fernandez, C. Ricordi, R. Lehmann, M.-F. Tsan, R. Oliver, L. Inverardi, Transplantation of allogeneic islets of Langerhans in the rat liver: Effects of macrophage depletion on graft survival and microenvironment activation. *Diabetes* **47**, 316–323 (1998).
9. N. S. Kenyon, L. A. Fernandez, R. Lehmann, M. Masetti, A. Ranuncoli, M. Chatzipetrou, G. Iaria, D. Han, J. L. Wagner, P. Ruiz, M. Berho, L. Inverardi, R. Alejandro, D. H. Mintz, A. D. Kirk, D. M. Harlan, L. C. Burkly, C. Ricordi, Long-term survival and function of intrahepatic islet allografts in baboons treated with humanized anti-CD154. *Diabetes* **48**, 1473–1481 (1999).
10. M. Biarnés, M. Montolio, V. Nacher, M. Raurell, J. Soler, E. Montanya, β-Cell death and mass in syngeneically transplanted islets exposed to short-and long-term hyperglycemia. *Diabetes* **51**, 66–72 (2002).
11. F. B. Barton, M. R. Rickels, R. Alejandro, B. J. Hering, S. Wease, B. Naziruddin, J. Oberholzer, J. S. Odorico, M. R. Garfinkel, M. Levy, F. Pattou, T. Berney, A. Secchi, S. Messinger, P. A. Senior, P. Maffi, A. Posselt, P. G. Stock, D. B. Kaufman, X. Luo, F. Kandeel, E. Cagliero, N. A. Turgeon, P. Witkowski, A. Naji, P. J. O'Connell, C. Greenbaum, Y. C. Kudva, K. L. Brayman, M. J. Aull, C. Larsen, T. W. H. Kay, L. A. Fernandez, M.-C. Vantyghem, M. Bellin, A. M. J. Shapiro, Improvement in outcomes of clinical islet transplantation: 1999–2010. *Diabetes Care* **35**, 1436–1445 (2012).
12. A. R. Pepper, B. Gala-Lopez, R. Pawlick, S. Merani, T. Kin, A. M. J. Shapiro, A prevascularized subcutaneous device-less site for islet and cellular transplantation. *Nat. Biotechnol.* **33**, 518–523 (2015).
13. S. Veriter, P. Gianello, Y. Igarashi, G. Beaurin, A. Ghyselinck, N. Aouassar, B. Jordan, B. Gallez, D. Dufrane, Improvement of subcutaneous bioartificial pancreas vascularization and function by coencapsulation of pig islets and mesenchymal stem cells in primates. *Cell Transplant.* **23**, 1349–1364 (2014).
14. M. S. Kim, H. H. Ahn, Y. N. Shin, M. H. Cho, G. Khang, H. B. Lee, An in vivo study of the host tissue response to subcutaneous implantation of PLGA-and/or porcine small intestinal submucosa-based scaffolds. *Biomaterials* **28**, 5137–5143 (2007).
15. A. Pileggi, R. D. Molano, C. Ricordi, E. Zahr, J. Collins, R. Valdes, L. Inverardi, Reversal of diabetes by pancreatic islet transplantation into a subcutaneous, neovascularized device. *Transplantation* **81**, 1318–1324 (2006).
16. C. B. Kemp, M. J. Knight, D. W. Scharp, W. F. Ballinger, P. E. Lacy, Effect of transplantation site on the results of pancreatic islet isografts in diabetic rats. *Diabetologia* **9**, 486–491 (1973).
17. E. A. Phelps, D. M. Headen, W. R. Taylor, P. M. Thule, A. J. García, Vasculogenic bio-synthetic hydrogel for enhancement of pancreatic islet engraftment and function in type 1 diabetes. *Biomaterials* **34**, 4602–4611 (2013).
18. A. O. Gaber, A. Chamsuddin, D. Fraga, J. Fisher, A. Lo, Insulin independence achieved using the transmesenteric approach to the portal vein for islet transplantation. *Transplantation* **77**, 309–311 (2004).
19. T. Kin, G. S. Korbutt, R. V. Rajotte, Survival and metabolic function of syngeneic rat islet grafts transplanted in the omental pouch. *Am. J. Transplant.* **3**, 281–285 (2003).
20. Y. Yasunami, P. E. Lacy, E. H. Finke, A new site for islet transplantation—A peritoneal-omental pouch. *Transplantation* **36**, 181–182 (1983).
21. S. Merani, C. Toso, J. Emamaullee, A. M. J. Shapiro, Optimal implantation site for pancreatic islet transplantation. *Br. J. Surg.* **95**, 1449–1461 (2008).
22. D. M. Berman, J. J. O'Neil, L. C. K. Coffey, P. C. J. Chaffanjon, N. M. Kenyon, P. Ruiz Jr., A. Pileggi, C. Ricordi, N. S. Kenyon, Long-term survival of nonhuman primate islets implanted in an omental pouch on a biodegradable scaffold. *Am. J. Transplant.* **9**, 91–104 (2009).
23. X. Chen, X. Zhang, C. Larson, F. Chen, H. Kissler, D. B. Kaufman, The epididymal fat pad as a transplant site for minimal islet mass. *Transplantation* **84**, 122–125 (2007).
24. A.-C. Brady, M. M. Martino, E. Pedraza, S. Sukert, A. Pileggi, C. Ricordi, J. A. Hubbell, C. L. Stabler, Proangiogenic hydrogels within macroporous scaffolds enhance islet engraftment in an extrahepatic site. *Tissue Eng. Part A* **19**, 2544–2552 (2013).
25. C. E. Brubaker, H. Kissler, L.-J. Wang, D. B. Kaufman, P. B. Messersmith, Biological performance of mussel-inspired adhesive in extrahepatic islet transplantation. *Biomaterials* **31**, 420–427 (2010).
26. A. Rajab, Islet transplantation: Alternative sites. *Curr. Diab. Rep.* **10**, 332–337 (2010).
27. D. J. van der Windt, G. J. Echeverri, J. N. Ijzermans, D. K. C. Cooper, The choice of anatomical site for islet transplantation. *Cell Transplant.* **17**, 1005–1014 (2008).
28. R. P. Robertson, Islet transplantation as a treatment for diabetes—A work in progress. *N. Engl. J. Med.* **350**, 694–705 (2004).
29. A. Andersson, O. Korsgren, L. Jansson, Intraportally transplanted pancreatic islets revascularized from hepatic arterial system. *Diabetes* **38** suppl. 1, 192–195 (1989).
30. T. K. Hart, R. M. Pino, Pseudoislet vascularization. Induction of diaphragm-fenestrated endothelia from the hepatic sinusoids. *Lab. Invest.* **54**, 304–313 (1986).
31. M. Brissova, A. C. Powers, Revascularization of transplanted islets: Can it be improved? *Diabetes* **57**, 2269–2271 (2008).
32. P.-O. Carlsson, F. Palm, A. Andersson, P. Liss, Markedly decreased oxygen tension in transplanted rat pancreatic islets irrespective of the implantation site. *Diabetes* **50**, 489–495 (2001).
33. G. Mattsson, L. Jansson, P.-O. Carlsson, Decreased vascular density in mouse pancreatic islets after transplantation. *Diabetes* **51**, 1362–1366 (2002).
34. N. R. Barshes, S. Wyllie, J. A. Goss, Inflammation-mediated dysfunction and apoptosis in pancreatic islet transplantation: Implications for intrahepatic grafts. *J. Leukoc. Biol.* **77**, 587–597 (2005).
35. J. A. Emamaullee, A. M. J. Shapiro, Factors influencing the loss of β-cell mass in islet transplantation. *Cell Transplant.* **16**, 1–8 (2007).
36. T. Linn, J. Schmitz, I. Hauck-Schmalenberger, Y. Lai, R. G. Bretzel, H. Brandhorst, D. Brandhorst, Ischaemia is linked to inflammation and induction of angiogenesis in pancreatic islets. *Clin. Exp. Immunol.* **144**, 179–187 (2006).
37. K. Cheng, D. Fraga, C. Zhang, M. Kotb, A. O. Gaber, R. V. Guntaka, R. I. Mahato, Adenovirus-based vascular endothelial growth factor gene delivery to human pancreatic islets. *Gene Ther.* **11**, 1105–1116 (2004).
38. A. S. Narang, K. Cheng, J. Henry, C. Zhang, O. Sabek, D. Fraga, M. Kotb, A. O. Gaber, R. I. Mahato, Vascular endothelial growth factor gene delivery for revascularization in transplanted human islets. *Pharm. Res.* **21**, 15–25 (2004).

39. S. Sigrist, A. Mechine-Neuville, K. Mandes, V. Calenda, S. Braun, G. Legeay, J.-P. Bellocq, M. Pinget, L. Kessler, Influence of VEGF on the viability of encapsulated pancreatic rat islets after transplantation in diabetic mice. *Cell Transplant.* **12**, 627–635 (2003).
40. N. Zhang, A. Richter, J. Suriawinata, S. Harbaran, J. Altomonte, L. Cong, H. Zhang, K. Song, M. Meseck, J. Bromberg, H. Dong, Elevated vascular endothelial growth factor production in islets improves islet graft vascularization. *Diabetes* **53**, 963–970 (2004).
41. J. C. Stendahl, L.-J. Wang, L. W. Chow, D. B. Kaufman, S. I. Stupp, Growth factor delivery from self-assembling nanofibers to facilitate islet transplantation. *Transplantation* **86**, 478–481 (2008).
42. M. Najjar, V. Manzoli, M. Abreu, C. Villa, M. M. Martino, R. D. Molano, Y. Torrente, A. Pileggi, L. Inverardi, C. Ricordi, J. A. Hubbell, A. A. Tomei, Fibrin gels engineered with pro-angiogenic growth factors promote engraftment of pancreatic islets in extrahepatic sites in mice. *Biotechnol. Bioeng.* **112**, 1916–1926 (2015).
43. E. A. Phelps, N. O. Enemchukwu, V. F. Fiore, J. C. Sy, N. Murthy, T. A. Sulchek, T. H. Barker, A. J. García, Maleimide cross-linked bioactive PEG hydrogel exhibits improved reaction kinetics and cross-linking for cell encapsulation and in situ delivery. *Adv. Mater.* **24**, 64–70 (2012).
44. B. Nilsson, O. Korsgren, J. D. Lambris, K. N. Ekdahl, Can cells and biomaterials in therapeutic medicine be shielded from innate immune recognition? *Trends Immunol.* **31**, 32–38 (2010).
45. W. Bennet, C.-G. Groth, R. Larsson, B. Nilsson, O. Korsgren, Isolated human islets trigger an instant blood mediated inflammatory reaction: Implications for intraportal islet transplantation as a treatment for patients with type 1 diabetes. *Ups. J. Med. Sci.* **105**, 125–133 (2000).
46. O. Korsgren, T. Lundgren, M. Felldin, A. Foss, B. Isaksson, J. Permert, N. H. Persson, E. Rafael, M. Rydén, K. Salmela, A. Tibell, G. Tufveson, B. Nilsson, Optimising islet engraftment is critical for successful clinical islet transplantation. *Diabetologia* **51**, 227–232 (2008).
47. A. O. Gaber, M. H. Shokouh-Amiri, D. K. Hathaway, L. Hammontree, A. E. Kitabchi, L. W. Gaber, M. F. Saad, L. G. Britt, Results of pancreas transplantation with portal venous and enteric drainage. *Ann. Surg.* **221**, 613–624 (1995).
48. A. Pettersson, J. A. Nagy, L. F. Brown, C. Sundberg, E. Morgan, S. Jungles, R. Carter, J. E. Krieger, E. J. Manseau, V. S. Harvey, I. A. Eckelhoefer, D. Feng, A. M. Dvorak, R. C. Mulligan, H. F. Dvorak, Heterogeneity of the angiogenic response induced in different normal adult tissues by vascular permeability factor/vascular endothelial growth factor. *Lab. Invest.* **80**, 99–115 (2000).
49. M. Ehrbar, S. M. Zeisberger, G. P. Raeber, J. A. Hubbell, C. Schnell, A. H. Zisch, The role of actively released fibrin-conjugated VEGF for *VEGF receptor 2* gene activation and the enhancement of angiogenesis. *Biomaterials* **29**, 1720–1729 (2008).
50. W. M. Elbjeirami, J. L. West, Angiogenesis-like activity of endothelial cells co-cultured with VEGF-producing smooth muscle cells. *Tissue Eng. Part A* **12**, 381–390 (2006).
51. V. Sacchi, R. Mittermayr, J. Hartinger, M. M. Martino, K. M. Lorentz, S. Wolbank, A. Hofmann, R. A. Largo, J. S. Marschall, E. Groppa, R. Gianni-Barrera, M. Ehrbar, J. A. Hubbell, H. Redl, A. Banfi, Long-lasting fibrin matrices ensure stable and functional angiogenesis by highly tunable, sustained delivery of recombinant $VEGF_{164}$. *Proc. Natl. Acad. Sci. U.S.A.* **111**, 6952–6957 (2014).
52. E. A. Phelps, N. Landázuri, P. M. Thulé, W. R. Taylor, A. J. García, Bioartificial matrices for therapeutic vascularization. *Proc. Natl. Acad. Sci. U.S.A.* **107**, 3323–3328 (2010).
53. M. Brissova, A. Shostak, M. Shiota, P. O. Wiebe, G. Poffenberger, J. Kantz, Z. Chen, C. Carr, W. G. Jerome, J. Chen, H. S. Baldwin, W. Nicholson, D. M. Bader, T. Jetton, M. Gannon, A. C. Powers, Pancreatic islet production of vascular endothelial growth factor-A is essential for islet vascularization, revascularization, and function. *Diabetes* **55**, 2974–2985 (2006).
54. K. Bramis, A. N. Gordon-Weeks, P. J. Friend, E. Bastin, A. Burls, M. A. Silva, A. R. Dennison, Systematic review of total pancreatectomy and islet autotransplantation for chronic pancreatitis. *Br. J. Surg.* **99**, 761–766 (2012).
55. M. D. Menger, J.-i. Yamauchi, B. Vollmar, Revascularization and microcirculation of freely grafted islets of Langerhans. *World J. Surg.* **25**, 509–515 (2001).

Acknowledgments

Funding: This research was supported by the Juvenile Diabetes Research Foundation (grant 2-SRA-2014-287-Q-R to A.J.G., H.S., and L.D.S.), the NIH Innovation and Leadership in Engineering Technologies and Therapies Postdoctoral Training (grant T90-DK097787-03 to J.D.W.), and the Ruth L. Kirschstein National Research Service Award (F30AR069472) from the National Institute of Arthritis and Musculoskeletal and Skin Diseases (to C.T.J.). **Author contributions:** J.D.W. and A.J.G. designed the experiments; J.D.W., D.M.H., J.A., and C.T.J. performed the experiments; J.D.W., A.J.G., L.D.S., H.S., and D.M.H. discussed the results; J.D.W. prepared the figures; and J.D.W. and A.J.G. prepared the manuscript. **Competing interests:** H.S. is Founder and CEO of FasCure Therapeutics LLC. All other authors declare that they have no competing interests. **Data and materials availability:** All data needed to evaluate the conclusions in the paper are present in the paper and/or the Supplementary Materials. Additional data related to this paper may be requested from the authors.

Submitted 17 January 2017
Accepted 3 April 2017
Published 2 June 2017
10.1126/sciadv.1700184

Citation: J. D. Weaver, D. M. Headen, J. Aquart, C. T. Johnson, L. D. Shea, H. Shirwan, A. J. García, Vasculogenic hydrogel enhances islet survival, engraftment, and function in leading extrahepatic sites. *Sci. Adv.* **3**, e1700184 (2017).

REFERENCES

1. R. O. Darouiche, Treatment of infections associated with surgical implants. *The New England journal of medicine* **350**, 1422-1429 (2004).

2. D. Campoccia, L. Montanaro, C. R. Arciola, The significance of infection related to orthopedic devices and issues of antibiotic resistance. *Biomaterials* **27**, 2331-2339 (2006).

3. T. Baba, O. Schneewind, Target cell specificity of a bacteriocin molecule: a C-terminal signal directs lysostaphin to the cell wall of Staphylococcus aureus. *The EMBO journal* **15**, 4789 (1996).

4. C. A. Schindler, V. Schuhardt, Lysostaphin: a new bacteriolytic agent for the Staphylococcus. *Proceedings of the National Academy of Sciences* **51**, 414-421 (1964).

5. M. W. Climo, K. Ehlert, G. L. Archer, Mechanism and suppression of lysostaphin resistance in oxacillin-resistant Staphylococcus aureus. *Antimicrobial agents and chemotherapy* **45**, 1431-1437 (2001).

6. J. A. Wu, C. Kusuma, J. J. Mond, J. F. Kokai-Kun, Lysostaphin disrupts Staphylococcus aureus and Staphylococcus epidermidis biofilms on artificial surfaces. *Antimicrobial agents and chemotherapy* **47**, 3407-3414 (2003).

7. M. W. Climo, R. L. Patron, B. P. Goldstein, G. L. Archer, Lysostaphin treatment of experimental methicillin-resistant Staphylococcus aureus aortic valve endocarditis. *Antimicrobial agents and chemotherapy* **42**, 1355-1360 (1998).

8. M. F. Mohamed, M. I. Hamed, A. Panitch, M. N. Seleem, Targeting methicillin-resistant Staphylococcus aureus with short salt-resistant synthetic peptides. *Antimicrobial agents and chemotherapy* **58**, 4113-4122 (2014).

9. R. L. Patron, M. W. Climo, B. P. Goldstein, G. L. Archer, Lysostaphin treatment of experimental aortic valve endocarditis caused by a Staphylococcus aureus isolate with reduced susceptibility to vancomycin. *Antimicrobial agents and chemotherapy* **43**, 1754-1755 (1999).

10. J. F. Kokai-Kun, T. Chanturiya, J. J. Mond, Lysostaphin as a treatment for systemic Staphylococcus aureus infection in a mouse model. *Journal of antimicrobial chemotherapy* **60**, 1051-1059 (2007).

11. J. F. Kokai-Kun, T. Chanturiya, J. J. Mond, Lysostaphin eradicates established Staphylococcus aureus biofilms in jugular vein catheterized mice. *Journal of antimicrobial chemotherapy*, dkp145 (2009).

12. O. Oluola, L. Kong, M. Fein, L. E. Weisman, Lysostaphin in treatment of neonatal Staphylococcus aureus infection. *Antimicrobial agents and chemotherapy* **51**, 2198-2200 (2007).

13. A. Shah, J. Mond, S. Walsh, Lysostaphin-coated catheters eradicate Staphylococccus aureus challenge and block surface colonization. *Antimicrobial agents and chemotherapy* **48**, 2704-2707 (2004).

14. A. G. Gristina, Biomaterial-centered infection: microbial adhesion versus tissue integration. *Science* **237**, 1588-1595 (1987).

15. G. Ramage, M. M. Tunney, S. Patrick, S. P. Gorman, J. R. Nixon, Formation of Propionibacterium acnes biofilms on orthopaedic biomaterials and their susceptibility to antimicrobials. *Biomaterials* **24**, 3221-3227 (2003).

16. A. Trampuz, A. F. Widmer, Infections associated with orthopedic implants. *Current opinion in infectious diseases* **19**, 349-356 (2006).

17. L. Lazzarini, J. T. Mader, J. H. Calhoun, Osteomyelitis in long bones. *The Journal of bone and joint surgery. American volume* **86-A**, 2305-2318 (2004).

18. D. P. Lew, F. A. Waldvogel, Osteomyelitis. *Lancet* **364**, 369-379 (2004).

19. S. K. Fridkin, Increasing prevalence of antimicrobial resistance in intensive care units. *Critical care medicine* **29**, N64-68 (2001).

20. G. E. Pierce, Pseudomonas aeruginosa, Candida albicans, and device-related nosocomial infections: implications, trends, and potential approaches for control. *Journal of industrial microbiology & biotechnology* **32**, 309-318 (2005).

21. T. Bjarnsholt, O. Ciofu, S. Molin, M. Givskov, N. Hoiby, Applying insights from biofilm biology to drug development - can a new approach be developed? *Nature reviews. Drug discovery* **12**, 791-808 (2013).

22. A. Trampuz, W. Zimmerli, Diagnosis and treatment of infections associated with fracture-fixation devices. *Injury* **37 Suppl 2**, S59-66 (2006).

23. J. W. Costerton, Z. Lewandowski, D. E. Caldwell, D. R. Korber, H. M. Lappin-Scott, Microbial biofilms. *Annual review of microbiology* **49**, 711-745 (1995).

24. K. Lewis, Riddle of biofilm resistance. *Antimicrobial agents and chemotherapy* **45**, 999-1007 (2001).

25. K. Driffield, K. Miller, J. M. Bostock, A. J. O'Neill, I. Chopra, Increased mutability of Pseudomonas aeruginosa in biofilms. *The Journal of antimicrobial chemotherapy* **61**, 1053-1056 (2008).

26. C. T. O'Loughlin, L. C. Miller, A. Siryaporn, K. Drescher, M. F. Semmelhack, B. L. Bassler, A quorum-sensing inhibitor blocks Pseudomonas aeruginosa virulence and biofilm formation. *Proceedings of the National Academy of Sciences of the United States of America* **110**, 17981-17986 (2013).

27. M. D. Macia, J. L. Perez, S. Molin, A. Oliver, Dynamics of mutator and antibiotic-resistant populations in a pharmacokinetic/pharmacodynamic model of Pseudomonas aeruginosa biofilm treatment. *Antimicrobial agents and chemotherapy* **55**, 5230-5237 (2011).

28. K. Lewis, Persister cells. *Annual review of microbiology* **64**, 357-372 (2010).

29. H. Ma, E. T. Darmawan, M. Zhang, L. Zhang, J. D. Bryers, Development of a poly(ether urethane) system for the controlled release of two novel anti-biofilm agents based on gallium or zinc and its efficacy to prevent bacterial biofilm formation. *Journal of controlled release : official journal of the Controlled Release Society* **172**, 1035-1044 (2013).

30. W. G. De Long, Jr., T. A. Einhorn, K. Koval, M. McKee, W. Smith, R. Sanders, T. Watson, Bone grafts and bone graft substitutes in orthopaedic trauma surgery. A critical analysis. *The Journal of bone and joint surgery. American volume* **89**, 649-658 (2007).

31. S. F. Journeaux, N. Johnson, S. L. Bryce, S. J. Friedman, S. M. Sommerville, D. A. Morgan, Bacterial contamination rates during bone allograft retrieval. *The Journal of arthroplasty* **14**, 677-681 (1999).

32. C. F. Lord, M. C. Gebhardt, W. W. Tomford, H. J. Mankin, Infection in bone allografts. Incidence, nature, and treatment. *The Journal of bone and joint surgery. American volume* **70**, 369-376 (1988).

33. H. J. Mankin, F. J. Hornicek, K. A. Raskin, Infection in massive bone allografts. *Clinical orthopaedics and related research*, 210-216 (2005).

34. R. Dimitriou, E. Jones, D. McGonagle, P. V. Giannoudis, Bone regeneration: current concepts and future directions. *BMC medicine* **9**, 66 (2011).

35. D. Campoccia, L. Montanaro, C. R. Arciola, A review of the biomaterials technologies for infection-resistant surfaces. *Biomaterials* **34**, 8533-8554 (2013).

36. D. Campoccia, L. Montanaro, C. R. Arciola, A review of the clinical implications of anti-infective biomaterials and infection-resistant surfaces. *Biomaterials* **34**, 8018-8029 (2013).

37. L. A. Mills, A. H. Simpson, In vivo models of bone repair. *The Journal of bone and joint surgery. British volume* **94**, 865-874 (2012).

38. A. W. Yasko, J. M. Lane, E. J. Fellinger, V. Rosen, J. M. Wozney, E. A. Wang, The healing of segmental bone defects, induced by recombinant human bone morphogenetic protein (rhBMP-2). A radiographic, histological, and biomechanical study in rats. *The Journal of bone and joint surgery. American volume* **74**, 659-670 (1992).

39. X. Chen, L. S. Kidder, W. D. Lew, Osteogenic protein-1 induced bone formation in an infected segmental defect in the rat femur. *Journal of orthopaedic research : official publication of the Orthopaedic Research Society* **20**, 142-150 (2002).

40. X. Chen, A. H. Schmidt, S. Mahjouri, D. W. Polly, Jr., W. D. Lew, Union of a chronically infected internally stabilized segmental defect in the rat femur after debridement and application of rhBMP-2 and systemic antibiotic. *Journal of orthopaedic trauma* **21**, 693-700 (2007).

41. X. Chen, A. H. Schmidt, D. T. Tsukayama, C. A. Bourgeault, W. D. Lew, Recombinant human osteogenic protein-1 induces bone formation in a chronically infected, internally stabilized segmental defect in the rat femur. *The Journal of bone and joint surgery. American volume* **88**, 1510-1523 (2006).

42. X. Chen, D. T. Tsukayama, L. S. Kidder, C. A. Bourgeault, A. H. Schmidt, W. D. Lew, Characterization of a chronic infection in an internally-stabilized segmental defect in the rat femur. *Journal of orthopaedic research : official publication of the Orthopaedic Research Society* **23**, 816-823 (2005).

43. Z. Zheng, W. Yin, J. N. Zara, W. Li, J. Kwak, R. Mamidi, M. Lee, R. K. Siu, R. Ngo, J. Wang, D. Carpenter, X. Zhang, B. Wu, K. Ting, C. Soo, The use of BMP-2 coupled - Nanosilver-PLGA composite grafts to induce bone repair in grossly infected segmental defects. *Biomaterials* **31**, 9293-9300 (2010).

44. J. G. Penn-Barwell, B. C. Rand, K. V. Brown, J. C. Wenke, A versatile model of open-fracture infection : a contaminated segmental rat femur defect. *Bone & joint research* **3**, 187-192 (2014).

45. L. L. Southwood, D. D. Frisbie, C. E. Kawcak, S. C. Ghivizzani, C. H. Evans, C. W. McIlwraith, Evaluation of Ad-BMP-2 for enhancing fracture healing in an infected defect fracture rabbit model. *Journal of orthopaedic research : official publication of the Orthopaedic Research Society* **22**, 66-72 (2004).

46. L. Bi, Y. Hu, H. Fan, G. Meng, J. Liu, D. Li, R. Lv, Treatment of contaminated bone defects with clindamycin-reconstituted bone xenograft-composites. *Journal of biomedical materials research. Part B, Applied biomaterials* **82**, 418-427 (2007).

47. W. Reizner, J. G. Hunter, N. T. O'Malley, R. D. Southgate, E. M. Schwarz, S. L. Kates, A systematic review of animal models for Staphylococcus aureus osteomyelitis. *European cells & materials* **27**, 196-212 (2014).

48. J. A. Niska, J. A. Meganck, J. R. Pribaz, J. H. Shahbazian, E. Lim, N. Zhang, B. W. Rice, A. Akin, R. I. Ramos, N. M. Bernthal, K. P. Francis, L. S. Miller, Monitoring bacterial burden, inflammation and bone damage longitudinally using optical and muCT imaging in an orthopaedic implant infection in mice. *PloS one* **7**, e47397 (2012).

49. J. A. Niska, J. H. Shahbazian, R. I. Ramos, J. R. Pribaz, F. Billi, K. P. Francis, L. S. Miller, Daptomycin and tigecycline have broader effective dose ranges than

vancomycin as prophylaxis against a Staphylococcus aureus surgical implant infection in mice. *Antimicrobial agents and chemotherapy* **56**, 2590-2597 (2012).

50. J. R. Pribaz, N. M. Bernthal, F. Billi, J. S. Cho, R. I. Ramos, Y. Guo, A. L. Cheung, K. P. Francis, L. S. Miller, Mouse model of chronic post-arthroplasty infection: noninvasive in vivo bioluminescence imaging to monitor bacterial burden for long-term study. *Journal of orthopaedic research : official publication of the Orthopaedic Research Society* **30**, 335-340 (2012).

51. A. G. Ashbaugh, X. Jiang, J. Zheng, A. S. Tsai, W.-S. Kim, J. M. Thompson, R. J. Miller, J. H. Shahbazian, Y. Wang, C. A. Dillen, A. A. Ordonez, Y. S. Chang, S. K. Jain, L. C. Jones, R. S. Sterling, H.-Q. Mao, L. S. Miller, Polymeric nanofiber coating with tunable combinatorial antibiotic delivery prevents biofilm-associated infection in vivo. *Proceedings of the National Academy of Sciences* **113**, E6919-E6928 (2016).

52. Y. Wang, L. I. Cheng, D. R. Helfer, A. G. Ashbaugh, R. J. Miller, A. J. Tzomides, J. M. Thompson, R. V. Ortines, A. S. Tsai, H. Liu, C. A. Dillen, N. K. Archer, T. S. Cohen, C. Tkaczyk, C. K. Stover, B. R. Sellman, L. S. Miller, Mouse model of hematogenous implant-related Staphylococcus aureus biofilm infection reveals therapeutic targets. *Proceedings of the National Academy of Sciences* **114**, E5094-E5102 (2017).

53. J. A. Inzana, E. M. Schwarz, S. L. Kates, H. A. Awad, A novel murine model of established Staphylococcal bone infection in the presence of a fracture fixation plate to study therapies utilizing antibiotic-laden spacers after revision surgery. *Bone* **72**, 128-136 (2015).

54. J. Sjollema, P. K. Sharma, R. J. Dijkstra, G. M. van Dam, H. C. van der Mei, A. F. Engelsman, H. J. Busscher, The potential for bio-optical imaging of biomaterial-associated infection in vivo. *Biomaterials* **31**, 1984-1995 (2010).

55. J. L. Kadurugamuwa, L. Sin, E. Albert, J. Yu, K. Francis, M. DeBoer, M. Rubin, C. Bellinger-Kawahara, T. R. Parr, P. R. Contag, Direct Continuous Method for Monitoring Biofilm Infection in a Mouse Model. *Infection and immunity* **71**, 882-890 (2003).

56. J. L. Kadurugamuwa, L. V. Sin, J. Yu, K. P. Francis, R. Kimura, T. Purchio, P. R. Contag, Rapid Direct Method for Monitoring Antibiotics in a Mouse Model of Bacterial Biofilm Infection. *Antimicrobial agents and chemotherapy* **47**, 3130-3137 (2003).

57. A. F. Engelsman, H. C. van der Mei, K. P. Francis, H. J. Busscher, R. J. Ploeg, G. M. van Dam, Real time noninvasive monitoring of contaminating bacteria in a soft tissue implant infection model. *Journal of biomedical materials research. Part B, Applied biomaterials* **88**, 123-129 (2009).

58. H. Funao, K. Ishii, S. Nagai, A. Sasaki, T. Hoshikawa, M. Aizawa, Y. Okada, K. Chiba, S. Koyasu, Y. Toyama, M. Matsumoto, Establishment of a real-time, quantitative, and reproducible mouse model of Staphylococcus osteomyelitis using bioluminescence imaging. *Infection and immunity* **80**, 733-741 (2012).

59. S. A. Horst, V. Hoerr, A. Beineke, C. Kreis, L. Tuchscherr, J. Kalinka, S. Lehne, I. Schleicher, G. Kohler, T. Fuchs, M. J. Raschke, M. Rohde, G. Peters, C. Faber, B. Loffler, E. Medina, A novel mouse model of Staphylococcus aureus chronic osteomyelitis that closely mimics the human infection: an integrated view of disease pathogenesis. *The American journal of pathology* **181**, 1206-1214 (2012).

60. H. Eggleston, P. Panizzi, Molecular Imaging of Bacterial Infections in vivo: The Discrimination between Infection and Inflammation. *Informatics* **1**, 72-99 (2014).

61. S. Suri, S. M. Lehman, S. Selvam, K. Reddie, S. Maity, N. Murthy, A. J. Garcia, In vivo fluorescence imaging of biomaterial-associated inflammation and infection in a minimally invasive manner. *Journal of biomedical materials research. Part A*, (2014).

62. N. Dinjaski, S. Suri, J. Valle, S. M. Lehman, I. Lasa, M. A. Prieto, A. J. Garcia, Near-infrared fluorescence imaging as an alternative to bioluminescent bacteria to monitor biomaterial-associated infections. *Acta biomaterialia* **10**, 2935-2944 (2014).

63. C. P. Brouwer, L. Sarda-Mantel, A. Meulemans, D. Le Guludec, M. M. Welling, The use of technetium-99m radiolabeled human antimicrobial peptides for infection specific imaging. *Mini reviews in medicinal chemistry* **8**, 1039-1052 (2008).

64. M. van Oosten, T. Schafer, J. A. Gazendam, K. Ohlsen, E. Tsompanidou, M. C. de Goffau, H. J. Harmsen, L. M. Crane, E. Lim, K. P. Francis, L. Cheung, M. Olive, V. Ntziachristos, J. M. van Dijl, G. M. van Dam, Real-time in vivo imaging of invasive- and biomaterial-associated bacterial infections using fluorescently labelled vancomycin. *Nature communications* **4**, 2584 (2013).

65. R. Kuijer, E. J. Jansen, P. J. Emans, S. K. Bulstra, J. Riesle, J. Pieper, D. W. Grainger, H. J. Busscher, Assessing infection risk in implanted tissue-engineered devices. *Biomaterials* **28**, 5148-5154 (2007).

66. N. J. Afacan, A. T. Yeung, O. M. Pena, R. E. Hancock, Therapeutic potential of host defense peptides in antibiotic-resistant infections. *Current pharmaceutical design* **18**, 807-819 (2012).

67. J. Davies, D. Davies, Origins and evolution of antibiotic resistance. *Microbiology and molecular biology reviews : MMBR* **74**, 417-433 (2010).

68. G. W. Hanlon, Bacteriophages: an appraisal of their role in the treatment of bacterial infections. *International journal of antimicrobial agents* **30**, 118-128 (2007).

69. A. L. Hilchie, K. Wuerth, R. E. Hancock, Immune modulation by multifaceted cationic host defense (antimicrobial) peptides. *Nature chemical biology* **9**, 761-768 (2013).

70. C. Marambio-Jones, E. M. V. Hoek, A review of the antibacterial effects of silver nanomaterials and potential implications for human health and the environment. *Journal of Nanoparticle Research* **12**, 1531-1551 (2010).

71. V. A. Fischetti, Bacteriophage lysins as effective antibacterials. *Current opinion in microbiology* **11**, 393-400 (2008).

72. J. K. Kumar, Lysostaphin: an antistaphylococcal agent. *Appl Microbiol Biotechnol* **80**, 555-561 (2008).

73. L. R. Hoffman, D. A. D'Argenio, M. J. MacCoss, Z. Zhang, R. A. Jones, S. I. Miller, Aminoglycoside antibiotics induce bacterial biofilm formation. *Nature* **436**, 1171-1175 (2005).

74. P. S. Stewart, J. W. Costerton, Antibiotic resistance of bacteria in biofilms. *Lancet* **358**, 135-138 (2001).

75. S. Kalghatgi, C. S. Spina, J. C. Costello, M. Liesa, J. R. Morones-Ramirez, S. Slomovic, A. Molina, O. S. Shirihai, J. J. Collins, Bactericidal antibiotics induce

mitochondrial dysfunction and oxidative damage in Mammalian cells. *Science translational medicine* **5**, 192ra185 (2013).

76. S. Silver, Bacterial silver resistance: molecular biology and uses and misuses of silver compounds. *FEMS microbiology reviews* **27**, 341-353 (2003).

77. L. Braydich-Stolle, S. Hussain, J. J. Schlager, M. C. Hofmann, In vitro cytotoxicity of nanoparticles in mammalian germline stem cells. *Toxicological sciences : an official journal of the Society of Toxicology* **88**, 412-419 (2005).

78. P. V. AshaRani, G. Low Kah Mun, M. P. Hande, S. Valiyaveettil, Cytotoxicity and genotoxicity of silver nanoparticles in human cells. *ACS nano* **3**, 279-290 (2009).

79. J. R. Morones-Ramirez, J. A. Winkler, C. S. Spina, J. J. Collins, Silver enhances antibiotic activity against gram-negative bacteria. *Science translational medicine* **5**, 190ra181 (2013).

80. N. A. Trujillo, R. A. Oldinski, H. Y. Ma, J. D. Bryers, J. D. Williams, K. C. Popat, Antibacterial effects of silver-doped hydroxyapatite thin films sputter deposited on titanium. *Mat Sci Eng C-Mater* **32**, 2135-2144 (2012).

81. M. N. Storm-Versloot, C. G. Vos, D. T. Ubbink, H. Vermeulen, Topical silver for preventing wound infection. *The Cochrane database of systematic reviews*, CD006478 (2010).

82. M. H. Kollef, B. Afessa, A. Anzueto, C. Veremakis, K. M. Kerr, B. D. Margolis, D. E. Craven, P. R. Roberts, A. C. Arroliga, R. D. Hubmayr, M. I. Restrepo, W. R. Auger, R. Schinner, N. I. Group, Silver-coated endotracheal tubes and incidence of ventilator-associated pneumonia: the NASCENT randomized trial. *JAMA : the journal of the American Medical Association* **300**, 805-813 (2008).

83. M. Beattie, J. Taylor, Silver alloy vs. uncoated urinary catheters: a systematic review of the literature. *Journal of clinical nursing* **20**, 2098-2108 (2011).

84. A. Izadpanah, R. L. Gallo, Antimicrobial peptides. *Journal of the American Academy of Dermatology* **52**, 381-390; quiz 391-382 (2005).

85. K. De Smet, R. Contreras, Human antimicrobial peptides: defensins, cathelicidins and histatins. *Biotechnology letters* **27**, 1337-1347 (2005).

86. A. Nijnik, R. Hancock, Host defence peptides: antimicrobial and immunomodulatory activity and potential applications for tackling antibiotic-resistant infections. *Emerging health threats journal* **2**, e1 (2009).

87. N. K. Brogden, K. A. Brogden, Will new generations of modified antimicrobial peptides improve their potential as pharmaceuticals? *International journal of antimicrobial agents* **38**, 217-225 (2011).

88. T. K. Lu, M. S. Koeris, The next generation of bacteriophage therapy. *Current opinion in microbiology* **14**, 524-531 (2011).

89. R. Schuch, H. M. Lee, B. C. Schneider, K. L. Sauve, C. Law, B. K. Khan, J. A. Rotolo, Y. Horiuchi, D. E. Couto, A. Raz, V. A. Fischetti, D. B. Huang, R. C. Nowinski, M. Wittekind, Combination therapy with lysin CF-301 and antibiotic is superior to antibiotic alone for treating methicillin-resistant Staphylococcus aureus-induced murine bacteremia. *The Journal of infectious diseases* **209**, 1469-1478 (2014).

90. K. A. Hughes, I. W. Sutherland, M. V. Jones, Biofilm susceptibility to bacteriophage attack: the role of phage-borne polysaccharide depolymerase. *Microbiology* **144 (Pt 11)**, 3039-3047 (1998).

91. T. K. Lu, J. J. Collins, Dispersing biofilms with engineered enzymatic bacteriophage. *Proceedings of the National Academy of Sciences of the United States of America* **104**, 11197-11202 (2007).

92. E. M. Ryan, M. Y. Alkawareek, R. F. Donnelly, B. F. Gilmore, Synergistic phage-antibiotic combinations for the control of Escherichia coli biofilms in vitro. *FEMS immunology and medical microbiology* **65**, 395-398 (2012).

93. W. Fu, T. Forster, O. Mayer, J. J. Curtin, S. M. Lehman, R. M. Donlan, Bacteriophage cocktail for the prevention of biofilm formation by Pseudomonas aeruginosa on catheters in an in vitro model system. *Antimicrobial agents and chemotherapy* **54**, 397-404 (2010).

94. E. Morello, E. Saussereau, D. Maura, M. Huerre, L. Touqui, L. Debarbieux, Pulmonary bacteriophage therapy on Pseudomonas aeruginosa cystic fibrosis strains: first steps towards treatment and prevention. *PloS one* **6**, e16963 (2011).

95. D. Alemayehu, P. G. Casey, O. McAuliffe, C. M. Guinane, J. G. Martin, F. Shanahan, A. Coffey, R. P. Ross, C. Hill, Bacteriophages phiMR299-2 and phiNH-4 can eliminate Pseudomonas aeruginosa in the murine lung and on cystic fibrosis lung airway cells. *mBio* **3**, e00029-00012 (2012).

96. A. Bruttin, H. Brussow, Human volunteers receiving Escherichia coli phage T4 orally: a safety test of phage therapy. *Antimicrobial agents and chemotherapy* **49**, 2874-2878 (2005).

97. D. D. Rhoads, R. D. Wolcott, M. A. Kuskowski, B. M. Wolcott, L. S. Ward, A. Sulakvelidze, Bacteriophage therapy of venous leg ulcers in humans: results of a phase I safety trial. *Journal of wound care* **18**, 237-238, 240-233 (2009).

98. A. Wright, C. H. Hawkins, E. E. Anggard, D. R. Harper, A controlled clinical trial of a therapeutic bacteriophage preparation in chronic otitis due to antibiotic-resistant Pseudomonas aeruginosa; a preliminary report of efficacy. *Clinical otolaryngology : official journal of ENT-UK ; official journal of Netherlands Society for Oto-Rhino-Laryngology & Cervico-Facial Surgery* **34**, 349-357 (2009).

99. M. Schmelcher, D. M. Donovan, M. J. Loessner, Bacteriophage endolysins as novel antimicrobials. *Future microbiology* **7**, 1147-1171 (2012).

100. M. J. Lai, N. T. Lin, A. Hu, P. C. Soo, L. K. Chen, L. H. Chen, K. C. Chang, Antibacterial activity of Acinetobacter baumannii phage varphiAB2 endolysin (LysAB2) against both gram-positive and gram-negative bacteria. *Appl Microbiol Biotechnol* **90**, 529-539 (2011).

101. M. Pastagia, R. Schuch, V. A. Fischetti, D. B. Huang, Lysins: the arrival of pathogen-directed anti-infectives. *Journal of Medical Microbiology* **62**, 1506-1516 (2013).

102. Y. Shen, T. Koller, B. Kreikemeyer, D. C. Nelson, Rapid degradation of Streptococcus pyogenes biofilms by PlyC, a bacteriophage-encoded endolysin. *The Journal of antimicrobial chemotherapy* **68**, 1818-1824 (2013).

103. N. Kiri, G. Archer, M. W. Climo, Combinations of Lysostaphin with β-Lactams Are Synergistic against Oxacillin-Resistant Staphylococcus epidermidis. *Antimicrobial agents and chemotherapy* **46**, 2017-2020 (2002).

104. A. Daniel, C. Euler, M. Collin, P. Chahales, K. J. Gorelick, V. A. Fischetti, Synergism between a novel chimeric lysin and oxacillin protects against infection by methicillin-resistant Staphylococcus aureus. *Antimicrobial agents and chemotherapy* **54**, 1603-1612 (2010).

105. M. Zilberman, J. J. Elsner, Antibiotic-eluting medical devices for various applications. *Journal of controlled release : official journal of the Controlled Release Society* **130**, 202-215 (2008).

106. C. S. Adams, V. Antoci, Jr., G. Harrison, P. Patal, T. A. Freeman, I. M. Shapiro, J. Parvizi, N. J. Hickok, S. Radin, P. Ducheyne, Controlled release of vancomycin from thin sol-gel films on implant surfaces successfully controls osteomyelitis. *Journal of orthopaedic research : official publication of the Orthopaedic Research Society* **27**, 701-709 (2009).

107. S. Bhattacharyya, A. Agrawal, C. Knabe, P. Ducheyne, Sol-gel silica controlled release thin films for the inhibition of methicillin-resistant Staphylococcus aureus. *Biomaterials* **35**, 509-517 (2014).

108. K. Feng, H. Sun, M. A. Bradley, E. J. Dupler, W. V. Giannobile, P. X. Ma, Novel antibacterial nanofibrous PLLA scaffolds. *Journal of controlled release : official journal of the Controlled Release Society* **146**, 363-369 (2010).

109. T. T. Ruckh, R. A. Oldinski, D. A. Carroll, K. Mikhova, J. D. Bryers, K. C. Popat, Antimicrobial effects of nanofiber poly(caprolactone) tissue scaffolds releasing rifampicin. *Journal of materials science. Materials in medicine* **23**, 1411-1420 (2012).

110. X. Shi, Y. Wang, L. Ren, W. Huang, D. A. Wang, A protein/antibiotic releasing poly(lactic-co-glycolic acid)/lecithin scaffold for bone repair applications. *International journal of pharmaceutics* **373**, 85-92 (2009).

111. H. A. Doty, M. R. Leedy, H. S. Courtney, W. O. Haggard, J. D. Bumgardner, Composite chitosan and calcium sulfate scaffold for dual delivery of vancomycin and recombinant human bone morphogenetic protein-2. *Journal of materials science. Materials in medicine* **25**, 1449-1459 (2014).

112. K. Kanellakopoulou, I. Galanopoulos, V. Soranoglou, T. Tsaganos, V. Tziortzioti, I. Maris, A. Papalois, H. Giamarellou, E. J. Giamarellos-Bourboulis, Treatment of experimental osteomyelitis caused by methicillin-resistant Staphylococcus aureus with a synthetic carrier of calcium sulphate (Stimulan) releasing moxifloxacin. *International journal of antimicrobial agents* **33**, 354-359 (2009).

113. Z. Xie, X. Liu, W. Jia, C. Zhang, W. Huang, J. Wang, Treatment of osteomyelitis and repair of bone defect by degradable bioactive borate glass releasing vancomycin. *Journal of controlled release : official journal of the Controlled Release Society* **139**, 118-126 (2009).

114. B. Li, K. V. Brown, J. C. Wenke, S. A. Guelcher, Sustained release of vancomycin from polyurethane scaffolds inhibits infection of bone wounds in a rat femoral segmental defect model. *Journal of controlled release : official journal of the Controlled Release Society* **145**, 221-230 (2010).

115. S. A. Guelcher, K. V. Brown, B. Li, T. Guda, B. H. Lee, J. C. Wenke, Dual-purpose bone grafts improve healing and reduce infection. *Journal of orthopaedic trauma* **25**, 477-482 (2011).

116. B. Thomes, P. Murray, D. Bouchier-Hayes, Development of resistant strains of Staphylococcus epidermidis on gentamicin-loaded bone cement in vivo. *The Journal of bone and joint surgery. British volume* **84**, 758-760 (2002).

117. G. J. ter Boo, D. W. Grijpma, T. F. Moriarty, R. G. Richards, D. Eglin, Antimicrobial delivery systems for local infection prophylaxis in orthopedic- and trauma surgery. *Biomaterials* **52**, 113-125 (2015).

118. M. E. Hake, H. Young, D. J. Hak, P. F. Stahel, E. M. Hammerberg, C. Mauffrey, Local antibiotic therapy strategies in orthopaedic trauma: Practical tips and tricks and review of the literature. *Injury* **46**, 1447-1456 (2015).

119. A. Mandal, V. Meda, W. J. Zhang, K. M. Farhan, A. Gnanamani, Synthesis, characterization and comparison of antimicrobial activity of PEG/TritonX-100 capped silver nanoparticles on collagen scaffold. *Colloids and surfaces. B, Biointerfaces* **90**, 191-196 (2012).

120. E. I. Alarcon, K. Udekwu, M. Skog, N. L. Pacioni, K. G. Stamplecoskie, M. Gonzalez-Bejar, N. Polisetti, A. Wickham, A. Richter-Dahlfors, M. Griffith, J. C. Scaiano, The biocompatibility and antibacterial properties of collagen-stabilized,

photochemically prepared silver nanoparticles. *Biomaterials* **33**, 4947-4956 (2012).

121. X. Chatzistavrou, J. C. Fenno, D. Faulk, S. Badylak, T. Kasuga, A. R. Boccaccini, P. Papagerakis, Fabrication and characterization of bioactive and antibacterial composites for dental applications. *Acta biomaterialia*, (2014).

122. S. Saravanan, S. Nethala, S. Pattnaik, A. Tripathi, A. Moorthi, N. Selvamurugan, Preparation, characterization and antimicrobial activity of a bio-composite scaffold containing chitosan/nano-hydroxyapatite/nano-silver for bone tissue engineering. *International journal of biological macromolecules* **49**, 188-193 (2011).

123. C. Wu, Y. Zhou, M. Xu, P. Han, L. Chen, J. Chang, Y. Xiao, Copper-containing mesoporous bioactive glass scaffolds with multifunctional properties of angiogenesis capacity, osteostimulation and antibacterial activity. *Biomaterials* **34**, 422-433 (2013).

124. Q. Wang, X. Yu, M. Libera, Reducing bacterial colonization of 3-d nanofiber cell scaffolds by hierarchical assembly of microgels and an antimicrobial Peptide. *Advanced healthcare materials* **2**, 687-691 (2013).

125. S. Kaur, K. Harjai, S. Chhibber, Bacteriophage mediated killing of Staphylococcus aureus in vitro on orthopaedic K wires in presence of linezolid prevents implant colonization. *PloS one* **9**, e90411 (2014).

126. E. Meurice, E. Rguiti, A. Brutel, J. C. Hornez, A. Leriche, M. Descamps, F. Bouchart, New antibacterial microporous CaP materials loaded with phages for prophylactic treatment in bone surgery. *Journal of materials science. Materials in medicine* **23**, 2445-2452 (2012).

127. J. Wang, Y. Zhu, H. K. Bawa, G. Ng, Y. Wu, M. Libera, H. C. van der Mei, H. J. Busscher, X. Yu, Oxygen-generating nanofiber cell scaffolds with antimicrobial properties. *ACS applied materials & interfaces* **3**, 67-73 (2011).

128. D. Huang, Y. Zuo, Q. Zou, L. Zhang, J. Li, L. Cheng, J. Shen, Y. Li, Antibacterial chitosan coating on nano-hydroxyapatite/polyamide66 porous bone scaffold for drug delivery. *Journal of biomaterials science. Polymer edition* **22**, 931-944 (2011).

129. C. J. Sanchez, Jr., E. M. Prieto, C. A. Krueger, K. J. Zienkiewicz, D. R. Romano, C. L. Ward, K. S. Akers, S. A. Guelcher, J. C. Wenke, Effects of local delivery of D-amino acids from biofilm-dispersive scaffolds on infection in contaminated rat segmental defects. *Biomaterials* **34**, 7533-7543 (2013).

130. M. N. Rahaman, B. S. Bal, W. Huang, Review: emerging developments in the use of bioactive glasses for treating infected prosthetic joints. *Materials science & engineering. C, Materials for biological applications* **41**, 224-231 (2014).

131. X. Cui, C. Zhao, Y. Gu, L. Li, H. Wang, W. Huang, N. Zhou, D. Wang, Y. Zhu, J. Xu, S. Luo, C. Zhang, M. N. Rahaman, A novel injectable borate bioactive glass cement for local delivery of vancomycin to cure osteomyelitis and regenerate bone. *Journal of materials science. Materials in medicine* **25**, 733-745 (2014).

132. W. T. Jia, X. Zhang, C. Q. Zhang, X. Liu, W. H. Huang, M. N. Rahaman, D. E. Day, Elution characteristics of teicoplanin-loaded biodegradable borate glass/chitosan composite. *International journal of pharmaceutics* **387**, 184-186 (2010).

133. S. I. Berrios-Torres, C. A. Umscheid, D. W. Bratzler, B. Leas, E. C. Stone, R. R. Kelz, C. E. Reinke, S. Morgan, J. S. Solomkin, J. E. Mazuski, E. P. Dellinger, K. M. F. Itani, E. F. Berbari, J. Segreti, J. Parvizi, J. Blanchard, G. Allen, J. Kluytmans, R. Donlan, W. P. Schecter, C. Healthcare Infection Control Practices Advisory, Centers for Disease Control and Prevention Guideline for the Prevention of Surgical Site Infection, 2017. *JAMA Surg* **152**, 784-791 (2017).

134. J. A. Inzana, E. M. Schwarz, S. L. Kates, H. A. Awad, Biomaterials approaches to treating implant-associated osteomyelitis. *Biomaterials* **81**, 58-71 (2016).

135. H. Maradit Kremers, D. R. Larson, C. S. Crowson, W. K. Kremers, R. E. Washington, C. A. Steiner, W. A. Jiranek, D. J. Berry, Prevalence of Total Hip and Knee Replacement in the United States. *The Journal of bone and joint surgery. American volume* **97**, 1386-1397 (2015).

136. V. Antoci, A. F. Chen, J. Parvizi, in *Comprehensive Biomaterials II*. (Elsevier, Oxford, 2017), pp. 133-151.

137. A. Trampuz, Windmer, Andreas, Infections associated with orthopedic implants. (2006).

138. L. F. Amorosa, L. D. Buirs, R. Bexkens, D. S. Wellman, P. Kloen, D. G. Lorich, D. L. Helfet, A single-stage treatment protocol for presumptive aseptic diaphyseal nonunions: a review of outcomes. *Journal of orthopaedic trauma* **27**, 582-586 (2013).

139. M. P. Palmer, D. T. Altman, G. T. Altman, J. J. Sewecke, G. D. Ehrlich, F. Z. Hu, L. Nistico, R. Melton-Kreft, T. M. Gause, 3rd, J. W. Costerton, Can we trust intraoperative culture results in nonunions? *Journal of orthopaedic trauma* **28**, 384-390 (2014).

140. F. Guarner, J. R. Malagelada, Gut flora in health and disease. *Lancet* **361**, 512-519 (2003).

141. V. K. Viswanathan, Off-label abuse of antibiotics by bacteria. *Gut Microbes* **5**, 3-4 (2014).

142. J. D. Bryers, Medical biofilms. *Biotechnology and bioengineering* **100**, 1-18 (2008).

143. H. C. Flemming, J. Wingender, The biofilm matrix. *Nat Rev Microbiol* **8**, 623-633 (2010).

144. P. S. Stewart, J. William Costerton, Antibiotic resistance of bacteria in biofilms. *The Lancet* **358**, 135-138 (2001).

145. I. Roca, M. Akova, F. Baquero, J. Carlet, M. Cavaleri, S. Coenen, J. Cohen, D. Findlay, I. Gyssens, O. E. Heuer, G. Kahlmeter, H. Kruse, R. Laxminarayan, E. Liebana, L. Lopez-Cerero, A. MacGowan, M. Martins, J. Rodriguez-Bano, J. M. Rolain, C. Segovia, B. Sigauque, E. Tacconelli, E. Wellington, J. Vila, The global threat of antimicrobial resistance: science for intervention. *New Microbes New Infect* **6**, 22-29 (2015).

146. A. Gründling, D. M. Missiakas, O. Schneewind, Staphylococcus aureus mutants with increased lysostaphin resistance. *Journal of bacteriology* **188**, 6286-6297 (2006).

147. S. Boyle-Vavra, R. B. Carey, R. S. Daum, Development of vancomycin and lysostaphin resistance in a methicillin-resistant Staphylococcus aureus isolate. *Journal of Antimicrobial Chemotherapy* **48**, 617-625 (2001).

148. S. Hogan, M. Zapotoczna, N. T. Stevens, H. Humphreys, J. P. O'Gara, E. O'Neill, Potential use of targeted enzymatic agents in the treatment of Staphylococcus aureus biofilm-related infections. *J Hosp Infect* **96**, 177-182 (2017).

149. J. J. Dajcs, E. B. Hume, J. M. Moreau, A. R. Caballero, B. M. Cannon, R. J. O'Callaghan, Lysostaphin treatment of methicillin-resistant Staphylococcus aureus keratitis in the rabbit. *Investigative ophthalmology & visual science* **41**, 1432-1437 (2000).

150. C. D. Windolf, T. Logters, M. Scholz, J. Windolf, S. Flohe, Lysostaphin-coated titan-implants preventing localized osteitis by Staphylococcus aureus in a mouse model. *PloS one* **9**, e115940 (2014).

151. K. E. Quickel, R. Selden, J. R. Caldwell, N. F. Nora, W. Schaffner, Efficacy and safety of topical lysostaphin treatment of persistent nasal carriage of Staphylococcus aureus. *Applied microbiology* **22**, 446-450 (1971).

152. F. R. Stark , C. Thornsvard , E. P. Flannery , M. S. Artenstein Systemic Lysostaphin in Man — Apparent Antimicrobial Activity in a Neutropenic Patient. *New England Journal of Medicine* **291**, 239-240 (1974).

153. S. Walsh, A. Shah, J. Mond, Improved Pharmacokinetics and Reduced Antibody Reactivity of Lysostaphin Conjugated to Polyethylene Glycol. *Antimicrobial agents and chemotherapy* **47**, 554-558 (2003).

154. I. Belyansky, V. B. Tsirline, T. R. Martin, D. A. Klima, J. Heath, A. E. Lincourt, R. Satishkumar, A. Vertegel, B. T. Heniford, The addition of lysostaphin dramatically improves survival, protects porcine biomesh from infection, and improves graft tensile shear strength. *The Journal of surgical research* **171**, 409-415 (2011).

155. J. Miao, R. C. Pangule, E. E. Paskaleva, E. E. Hwang, R. S. Kane, R. J. Linhardt, J. S. Dordick, Lysostaphin-functionalized cellulose fibers with antistaphylococcal activity for wound healing applications. *Biomaterials* **32**, 9557-9567 (2011).

156. G. Yeroslavsky, O. Girshevitz, J. Foster-Frey, D. M. Donovan, S. Rahimipour, Antibacterial and antibiofilm surfaces through polydopamine-assisted immobilization of lysostaphin as an antibacterial enzyme. *Langmuir : the ACS journal of surfaces and colloids* **31**, 1064-1073 (2015).

157. C. T. Johnson, A. J. Garcia, Scaffold-based Anti-infection Strategies in Bone Repair. *Annals of biomedical engineering*, (2014).

158. G.-J. A. ter Boo, D. W. Grijpma, T. F. Moriarty, R. G. Richards, D. Eglin, Antimicrobial delivery systems for local infection prophylaxis in orthopedic- and trauma surgery. *Biomaterials* **52**, 113-125 (2015).

159. B. V. Slaughter, S. S. Khurshid, O. Z. Fisher, A. Khademhosseini, N. A. Peppas, Hydrogels in regenerative medicine. *Advanced materials* **21**, 3307-3329 (2009).

160. J. R. Garcia, A. Y. Clark, A. J. Garcia, Integrin-specific hydrogels functionalized with VEGF for vascularization and bone regeneration of critical-size bone defects. *Journal of biomedical materials research. Part A* **104**, 889-900 (2016).

161. T. T. Lee, J. R. Garcia, J. I. Paez, A. Singh, E. A. Phelps, S. Weis, Z. Shafiq, A. Shekaran, A. Del Campo, A. J. Garcia, Light-triggered in vivo activation of adhesive peptides regulates cell adhesion, inflammation and vascularization of biomaterials. *Nature materials* **14**, 352-360 (2015).

162. E. A. Phelps, N. O. Enemchukwu, V. F. Fiore, J. C. Sy, N. Murthy, T. A. Sulchek, T. H. Barker, A. J. Garcia, Maleimide cross-linked bioactive PEG hydrogel exhibits improved reaction kinetics and cross-linking for cell encapsulation and in situ delivery. *Advanced materials* **24**, 64-70, 62 (2012).

163. E. A. Phelps, D. M. Headen, W. R. Taylor, P. M. Thule, A. J. Garcia, Vasculogenic bio-synthetic hydrogel for enhancement of pancreatic islet engraftment and function in type 1 diabetes. *Biomaterials* **34**, 4602-4611 (2013).

164. A. Shekaran, J. R. Garcia, A. Y. Clark, T. E. Kavanaugh, A. S. Lin, R. E. Guldberg, A. J. Garcia, Bone regeneration using an alpha 2 beta 1 integrin-specific hydrogel as a BMP-2 delivery vehicle. *Biomaterials*, (2014).

165. J. D. Weaver, D. M. Headen, J. Aquart, C. T. Johnson, L. D. Shea, H. Shirwan, A. J. Garcia, Vasculogenic hydrogel enhances islet survival, engraftment, and function in leading extrahepatic sites. *Science advances* **3**, e1700184 (2017).

166. J. Patterson, J. A. Hubbell, Enhanced proteolytic degradation of molecularly engineered PEG hydrogels in response to MMP-1 and MMP-2. *Biomaterials* **31**, 7836-7845 (2010).

167. I. Sabala, I. M. Jonsson, A. Tarkowski, M. Bochtler, Anti-staphylococcal activities of lysostaphin and LytM catalytic domain. *BMC Microbiol* **12**, 97 (2012).

168. A. F. Gillaspy, S. G. Hickmon, R. A. Skinner, J. R. Thomas, C. L. Nelson, M. S. Smeltzer, Role of the accessory gene regulator (agr) in pathogenesis of staphylococcal osteomyelitis. *Infection and immunity* **63**, 3373-3380 (1995).

169. R. D. Wolcott, D. D. Rhoads, S. E. Dowd, Biofilms and chronic wound inflammation. *Journal of wound care* **17**, (2008).

170. B. A. Diep, S. R. Gill, R. F. Chang, T. H. Phan, J. H. Chen, M. G. Davidson, F. Lin, J. Lin, H. A. Carleton, E. F. Mongodin, G. F. Sensabaugh, F. Perdreau-Remington, Complete genome sequence of USA300, an epidemic clone of community-acquired meticillin-resistant Staphylococcus aureus. *Lancet* **367**, 731-739 (2006).

171. K. H. Park, K. E. Greenwood-Quaintance, A. N. Schuetz, J. N. Mandrekar, R. Patel, Activity of Tedizolid in Methicillin-Resistant Staphylococcus epidermidis Experimental Foreign Body-Associated Osteomyelitis. *Antimicrobial agents and chemotherapy* **61**, (2017).

172. R. P. Evans, C. L. Nelson, W. R. Bowen, M. G. Kleve, S. G. Hickmon, Visualization of bacterial glycocalyx with a scanning electron microscope. *Clinical orthopaedics and related research*, 243-249 (1998).

173. A. Shekaran, J. T. Shoemaker, T. E. Kavanaugh, A. S. Lin, M. C. LaPlaca, Y. Fan, R. E. Guldberg, A. J. Garcia, The effect of conditional inactivation of beta 1 integrins using twist 2 Cre, Osterix Cre and osteocalcin Cre lines on skeletal phenotype. *Bone* **68**, 131-141 (2014).

174. G. Yeroslavsky, O. Girshevitz, J. Foster-Frey, D. M. Donovan, S. Rahimipour, Antibacterial and Antibiofilm Surfaces through Polydopamine-Assisted Immobilization of Lysostaphin as an Antibacterial Enzyme. *Langmuir : the ACS journal of surfaces and colloids* **31**, 1064-1073 (2015).

175. H. Hathaway, J. Ajuebor, L. Stephens, A. Coffey, U. Potter, J. M. Sutton, A. T. A. Jenkins, Thermally triggered release of the bacteriophage endolysin CHAPK and the bacteriocin lysostaphin for the control of methicillin resistant Staphylococcus aureus (MRSA). *Journal of Controlled Release* **245**, 108-115 (2017).

176. J. J. Dajcs, B. A. Thibodeaux, D. O. Girgis, M. D. Shaffer, S. M. Delvisco, R. J. O'Callaghan, Immunity to lysostaphin and its therapeutic value for ocular MRSA infections in the rabbit. *Investigative ophthalmology & visual science* **43**, 3712-3716 (2002).

177. K. Blazanovic, H. Zhao, Y. Choi, W. Li, R. S. Salvat, D. C. Osipovitch, J. Fields, L. Moise, B. L. Berwin, S. N. Fiering, Structure-based redesign of lysostaphin yields potent antistaphylococcal enzymes that evade immune cell surveillance. *Molecular therapy. Methods & clinical development* **2**, 15021 (2015).

178. H. Zhao, D. Verma, W. Li, Y. Choi, C. Ndong, S. N. Fiering, C. Bailey-Kellogg, K. E. Griswold, Depletion of T cell epitopes in lysostaphin mitigates anti-drug antibody response and enhances antibacterial efficacy in vivo. *Chem Biol* **22**, 629-639 (2015).

179. J. Raphel, M. Holodniy, S. B. Goodman, S. C. Heilshorn, Multifunctional coatings to simultaneously promote osseointegration and prevent infection of orthopaedic implants. *Biomaterials* **84**, 301-314 (2016).

180. S. B. Goodman, Z. Yao, M. Keeney, F. Yang, The future of biologic coatings for orthopaedic implants. *Biomaterials* **34**, 3174-3183 (2013).

181. C. D. Reyes, A. J. Garcia, Alpha2beta1 integrin-specific collagen-mimetic surfaces supporting osteoblastic differentiation. *Journal of biomedical materials research. Part A* **69**, 591-600 (2004).

182. E. O'Neill, C. Pozzi, P. Houston, D. Smyth, H. Humphreys, D. A. Robinson, J. P. O'Gara, Association between methicillin susceptibility and biofilm regulation in Staphylococcus aureus isolates from device-related infections. *Journal of clinical microbiology* **45**, 1379-1388 (2007).

183. M. M. Williams, M. A. Yakrus, M. J. Arduino, R. C. Cooksey, C. B. Crane, S. N. Banerjee, E. D. Hilborn, R. M. Donlan, Structural analysis of biofilm formation by rapidly and slowly growing nontuberculous mycobacteria. *Appl Environ Microbiol* **75**, 2091-2098 (2009).

184. M. Kadhim, L. Holmes Jr, M. G. Gesheff, J. D. Conway, Treatment Options for Nonunion With Segmental Bone Defects: Systematic Review and Quantitative Evidence Synthesis. *Journal of orthopaedic trauma* **31**, 111-119 (2017).

185. R. W. Bucholz, Nonallograft osteoconductive bone graft substitutes. *Clinical orthopaedics and related research*, 44-52 (2002).

186. J. D. Kretlow, A. G. Mikos, Review: mineralization of synthetic polymer scaffolds for bone tissue engineering. *Tissue engineering* **13**, 927-938 (2007).

187. J. I. Sorger, F. J. Hornicek, M. Zavatta, J. P. Menzner, M. C. Gebhardt, W. W. Tomford, H. J. Mankin, Allograft fractures revisited. *Clinical orthopaedics and related research*, 66-74 (2001).

188. M. K. Sen, T. Miclau, Autologous iliac crest bone graft: Should it still be the gold standard for treating nonunions? *Injury* **38**, S75-S80 (2007).

189. C. E. Schwartz, J. F. Martha, P. Kowalski, D. A. Wang, R. Bode, L. Li, D. H. Kim, Prospective evaluation of chronic pain associated with posterior autologous iliac crest bone graft harvest and its effect on postoperative outcome. *Health and quality of life outcomes* **7**, 49 (2009).

190. N. Bormann, P. Schwabe, M. D. Smith, B. Wildemann, Analysis of parameters influencing the release of antibiotics mixed with bone grafting material using a reliable mixing procedure. *Bone*, (2013).

191. A. Matsuno, H. Tanaka, H. Iwamuro, S. Takanashi, S. Miyawaki, M. Nakashima, H. Nakaguchi, T. Nagashima, Analyses of the factors influencing bone graft infection after delayed cranioplasty. *Acta neurochirurgica* **148**, 535-540; discussion 540 (2006).

192. A. Gründling, O. Schneewind, Cross-linked peptidoglycan mediates lysostaphin binding to the cell wall envelope of Staphylococcus aureus. *Journal of bacteriology* **188**, 2463-2472 (2006).

193. A. P. Desbois, C. G. Gemmell, P. J. Coote, In vivo efficacy of the antimicrobial peptide ranalexin in combination with the endopeptidase lysostaphin against wound and systemic meticillin-resistant Staphylococcus aureus (MRSA) infections. *International journal of antimicrobial agents* **35**, 559-565 (2010).

194. W. Schaffner, M. Melly, M. Koenig, Lysostaphin: an enzymatic approach to staphylococcal disease. II. In vivo studies. *The Yale journal of biology and medicine* **39**, 230 (1967).

195. J. F. Kokai-Kun, S. M. Walsh, T. Chanturiya, J. J. Mond, Lysostaphin cream eradicates Staphylococcus aureus nasal colonization in a cotton rat model. *Antimicrobial agents and chemotherapy* **47**, 1589-1597 (2003).

196. B. Xue, C. Zhang, Y. Wang, J. Wang, J. Zhang, M. Lu, G. Li, Z. Cao, Q. Huang, A novel controlled-release system for antibacterial enzyme lysostaphin delivery using hydroxyapatite/chitosan composite bone cement. *PLoS One* **9**, e113797 (2014).

197. F. Cui, G. Li, J. Huang, J. Zhang, M. Lu, W. Lu, J. Huan, Q. Huang, Development of chitosan-collagen hydrogel incorporated with lysostaphin (CCHL) burn dressing with anti-methicillin-resistant Staphylococcus aureus and promotion wound healing properties. *Drug Deliv* **18**, 173-180 (2011).

198. F. Cui, G. Li, J. Huang, J. Zhang, M. Lu, W. Lu, Q. Huang, Extension of nasal anti-Staphylococcus aureus efficacy of lysostaphin by its incorporation into a chitosan-o/w cream. *Drug Deliv* **17**, 617-623 (2010).

199. S. Walsh, J. Kokai-Kun, A. Shah, J. Mond, Extended nasal residence time of lysostaphin and an anti-staphylococcal monoclonal antibody by delivery in semisolid or polymeric carriers. *Pharm Res* **21**, 1770-1775 (2004).

200. G. Tegos, E. Mylonakis, *Antimicrobial drug discovery : emerging strategies*. Advances in molecular and cellular microbiology (CABI, Wallingford, Oxfordshire, 2012), pp. x, 357 p.

201. S. D. Boden, T. A. Zdeblick, H. S. Sandhu, S. E. Heim, The use of rhBMP-2 in interbody fusion cages. Definitive evidence of osteoinduction in humans: a preliminary report. *Spine* **25**, 376-381 (2000).

202. A. R. Vaccaro, P. G. Whang, T. Patel, F. M. Phillips, D. G. Anderson, T. J. Albert, A. S. Hilibrand, R. S. Brower, M. F. Kurd, A. Appannagari, M. Patel, J. S. Fischgrund, The safety and efficacy of OP-1 (rhBMP-7) as a replacement for iliac crest autograft for posterolateral lumbar arthrodesis: minimum 4-year follow-up of a pilot study. *The spine journal : official journal of the North American Spine Society* **8**, 457-465 (2008).

203. D. Neen, D. Noyes, M. Shaw, S. Gwilym, N. Fairlie, N. Birch, Healos and bone marrow aspirate used for lumbar spine fusion: a case controlled study comparing healos with autograft. *Spine* **31**, E636-640 (2006).

204. J. K. Burkus, M. F. Gornet, C. A. Dickman, T. A. Zdeblick, Anterior lumbar interbody fusion using rhBMP-2 with tapered interbody cages. *Journal of spinal disorders & techniques* **15**, 337-349 (2002).

205. J. W. Hustedt, D. J. Blizzard, The Controversy Surrounding Bone Morphogenetic Proteins in the Spine: A Review of Current Research. *The Yale Journal of Biology and Medicine* **87**, 549-561 (2014).

206. H. P. Stallmann, C. Faber, A. L. Bronckers, A. V. Nieuw Amerongen, P. I. Wuisman, In vitro gentamicin release from commercially available calcium-phosphate bone substitutes influence of carrier type on duration of the release profile. *BMC Musculoskelet Disord* **7**, 18 (2006).

207. J. S. Moskowitz, M. R. Blaisse, R. E. Samuel, H. P. Hsu, M. B. Harris, S. D. Martin, J. C. Lee, M. Spector, P. T. Hammond, The effectiveness of the controlled release of gentamicin from polyelectrolyte multilayers in the treatment of Staphylococcus aureus infection in a rabbit bone model. *Biomaterials* **31**, 6019-6030 (2010).

208. G. P. Otto, B. Rathkolb, M. A. Oestereicher, C. J. Lengger, C. Moerth, K. Micklich, H. Fuchs, V. Gailus-Durner, E. Wolf, M. H. de Angelis, Clinical Chemistry Reference Intervals for C57BL/6J, C57BL/6N, and C3HeB/FeJ Mice (Mus musculus). *Journal of the American Association for Laboratory Animal Science : JAALAS* **55**, 375-386 (2016).

209. S. K. Ramaiah, A toxicologist guide to the diagnostic interpretation of hepatic biochemical parameters. *Food and Chemical Toxicology* **45**, 1551-1557 (2007).

210. R. Prabhakara, J. M. Harro, J. G. Leid, M. Harris, M. E. Shirtliff, Murine immune response to a chronic Staphylococcus aureus biofilm infection. *Infection and immunity* **79**, 1789-1796 (2011).

211. G. A. Koretzky, Multiple Roles of CD4 and CD8 in T Cell Activation. *The Journal of Immunology* **185**, 2643 (2010).

212. R. H. Scheuermann, E. Racila, CD19 antigen in leukemia and lymphoma diagnosis and immunotherapy. *Leukemia & lymphoma* **18**, 385-397 (1995).

213. K. Wang, G. Wei, D. Liu, CD19: a biomarker for B cell development, lymphoma diagnosis and therapy. *Experimental Hematology & Oncology* **1**, 36-36 (2012).

214. A. V. Misharin, L. Morales-Nebreda, G. M. Mutlu, G. R. S. Budinger, H. Perlman, Flow Cytometric Analysis of Macrophages and Dendritic Cell Subsets in the Mouse Lung. *American Journal of Respiratory Cell and Molecular Biology* **49**, 503-510 (2013).

215. A. O. Awojoodu, M. E. Ogle, L. S. Sefcik, D. T. Bowers, K. Martin, K. L. Brayman, K. R. Lynch, S. M. Peirce-Cottler, E. Botchwey, Sphingosine 1-phosphate receptor 3 regulates recruitment of anti-inflammatory monocytes to microvessels during implant arteriogenesis. *Proceedings of the National Academy of Sciences of the United States of America* **110**, 13785-13790 (2013).

216. F. Geissmann, S. Jung, D. R. Littman, Blood monocytes consist of two principal subsets with distinct migratory properties. *Immunity* **19**, 71-82 (2003).

217. M. M. Mircescu, L. Lipuma, N. van Rooijen, E. G. Pamer, T. M. Hohl, Essential role for neutrophils but not alveolar macrophages at early time points following Aspergillus fumigatus infection. *The Journal of infectious diseases* **200**, 647-656 (2009).

218. C. K. Murray, J. R. Hsu, J. S. Solomkin, J. J. Keeling, R. C. Andersen, J. R. Ficke, J. H. Calhoun, Prevention and management of infections associated with combat-related extremity injuries. *Journal of Trauma and Acute Care Surgery* **64**, S239-S251 (2008).

219. W. Obremskey, C. Molina, C. Collinge, P. Tornetta, C. Sagi, A. Schmidt, R. Probe, J. Ahn, A. Nana, Current Practice in the Management of Open Fractures Among Orthopaedic Trauma Surgeons. Part B. *Journal of orthopaedic trauma* **28**, e203-e207 (2014).

220. V. Chadayammuri, M. Hake, C. Mauffrey, Innovative strategies for the management of long bone infection: a review of the Masquelet technique. *Patient Safety in Surgery* **9**, 32 (2015).

221. H. Lu, Y. Liu, J. Guo, H. Wu, J. Wang, G. Wu, Biomaterials with Antibacterial and Osteoinductive Properties to Repair Infected Bone Defects. *International Journal of Molecular Sciences* **17**, 334 (2016).

222. A. J. Harmata, Y. Ma, C. J. Sanchez, K. J. Zienkiewicz, F. Elefteriou, J. C. Wenke, S. A. Guelcher, d-amino Acid Inhibits Biofilm but not New Bone Formation in an Ovine Model. *Clinical Orthopaedics and Related Research®* **473**, 3951-3961 (2015).

223. E. J. Kwon, M. Skalak, A. Bertucci, G. Braun, F. Ricci, E. Ruoslahti, M. J. Sailor, S. N. Bhatia, Porous Silicon Nanoparticle Delivery of Tandem Peptide Anti-Infectives for the Treatment of Pseudomonas aeruginosa Lung Infections. *Advanced materials* **29**, 1701527-n/a (2017).

224. S. Lin, C. Mauffrey, E. M. Hammerberg, P. F. Stahel, D. J. Hak, Surgical site infection after open reduction and internal fixation of tibial plateau fractures. *European Journal of Orthopaedic Surgery & Traumatology* **24**, 797-803 (2014).

225. C. A. Willis-Owen, A. Konyves, D. K. Martin, Factors affecting the incidence of infection in hip and knee replacement. *Journal of Bone & Joint Surgery, British Volume* **92-B**, 1128 (2010).

226. C. Shi, E. G. Pamer, Monocyte recruitment during infection and inflammation. *Nature Reviews Immunology* **11**, 762 (2011).

227. C. Nathan, Neutrophils and immunity: challenges and opportunities. *Nature Reviews Immunology* **6**, 173 (2006).

228. M. McHeyzer-Williams, S. Okitsu, N. Wang, L. McHeyzer-Williams, Molecular programming of B cell memory. *Nat Rev Immunol* **12**, 24-34 (2011).

229. B. M. Bröker, D. Mrochen, V. Péton, The T Cell Response to Staphylococcus aureus. *Pathogens* **5**, 31 (2016).

230. C. E. Heim, D. Vidlak, T. Kielian, Interleukin-10 production by myeloid-derived suppressor cells contributes to bacterial persistence during Staphylococcus aureus orthopedic biofilm infection. *Journal of leukocyte biology* **98**, 1003-1013 (2015).

231. C. E. Heim, D. Vidlak, T. D. Scherr, C. W. Hartman, K. L. Garvin, T. Kielian, IL-12 promotes myeloid-derived suppressor cell recruitment and bacterial persistence during Staphylococcus aureus orthopedic implant infection. *Journal of immunology* **194**, 3861-3872 (2015).

232. C. E. Heim, D. Vidlak, T. D. Scherr, J. A. Kozel, M. Holzapfel, D. E. Muirhead, T. Kielian, Myeloid-derived suppressor cells contribute to Staphylococcus aureus orthopedic biofilm infection. *Journal of immunology* **192**, 3778-3792 (2014).

233. J. M. Wagner, H. Jaurich, C. Wallner, S. Abraham, M. Becerikli, M. Dadras, K. Harati, V. Duhan, V. Khairnar, M. Lehnhardt, B. Behr, Diminished bone regeneration after debridement of posttraumatic osteomyelitis is accompanied by altered cytokine levels, elevated B cell activity, and increased osteoclast activity. *Journal of orthopaedic research : official publication of the Orthopaedic Research Society* **35**, 2425-2434 (2017).

234. E. T. J. Rochford, M. Sabaté Brescó, S. Zeiter, K. Kluge, A. Poulsson, M. Ziegler, R. G. Richards, L. O'Mahony, T. F. Moriarty, Monitoring immune responses in a mouse model of fracture fixation with and without Staphylococcus aureus osteomyelitis. *Bone* **83**, 82-92 (2016).

235. D. Vidlak, T. Kielian, Infectious Dose Dictates the Host Response during Staphylococcus aureus Orthopedic-Implant Biofilm Infection. *Infection and immunity* **84**, 1957-1965 (2016).

236. J. R. Garcia, A. Y. Clark, A. J. Garcia, Integrin-specific hydrogels functionalized with VEGF for vascularization and bone regeneration of critical-size bone defects. *Journal of biomedical materials research. Part A* **104**, 1845 (2016).

237. M. C. P. Sok, M. C. Tria, C. E. Olingy, C. L. San Emeterio, E. A. Botchwey, Aspirin-Triggered Resolvin D1-modified materials promote the accumulation of pro-regenerative immune cell subsets and enhance vascular remodeling. *Acta biomaterialia* **53**, 109-122 (2017).

238. N. Bormann, P. Schwabe, M. D. Smith, B. Wildemann, Analysis of parameters influencing the release of antibiotics mixed with bone grafting material using a reliable mixing procedure. *Bone* **59**, 162-172 (2014).

239. T. Moriarty, D. Grainger, R. Richards, Challenges in linking preclinical anti-microbial research strategies with clinical outcomes for device-associated infections. *European cells & materials* **28**, 112-128 (2014).

240. T. D. Scherr, C. E. Heim, J. M. Morrison, T. Kielian, Hiding in Plain Sight: Interplay between Staphylococcal Biofilms and Host Immunity. *Front Immunol* **5**, 37 (2014).

241. W. Obremskey, C. Molina, C. Collinge, P. Tornetta III, C. Sagi, A. Schmidt, R. Probe, J. Ahn, A. Nana, Current practice in the management of open fractures among orthopaedic trauma surgeons. Part B: Management of segmental long bone

defects. A survey of orthopaedic trauma association members. *Journal of orthopaedic trauma* **28**, e203-e207 (2014).

242. J. Z. Lu, T. Fujiwara, H. Komatsuzawa, M. Sugai, J. Sakon, Cell wall-targeting domain of glycylglycine endopeptidase distinguishes among peptidoglycan cross-bridges. *Journal of Biological Chemistry* **281**, 549-558 (2006).

243. J. M. Wagner, H. Zöllner, C. Wallner, B. Ismer, J. Schira, S. Abraham, K. Harati, M. Lehnhardt, B. Behr, Surgical debridement is superior to sole antibiotic therapy in a novel murine posttraumatic osteomyelitis model. *PloS one* **11**, e0149389 (2016).

244. J. M. Wagner, H. Jaurich, C. Wallner, S. Abraham, M. Becerikli, M. Dadras, K. Harati, V. Duhan, V. Khairnar, M. Lehnhardt, B. Behr, Diminished bone regeneration after debridement of posttraumatic osteomyelitis is accompanied by altered cytokine levels, elevated B cell activity, and increased osteoclast activity. *Journal of Orthopaedic Research*, n/a-n/a (2017).

245. D. H. Dusane, D. Kyrouac, I. Petersen, L. Bushrow, J. H. Calhoun, J. F. Granger, L. S. Phieffer, P. Stoodley, Targeting intracellular Staphylococcus aureus to lower recurrence of orthopaedic infection. *Journal of Orthopaedic Research*, (2017).

246. T. J. Foster, J. A. Geoghegan, V. K. Ganesh, M. Hook, Adhesion, invasion and evasion: the many functions of the surface proteins of Staphylococcus aureus. *Nat Rev Microbiol* **12**, 49-62 (2014).

247. S. C. Becker, D. R. Roach, V. S. Chauhan, Y. Shen, J. Foster-Frey, A. M. Powell, G. Bauchan, R. A. Lease, H. Mohammadi, W. J. Harty, C. Simmons, M. Schmelcher, M. Camp, S. Dong, J. R. Baker, T. R. Sheen, K. S. Doran, D. G. Pritchard, R. A. Almeida, D. C. Nelson, I. Marriott, J. C. Lee, D. M. Donovan, Triple-acting Lytic Enzyme Treatment of Drug-Resistant and Intracellular Staphylococcus aureus. *Scientific reports* **6**, 25063 (2016).

248. P. M. Tulkens, Intracellular distribution and activity of antibiotics. *Eur J Clin Microbiol Infect Dis* **10**, 100-106 (1991).

249. B.-N. Kim, E. S. Kim, M.-D. Oh, Oral antibiotic treatment of staphylococcal bone and joint infections in adults. *Journal of Antimicrobial Chemotherapy* **69**, 309-322 (2014).

250. W. Zimmerli, A. F. Widmer, M. Blatter, R. Frei, P. E. Ochsner, Role of rifampin for treatment of orthopedic implant-related staphylococcal infections: a randomized controlled trial. Foreign-Body Infection (FBI) Study Group. *JAMA : the journal of the American Medical Association* **279**, 1537-1541 (1998).

251. J. Perlroth, M. Kuo, J. Tan, A. S. Bayer, L. G. Miller, Adjunctive use of rifampin for the treatment of Staphylococcus aureus infections: a systematic review of the literature. *Arch Intern Med* **168**, 805-819 (2008).

252. V. Thammavongsa, H. K. Kim, D. Missiakas, O. Schneewind, Staphylococcal manipulation of host immune responses. *Nature Reviews Microbiology* **13**, 529 (2015).

253. C. M. Gries, T. Kielian, Staphylococcal Biofilms and Immune Polarization During Prosthetic Joint Infection. *J Am Acad Orthop Surg* **25 Suppl 1**, S20-S24 (2017).

254. M. Otto, in *Staphylococcus Epidermidis: Methods and Protocols*, P. D. Fey, Ed. (Humana Press, Totowa, NJ, 2014), pp. 17-31.